TECHNICAL REPORT

Remediation and Treatment Technology Development and Support for DOE Oak Ridge Office: Simulation of NPDES- and TMDL-Regulated Discharges from Non-Point Sources for the EFPC and Y-12 NSC

Date submitted:

July 31, 2014

Principal Investigators:

Leonel E. Lagos, PhD, PMP®

Florida International University Collaborators:

Georgio Tachiev, PhD, PE (Project Manager)
Angelique Lawrence, MS, GISP
David Roelant, PhD
Siamak Malek-Mohammadi, PhD
Amy Cook, MS
Mandar Zope, MS
Lilian Marrero, MS and DOE Fellow
Heidi Henderson, PE, MS and DOE Fellow
Elsa Cabrejo, MS and DOE Fellow
Nantaporn Noosai, PhD
Viviana Villamizar, MS
Michelle Embon, DOE Fellow

Submitted to:

U.S. Department of Energy
Office of Environmental Management
Under Grant # DE-EM0000598

FIU | Applied Research Center
FLORIDA INTERNATIONAL UNIVERSITY

DISCLAIMER

EXECUTIVE SUMMARY

The research is this report is the final documentation of a multiple year effort by Florida International University to correlate the hydrology of East Fork Poplar Creek (EFPC), White Oak Creek (WOC) and Bear Creek (BC) with the long-term distribution of mercury within the overland, subsurface, and river sub-domains. One objective of this study was to add a sedimentation module (ECO Lab) to FIU's integrated surface and groundwater models. This sedimentation module has been developed and shown to be capable of simulating the reactive transport mercury exchange mechanisms within sediments and porewater throughout the EFPC watershed. The enhanced model was then applied to a Total Maximum Daily Load (TMDL) mercury analysis for EFPC. That application used historical precipitation, groundwater levels, river discharges, and mercury concentrations data that were retrieved from government databases and input to the model. The model was run to reduce computational time, predict flow discharges, total mercury concentration, flow duration and mercury load curves at key monitoring stations under various hydrological and environmental conditions and scenarios. The computational results provided much detail on the relationship between discharges and mercury loads at various stations throughout EFPC, which is important to best understand and support the management of mercury contamination and remediation efforts within EFPC. The coupling of equilibrium chemical reactions with transport processes in the model PHREEQC offers an advantage in simulating and predicting the fate and transport of aqueous chemical species of interest. Thus, a great variety of reactive transport problems could be addressed in aquatic systems with boundary conditions of specific interest. Nevertheless, PHREEQC lacks a comprehensive thermodynamic database for Hg. Therefore, in order to use PHREEQC to address the fate and transport of Hg in aquatic environments, it was necessary to expand its thermodynamic database, confirm it and then evaluate it in applications where data exists for its calibration and continued validation.

The objectives of the thermodynamic study were twofold: 1) to develop, expand, and confirm the Hg database of the hydrogeochemical PHREEQC to enhance its capability to simulate the fate of Hg species in the presence of complexing constituents and natural sorbents under different conditions of pH, redox, salinity and temperature; and 2) to apply and evaluate the new database

in flow and transport scenarios at two field test beds: Oak Ridge Reservation, Oak Ridge, TN and Everglades National Park, FL, where Hg is present and is of much concern.

Overall, this research enhanced the capability of the PHREEQC model to simulate the coupling of the Hg reactions in transport conditions. It also demonstrated its usefulness when applied to field applications.

TABLE OF CONTENTS

LIST OF TABLES

LIST OF FIGURES

LIST OF ACRONYMS

ARC	Applied Research Center at Florida International University
BC	Bear Creek
CI	Confidence Interval
DHI	Danish Hydraulic Institute
DOE	Department of Energy
EFPC	East Fork Poplar Creek
EPA	Environmental Protection Agency
OREIS	Oak Ridge Environmental Information System
ORNL	Oak Ridge National Laboratory
ORR	Oak Ridge Reservation
PPT	Parts Per Trillion
ROD	Record of Decision
RMSE	Root Mean Square Error
TMDL	Total Maximum Daily Load
TSS	Total Suspended Solids
UEFPC	Upper East Fork Poplar Creek
USGS	United States Geological Survey
Y-12	Y-12 National Security Complex

LIST OF VARIABLES

A_{fl}	Cross sectional area
AD_c	ECO Lab advection-dispersion coefficient
adss	Adsorption
c	ECO Lab concentration
C	Soil water capacity
dess	Desorption
difv	Diffusion transfer coefficient in water
dz	Computational grid layer thickness
dzds	Thickness of diffusion layer in sediment
dzwf	Average thickness of water film through which metals diffuse
D_x, D_y, D_z	Dispersion coefficients in the x,y, and z-direction
$f_{biot \cdot difw}$	Factor for diffusion due to bioturbation
h	Flow depth or hydraulic head
k_a	Adsorption rate [d^{-1}]
K_d	Mercury partitioning coefficient between particulate matter and water
K_{ds}	Mercury partitioning coefficient between sediment and pore water
K_s	Saturated hydraulic conductivity
k_s	Desorption rate in sediment [d^{-1}]
k_w	Desorption rate [d^{-1}]
M	Manning's M, the reciprocal of Manning's n (1/n)
P_c	ECO Lab processes

pors	Porosity of sediment
PPR	Particle production rate [g/m^{2}d]
q	Volumetric flow or discharge
resv	Resuspension
RR	Resuspension rate [g/m^{2}d]
S	Specific storage coefficient
S_c	ECO Lab sources and sinks
sev	Sedimentation
S_{fx}, S_{fy}	Friction slopes in x and y-direction
S_{HM}	Dissolved mercury concentration in water
S_{HMS}	Dissolved mercury concentration in sediment pore water
t	Time
TSS	Total suspended solids concentration
u, *v*, *w*	Flow velocities in the x, y, and z-direction
uh, *vh*	Discharge per unit length in x and y-direction
v_s	Settling velocity [m/d]
v_c	Critical current velocity for initiation of the movement [m/s]
X_{HM}	Adsorbed mercury concentration in suspended matter
X_{HMS}	Adsorbed mercury concentration in sediment
X_{SED}	Mass of sediment
Z	Ground surface elevation

INTRODUCTION

The United States Department of Energy (DOE) decontamination and decommissioning activities of industrial, radiological and nuclear facilities seek to restore environmental conditions of contaminated sites to accepted levels designated by local, state and federal regulations. The East Fork Poplar Creek (EFPC) Watershed, shown in Figure 1, is located in the state of Tennessee and represents one of several DOE sites for which the mission of remediation is of extreme importance. The Oak Ridge Reservation (ORR) has been on the Comprehensive Environmental Response, Compensation, and Liability Act (CERCLA) National Priorities List since November 21, 1989 (DOE, 2005). Upstream EFPC (UEFPC) is subject to a complex array of contamination sources including but not limited to uranium, nitrate, boron, cadmium, chromium, polychlorinated biphenyls, and volatile organic compounds (VOCs) such as trichloroethene, tetrachloroethene, and 1,2,-dichloroethene (DOE, DOE/OR/01-1641/V1&D2, 1998). Mercury contamination is the focus of this study.

Several studies have used computer modeling to highlight the importance of sediments and suspended matter in the fate and transport of contaminants in the aquatic environment. The North Carolina Department of Natural Resources estimated that eroded sediments were the source of about 75% of the total mercury load in the Cashie River Watershed [13]. At Lahontan Reservoir in southwestern Nevada (USA), 90% of the mercury that entered the system was retained by sediments and kept as a continuous source of pollution [28]. At the White Oak Creek watershed in Tennessee, the major source of cesium-137 (a contaminant that tends to bind to suspended solids) in surface water was channel bed sediments [1].

Different computer model approaches have been used to study the effects of sediment as a source of contaminants. Bao (1999) developed a sediment transport study using a hydrological simulation program in Fortran, for cesium-137 at the White Oak Creek watershed in Tennessee. The US Environmental Protection Agency used the IEM-2M model to estimate mercury concentrations, dissolved and particle-bound, in the water column and in bed sediments [59], mass balance equations accounted for the sources of mercury loadings (runoff, soil erosion and diffusive transport from the atmosphere), as well as for sinks (burial in bed sediments, volatilization, and advection out of the water body). At the Cashie River Watershed and other

Georgia rivers, a combination of the Watershed Characterization System (WCS) developed by Tetra Tech, and the WASP-TOXI computer model were used to support the development of total maximum daily loads [13]. At the Lahontan Reservoir in southwestern Nevada, a kinetic speciation mercury transport computer model, BIOTRANSPEC, was developed based on mass balance calculations, the model simulates dissolved, colloidal and particulate mercury concentrations in the water-sediment interface [28].

Kubawara et al. (2002) developed a mercury flux (internal recycling) study for the bottom sediment-water column interface in the Lahontan Reservoir, Nevada. The objective of this study was to measure the benthic flux of dissolved mercury and methyl mercury. The results showed that the interaction occurs both ways, with dissolved mercury moving into the water column from the sediment (positive flux) or moving out of the water column into the sediment (negative flux). In addition, the rate at which this process occurs depended on the concentration gradients of other chemicals present in the interfaces.

The initial release of elemental mercury is followed by a series of chemical transformations as it is transported through the topsoil to the surface and/or shallow groundwater and sediments, and then through the reach of the stream drainage. Elemental mercury is oxidized and converted to mercuric ion, which has greater solubility in aqueous media, and respectively greater mobility within the watershed. Furthermore, natural organic matter can enhance the dissolution of mercuric sulfide, HgS(s), which is the predominant form of mercury in soil and sediments, and result in release of dissolved and particulate (primarily colloidal) Hg species into soil and sediment porewater. The primary hypothesis of this work is that the aqueous concentrations of total mercury in the hydrologic subdomains (surface, subsurface, streams and sediments) and the intricate series of physico-chemical transformations of mercury are the governing factors which determine the levels of mercury in fish from East Fork Popular Creek. The model provides a tool for analyzing the coupling between watershed hydrology and transport of total mercury. The model includes sections of the Upper East Fork Poplar Creek and Upper Bear Creek Watersheds. In addition, a sedimentation module was implemented which takes into account the exchange of mercury between sediments and stream flow. The model was calibrated using observed data of flow, stage, and mercury concentrations in soil, surface water, groundwater and sediments. The

model was applied to determine the effect of 9 remediation scenarios by analyzing the flow and load duration curves at Station 17. The modeling work focused on analyzing the results for which the flow augmentation strategy adding average of 2.4 million gallons per day (MGD) was already in place. While HgS(s) is a mineral of low solubility, it can complex and be transported in surface water, closing off the outfalls by plugging and abandonment eliminates this pathway to UEFPC. The migration of HgS complexes in groundwater does not occur in low permeability soils with high distribution coefficients. Thus, removing the outfalls is effectively hydrologic isolation of mercury sources in soil and groundwater above shale.

These studies highlight the importance of the effects of adsorption-desorption processes in the fate and transport of contaminants like mercury that have a tendency to sorb to soils (in the floodplain or in the sediment bed).

The Upper East Fork Poplar Creek (UEFPC) is located within the Oak Ridge Reservation (ORR) in the state of Tennessee, in the counties of Roane and Anderson. The reservation encompasses an area of about 14,260 ha, and has three major US Department of Energy facilities: the Y-12 National Security Complex, the East Tennessee Technology Park (ETTP) or K-25 complex, and the Oak Ridge National Laboratory.

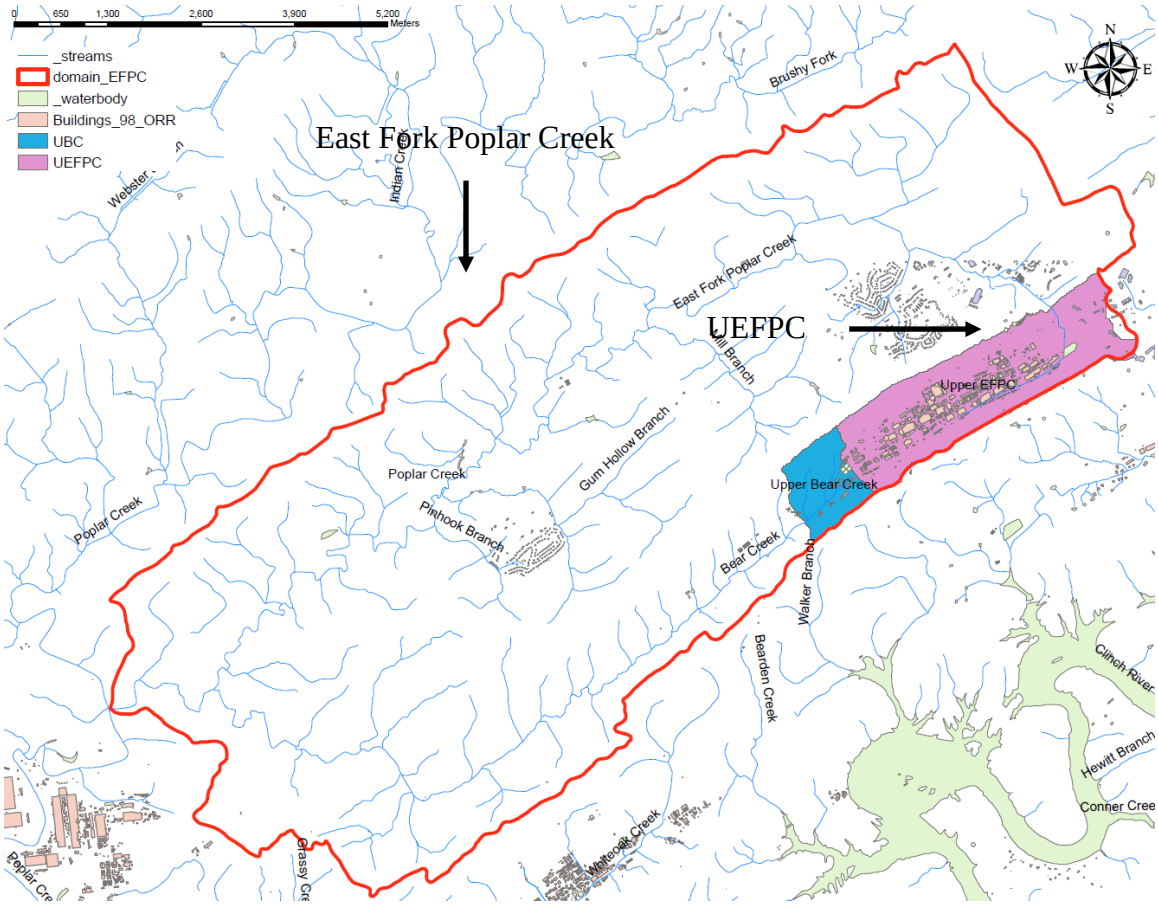

Figure 1. UEFPC watershed.

The UEFPC is defined as the upper waters of the East Fork Poplar Creek (Figure 1); the basin is a sub-watershed of the Lower Clinch River and has a drainage area of 4.73 km^2, approximately 68% from the industrialized areas of the Y-12 Plant. Its boundaries are at the top of Pine Ridge to the north, the top of Chestnut Ridge to the south, the Bear Creek Watershed to the west, and the eastern boundary of the ORR along Scarboro Road to the east.

The creek length is approximately 2.6 km, and runs from the emerging point at the North-South pipe to Station 17 (Figure 2), which is the point where the creek leaves the ORR boundary and becomes the Lower East Fork Poplar Creek. Elevation varies from 283 to 271 m, a gradient of 0.0046, or 4.6 m/km [43].

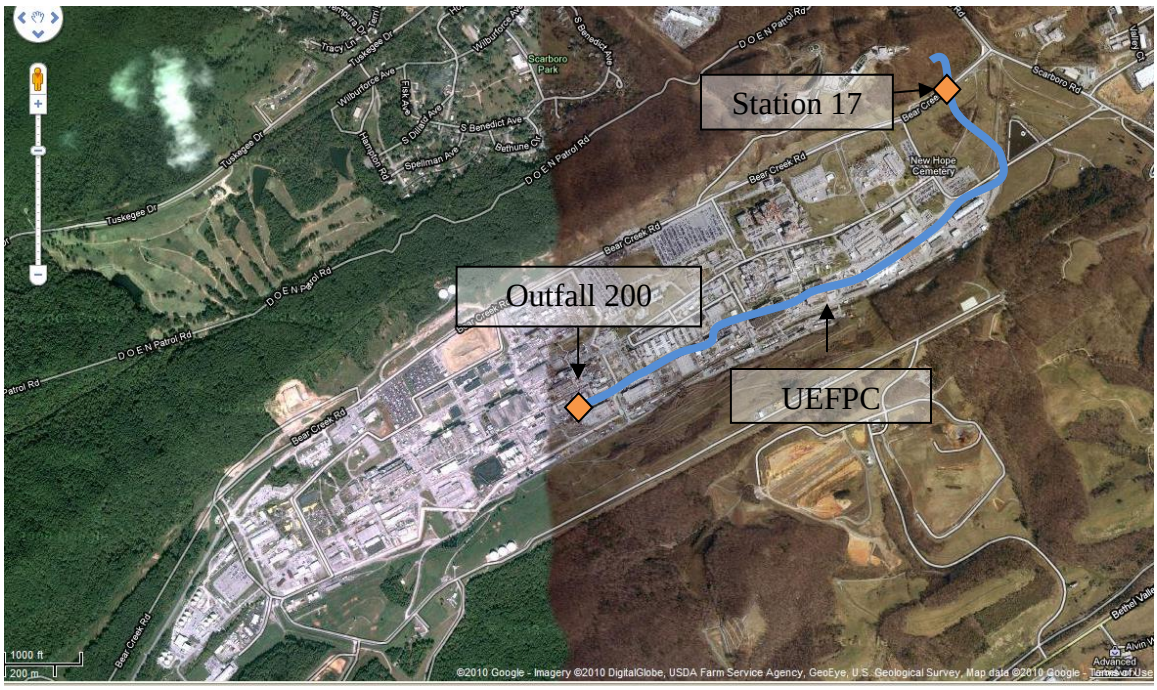

Figure 2. UEFPC channel.

During the construction of the Y-12 Plant, the original topography of the watershed was altered. Tributaries and part of the west and central main UEFPC channel were covered with fill materials, with depths of up to 30 ft., and the creek was captured in a subsurface drainage system.

The upper waters of the stream are composed of discharge from Outfall 200, which drains the West End Mercury Area (WEMA), and water redirected from Melton Hill Lake (MHL), which is added to the creek 6 m downstream from Outfall 200 as part of the flow management program. The flow management program started in August 1996, for the purposes of maintaining the base flow required by the National Pollution Discharge Elimination System (NPDES), returning the creek to the original flow levels from the 1980s, preserving the wildlife habitat, and reducing the mercury concentration in the water passing Station 17 by dilution [52].

Under base flow conditions, as measured in February 2009, 80% of the total flow is originated from MHL and 20% from the industrial waters of the outfall 200 [42]. The flow management program adds continuously to the creek water at a flow rate of about 0.2 m^3/s (OREIS database);

the contribution of total suspended solids to the stream by the raw water is between 5-10 mg/L (OREIS database).

EFPC has been severely impacted by the release of more than 100 metric tons of elemental mercury as a byproduct of nuclear processing activities employed in the lithium-isotope separation process used in the production of nuclear fusion weapons during the 1950's (Turner, R.R., and Southworth, G.R., (1999)) (DOE, DOE/OR/01-1641/V1&D2, 1998). Contamination was introduced into groundwater through multiple paths including historical spills, pipeline leaks, and dissolution from contaminated soils and sediments and is still present in the watershed surrounding the Y-12 National Security Complex (Y-12 NSC) ((ORNL), 2011) (Han, Su, Monts, Waggoner, & Plodinec, 2006). The Tennessee Valley Authority estimated that floodplain sources contributed an estimated 80% of the total annual mercury from the EFPC system (Southworth, Greeley, Peterson, Lowe, & Kettelle, 2010). Studies have identified over 77,000 kg of mercury present in the upper 10 feet of soils along a 15-mile long stretch of EFPC (Han, Su, Monts, Waggoner, & Plodinec, 2006).

Figure 3. Mercury present in sub-surface soil samples from Oak Ridge (Applied Research Initiative, Oak Ridge National Laboratory, 2013).

Mercury is present in the sediment, surface water, groundwater, and infrastructure in the Y-12 area and in the upper reaches of EFPC (Han, Su, Monts, Waggoner, & Plodinec, 2006). Mercury releases into the creek ceased in 1963 (Brooks & Southworth, 2011). Nonetheless, although remediation strategies have been implemented since the problem's inception, the issue of

mercury contamination continues to prevail. Even though water quality has been improved by remediation strategies, methyl-mercury concentrations in water and in fish have not decreased and in some cases exhibit trends of increasing concentration (Brooks & Southworth, 2011).

The state of Tennessee continues to list portions of the EFPC as not supporting their designated use classifications, such as aquatic life, irrigation, livestock watering, wildlife, and recreation due to mercury contamination (Tennessee Department of Environment and Conservation, 2008). Streams and lakes in violation of one or more water quality standards within the state of Tennessee are described in the 303 (d) list. Portions of this list are summarized in the table below for streams near the Oak Ridge Reservation (ORR). Contaminated streams relevant to the present study include 9.7 impaired miles of EFPC within Roane County, and 11.3 miles within Anderson and Roane. Approximately 141 acres of the Poplar Creek Embayment, Watts Bar Reservoir, within Roane County are also contaminated. Total Maximum Daily Load (TMDL) studies identify the sources of pollutant in a stream, quantify the amount, and recommend appropriate action to be taken in order for the stream to no longer be polluted. Further analysis and modeling of the area is necessary so that TMDL studies may be developed in the future.

Elemental mercury dissolves and oxidizes to mercuric ion under environmental conditions, resulting in increased mobility of mercury due to its increased solubility. Due to its highly stable complex formations often considered as irreversible forms and its strong binding to high affinity environments, mercury is often regarded as highly immobile in soils (Liao, Selim, & DeLaune, 2009). Higher concentrations of mercury and suspended solids have been recorded as a byproduct of higher volumes and higher stream velocities during and post flood events (Cabrejo, Mercury Interaction with Suspended Solids at the Upper East Fork Poplar Creek, Oak Ridge, Tennessee., 2011). Generally in stratified systems, concentrations of total mercury and methyl-mercury are higher near the sediments (Morel, Kraepiel, & Amyot, 1998). The kinetics of mercury with dissolved organic matter in aquatic ecosystems requires additional evaluation as the dominant complexes are difficult to determine (Miller, Southworth, Brooks, & Gu, 2009).

.

Table 1. Streams in Violation of Water Quality Standards

Water Body ID	Waterbody Impacted	County	Miles/Acres Impaired
TN06010207026 – 0600	Bear Creek	Roane	10.87
TN06010207026 – 1000	EFPC	Roane	9.7
TN06010207026 – 2000	EFPC	Anderson/Roane	11.3
TN08010208009 - 1000	Poplar Creek	Haywood/Fayette	23.6
TN08010208011 - 2000	Bear Creek	Fayette	7.9
TN08010209021 – 0110	Bear Creek	Shelby/Tipton	14.5
TN05130104050 - 0100	East Branch Bear Creek	Scott	5.7
TN05130104050 - 1000	Bear Creek	Scott	2.6
TN06010102003 – 0500	Bear Creek	Sullivan	4.6
TN08010204004 - 0100	Bethel Branch	Dyer/Gibson	30.4
TN06010207001 - 0100	Poplar Creek Embayment, Watts Bar Reservior	Roane	141 ac

Mercury present in surface water is converted to various forms. Mercury particles may settle with sediments, may be consequently diffused into the water column, re-suspended, or hidden within sediments until a hydrological event disturbs the particles and reignites the complex cycle through which it is recycled (Cabrejo, Mercury Interaction with Suspended Solids at the Upper East Fork Poplar Creek, Oak Ridge, Tennessee., 2011). Mercury in the sediment column may be released into the water via remobilization, dissolution and desorption; and subsequently bio-accumulated by aquatic organisms (Parkpoin, Thongra-ar, DeLaune, & Jugsujinda, 2001). Mercury is released from bed sediments as bed layer particles are re-suspended. Mercury exchange occurs between the water column and sediment as well as between the dissolved and adsorbed phases of mercury via adsorption-desorption processes (Malek-Mohammadi, Tachiev, Cabrejo, & Lawrence, 2012).

Methyl-mercury is the most toxic form of mercury because it can accumulate at a faster rate within organisms in comparison to the rate at which it can be eliminated; it takes longer for organisms to remove it from their systems (U.S. Department of the Interior. U.S. geological Survey (USGS), 2000). Effects are dependent upon the chemical form and type of exposure. The mercury within the EFPC system is continuously recycled by the surrounding environment, making the successful implementation of remediation strategies difficult to execute.

Mercury contamination in the environment represents a health concern for wildlife, as well as humans (U.S. Department of the Interior. U.S. geological Survey (USGS), 2000). Studies have shown a correlation between total mercury concentration within the creek and methyl-mercury concentrations and long-term bioaccumulation and biomagnification. Another mercury study revealed a positive trend among increases in total mercury and methyl mercury, and increases in organic carbon (Pant & Allen, 2007) (Brigham, Wentz, Aiken, & Krabbenhoft, Mercury Cycling in Stream Ecosystems. 1. Water Column Chemistry and Transport, 2009). The irreversibility of mercury adsorption-desorption on soils involve complex mechanisms (USEPA, Guidance on the Development, Evaluation, and Application of Environmental Models, 2009). Understanding the processes by which mercury is transported and recycled within the EFPC environment is an essential step towards complying with applicable and relevant or appropriate requirements (ARARs) in the DOE's Record of Decision (ROD) Phase I and Phase II (U.S. Department of Energy (US DOE), 2002) (DOE), Record Decision for Phase II Interim Source Control Actions in Upper East Fork Poplar Creek Characterization Area, Oak Ridge, Tennessee, 2006).

Previous efforts to model the hydrological environment and mercury transport dynamics within the ORR include the major contributions made by Long (2009) and Cabrejo (2011). Long created a baseline model capable of simulating the hydrology and mercury transport throughout the entire EFPC Watershed. Cabrejo focused on a sub-section of the watershed, known as Upper East Fork Poplar Creek (UEFPC), and instead considered as factors adding to the total mercury concentration, the diffusive transport between the water column and sediment pore water and the adsorption-desorption processes between dissolved mercury and suspended matter in the water column. This research combines both methods by incorporating ECO Lab to simulate the fate and transport of mercury at the water and sediment interface throughout EFPC.

In this report, results for simulated discharges, contaminant concentration levels, and mercury loads are presented in the form of time-series. Probability of exceedance curves were developed for each set of time-series. Flow, discharge and load duration curves were developed for various hydrological regimes. The model was used as an investigative tool for the development of a mercury TMDL analysis.

Other studies employed computer models to emphasize the significance of sediments and suspended matter in contaminant transport. A mass balance model was used to evaluate the internal load of mercury particulates associated with re-suspension of contaminated sediment (Emmet et al., 2009). Models have also been used to predict mercury exposure in hypothetical piscivorous birds and mammals through fish consumption (USEPA, Mercury Study Report to Congress. Volume III. Fate and Transport of Mercury in the Environment, 1997). A study performed by the North Carolina Department of Natural Resources revealed that 75% of the total mercury load present in the Cashie River Watershed resulted from eroded sediments (North Carolina Department of Environment and Natural Resources, 2004). A study on the development of a mercury speciation applied to the Lohatan Reservoir in Nevada, showed that 90% of the mercury released into the system was maintained within the sediments and constituted a continuous source of pollution (Gandhi, et al., 2007). Similarly, Cabrejo analyzed how mercury within the sediment serves as a continuous source of pollution within portions of Y-12, a sub-domain of the EFPC Watershed (Cabrejo, Mercury Interaction with Suspended Solids at the Upper East Fork Poplar Creek, Oak Ridge, Tennessee., 2011). A study simulating flow and mercury transport in upper portions of EFPC also confirmed that for the sub-domain, a large portion of the mercury in the river is present as mercury bound to sediment particles (Malek-Mohammadi, Tachiev, Cabrejo, & Lawrence, 2012). These studies summarize the importance of the adsorption-desorption process in mercury contaminated environments, especially when the contaminant has an affinity to sorb to soils in the sediment bed layer.

The geological characteristics of the EFPC watershed have been extensively investigated by past Remedial Investigations for the site (DOE, Report on the Remedial Investigation of the Upper East Fork Poplar Creek Characterization Area at the Oak Ridge Y-12 Plant. Volume 1, 1998). Tributaries' attributes and vegetation cover have also been described in great detail by Long (Long, 2009). This section serves as a summary of efforts previously executed in characterizing the site since the project's inception.

EFPC is located within the ORR in the state of Tennessee, in the counties of Roane and Anderson. The reservation houses three major US DOE facilities within 14,260 ha. These include Y-12, the East Tennessee Technology Park (ETTP) or K-25 complex, and the Oak Ridge

National Laboratory (ORNL). EFPC watershed is a sub-watershed of the larger Poplar Creek watershed. The United States Geologic Survey (USGS) classifies it as one of four sub-watersheds of the Lower Clinch River watershed (Hydrologic Unit Code 06010207). The EFPC watershed domain area covers approximately 29.7 square miles.

An estimated 88 square miles of streams and tributary branches have been identified within the domain. Bear Creek (BC) and EFPC are two small rivers with a length of more than 12,500 kilometers. Gum Hallow Branch, Mill Branch, and Pinhook Branch represent other tributaries of significant length. EFPC is recharged by BC, Gum Hollow Branch, Mill Branch, and Pin Hook Branch, in addition to 30 unnamed tributaries. These tributaries were all included in the model.

Geological formations beneath ORR include primary groups recognized as: the Knox, Rome, Chickamauga, and Conasuaga, Sequatchie, Fort Payne Chert, Rockwood, Copper Ridge Dolomite, and Maynardville Limestone formations. The Knox Aquifer and the Chickamauga Group are the dominant hydrologic units. In these leaky confining units, flow is dominated by fractures and relatively low hydraulic conductivities.

Landcover includes intensive agriculture, urban and industrial, or areas of thick forest. White oak forests, bottomland oak forests, and sycamore-ash-elm riparian forests are the common forest types, and grassland barrens intermixed with cedar-pine glades also occur here.

PROJECT OBJECTIVE

This research is a continuation of efforts to correlate the hydrology of the EFPC and BC with the long-term distribution of mercury within the overland, subsurface, river, and vadose zone sub-domains. The main objective of this thesis is to successfully integrate ECO Lab in the EFPC Watershed model as a computational mechanism for mercury exchange throughout the water column and to apply the enhanced model towards the development of TMDL analysis components. The application seeks to demonstrate the capability of the enhanced model to support efforts to understand and manage mercury contamination and remediation.

The principal objective of this study is to understand and quantify the variables affecting the processes of adsorption-desorption of mercury with suspended particles, the sedimentation and

resuspension of the sorbed mercury, and the diffusive transport of dissolved mercury that takes place between the sediment and water phases, under the conditions present at the UEFPC.

The research hypothesis is that higher levels of mercury concentrations observed at UEFPC Station 17 during high flow events are a result of non-point sources that include the resuspension of smaller particles into the water column and the increased mobility of mercury-contaminated suspended solid loads.

The present study took the described dynamics into account, adding to the existent flow and transport model for the UEFPC, the exchange of mercury between sediment bed and water column, which improved the simulation of mercury concentrations in the creek when compared with the previous model, which only included the transport of mercury by advection dispersion.

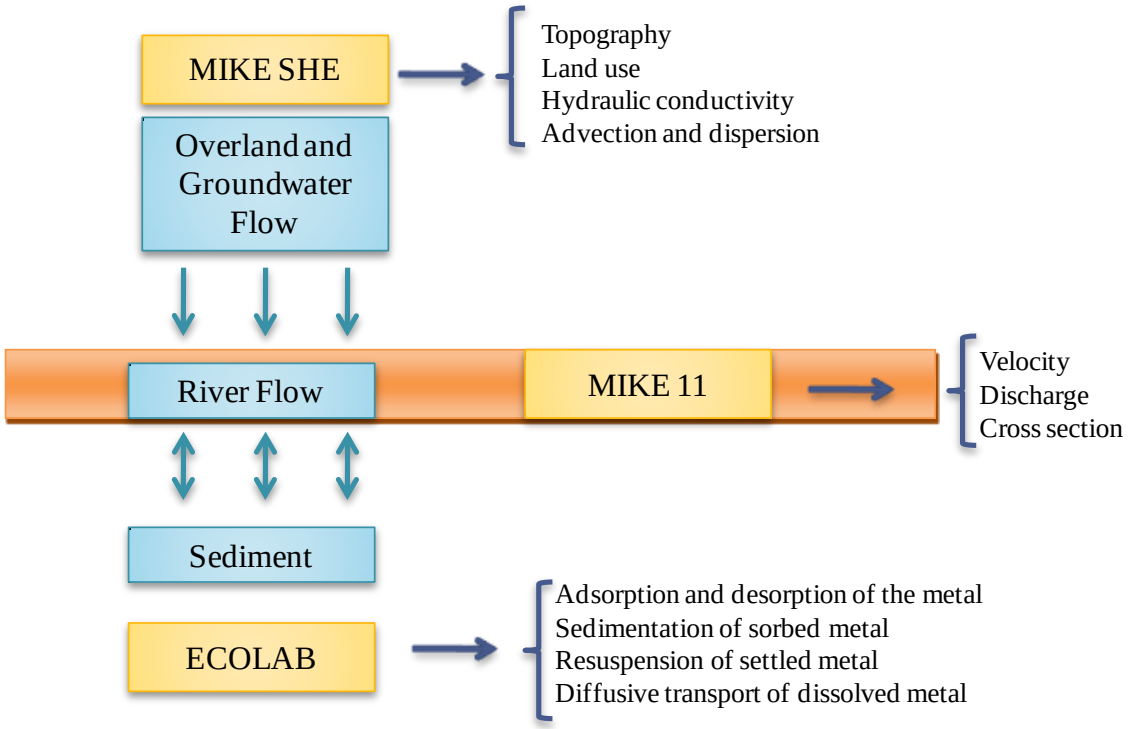

Figure 4. MIKE SHE, MIKE11 and ECO Lab.

ECO Lab was used to simulate the fate and transport of mercury at the water and sediment interface for the UEFPC. ECO Lab is a numerical model supported by the Danish Hydraulic

Institute (DHI) that can be coupled with MIKE SHE and MIKE 11 software, where the hydrodynamics and advection dispersion calculations are carried out (Figure 4). The model allows for the simulation of physical and chemical dynamics of heavy metals interacting with sediments in the water body. One of the model's advantages over previous models is that it can estimate dissolved and particulate mercury in the water column and in sediments [15, 16].

The techniques implemented build upon the process established by the EPA for model development by considering the three main steps: (a) identification of the environmental problem the model is intended to resolve, (b) development and or evaluation of the mathematical model, and (c) parameterization of the model for viability as an applicable tool (USEPA, Guidance on the Development, Evaluation, and Application of Environmental Models, 2009).

It is important to note that the approach in this study took advantage of the previous efforts to model the hydrological environment and mercury transport dynamics within the ORR made by Long and Cabrejo. Long created a baseline model capable of simulating the hydrology and mercury transport throughout the entire EFPC Watershed. Cabrejo focused on a sub-section of the watershed, known as UEFPC, and instead considered as factors adding to the total mercury concentration, the diffusive transport between the water column and sediment pore water and the adsorption-desorption processes between dissolved mercury and suspended matter in the water column. This research combines both methods by incorporating ECO Lab to simulate the fate and transport of mercury at the water and sediment interface throughout EFPC.

The integrated surface/sub-surface model was built using the numerical package, MIKE (MIKE 11 coupled with MIKE SHE and ECO Lab), which was developed by the Danish Hydraulic Institute (DHI). The sedimentation module originally included UEFPC, and was extended to include the entire EFPC, down to EFK 6.4 and the BC.

The sedimentation and water quality modules were extended to the entire EFPC watershed in the following phases:

1. The water quality and sedimentation modules (ECO Lab) were extended for BC and for the remaining section of EFPC (downstream of Station 17) to include EFK 6.4.

2. Water quality, transport, and sediment-related parameters, such as carbon partitioning coefficient, adsorption rates of mercury species to sediment particles and water molecules, re-suspension rate of sediments, settling velocity of suspended particles, and critical current velocity for sediment re-suspension, were estimated from literature. These include DOE reports of field surveys, laboratory experiments reported by FIU or other research institutes, and referenced publications.
3. The following outlines the approach implemented for ORNL data processing:
    a. Data was checked for validity based on database markers and categorized into spreadsheets.
    b. New stations were added to GIS maps of the site.
    c. Time-series files were developed from field records and dynamically linked to model boundary conditions.

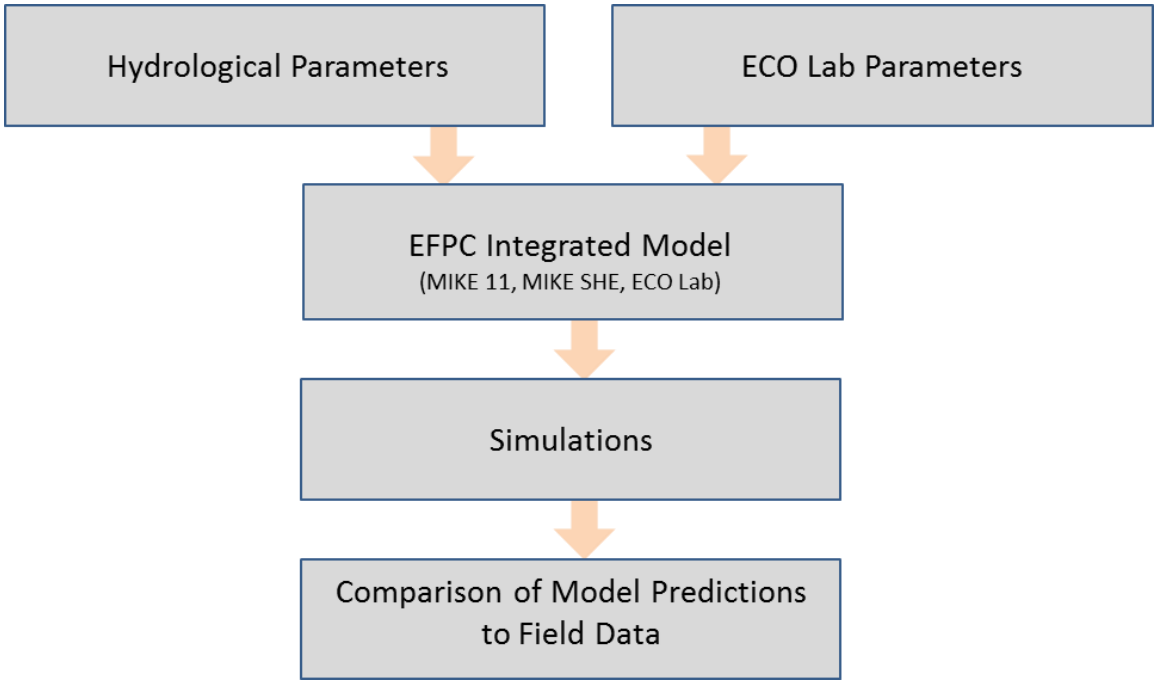

Figure 5. Procedure flow diagram for modeling the hydrology and transport using for the updated EFPC watershed model.

Model nodes, cross-sections, and boundaries were added and modified as necessary due to the addition of new observation stations and the need to reduce both numerical instabilities and

computational time. Simulations were executed to correlate stochastic hydrologic events and stream flow with mercury-distribution patterns.

> This study did not include any calibration or validation for either flow or transport parameters. Instead, the study focused on the analysis of a comparison between predictions by the model, using parameters and available field data for flow at a number of field stations and for total measurements of mercury at the only monitoring station in the EFPC (i.e. Station 17).

The integrated flow and transport model couples the hydrological and sediment transport processes (including the interactions between sediment particles, mercury species and water).

Sediment transport

The rate of transport and distribution of sediment in river channels has important implications in the determination of the quality of the water and in the understanding of the fate and transport of contaminants.

The transport of sediments is a process driven by gravity and drag forces between the particles and the fluid, and turbulence in the water stream. It depends on fluid and sediment properties, and characteristics of the sediment bed. The total sediment load carried by a stream can be divided into bed load, suspended load and dissolved load (wash load).

Bed load describes the particles that are transported along or close to the bed of the stream. In general, the movement occurs by rolling, sliding, traction, saltation, and collision between particles and with the bed. Particles will be rolling and sliding in continuous contact with the bed, for conditions with bed shear velocity slightly higher than the critical value for initiation of motion. For higher values of bed shear velocity, saltation will occur.

Once a particle is lifted up by the flow and, if the turbulence level is high enough, the particle will travel as part of the suspended load, in which case the bed shear velocity overcomes the fall

velocity of the particle. Under this approach, the bed load transport is dominated by gravity forces, while the suspended load is dominated by turbulent eddies [62].

Suspended load is composed of the particles transported in suspension, with velocity almost equal to the velocity of the water. The movement in this case is controlled by the physical properties of the material and by the dynamics of the velocity field. Particles traveling in suspension are then influenced by two main actions, one causing the resuspension as a result of the upward and downward velocity components of the turbulent eddies, and a second one, the gravitational action, which causes the settling of the particles [29]. Fine particles like clays and silts are carried in suspension and tend to move with the flow, carrying adsorbed contaminants downstream.

The present study focuses on the total suspended solids (TSS) which are part of the suspended load. The main difference between the two is based in the diameters of particles that each parameter includes. The suspended load concentration is measured from the whole sample, according to the American Society for Testing and Materials' method (designation: D 3977-97), and incorporates coarser particles. The TSS concentration is measured from a sub-sample, according to Method 160.2 [60], and excludes the coarser solids in the influent due to settling. Guo (2006) showed a good correlation between TSS and suspended load concentration for particles up to 0.1mm, which corresponds to very fine sands, silts and clays.

The total suspended solids concentration in the water is expressed in terms of dry weight per unit volume (i.e., mg/l), and is quantified by filtering a known volume of water through a weighed standard glass-fiber filter, and then drying the residue retained on the filter to a constant weight at 103-105ºC [60].

TSS incorporates material like silt and clay, decaying plants, industrial wastes, and sewage. In general, levels and sizes of suspended particles transported by a stream are affected by changes in the flow rate. More particles and of higher sizes are carried when the flow rate increases due to resuspension of particulate matter from the stream bed generated by the increase in the current' speed [10].

Transport and fate of mercury in the water environment

Mercury can be found in the environment in the form of gas (elemental mercury), as ionic mercury, and as organic mercury or methyl mercury (MeHg). Its behavior depends on the oxidation state, which varies between metallic (Hg^0), mercurous (Hg_2^{2+}), and mercuric (Hg^{2+}) [45].

Elemental mercury (Hg^0) is a volatile metal with low viscosity, high surface tension and is mobile, liquid at ambient temperatures, and practically insoluble in water. Hg^0 oxidizes mainly in the presence of ozone, and also with other oxidants including HClO, HSO_3^-, and OH^+. In the atmosphere, Hg^0 is the most common form of mercury [44]. In natural waters it is generally bound to chloride, sulfide, or organic acids.

Methyl mercury is soluble in water and can be formed from inorganic mercury by microbial processes in soils, sediments, and water, a process known as methylation. The reverse process, demethylation, is also possible, in which case MeHg is reduced to Hg^0 and is reintroduced to the atmosphere. Due to its affinity for sulfhydryl groups of proteins, MeHg is rapidly absorbed by living organisms, and since the rate of absorption is much higher than the elimination rate, it can accumulate for years [36].

In soils, sediments and surface waters, mercury is most commonly found as inorganic mercuric salts and organomercurics, the most frequent compounds being the mercuric salts $HgCl_2$, $Hg(OH)_2$ and HgS. Due to the affinity of inorganic mercury for sulfur containing compounds, in soils it tends to form complexes mainly with soil organic matter and, to a lesser extent, to mineral colloids, a process which limits mercury's mobility in the soil.

Mercury can enter freshwater in different forms, organic or inorganic, wet or dry, and from different sources, such as a deposition from the atmosphere, as part of the runoff "bound to suspended soils/humus or attached to dissolved organic carbon" [59], or from groundwater as a result of leaching from soil.

In the water column the metal can be partitioned between dissolved and particulate-bound phases, being found mainly forming complexes with organic matter, such as being bound to dissolved organic carbon in the dissolved phase, and bound to suspended solids in the particulate phase. Changes in the bacteria and phytoplankton populations in the water body affect the temporal distribution of the metal between those phases [44].

Once in the water mercury can be exchanged in three main processes: between water and sediment during the sedimentation and/or resuspension of particles; between water and sediment pore water due to differences in concentrations resulting in diffusive transport; and within water column and within the sediment by processes of adsorption-desorption changing between dissolved and adsorbed phases [14]. Honeyman, et al., (1988), summarized the processes occurring with a dissolved heavy metal reacting with a solid phase as follows: adsorption/desorption in the water phase, adsorption/desorption in the sediment phase, sedimentation and resuspension of particulate metal, diffusive transport of dissolved metal, and advection and dispersion.

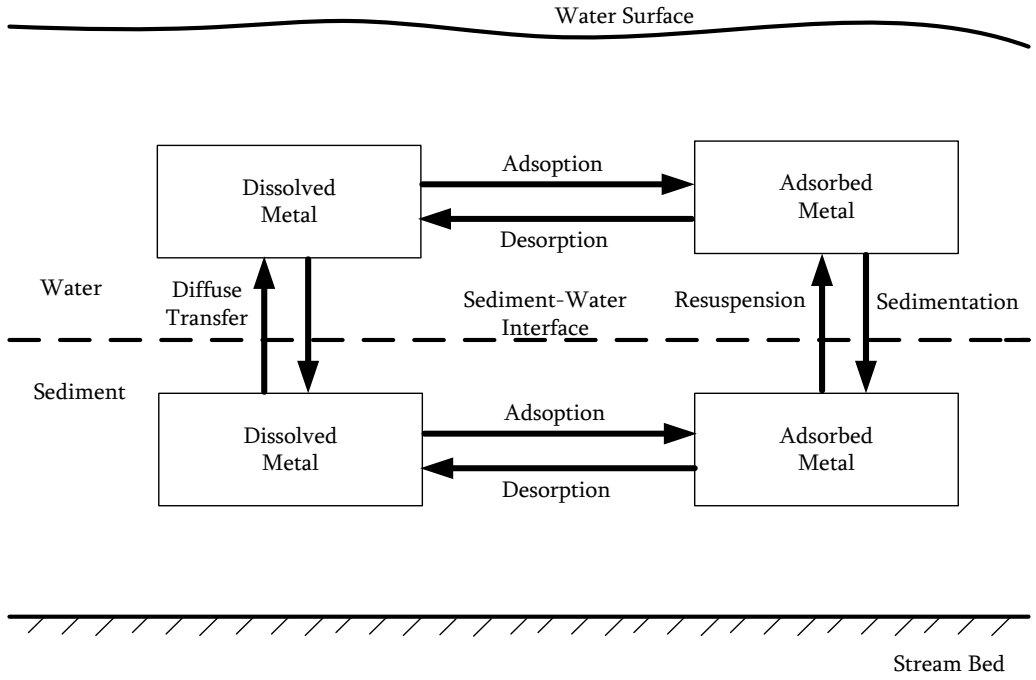

Figure 6. Schematic illustrating the interactions between metal, sediment, and water implemented in ECO LAB and MIKE 11.

Adsorption and desorption are processes by which the metal is transferred between solute and solid phases. The extent at which the metal is adsorbed depends on factors like density and acidity of the adsorbent, metal-surface association constants, the presence of complexing ligands, type and concentration of particles, particle size, and interactions between particles [35].

Diffusion results from movement of particles along concentration gradients. According to Fick's first law the mass flux is proportional to the gradient of concentrations, and goes in the direction of higher to lower concentration [10]. When the concentration of dissolved mercury in the water column is lower than that in the sediment pore water, there will be a release of the contaminant into the water.

Advection is the part of the transport that is originated by the motion of the water.

Dispersion is the component of transport that describes local mixing, which results in varying fluid flow velocity [10].

Mercury mobilization and transport within the water creek involves an exchange between the following principal domains:

- **i)** Deposition and resuspension of sediment particles,
- **ii)** Diffusive transfer of mercury species between sediment pore water and creek water,
- **iii)** Adsorption and desorption processes of mercury between sediment particles and sediment pore water,
- **iv)** Adsorption and desorption processes of mercury between suspended sediment particles and creek water.

The ECO Lab water quality model is comprised of four compartments to define mercury's transport processes, which are described in the following sections of the present document.

Dissolved mercury in the water (S_{HM})

Dissolved mercury concentration in water is the result of the relationships between mercury desorbed from suspended solids into the water column, mercury adsorbed by the suspended

solids from the water column, and the dissolved mercury exchanged between the water column and the sediment pore water, which is positive (mercury moving into the water column) when the concentration of mercury in the sediment pore water is higher than that in the water column, and negative in the opposite case.

The most important parameters driving this relationship are the partitioning coefficient for mercury between particulate matter and water (K_d), and the concentrations of mercury and suspended solids in the water.

K_d indicates the affinity of the contaminant for the soil phase; therefore, the higher the parameter, the less the metal desorbs from the suspended matter into the water. Since mercury binds to the organic part of the suspended solids, K_d in the model is defined from the organic carbon partition coefficient (Equation 18) as mentioned before, which explains the importance of the level of organic matter in the suspended solids, or fraction of organic carbon, (foc). Higher organic carbon content in the sediment promotes the adsorption of the metal to the suspended solids.

Dissolved mercury is calculated from the following relationship [14]:

$$\frac{dS_{HM}}{dt} = -adss + dess + difv \quad [\frac{gHg}{m^3 bulk.d}] \tag{1}$$

Where: *adss* is the adsorption, *dess* is the desorption, and *difv* is the diffusion.

With adsorption calculated from the following formula. Where: S_{HM} is the dissolved mercury concentration in the water [g Hg/m^3 H_2O], TSS is the suspended solids concentration in the water [g DW/m^3 bulk], k_W is desorption rate in water [d^{-1}], and K_d is the partitioning coefficient for mercury between particulate matter and water [m^3 H_2O/gDW].

$$Adsorption = k_w . K_d . S_{HM} . TSS \quad [\frac{gHg}{m^3 bulk.d}] \tag{2}$$

Desorption is calculated from the following expression. Where: k_w is the desorption rate in water [d^{-1}] and X_{HM} is the adsorbed mercury concentration in the water [gHg /m^3 Bulk].

$$Desorption = k_w.X_{HM} \quad [\frac{gHg}{m^3 bulk.d}] \tag{3}$$

The diffusive transfer is the transport across the water and sediment interfaces; it occurs due to the difference between solute concentrations in the water column with respect to the concentrations in the sediment pore waters.

In ECO Lab the diffusion is calculated from the following relationship, which is based on Fick's law.

$$difv = \frac{fbiot.difw.\left(\frac{S_{HMS}}{pors.dzds} - S_{HM}\right)}{(dzwf + dzds).dz} \quad [\frac{gHg}{m^3 bulk.d}] \tag{4}$$

Where: difv is the diffusion coefficient in water, estimated from the metal's mole weight [m^2/d]; $f_{biot \cdot difw}$ is the factor for diffusion due to bioturbation [dimensionless], assumed 1 for the model; S_{HMS} is the dissolved heavy metal concentration in sediment porewater [g Hg/m^2]; S_{HM} is dissolved heavy metal concentration in the water [g Hg/m^3 bulk] ≈ [g Hg/m^3 H_2O]; dzwf is the average thickness water film that metals have to diffuse through, default value of 0.1mm; dzds is the thickness of diffusion layer in sediment [m], calculated by the model from a built-in function; and dz is the thickness of the actual layer in the computational grid [m], which is calculated by MIKE11.

Adsorbed mercury concentration on suspended matter (XHM)

The adsorbed mercury concentration in the water column (particulate mercury) is the result of mercury adsorbed by the suspended solids present in the water column, and mercury adsorbed to the particles that are resuspended from the river bed (increasing the concentration) minus mercury desorbed from suspended solids into the water column and mercury adsorbed to particles settling (decreasing the concentration). ECO Lab defines the adsorbed mercury concentration on suspended matter as follows [14],

$$\frac{dX_{HM}}{dt} = adss - dess - sev + resv \quad [\frac{gHg}{m^3 bulk.d}] \tag{5}$$

Where: *adss* is adsorption defined from equation (2), *dess* is desorption defined by equation (3), *sev* is sedimentation, and *resv* is resuspension.

Sedimentation defined as follows,

$$sev = \frac{v_s . X_{HM}}{dz} \quad [\frac{gHg}{m^3 bulk.d}] \tag{6}$$

Where: v_s is the settling velocity of suspended solids [m/d], X_{HM} is the adsorbed mercury concentration in the water [g Hg/m^3 bulk], and dz is the thickness of the actual layer in the computational grid [m] calculated by MIKE11.

Assuming that the current speed is higher than the critical value for initiation of the movement, Resuspension (res) is determined from the following relationship [14]. Where: RR is the resuspension rate [gDW/m^2/d], which is a constant, subject to calibration, X_{HMS} is the adsorbed mercury concentration in the sediment [g Hg/m^2], X_{SED} is the mass of sediment [g DW/m^2], and dz is the thickness of the actual layer in the computational grid [m] calculated by MIKE 11.

$$res = \frac{RR . \frac{X_{HMS}}{X_{SED}}}{dz} \quad [\frac{gHg}{m^3 bulk.d}] \tag{7}$$

Dissolved mercury in the sediment pore water (S_{HMS})

Mercury dissolved in the pore water is the result of the balance between mercury desorbed from the sediments in the river bed minus the contaminants adsorbed from the sediment pore water onto the sediments, and the result of the diffusive transport between dissolved mercury in the water column and dissolved mercury in the sediment pore water, as can be seen in the following relationship, and adsorption given by equation (9) [14].

$$\frac{dS_{HMS}}{dt} = -adsa + desa - difa \quad [\frac{gHg}{m^2.d}] \tag{8}$$

With adsorption given by,

$$adsa = k_s . K_{ds} . S_{HMS} . \frac{X_{SED}}{dzs.por_s} \quad [\frac{gHg}{m^2.d}] \tag{9}$$

Where: k_s is the desorption rate in sediment [d^{-1}], K_{ds} is the partitioning coefficient for metal between particulate matter and water in the sediment [m^3 H_2O/g DW], S_{HMS} is the dissolved mercury concentration in the sediment [gHg/m^2], dzs is the sediment layer thickness [m], X_{SED} is the mass of the sediment [g DW/m^2], and por_s is porosity of the sediment [m^3H_20/m^3 bulk], assumed as a constant value of 0.4.

Desorption is given by the following relation, where: X_{HM} is the adsorbed mercury concentration in the water [g Hg/m^3 bulk].

$$desa = k_s.X_{HMS} \quad [\frac{gHg}{m^2.d}] \tag{10}$$

Also, diffusion is calculated from equation (4).

Adsorbed mercury in the sediment (X_{HMS})

The concentration of mercury sorbed to the sediments in the river bed is calculated in ECO Lab from the following relationship [14], which takes into consideration the metal that adsorbs to particles in the sediment, metal that desorbs from sediment and becomes dissolved, the sedimentation and resuspension of mercury contaminated particles.

$$\frac{dX_{HMS}}{dt} = adsa - desa + sea - resa \quad [\frac{gHg}{m^2.d}] \tag{11}$$

With adsorption determined by,

$$adsa = k_s.K_{ds}.S_{HMS}.\frac{X_{SED}}{dzs.por_s} \quad [\frac{gHg}{m^2.d}] \tag{12}$$

Where: k_s is the desorption rate in sediment [d^{-1}], K_{ds} is the partitioning coefficient for metal between particulate matter and water [m^3 H_2O/g DW], S_{HMS} is the dissolved mercury concentration in the sediment [g Hg/m^2], d_{zs} is the sediment layer thickness [m], X_{SED} is the mass of sediment [g DW/m^2], and por_s is the porosity of sediment [m^3H_20/m^3 bulk], assumed to be a constant value of 0.4.

The mass of the sediment is calculated as the difference between sedimentation of particles from the water column, and resuspension of particles from the creek's bed, as shown in equation (13), where: X_{SED} is the mass of sediment [g DW/m^2], v_s is the settling velocity of suspended solids [m/d], a constant subject to calibration; and *RR* is the resuspension rate [$\frac{gDW}{m^2.d}$], also a constant subject to calibration.

$$\frac{dX_{SED}}{dt} = v_s.TSS - RR \ [\frac{gDW}{m^2.d}] \quad (13)$$

Sedimentation is defined as the product of settling velocity [m/d] and the concentration of mercury adsorbed to suspended particles, X_{HM} [g Hg/m^3 bulk], as presented in the following equation,

$$sea = v_s.X_{HM} \quad [\frac{g\ Hg}{m^2.d}] \quad (14)$$

Resuspension, for current velocity exceeding the critical value is given by,

$$resa = \frac{RR\ .\ X_{XMS}}{X_{SED}} \quad [\frac{g\ Hg}{m^2.d}] \quad (15)$$

Where: *RR* is the resuspension rate of suspended solids [gDW/m^2/d], X_{XMS} is the adsorbed mercury in the sediment [g Hg/m^2], and X_{SED} is the mass of sediment [g DW/m^2].

The model includes the main components of the hydrological cycle and contaminant transport; groundwater flow and transport (3D saturated and unsaturated), overland flow, flow in rivers, precipitation, and evapotranspiration. The model enables full dynamic coupling of surface and subsurface flow processes, which allows calculations of water and contaminant exchange between the land, rivers, and the groundwater. By providing detailed spatial information and characteristics, including hydrological and transport properties in the four sub-domains, saturated zone, unsaturated zone, overland flow, and transport in streams, the model provides accurate water and contaminant mass balance for the domain. MIKE SHE and MIKE 11 are used to simulate and assess the impact of hydrological events on mercury contamination. The processes simulated by each module (MIKE 11, MIKE SHE, and ECO Lab) in the EFPC model are shown

in Figure 7 and explained in greater detail within the subsequent sections. Figure 8 provides a conceptual schematic based on the EFPC model modular set up. The diagram denotes the various pathways of interaction among the MIKE SHE, MIKE 11, and ECO Lab modules and lists the numerical engines associated at each level of computation.

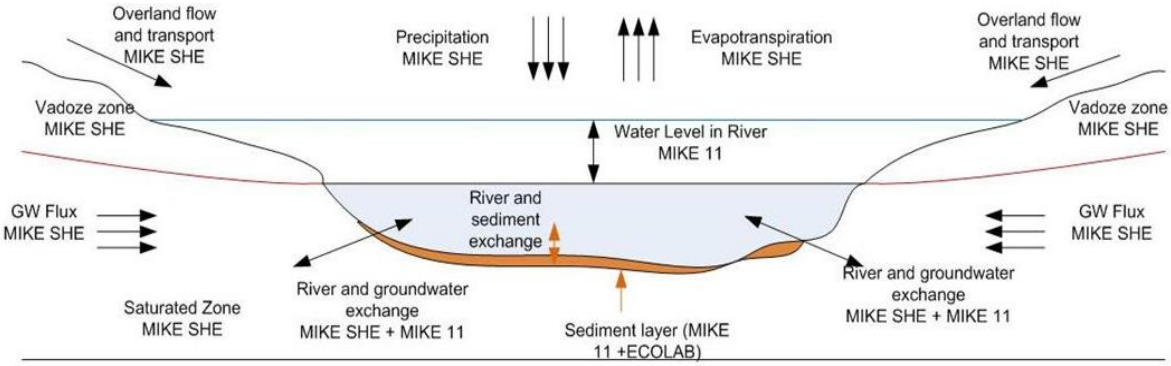

Figure 7. Processes simulated by MIKE modules (Malek-Mohammadi, Tachiev, Cabrejo, & Lawrence, 2012).

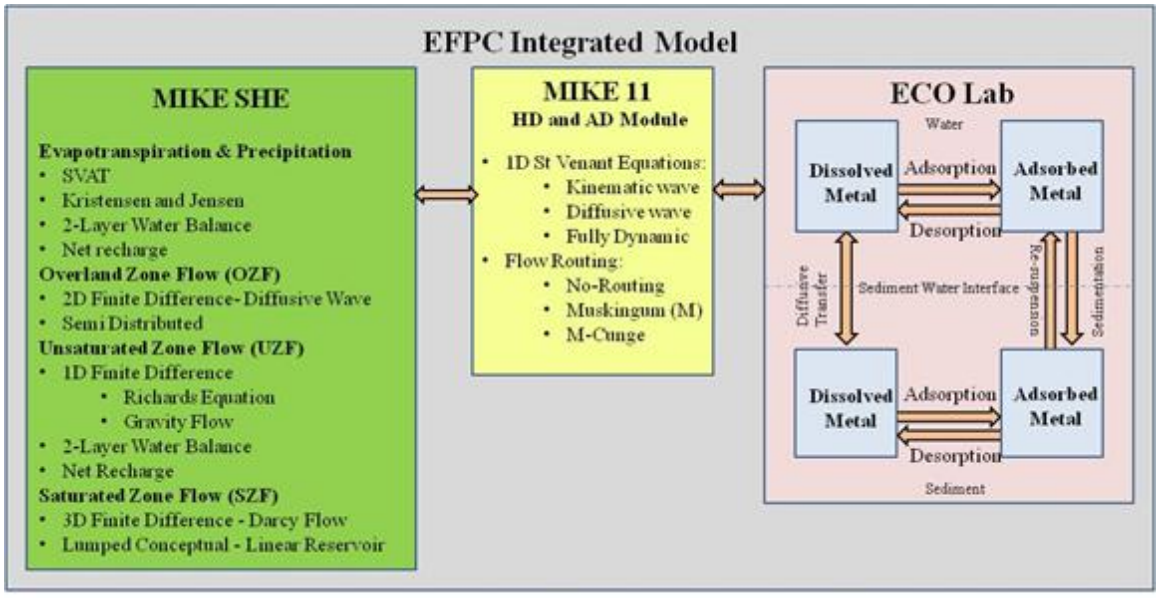

Figure 8. Schematic of the modular set-up and processes of MIKE SHE, MIKE 11, and ECO Lab arranged in accordance to the EFPC model structure (Concept obtained from DHI ((DHI), MIKE SHE User Manual, 2012) and modified by Lilian Marrero).

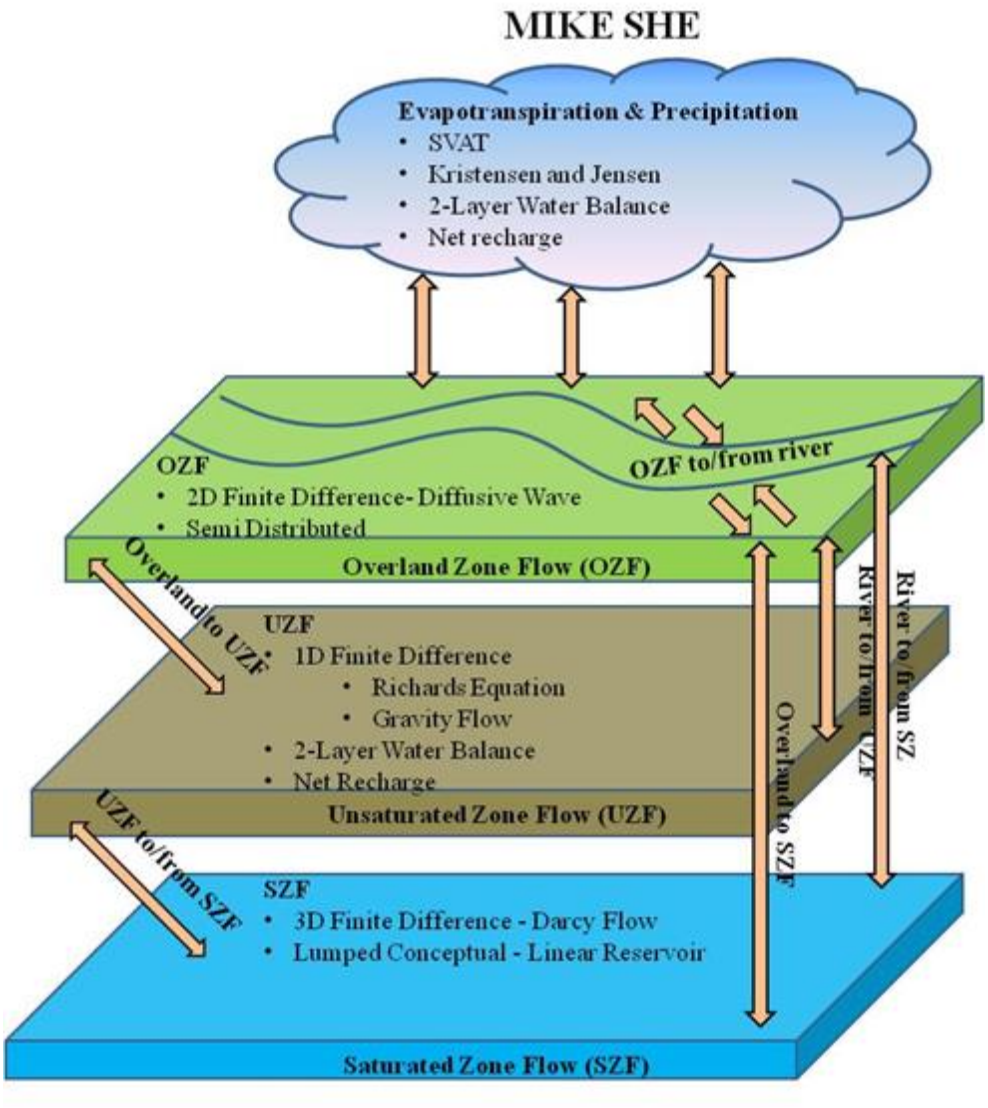

Figure 9. Detailed schematic of MIKE SHE setup and processes (concept obtained from DHI and modified by Lilian Marrero).

MIKE 11 and MIKE SHE

MIKE 11 is a one-dimensional river flow and transport model that requires longitudinal profiles, cross-sections, Manning's numbers, and other hydrodynamic parameters (Danish Hydraulic Institute (DHI), 2012). It uses the dynamic Saint Venant equations to determine river flow and water levels. The complete nonlinear equations of open channel flow (Saint-Venant) can be solved numerically between all grid points at specified time intervals for given boundary

conditions. In addition to this fully dynamic description, other descriptions are also available to choose from, including high-order, fully dynamic, diffusive wave, kinematic wave, quasi-steady state, and kinematic routing (Muskingum, Muskingum-Cunge).

MIKE SHE is a fully integrated model for the 3D simulation and linkage of hydrologic systems, including overland, subsurface, and river flows. It has been successfully applied at multiple scales, using spatially distributed and continuous climate data to simulate a broad range of integrated hydrologic, hydraulic, and transport problems. MIKE SHE represents the two-dimensional overland, one-dimensional unsaturated zone, three-dimensional saturated and vadose zone flow and transport components ((DHI), MIKE SHE User Manual, 2012). The hydrologic processes are described based on physical laws, such as the conservation of mass, energy and momentum. MIKE SHE couples several partial differential equations that describe flow in the saturated and unsaturated zones with the overland and river flow. Different numerical solution schemes are then used to solve the different partial differential equations for each process. A solution to the system of equations associated with each process is found iteratively by use of different numerical solvers.

The model enables MIKE SHE and MIKE 11 hydrodynamic modules to interact through branches or stream reaches defined within the domain. This coupling allows for the one-dimensional simulation of river flows and water levels through the fully dynamic Saint Venant equations. Hydraulic control structures, area-inundation modeling, dynamic overland flooding flow in relation to the MIKE 11 river network, and the dynamic coupling of surface and sub-surface flow is simulated. Floodplain flooding is simulated by first establishing the floodplain through the MIKE SHE topography and then activating the direct overbank spilling option in MIKE 11 while simultaneously restricting cross-sections to the main channel. The cross-sections defined in MIKE 11 are used to calculate the river water levels and volumes. Consistency with topographical elevations is of extreme importance since the bank elevation is the primary reference for cell flooding. River and groundwater exchange is modeled by defining the river in contact with the aquifer. In this case, the water exchange between MIKE 11 and MIKE SHE is performed through a river-link cross section.

The concept of mercury transport through stream sediments or total mercury load and the water column is compartmentalized into bed load, suspended load, and dissolved load (Van Rijn L. , Sediment Transport, Part II: Suspended Load Transport, 1984). ECO Lab is an equation solver; applied in this case to handle the sedimentation and exchange of mercury within sediments, suspended particles, pore water and dissolved mercury species (Institute, ECOLAB Short Scientific Description, 2012). An ECO Lab template can be developed by the user to model the ecological processes as required by any specific project; however, some templates have already been developed by DHI in the areas of water quality (17 templates), heavy metal transport (1 template), eutrophication (3 templates), and xenobiotics (1 template). For the modeling of mercury fate and transport in EFPC, the heavy metal transport template of ECO Lab is used coupled with both MIKE 11 and MIKE SHE to simulate the interaction of mercury species with the sediment particles and water molecules in the creek. The heavy metal template describes the adsorption/desorption of mercury to suspended matter, the sedimentation of sorbed mercury to the streambed, as well as re-suspension of the settled mercury. It also includes exchange of mercury between particulates of the bed sediment and the interstitial waters of the bed. The diffusive exchange of dissolved mercury in the water and in the interstitial waters is also considered.

The basic theory behind the EFPC Watershed model is discussed in the following sub-sections for the various modules included; such as, MIKE SHE, MIKE 11, and ECO Lab.

Saturated, unsaturated, and overland flows are some of the central processes accounted for through the MIKE SHE module. The theory behind the MIKE SHE module is summarized in this section and discussed in greater detail within the DHI MIKE SHE user manual ((DHI), MIKE SHE User Manual, 2012).

Overland flow is computed using the diffusive wave approximation of the Saint Venant equations. The diffusive wave approximation does not account for momentum losses due to local and convective acceleration and lateral inflows ((DHI), MIKE SHE User Manual, 2012). , yet reduces the complexity of the numerical solution. The simplified diffusive wave approximation solution is summarized in the equations below.

$$S_{fx} = -\frac{\partial h}{\partial x}\left(z_g + h\right) = -\frac{\partial z}{\partial x} \quad \text{(Equation 16)}$$

$$S_{fy} = -\frac{\partial h}{\partial y}\left(z_g + h\right) = -\frac{\partial z}{\partial y} \quad \text{(Equation 17)}$$

The friction slopes along the x and y directions are equivalent to the inverse of the Manning's n and referred to as Manning's M instead ((DHI), MIKE SHE User Manual, 2012). These coefficients are computed along the x and y direction by equation and equation below.

$$S_{fx} = -\frac{u^2}{Kx^2 h^{\frac{4}{3}}} \quad \text{(Equation 18)}$$

$$S_{fy} = -\frac{v^2}{Ky^2 h^{\frac{4}{3}}} \quad \text{(Equation 19)}$$

The discharge per unit length for the x and y direction along the cell boundary is generated by multiplying both sides of the equations by "h". Per the MIKE SHE manual, this relationship between the velocities (*u* along x-direction and *v* along y-direction) and depth is given as:

$$uh = -(Kx)\left(\frac{\partial z}{\partial x}\right)^{\frac{1}{2}} h^{\frac{5}{3}} \quad \text{(Equation 20)}$$

$$vh = -(Ky)\left(\frac{\partial z}{\partial y}\right)^{\frac{1}{2}} h^{\frac{5}{3}} \quad \text{(Equation 21)}$$

The discharge per unit length is represented by *uv* along x-direction and *vh* along y-direction. The finite difference form for the velocity terms are derived in the equations below where the north, south, east and west notations are associated with boundaries along a computational cell ((DHI), MIKE SHE User Manual, 2012). For example, the volume flow across the northern

boundary is given by vh_{north}. The flow into a computational cell is the sum of all flows entering the cell from the north, south, east and west.

$$\frac{\partial(uh)}{\partial x} = \frac{(uh)_{east} - (uh)_{west}}{\Delta x} \quad \text{(Equation 22)}$$

$$\frac{\partial(vh)}{\partial y} = \frac{(vh)_{north} - (vh)_{south}}{\Delta y} \quad \text{(Equation 23)}$$

MIKE SHE calculates three-dimensional flow in the saturated zone through equation 9. The hydraulic conductivity (K) is considered along the x, y, and z direction. The hydraulic head, sources, and specific storage coefficients are represented by the variables h, Q, and S respectively.

$$\frac{\partial}{\partial x}\left(K_{xx}\frac{\partial h}{\partial x}\right) + \frac{\partial}{\partial y}\left(K_{yy}\frac{\partial h}{\partial y}\right) + \frac{\partial}{\partial z}\left(K_{zz}\frac{\partial h}{\partial z}\right) - Q = S\frac{\partial h}{\partial t} \quad \text{(Equation 24)}$$

MIKE SHE computes the unsaturated flow vertically in one-dimension via the full Richards equation, a gravity procedure, or a two layer water balance method ((DHI), MIKE SHE User Manual, 2012). The full Richards equation was selected as the computing mechanism for unsaturated flow because it is the most accurate method when considering a dynamic unsaturated flow. The vertical hydraulic head (*h)* gradient shown in equation 10 includes a gravitational component and a pressure component essential for the vertical transport of water. The volumetric flow is computed using Darcy's law as shown in equation 11 and the principle of continuity is included via equation 12.

$$\Delta h = \frac{\partial h}{\partial z} \quad \text{(Equation 25)}$$

$$q = -K(\theta)\frac{\partial h}{\partial z} \quad \text{(Equation 26)}$$

$$\frac{\partial \theta}{\partial t} = -\frac{\partial q}{\partial z} - S(z) \quad \text{(Equation 27)}$$

Equation 13 below, results from combining equation 10 through 12. Equation 13 applies to homogeneous and heterogeneous profiles ((DHI), MIKE SHE User Manual, 2012). This equation accounts for the hydraulic conductivity function $K(\theta)$ and the soil moisture retention curve $(\partial \psi(\theta))$.

$$\frac{\partial \theta}{\partial t} = \frac{\partial}{\partial z}\left(K(\theta)\frac{\partial \psi}{\partial} \right) + \frac{\partial K(\theta)}{\partial z} - S(z) \quad \text{(Equation 28)}$$

When the concept of soil water capacity shown in equation 14 is introduced, equation 13 transforms into Richards equation (equation 15).

$$C = \frac{\partial \theta}{\partial \psi} \quad \text{(Equation 29)}$$

$$C\frac{\partial \psi}{\partial t} = \frac{\partial}{\partial z}\left(K(\theta)\frac{\partial \psi}{\partial z} \right) + \frac{\partial K(\theta)}{\partial z} - S \quad \text{(Equation 30)}$$

The one-dimensional numerical engine used to compute flow within the hydrodynamic module employs the Saint Venant Equations under various assumptions. The model disregards variations in density within the flow medium (water) (Danish Hydraulic Institute (DHI), 2012). Flow within rivers or streams are assumed to be parallel to the reach bottom (Danish Hydraulic Institute (DHI), 2012). Moreover, water movement perpendicular to the flow direction of the stream is disregarded (Danish Hydraulic Institute (DHI), 2012). These simplifications lead to the modified Saint Venant equations shown below; constituting the numerical foundation of the hydrodynamic module.

$$\frac{\partial q}{\partial x} + \frac{\partial A_{fl}}{\partial t} = q_{in} \quad \text{(Equation 31)}$$

$$\frac{\partial q}{\partial x} + \frac{\partial\left(\alpha \frac{\partial q^2}{A_{fl}}\right)}{\partial x} + gA_{fl}\frac{\partial h}{\partial x} + gA_{fl}A_I = \frac{f}{\rho_w} \qquad \text{(Equation 32)}$$

The continuity equation; shown first above, emphasizes the conservation of mass within stream sections. The second equation expresses the conservation of momentum. The variables q, A_{fl}, q_{in}, h, α, f, and ρ_w respectively represent the discharge, cross-sectional area, lateral inflow per unit length, water level, the momentum distribution coefficient, friction slope, momentum forcing, and water density (Danish Hydraulic Institute (DHI), 2012).

ECO Lab was incorporated into the model through the advection module. The set of transport equations governing the advective ECO Lab dynamics are shown below in their non-conservative form (Institute, ECOLAB Short Scientific Description, 2012):

$$\frac{\partial c}{\partial t} + C\frac{\partial c}{\partial x} + v\frac{\partial c}{\partial y} + w\frac{\partial c}{\partial z} = D_x\frac{\partial^2 c}{\partial z^2} + D_y\frac{\partial^2 c}{\partial z^2} + D_z\frac{\partial^2 c}{\partial z^2} + S_c + P_c \qquad \text{(Equation 33)}$$

The ECO Lab state variables c, S_c, and P_c represent concentration, sources and sinks, and ECO Lab processes. The flow velocity components in the x, y, and z-direction are represented by u, v, and w. Similarly, the dispersion coefficients in the x, y, and z-direction are represented by D_x, D_y, and D_z. The transport equation is modified as:

$$\frac{\partial c}{\partial t} = AD_c + P_c \qquad \text{(Equation 34)}$$

The rate of change in concentration as a byproduct of advection dispersion is accounted by the term AD_c. Per DHI, the ECO Lab solver calculates the concentration at each time step through an explicit time-integration where AD_c is constant at each time step (Institute, ECOLAB Short Scientific Description, 2012). The ECO Lab module is capable of performing the explicit time-integration using various methods. These methods include the Euler, Runge Kutta 4, and Runge

Kutta with quality check (Institute, ECOLAB Short Scientific Description, 2012). The newly added ECO Lab module within EFPC was set to perform the explicit-time integration using the Runge Kutta 4th order. This method was selected because it has higher accuracy. As illustrated within the scientific manual the function below in equation 20 is solved in the four steps shown by equation 21 through equation 24. The solution y is obtained from x_n to x_{n+1} and equivalent to x_{n+h} as shown in equation 25.

$$y_{n+1} = y_n + h \cdot f(x_n, y_n) \quad \text{(Equation 35)}$$

$$k_1 = h \cdot f(x_n, y_n) \quad \text{(Equation 36)}$$

$$k_2 = h \cdot f\left(x_n + \frac{h}{2}, y_n + \frac{k_1}{2}\right) \quad \text{(Equation 37)}$$

$$k_3 = h \cdot f\left(x_n + \frac{h}{2}, y_n + \frac{k_2}{2}\right) \quad \text{(Equation 38)}$$

$$k_4 = h \cdot f(x_n + h, y_n + k_3) \quad \text{(Equation 39)}$$

$$y_{n+1} = y_n + \frac{k_1}{6} + \frac{k_2}{3} + \frac{k_3}{3} + \frac{k_4}{6} - O(h^5) \quad \text{(Equation 40)}$$

In addition to the internal computational processes described, mercury transport processes in ECO Lab are defined by specifying the following (Institute, ECOLAB Short Scientific Description, 2012):

- Dissolved mercury concentration in the water (S_{HM}).
- Adsorbed mercury concentration on suspended matter (X_{HM}).
- Dissolved mercury concentration in the sediment pore water (S_{HMS}).
- Adsorbed mercury concentration in the sediment (X_{HMS}).

The byproduct of mercury exchange between suspended solids and the water column is represented by variable S_{HM}. This exchange is mainly driven by the organic carbon partitioning coefficient (K_d), indicating the contaminant's affinity towards the soil phase. Dissolved mercury is computed using the following set of interconnected equations (Institute, ECOLAB Short Scientific Description, 2012):

$$\frac{dS_{HM}}{dt} = -adss + dess + difv \quad \text{(Equation 41)}$$

$$adss = k_w K_d S_{HM} TSS \quad \text{(Equation 42)}$$

$$dess = k_w X_{HM} \quad \text{(Equation 43)}$$

$$difv = \frac{f_{biot(difw)}\left(\frac{S_{HMS}}{(pors)(dzds)} - S_{HMS}\right)}{(dzwf + dzds)dz} \quad \text{(Equation 44)}$$

The equations above clearly represent the relation between adsorption ($adss$), desorption ($dess$), and diffusive transfer ($difv$). The variables k_w, K_d, TSS, $f_{biot(difw)}$, $pors$, $dzwf$ and dz are equivalent to the desorption rate (d^{-1}), partitioning coefficient for mercury (m^3 H_2O/gDW), total suspended solids concentration (g DW/m^3 bulk), factor for diffusion due to bioturbation (dimensionless), thickness of diffusion layer in sediment (m), and thickness of the computational grid layer (m) respectively.

The adsorbed mercury concentration on suspended matter within the water column X_{HM} results from mercury being absorbed by both the suspended solids and particles re-suspended by the river bed layer, and eliminating the mercury desorbed from suspended solids into water column, and also those adsorbed by settling particles.

$$\frac{dX_{HM}}{dt} = adss - dess - sev + resv \quad \text{(Equation 45)}$$

$$sev = \frac{v_s X_{HM}}{dz} \quad \text{(Equation 46)}$$

$$resv = \frac{RR \frac{X_{HMS}}{X_{SED}}}{dz} \quad \text{(Equation 47)}$$

In the equations above, sev and $resv$ represent the sedimentation and re-suspension of particles. The settling velocity (m/d) of suspended solids is defined by v_s. RR denotes the re-suspension rate (gDW/m^2/d). X_{SED} is the sediment mass gDW/m^2). These equations assume that the current speed is greater than the critical speed responsible for initiating movement (Institute, ECOLAB Short Scientific Description, 2012). S_{HMS} is calculated based on the equations below:

$$\frac{dS_{HMS}}{dt} = -adss + dess - dif \quad \text{(Equation 48)}$$

$$adss = k_s K_{ds} S_{HMS} \frac{X_{SED}}{dzs \cdot por_s} \quad \text{(Equation 49)}$$

$$dess = k_s X_{HMS} \quad \text{(Equation 50)}$$

The desorption rate in sediment (d-1), metal partitioning coefficient between particulates and water (m^3 H_2O/gDW), and sediment porosity (m^3 H_2O/ m^3 bulk), are given by k_s, K_{ds}, and por_s. The variables in the above equations have been defined earlier in this section.

X_{HMS} is calculated using the following:

$$\frac{dX_{HMS}}{dt} = adss - dess - sev + resv \quad \text{(Equation 51)}$$

$$adss = k_s K_{ds} S_{HMS} \frac{X_{SED}}{dzs \cdot por_s} \quad \text{(Equation 52)}$$

$$sev = v_s X_{HM} \quad \text{(Equation 53)}$$

$$resv = \frac{RRX_{HMS}}{X_{SED}} \quad \text{(Equation 54)}$$

EFPC MODEL OVERVIEW AND IMPROVEMENTS FOR TMDL AND NPDES ANALYSIS

The EFPC model originally developed by Long has been extended and improved throughout the course of this study as reflected by Figure 10. The model has been extended to include observation stations not previously considered within the MIKE SHE module. This was performed upon evaluating the most recent publicly available historical data for the site. Internal numerical parameters within the simulation specifications were evaluated and updated to decrease the computational time within the model's pre-processing, water movement, and water quality computational phases. In addition, data was reformatted to increase pre-processing speed. For example, vegetation data input format was changed from shape to gridded codes.

The MIKE 11 component of the model also underwent various transformations. The AD module was modified to include ECO Lab, the watershed river network was extended significantly when compared to the baseline EFPC Watershed model, and cross-sections were added to reduce flooding at points of high numerical instabilities. Existing river cross-sections were also examined and altered to ensure consistency in bed level elevations at the branch junctions and thus reduce numerical instabilities. Furthermore, the newly incorporated ECO Lab template was adjusted to include state variables, forcing variables, values, and constants previously defined for the localized Y-12 model. The following sections provide an overview changes implemented to the baseline model.

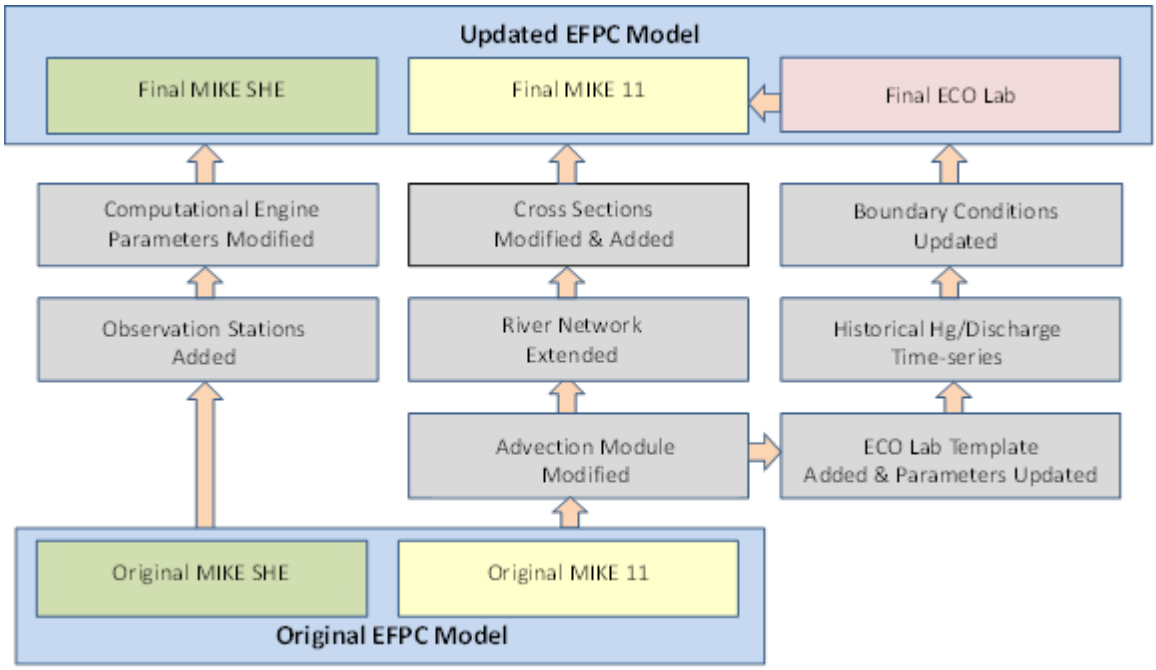

Figure 10. Overview of EFPC model update.

Data Extraction and Processing

The Oak Ridge Environmental Information System (OREIS) is a centralized, standardized, quality-assured, and configuration-controlled environmental data management system belonging to the US DOE. The environmental data retrieved from the OREIS database for the purposes of this research include known quality measurement and spatial data from groundwater, surface water, sediment, and soil. The spatial data was extracted by utilizing the OREIS spatial query tool. The interface is shown in the figure below.

During the data extraction process, the domain was divided into 16 sub segments in an effort to minimize the time and computer resources spent in the data extraction process. The data was initially extracted in the form text files. It was archived into Excel spreadsheets, converted into appropriate units, formatted as time-series, and added to the model as additional observation stations. Stations 2236AQ06, 3538250, 3215AQ05, 3904AQ04, EFK 13.8, 5313AQ03, EFK 18.2, 6262AQ02, and 6361AQ01 shown on the map below were initially identified as potential observation stations to be added to the model.

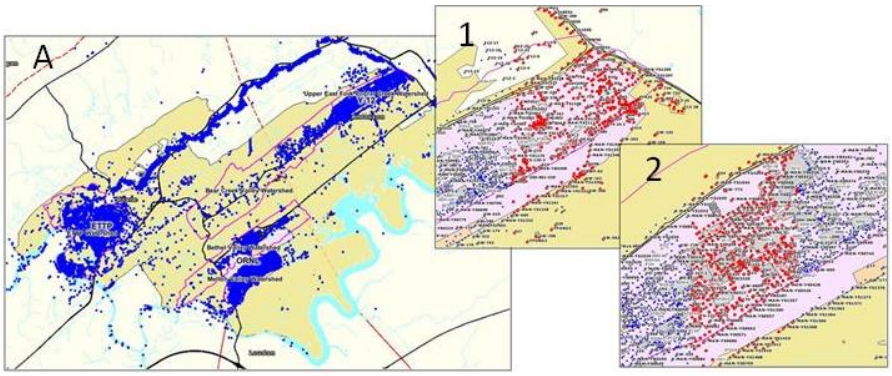

Figure 11. OREIS spatial query tool (A), and sample segments extracted (1) - (2).

Additional stations considered but discarded based on the invalid declaration of the OREIS validation qualifier include PCM 5.5-1, PCM 5.5-2, PCM 5.5-3, PCM 5.5-4, PCM 5.5-5, PCM 6.0, PCM 6.5, PCM 7.0, LASD01, and CCSD01. Ultimately, 3538250, EFK 13.8, and EFK 18.2 were the only new discharge (flow rates measurements) stations with sufficient data to be included in the model. The relative location of processed field stations and stations added to the model are shown in Figure 124. Specific coordinates are maintained confidential.

Model Domain, Topography

The domain/study area, shown as the red outline in Figure 12. , was defined by the USGS as HUC 060101070302. GIS files for the domain, USGS observation stations, streams, water bodies such as lakes, and topography were inserted into the model in the form of either shape files or MIKE Zero shell extensions (dfs0, dfs1, or dfs1). Figure 12. (A) shows an overlay of these files as it appears within the model's display section. Surface elevations were originally embedded in the model in the form of a dfs2 extension file. These surface elevations are measured in meters. Figure 12. (B), (C), and (D), show GIS shapefiles for soil imperviousness, soil type and land use. These files were introduced in MIKE SHE and prepared by previous members of the Applied Research Center (ARC) - Environment and Water Resources Group during the initial stages of model development. Refer to Long (Long, 2009) for a more detailed explanation of their assembly.

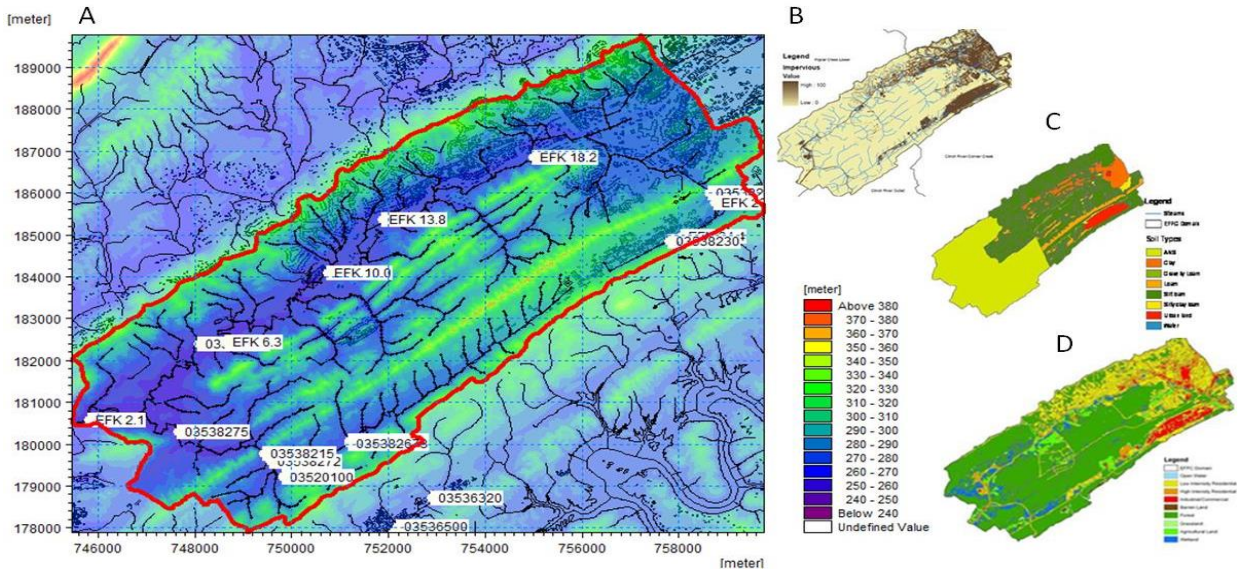

Figure 12. Image overlay of observation stations, streams, water bodies, and topography (A), imperviousness (B), soil type (C), and land use (D) (Obtained from Long and Malek-Mohammadi, modified by Lilian Marrero (Malek-Mohammadi, Tachiev, Cabrejo, & Lawrence, 2012) (Long, 2009)).

Climate

Hydrological climate patterns such as precipitation, snowmelt and evapotranspiration, form part of the climate sub-section within MIKE SHE. The precipitation component of the model determines surface water flows and defines the basics for the groundwater table. The precipitation time-series is presented as a rate in the form of mm/day from 1/1/1950 through 12/31/2008. The MIKE SHE module will only use the precipitation data within the user-specified time period. It must be noted that snow melt is not included as a sub-component of the climate since the precipitation values reported in the time-series already account for frozen precipitation.

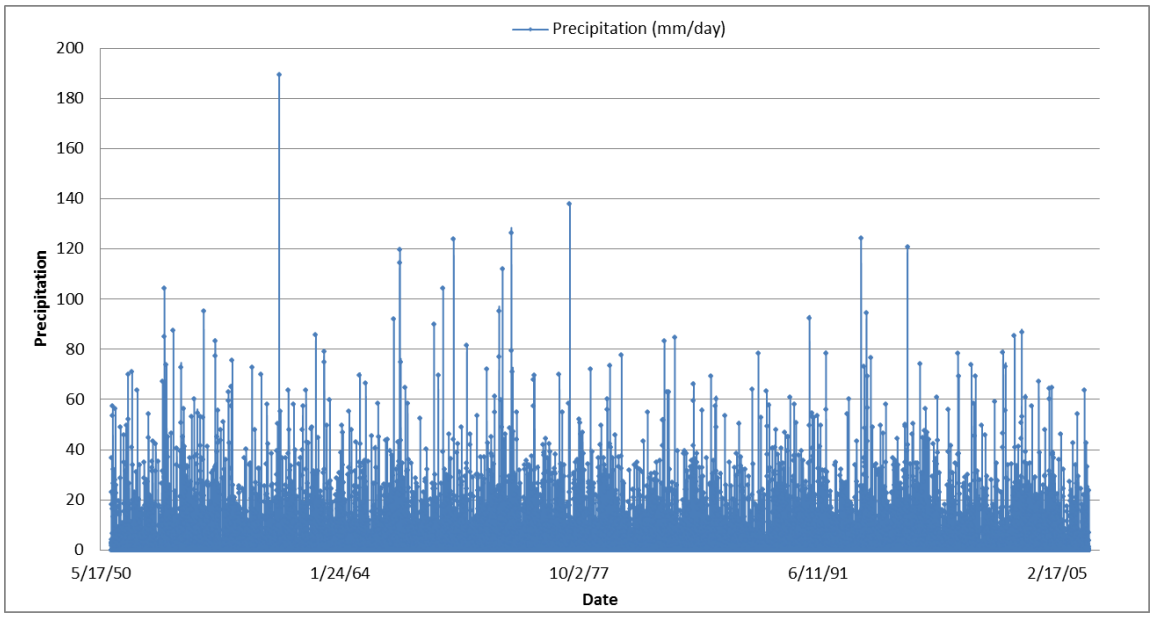

Figure 13. Precipitation time-series data for 1/1/1950 to 12/31/2008.

The evapotranspiration component of the model is dependent upon meteorological and vegetative data as it must predict evapotranspiration due to rainfall interception by canopy, canopy drainage to soil surface, evaporation from plant and soil surface, and water uptake by roots. A spatially uniform constant value of 2.01168 mm/day is observed based on records for the state of Tennessee (Long, 2009). The model adjusts ET based on the leaf area index and root depth specified under land use.

Land Use

The land use consists of vegetation maps with assigned leaf area index constants and root depth values obtained from USGS. Leaf area index and root depth spatially adjust the reference evapotranspiration stated previously. The table below depicts the gridded codes and their classification along with assigned leaf area index, root depth, and Manning's M (1/n).

Table 2. Land Use Classifications

GRID CODE	CLASS	LAI	RD (mm)	M
11	Open water	0	0	50
21	Developed, Open Space	3	2000	50
22	Developed, Low Intensity	2.5	2000	20
23	Developed, Medium Intensity	2	2000	10
24	Developed, High Intensity	1.5	2000	7
31	Barren Land, Rock, Sand, Clay	1.31	4000	11
41	Deciduous Forest	5.5	2000	10
42	Evergreen Forest	5.5	1800	9
43	Mixed Forest	5.5	2400	10
52	Shrub, Scrub	2.08	2500	20
71	Grassland, Herbaceous	1.71	1500	29
81	Pasture, Hay	1.71	1500	30
82	Cultivated Crops	3.62	1500	27
90	Woody Wetlands	6.34	2000	10
95	Emergent Herbaceous Wetlands	6.34	2400	22

Saturated Zone

The saturated zone includes subsurface drainage where the distribution of hydrogeologic parameters is assigned via geological layers (Danish Hydraulic Institute (DHI), 2012). A layer from 0 meters to 30 meters below ground level exists and another from 30 to 100 meters below ground surface. These set a two-layer surficial aquifer profile for the site. Parameters influencing saturated flow are considered in this section. A horizontal hydraulic conductivity, vertical hydraulic conductivity, specific yield, and specific storage of 1.0 e^{-04} (m/s), 1.0 e^{-05} (m/s), 0.2 (dimensionless) and 3.0 $x10^{-5}$ (m^{-1}) formed part of the original model and remain unchanged in the current version. The drainage level was assumed -1.0 m relative to the ground, and the

drainage time constant has been preset to $1.0x10^{-6}$ sec^{-1} based on calibration and uncertainty analysis performed by previous modelers.

Unsaturated Zone

The unsaturated zone employs the Van Genuchten algorithm in the computation of hydraulic conductivity K(θ) and water retention curve; where the water content $\theta(\psi)$ is at tension ψ ((DHI), MIKE SHE User Manual, 2012). The relationship among them based on defined parameters is summarized by the equations that follow ((DHI), MIKE SHE User Manual, 2012):

$$\theta(\psi) = \theta_r + \frac{(\theta_s - \theta_r)}{[1+(\alpha\psi)^n]^m} \quad \text{(Equation 55)}$$

$$m = 1 - 1/n \quad \text{(Equation 56)}$$

$$K(\psi) = K_s \frac{\left(\left(1+|\alpha\psi|^n\right) - |\alpha\psi|^{n-1}\right)^2}{\left(1+|\alpha\psi|^n\right)^{m(l+2)}} \quad \text{(Equation 57)}$$

The saturated moisture content (θ_s), residual moisture content (θ_r), the α-empirical constant inversely related to air entry (cm^{-1}), m and n-empirical constant, and shape factor (l) must be specified in order for the algorithm to function. These parameters are summarized in Table 3. The retention and conductivity curves are shown in Figure 14.

Table 3. Upper and lower aquifer retention curve parameters.

Hydraulic Conductivity Curve Parameters									
Upper Layer					Lower Layer				
K_s	α	n	Shape factor	m	K_s	α	n	Shape factor	m
4.05e-5	0.124	2.28	0.5	0.5614	1.95e-7	0.01	1.23	0.5	0.1869

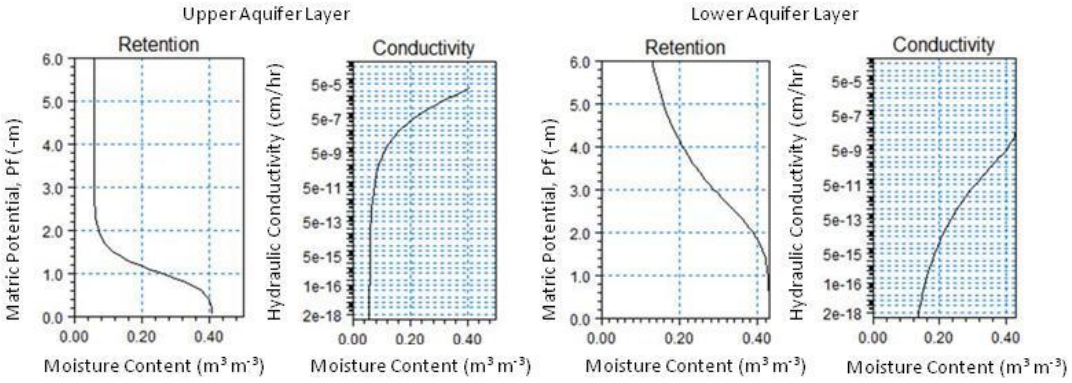

Figure 14. Retention and hydraulic conductivity curves for the upper and lower aquifer layers.

The hydraulic conductivity function ($K(\psi)$) is expressed as a ratio between the hydraulic conductivity for given water content and the saturated hydraulic conductivity (K_s). Input parameters for the equations were obtained from literature for the upper and lower aquifer hydraulic conductivity and moisture retention curves.

Overland Flow

Drainage in the overland zone is routed downhill based on adjacent drain levels. If drain flow is produced it is routed to the recipient point using a linear reservoir routing technique based on a pre-processor generated reference system that utilizes the slope of the drains calculated from the drainage levels in each cell.

Channel/River Flow

Water flow is simulated in MIKE 11 via a 1-dimensional engine directly linked to the network geometry (Danish Hydraulic Institute (DHI), 2012). The network developed for the EFPC model consists of reaches, nodes, grid points, and cross-sections. The river and stream network for the domain area is shown below. It consists of 112 branches or MIKE SHE links, and 1086 nodes. Cross-sections are set to allow for overbank spilling. The left and right bank elevations and bed

layer are consistent with topography files. Resistance (Manning's M) values range between 10 and 20 throughout the domain.

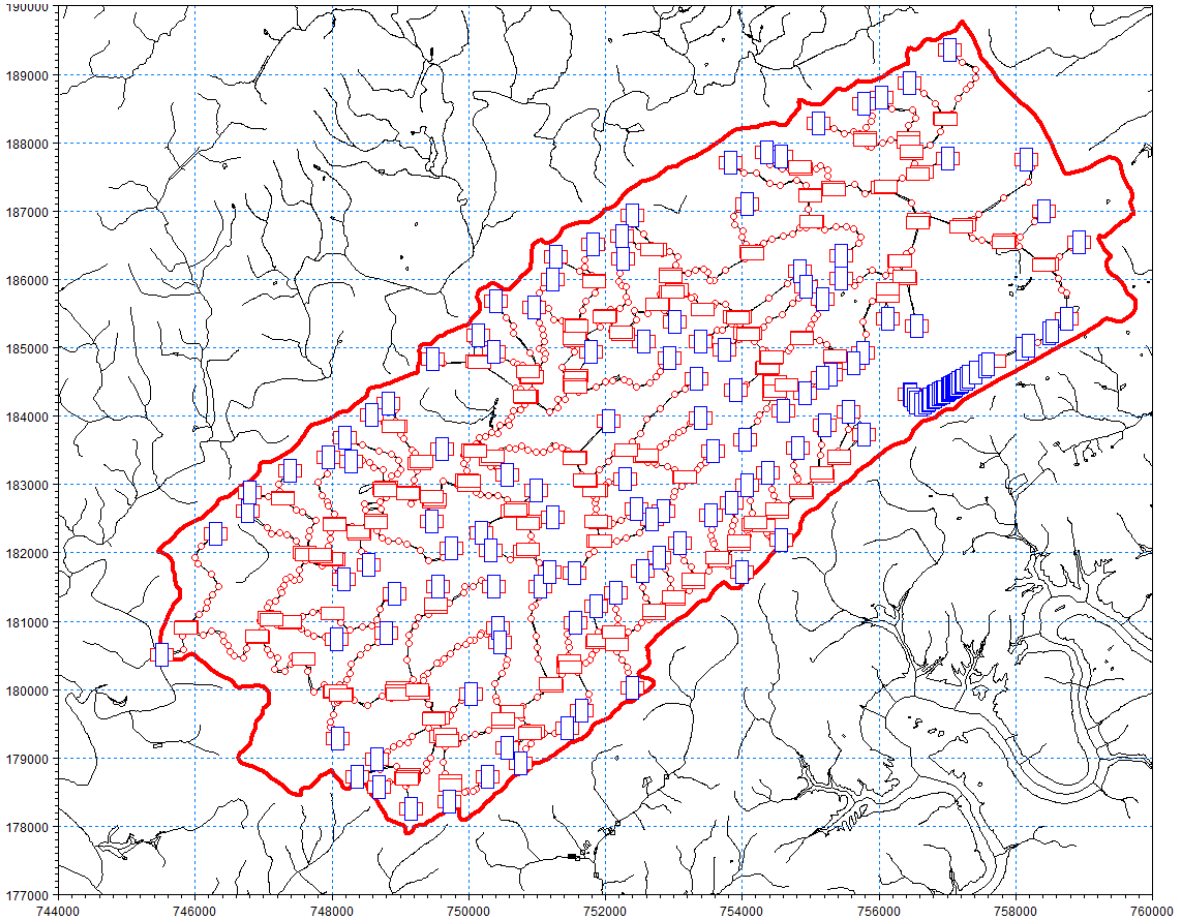

Figure 15. River network with point nodes, boundary conditions and cross-sections.

The watershed model has well defined boundary conditions. The boundary conditions guide the interaction between the model domain and the surrounding external areas ((DHI), MIKE SHE User Manual, 2012) (Danish Hydraulic Institute (DHI), 2012). Open boundary conditions were paired with additional boundary point sources to simulate the hydrology of the natural environment as well as the most significant anthropological alterations to the site.

The EFPC model was modified by adding outfalls (point sources) to the boundary file in both the hydrodynamic and advection module. The newly developed boundary conditions file for the modules consist of a merger between the previously existing EFPC Model boundary file and the

Y-12 Model. The new boundary condition file consists of a total of 157 branches of which 42 were declared point sources. These point sources listed in Appendix A includes discharge and mercury time-series for the hydrodynamic and advection modules.

The cross-sections are a 2-dimensional intersection of the stream (Danish Hydraulic Institute (DHI), 2012). These are perpendicular to the stream direction. As described within the MIKE 11 user manual, the geometry of the cross-section defines the volume of water for a specific water level at the cross-section. Alternatively, the user-specified resistance defines the easiness of flow through the stream. Cross-sections were generated for EFPC using a raw data approach requiring left and right bank elevations along with bed elevations. The raw data is automatically processed within the model during simulations. Storage width, flow area, resistance number, and hydraulic radius values are generated for each cross-section during the pre-processing stages of the simulation.

The original EFPC model had numerical instabilities within the MIKE 11 module as the water depth within the original set of cross-sections was routinely exceeding the allowable cross-sections depth. These numerical instabilities were eliminated by adding more cross-sections. The final network file used in simulations is shown in Figure 16, and reveals all the model cross-sections included within the domain. All cross-sections were checked for consistency in the left and right bank elevations, and bed layer elevation against available topography elevation maps for the site. Furthermore, overbank spilling was allowed in all cross-sections.

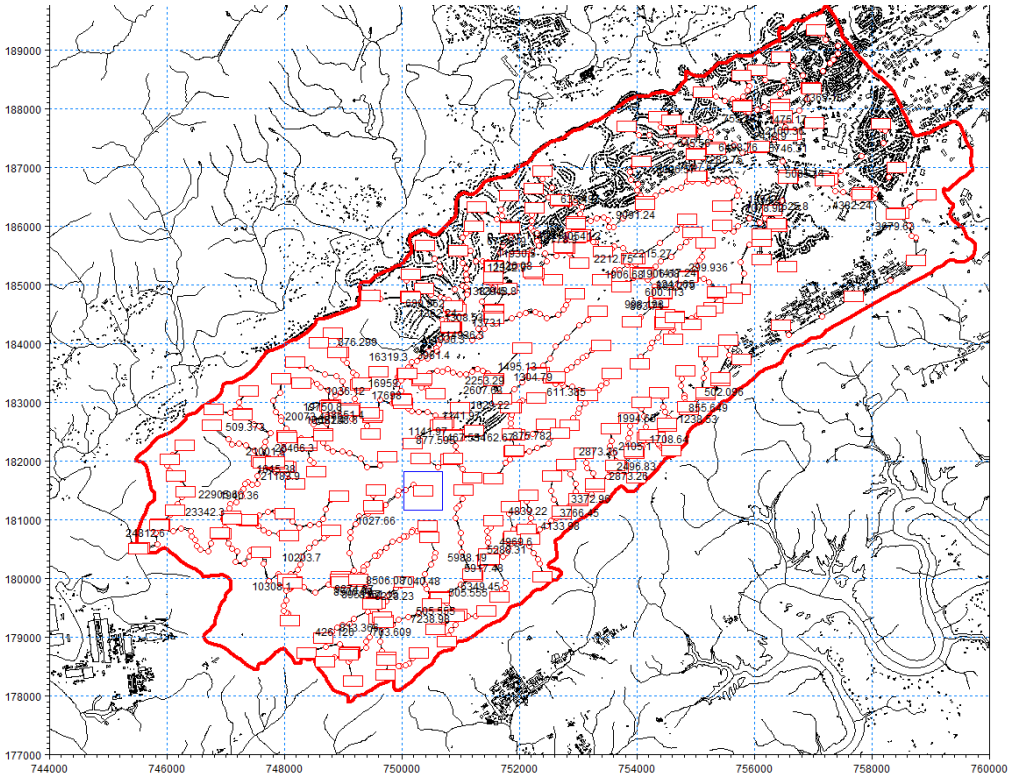

Figure 16. Overview of all river cross-sections in the model.

River cross-sections within the model were generalized as trapezoidal. A model snapshot depicting a detailed schematic of a river cross-section for EFPC is shown at chainage 0.000. Cross-sections downstream of the EFPC branch are also shown in gray in Figure 17.

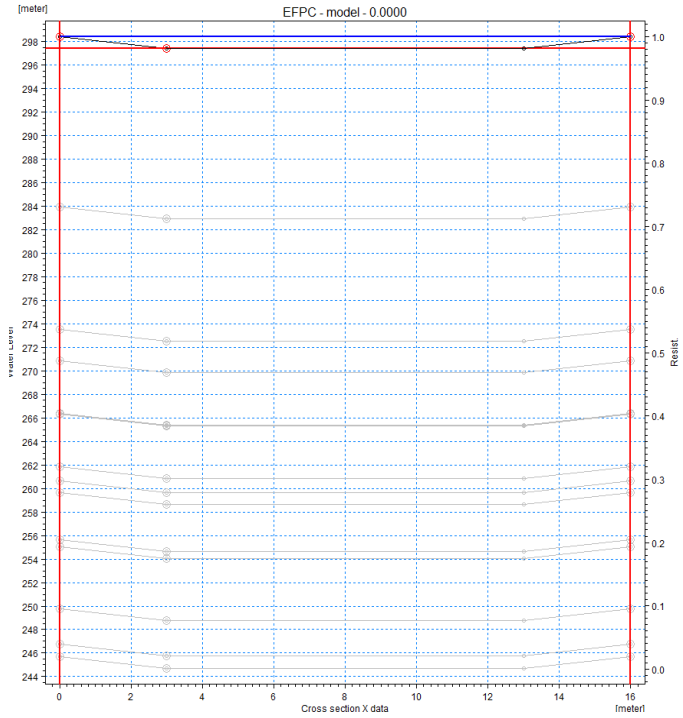

Figure 17. Detailed schematic of river cross-section for EFPC at chainage 0.000 and subsequent chainages downstream.

MIKE SHE and MIKE 11 were coupled by defining branches (reaches) where MIKE 11 HD interacts with MIKE SHE. The hydrologic components of MIKE SHE are directly coupled to DHI's river hydraulic program MIKE 11.

The MIKE SHE-MIKE 11 coupling enables one-dimensional simulation of river flows and water levels using the fully dynamic Saint Venant equations; simulation of a wide range of hydraulic control structures; area-inundation modeling; dynamic overland flooding flow to and from the MIKE 11 river network; and full coupling of surface and sub-surface flow processes in MIKE 11 and MIKE SHE.

To simulate the exchange between river and groundwater, an assumption was made that the river is in full contact with the aquifer material. In this case, the only head loss between the river and the grid node is that created by the flow from the grid node to the river itself. This is typical of gaining streams, or streams that are fast moving.

In this case, the conductance, C, between the grid node and the river link is given by:

$$C = \frac{K \,.da \,.dx}{ds} \tag{58}$$

Where *K* is the horizontal hydraulic conductivity in the grid cell, *da* is the vertical surface available for exchange flow, *dx* is the grid size used in the saturated zone component, and *ds* is the average flow length. The average flow length, *ds*, is the distance from the grid node to the middle of the river bank in the triangular, river-link cross-section. The value of *ds* is limited to between 1/2 and 1/4 of a cell width, since the maximum river-link width is one cell width (half-cell width per side).

The MIKE 11(HD) hydraulic model uses the precise cross-sections, as defined in the MIKE 11 .xns11 (cross-section) file, for calculating the river water levels and the river volumes. However, the exchange of water between MIKE 11 and MIKE SHE is calculated based on the river-link cross-section. The river-link is a simplified, triangular cross-section interpolated (distance weighted) from the two nearest MIKE 11 cross-sections. The top width is equal to the distance between the cross-section's left and right bank markers. The elevation of the bottom of the triangle equals the lowest depth of the MIKE 11 cross-section (the elevation of Marker 2 in the cross-section). The left and right bank elevations in MIKE 11 (cross-section markers 1 and 3 in MIKE 11) are used to define the left and right bank elevations of the river link.

An Open Boundary was specified assuming free upstream and downstream ends of the model domain. The boundary conditions used in the river model are shown in

Table 62. When the Open option is selected in a Boundary Description cell, a branch name and chainage are also needed in order to identify the location of the boundary.

An open boundary condition has two valid boundary types: 1) Inflow, which was specified when a time-varying or constant flow hydrograph condition (for the HD model) is required with or without a solute component (for the AD model); 2) Q-h was specified when the relationship between the discharge and the water level (HD model) is known and used with or without a solute component (used in the AD model).

In the ECO Lab module, there are four sub-domains among which mercury is exchanged: dissolved and adsorbed mercury in the water and dissolved and adsorbed mercury in the sediment (Figure 6).

The concentration of mercury in each sub-domain depends on: 1) the interactions that take place by processes of adsorption and desorption within the water column, and within the sediment phase; 2) the sedimentation and resuspension of small particles, to and from the river bed, bringing mercury contaminated particles into the water column; and 3) the diffusive transport of dissolved mercury between the water column and sediment pore water.

Numerical model results show that most of the mercury in the water column is in the form of particulate mercury; the high affinity of mercury to the organic component of the soil (high k_d) contributes to such behavior.

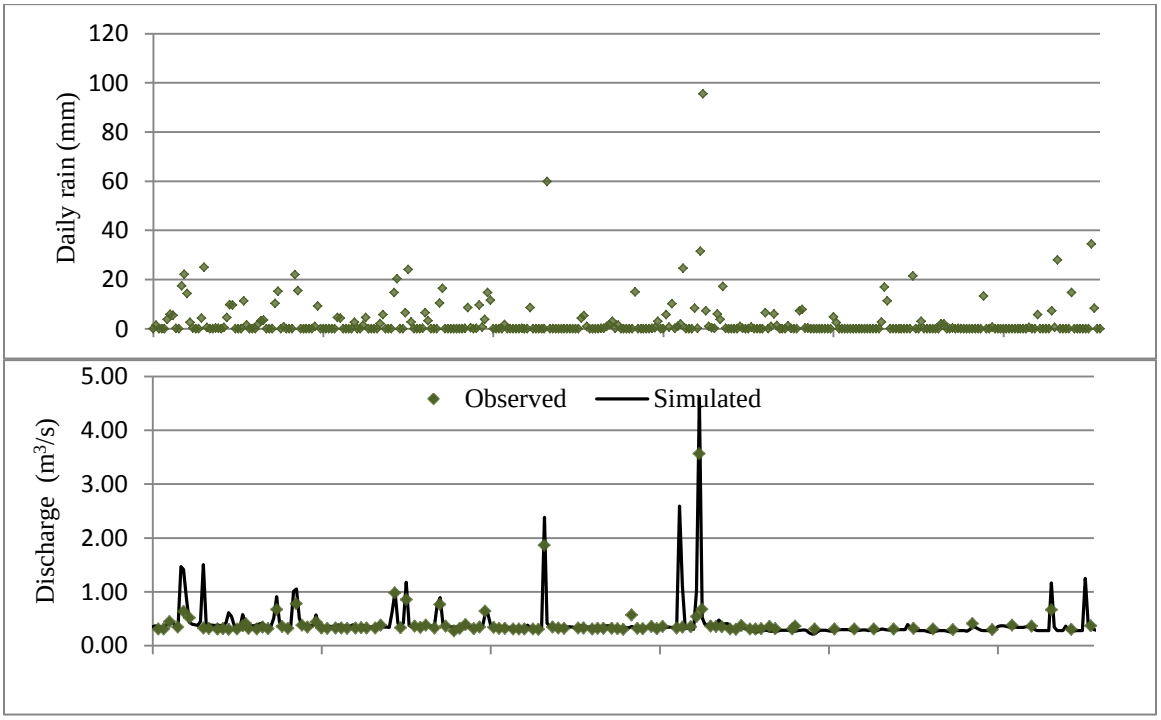

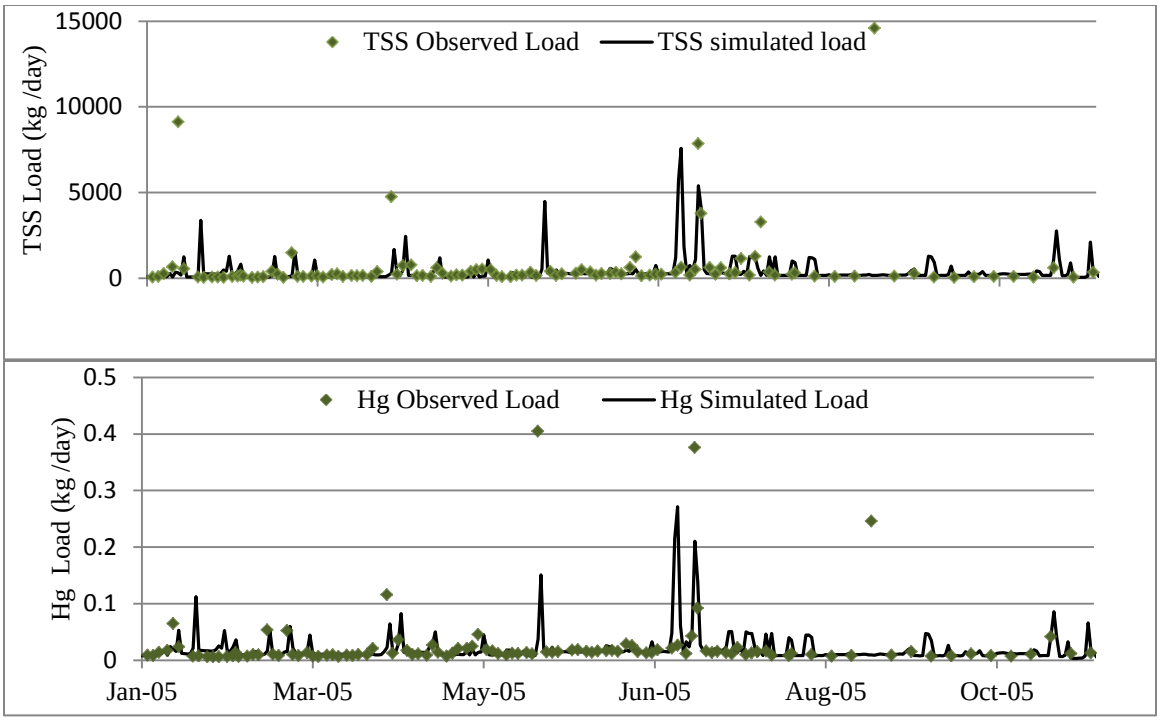

Figure 18. Observed and Simulated rainfall, Q, TSS load and Hg load, UEFPC-Station 17, year 2005. Observed values from OREIS database.

During rain events, the water flow is higher, which causes the shear stress (friction of the water against the bed of the channel) to overcome the critical value for initiation of movement, moving mercury contaminated particles into the water column. Figure 18 presents results from the calibrated model, along with observed values, for the year 2005. During the month of July, the highest rain events of the year occurred: 31 mm/day on the 13th, and 95 mm/day on the 14th, as measured at Station 17 (OREIS Database). Results from the model during the days following the high rain events show an increase in the water flow, up to 4.6 m^3/s, a significant increase from a yearly average of 0.4 m^3/s. The load of suspended solids increased up to 7,569 kg/d (simulated) and 7,848 kg/d (observed) from an average of 373 kg/d. The load of mercury in the water increased up to 0.27 kg/d (simulated), and 0.37 kg/d (observed), from a yearly average of 0.019 kg/d. This shows the correlation between the increased total mercury and the increased mercury-contaminated suspended solid loads.

About 43 outfalls discharge into the UEFPC and constitute a point source for mercury into the creek, bringing residual mercury from the Y12 plant as a result of the collection of stormwater.

Observed discharge and total mercury contribution from those outfalls are included in the model as a boundary condition. Results from the model show that during the year 2005, a total mass of 6.8 kg of mercury passed through Station 17, from which 4.6 kg (68%) were contributed by the outfalls. It can be inferred that the remaining 32% originated from non-point sources, presumably the exchange of particulate mercury with the river bed. The proportion between total mercury load and point source contribution, for the year 2005, can be observed in Figure 19. Furthermore, the accumulated load is presented in Figure 20.

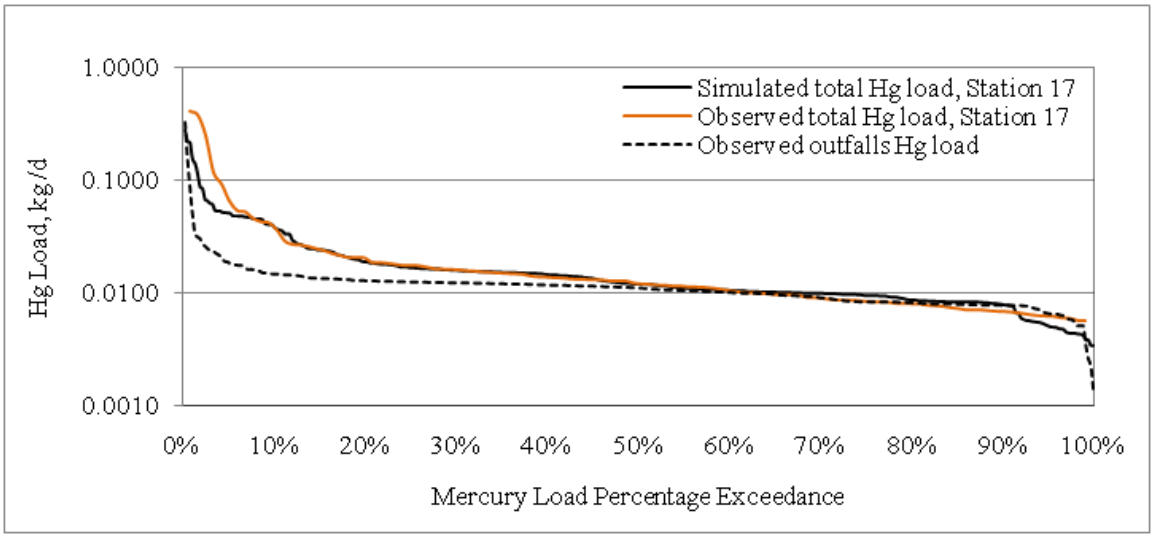

Figure 19. Mercury load from outfalls and total at Station 17.

Even though there was an increase in the total mercury load from outfalls during the high rain events, the maximum load generated from the outfalls in a single day (0.32 kg/d in July 2005) is not enough to explain the maximum load in a single day (0.38 kg/d) measured at Station 17, about 20% higher for this day.

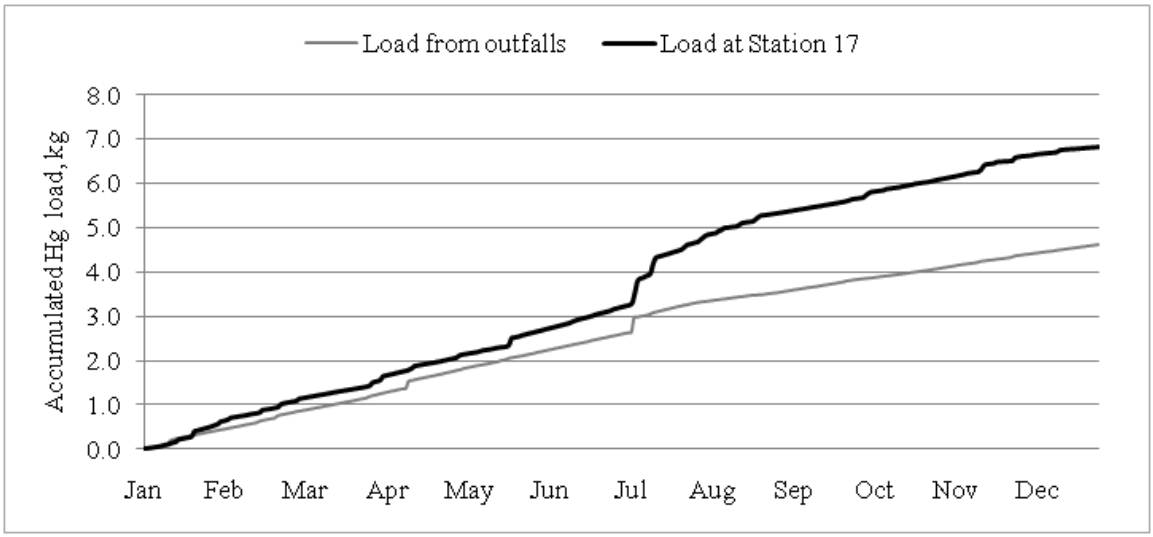

Figure 20. Accumulated mercury load from outfalls and total at Station 17.

As a result of the implementation of the sedimentation module (ECO Lab), the prediction capability of the model has been improved, as can be observed in Figure 21, where the simulated load of mercury with ECO Lab shows a better fit with the observed data. The simulation period covers years 2000 to 2008.

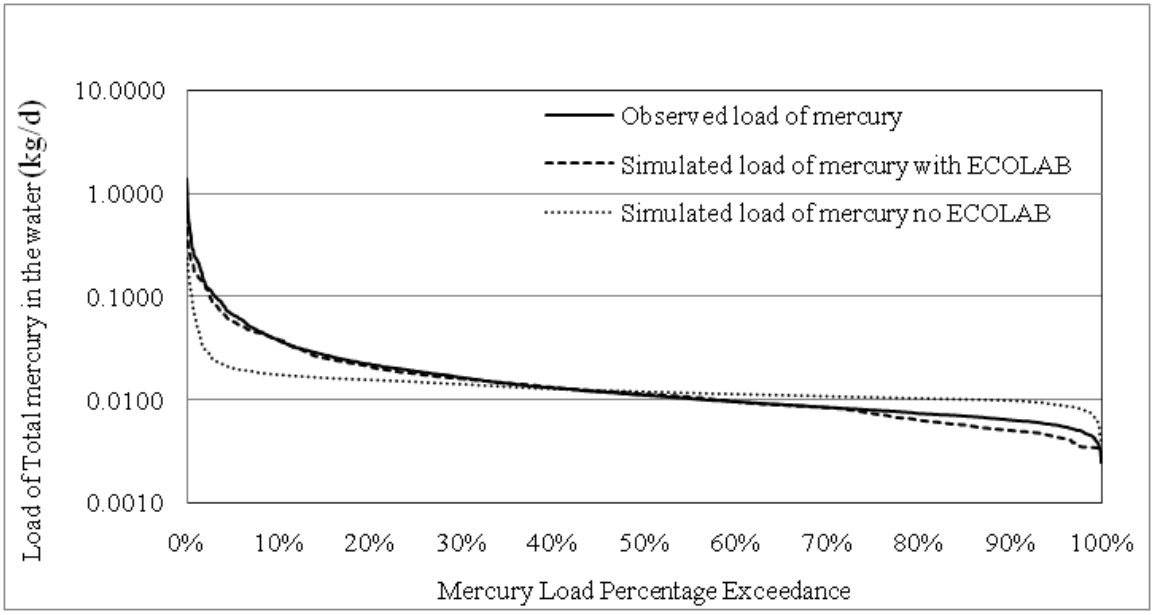

Figure 21. Simulated load with and without ECO Lab.

A variety of simulations have been executed with the purpose applying the recently modified model for flow and mercury in developing components of a total maximum daily loads study for the domain area. The term total maximum daily load, is defined in section 303 (d) of the U.S. Clean Water Act (1972) as the maximum amount of both point and non-point pollutant sources that a body of water can receive while still meeting water quality standards. The objective of developing a TMDL analysis for EFPC is to allocate loads to pollutant sources contributing to the watershed impairment, and consequently, implement appropriate control measures to achieve water quality standards.

A TMDL combines the sum of all point source loads known as waste load allocations (WLAs) and non-point source loads known as load allocations (LAs) with a margin of safety (MOS) that accounts for the uncertainty between the pollutant loads and the receiving water quality. The aforementioned relationship is described by the equation below:

$$TMDL = \Sigma WLA + \Sigma LA + MOS \quad \text{(Equation 59)}$$

Flow and load duration curves represent a valid tool for the analysis of data and form part of the TMDL development process. A flow duration curve reveals the relationship between the magnitude of the flow and the frequency in a particular stream (USEPA, 2008b). A flow duration curve created from averaged data is constructed by ranking available flow data from high to low, using the rank position to calculate a plotting position also known as the exceedance probability (USEPA, 2008b). Load duration curves were developed by multiplying the daily mean flow by the measured concentration of suspended solids. LDCs for mercury were also developed by multiplying the daily mean flow by the observed concentration of mercury in the water. In the past, TMDL efforts for the site have included an extensive analysis of recorded water quality data at outfall points regulated by the National Pollutant Discharge Elimination System (NPDES). Efforts associated with this research focus instead on identifying the percent reduction in mercury loading at Station 17 or EFK 23.4 necessary to meet designated water quality criterion.

The model network is shown in Figure 22. Field stations considered are shown (EFK 23.4, 03538250, 03538273, 03538270, and 03538673) as well as their model computational counterparts (EFPC 3209.9, EFPC 03538250, BC 8728.87, BC 7700.06, BC 6168.82). The discharge and mercury time-series shown in the subsequent sections reveal variations in discharge and mercury concentrations at various points throughout EFPC and BC being primarily driven by hydrological events.

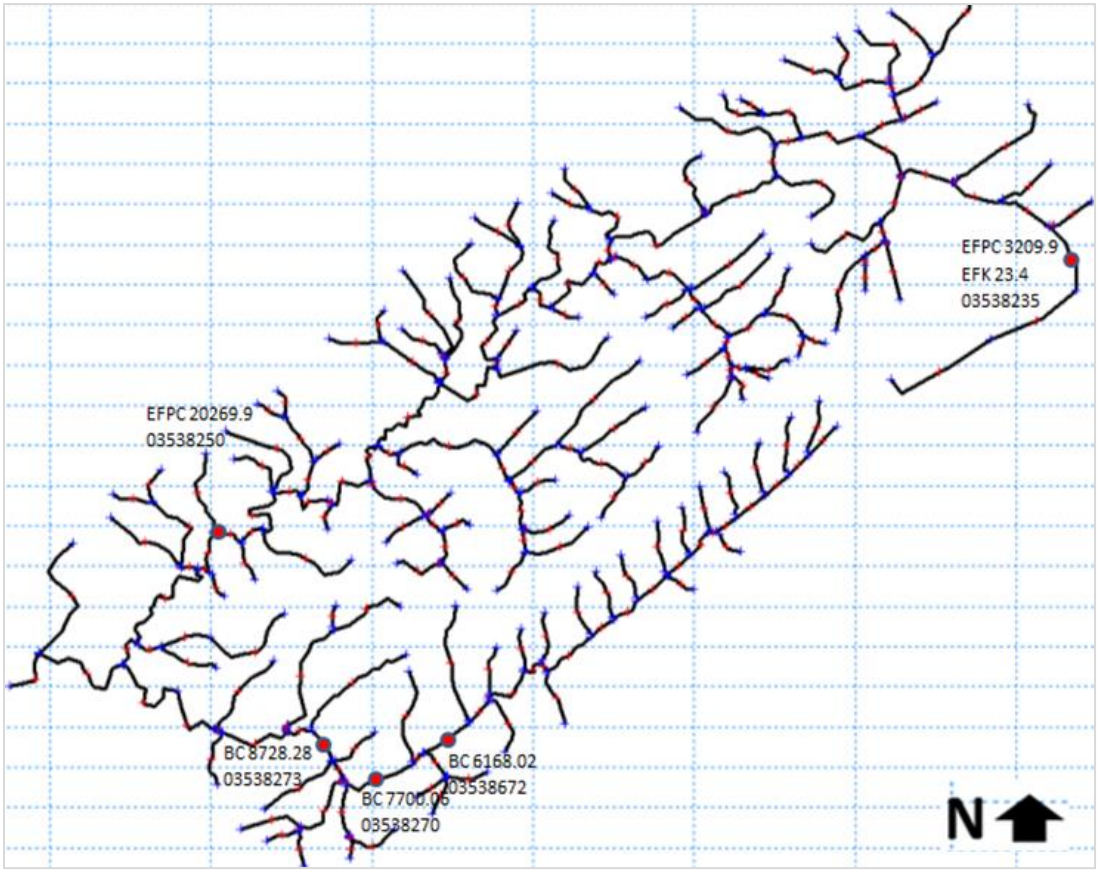

Figure 22. Model network highlighting the stations discussed in the results.

Overview of Flow Module Results

Flow simulations were set to a period from 7/12/1991 through 1/1/2005. This 13.5-year period contains a range of hydrologic conditions that include low and high stream flows. Simulated flow time-series are shown in Figure 16. Discharge time-series depicting the simulated flow at EFPC 3209.9 and EFK 23.4/Station 17 is shown in Figure 17. The simulated discharge time-series for EFPC 3209.9 exhibited a 22.6% difference in average when compared to field records at Station 17. In reality, flow at Station 17 is not solely dependent upon hydrological events that magnify discharges at a given time. This station is heavily influenced by discharges from regulated outfalls. Discharges from such regulated outfalls can be a contributing factor; amplifying the differences between computed and observed average flow as well as variability in observed and simulated peak flows at Station 17 and EFPC 3209.9. This area has been subjected to flow augmentation in past remediation attempts. Without considering approximately a 0.28 m^3/s flow augmentation, the simulated flow at EFPC 3209.9 is not expected to have a good fit with observed data from Station 17. At a minimum the flow augmentation scenario needs to be implemented to ensure correlation between the simulated and observed base flow. Discrepancies among the computed and observed average flow is smaller at other points throughout the watershed. For example, downstream EFPC at computational node EFPC 20731.6, the average flow was 1.22 m^3/s while the recorded value for USGS station 03538250 was 1.41 m^3/s. In this case, a 13.5% error between computed and observed average flow values was exhibited. The model reveals general trends consistent with measured data.

Simulated average flow for BC at chainage 8728.28, 7700.06, and 6168.82 were 0.279 m^3/s, 0.215 m^3/s, and 0.156 m^3/s, respectively. This was comparable to the observed average flow of 0.253 m^3/s, 0.212 m^3/s, and 0.143 m^3/s for USGS stations 03538273, 03538270, and 03538672 respectively. The average flow increases downstream EFPC and BC. Similarly, time-series for computed discharges at BC 7700.06 were compared to USGS station 03538270 and are shown in Figure 23. Observed and computed discharges at this station show a much better match in which the base flow is captured by the model.

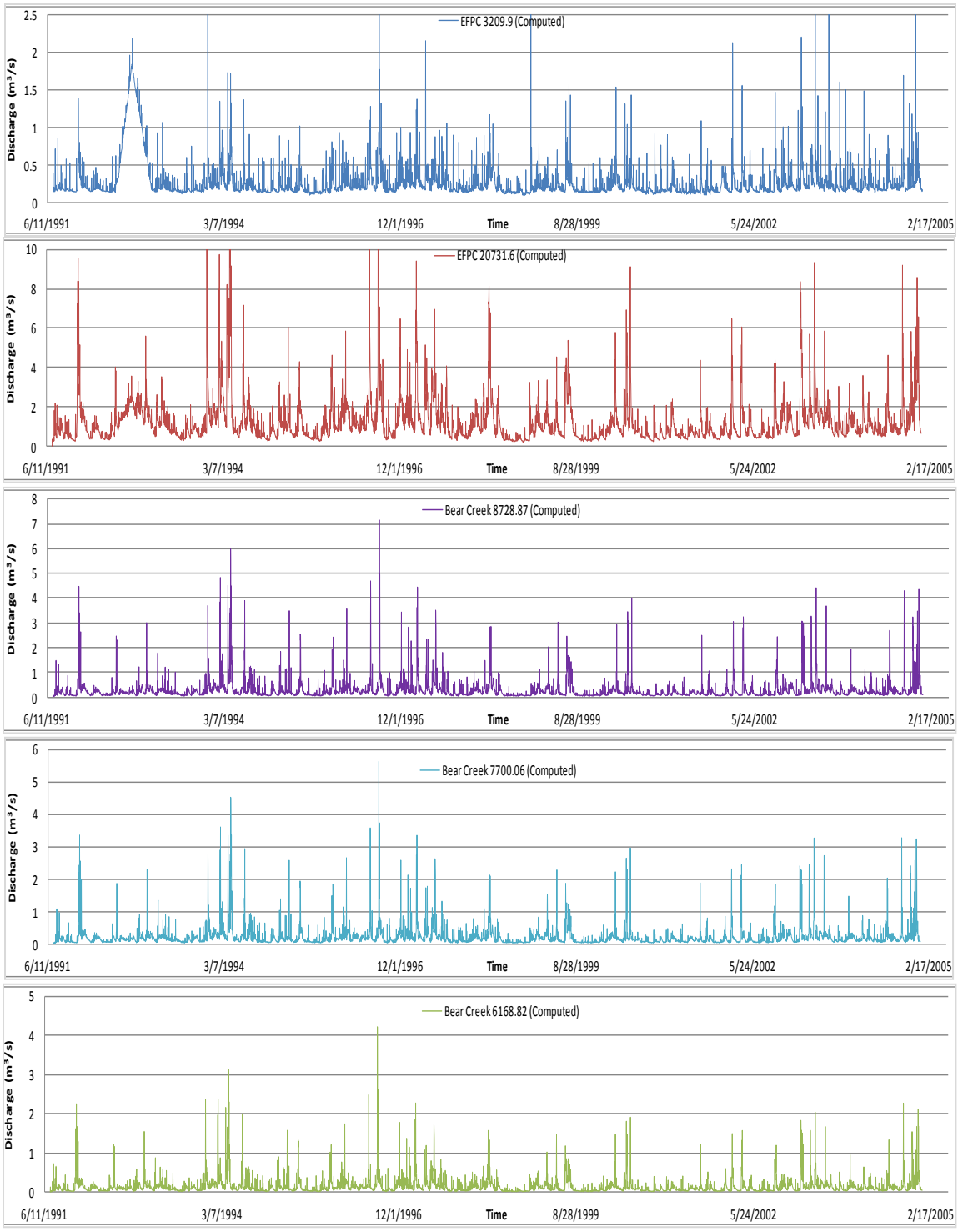

Figure 23. Computed discharges downstream EFPC and BC for various model nodes (EFPC 3209.9, EFPC

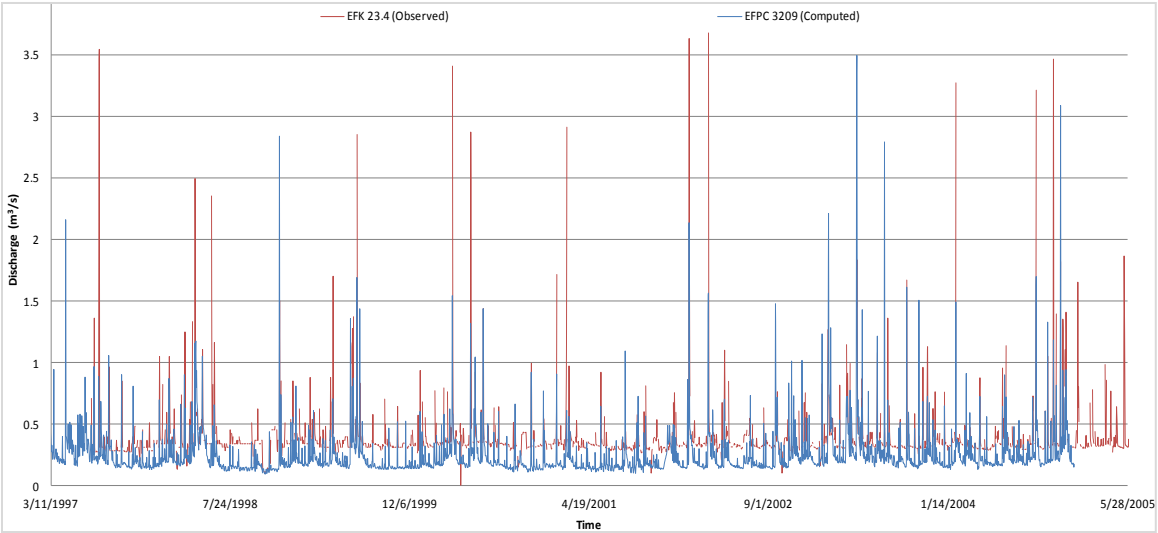

Figure 24. Comparison of discharges time-series at EFPC 3209.9(computed) and EFK 23.4 (observed).

The root mean square error (RSME) has been calculated for the time-series presented in this study in order to measure the average magnitude of the error. The RSME value for each time-series is depicted in the graphic. The difference between the simulated and the corresponding observed or field value was squared and then averaged over the sample data. The square root of the average was then taken. The RSME attributes a relatively large weight to errors.

Flow duration curves for EFPC and BC were constructed from daily flow measurements taken at each station considered. The flow duration curve for various stations is shown in Figure 25, Figure 26, Figure 28, Figure 29 and Figure 30. These figures represent the cumulative distribution of daily discharges arranged to show percentage of time specific flows were exceeded during the period of record. The underlying concept behind the cumulative distribution of flow duration curves attributes that the highest daily mean flow during this period is exceeded 0% of the time and the lowest daily mean flow is equaled or exceeded 100% of the time. Flow duration curves were divided into five zones. These included high flows (0-10%), moist conditions (10-40%), mid-range flows (40-60%), dry conditions (60-90%), and low flows (90-100%).

Portions where the simulated flow duration curve represents a good or bad fit with the observed are noted in the figures that follow. With each probability of exceedance curve developed for flow duration, mercury concentration, and mercury mass rate a summary of average flow, concentration, or mass rate is provided per flow regime and summarized in tabular format below the graph. The difference between the simulated and observed average per flow regime is also noted. The flow duration curves; Figure 18, Figure 19, and Figure 21 through 23 reveal the model's ability to best simulate flow or discharges during high flow, moist-conditions, and mid-range flows. Dry conditions and low flow regimes establish a greater margin of error and numerical instability.

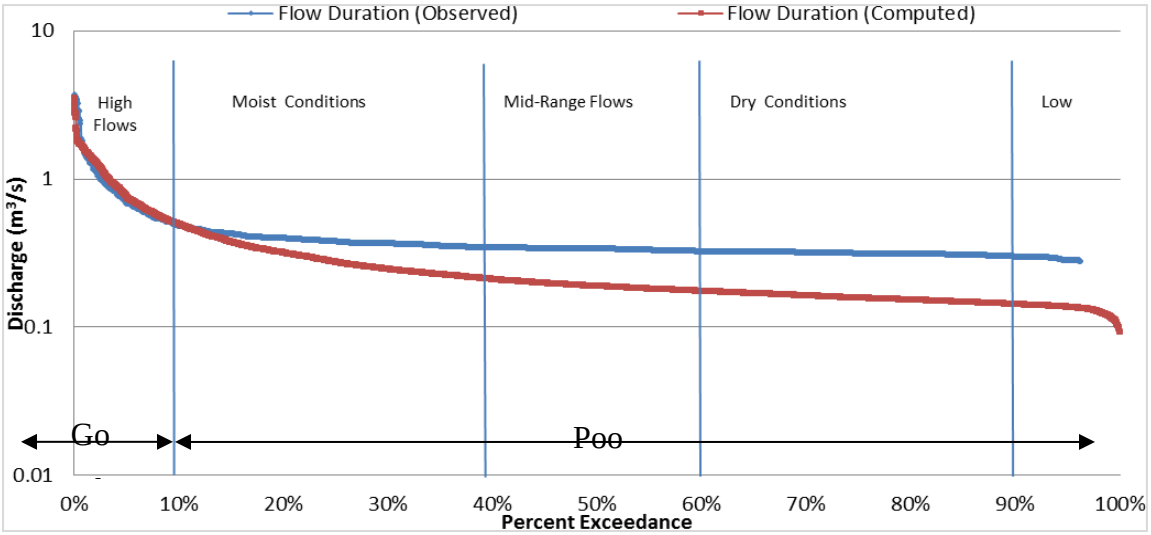

Average Flow (m^3/s)	High	Moist	Mid-Range	Dry	Low
Simulated	0.9370	0.2962	0.1896	0.1577	0.1328
Observed	0.9349	0.3861	0.3360	0.3134	0.2616
Averages Difference	0.0021	0.0899	0.1464	0.1557	0.1288

Figure 25. Comparison of flow duration curves for EFPC 3209.9 (computed) and EFK 23.4 (observed).

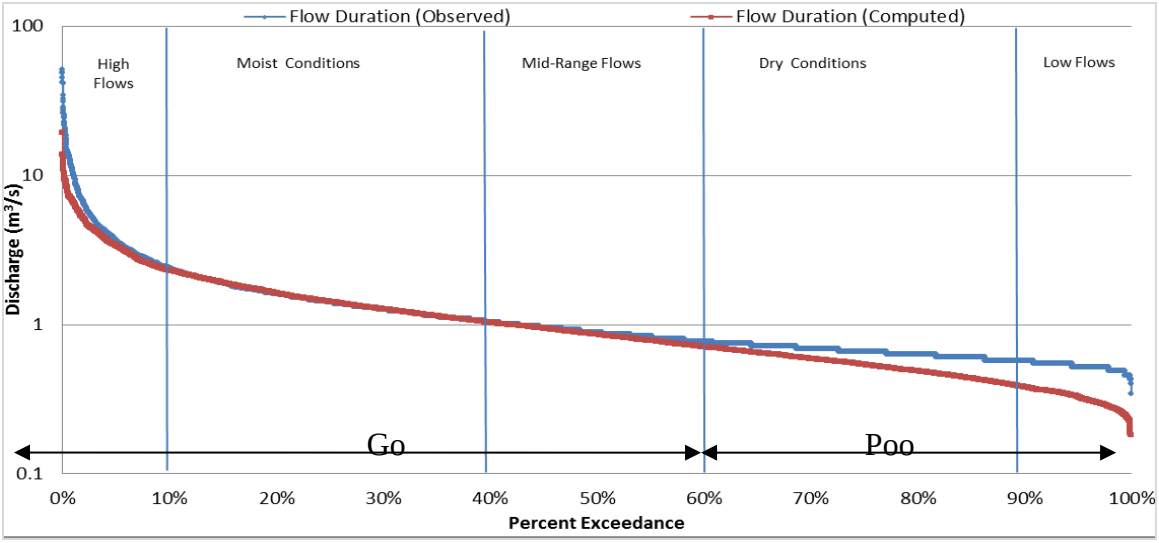

Average Flow (m^3/s)	High	Moist	Mid-Range	Dry	Low
Simulated	4.0445	1.5029	0.8628	0.5416	0.3205
Observed	5.4531	1.4730	0.8784	0.6530	0.5164
Averages Difference	1.4086	0.0299	0.0157	0.1114	0.1959

Figure 26. Comparison of flow duration curves for EFPC 20269.9 (computed) and 03538250 (observed).

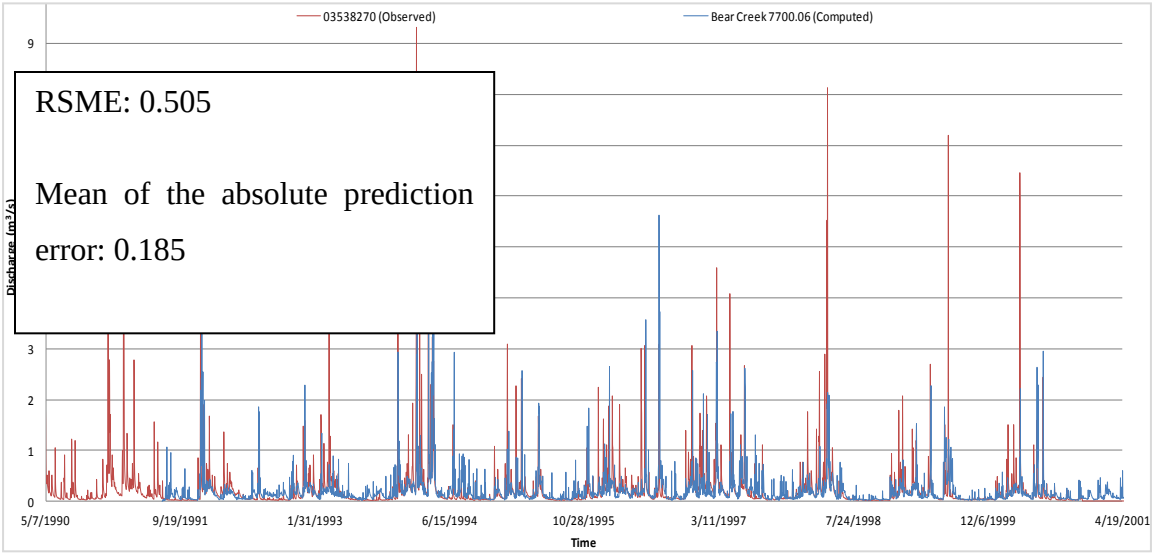

Figure 27. Comparison of discharges time-series at BC 7700.06 (computed) and 03538270 (observed).

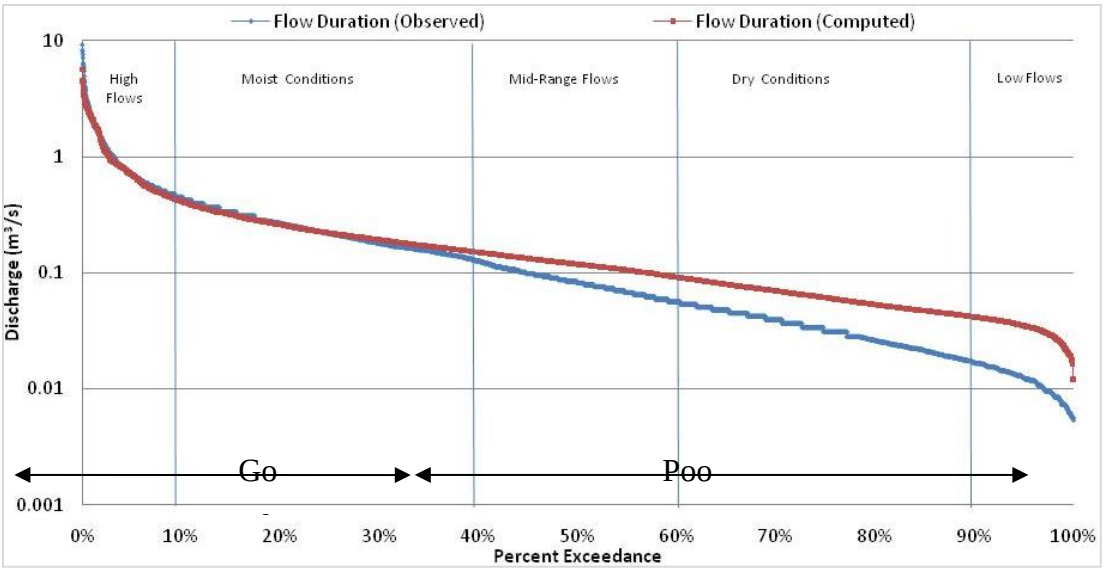

Average Flow (m^3/s)	High	Moist	Mid-Range	Dry	Low
Simulated	1.2825	0.3056	0.1541	0.0811	0.0429
Observed	1.1262	0.2385	0.0851	0.0337	0.0121
Averages Difference	0.1563	0.0671	0.0690	0.0474	0.0307

Figure 28. Comparison of flow duration curves at BC 7700.06 (computed) and 03538270 (observed).

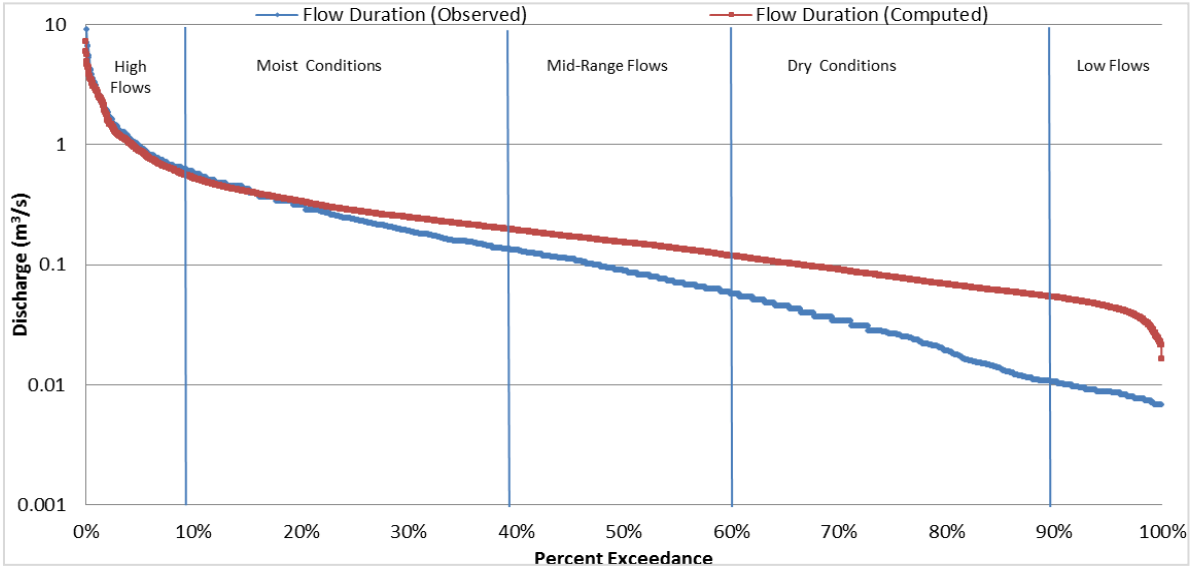

Figure 29. Comparison of flow duration curves for BC8728.87 (computed) and 03538273 (observed).

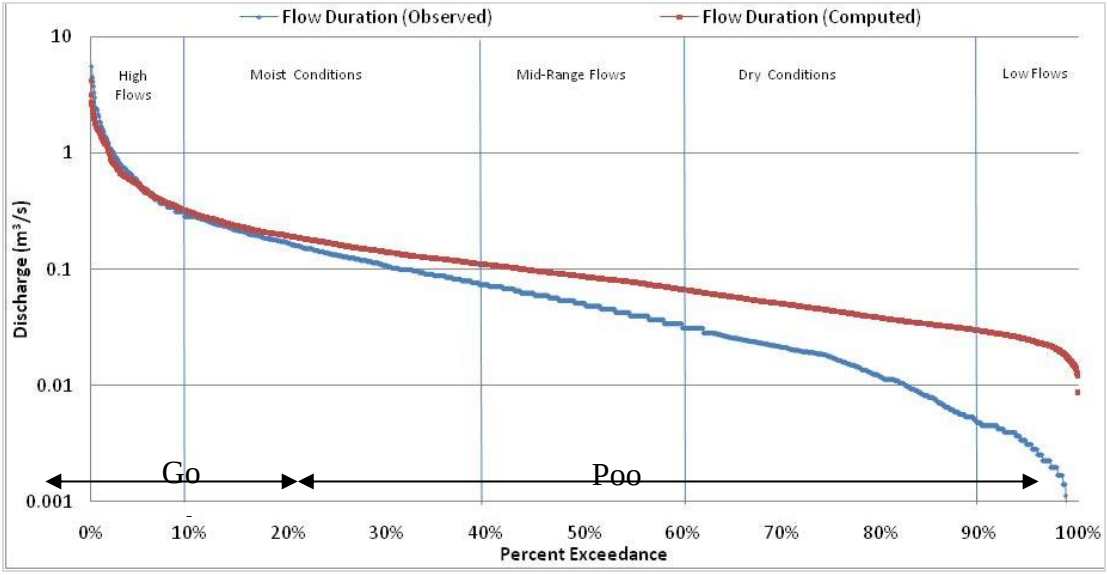

Average Flow (m^3/s)	High	Moist	Mid-Range	Dry	Low
Simulated	0.6950	0.1756	0.0871	0.0452	0.0238
Observed	0.8324	0.1470	0.0509	0.0171	0.0029
Averages Difference	0.1374	0.0286	0.0362	0.0282	0.0209

Figure 30. Comparison of flow duration curves at BC 6168.82 (computed) and 03538673(observed).

Water Quality Module Results

This section describes components of a preliminary TMDL primarily focused on identifying trends in mercury load duration curves and quantifying the percent reduction in loading necessary to meet the water quality criterion mandated for the site based on various water user classifications. TMDL components were developed for EFPC based on available water quality data and the application of the model. In accordance with the approach implemented in previous studies; where applicable, TMDLs, WLAs, and LAs are expressed as the percent reduction in flow or mercury concentrations required to maintain the desired target levels of mercury concentrations in fish tissue.

Designated water use classifications for EFPC encompass a wide range. Among these are the ability to sustain fish and aquatic life, irrigation, livestock watering and wildlife, and recreation.

In the case of recreation use, a water quality standard of 51 ppt total mercury concentration in surface water has been suggested by TDEC, EPA, and DOE. For the protection of fish and aquatic life from toxic inorganic substances the State of Tennessee Water Quality Standards suggested a water quality criterion of 770 ppt. There is also the ROD target of 200 ppt for the Station 17 (EFK 23.4) proposed by DOE. A specific water quality criterion has not been designated yet for irrigation, and livestock watering and wildlife designated uses. Water quality criteria for EFPC are summarized in the table below.

Table 4. Mercury Concentration Limits Per Designated Usage Classification

Usage Classification	Mercury Concentration (ppt)
Recreation	51
Fish and aquatic life	770
Irrigation	Not Available
Livestock watering and wildlife	Not Available

The EPA currently recommends a water quality criterion for methylmercury expressed as a fish tissue concentration value of 0.3 milligrams methylmercury per kilogram of wet-weight fish tissue, or 0.3 mg/kg. Per the EPA, a fish tissue residue water quality criterion for methylmercury is more appropriate than a water column-based water quality criterion. However, since the direct link between the EPA's fish methylmercury water quality criterion and the available water quality mercury concentration data for stations in the watershed were difficult to associate the TMDL comparison was based on the most stringent water quality criterion per usage classification. The most stringent water usage classification was employed and used to establish target levels for TMDL reductions at Station 17.

Simulated mercury time-series are shown in Figure 31 for computational nodes downstream EFPC and BC that overlap with field stations. Simulated average mercury concentrations for BC at chainage 8728.28, 7700.06, and 6168.82 were 1.6 μg/L, 2.2 μg/L, and 2.9 μg/L, respectively.

Mercury concentrations appear to decrease upstream BC. The slightly higher average mercury concentration of 2.9 μg/L computed at BC 8728.28 could be attributed to its proximity to EFPC as previous studies hypothesize on the potential of mercury particulates to be carried downstream during extreme hydrological events. In the case of EFPC, the model initially overestimated the mercury concentration at Station 17 reporting 186 μg/L when the recorded average was 0.89 μg/L. At EFPC 20731.6, the average mercury concentration was 13.7 μg/L. Since EFK 23.4 or Station 17 is the only station with significant mercury data, calibration efforts were thus

implemented within the model's computational dynamics to achieve more realistic results for mercury concentrations at observed Station 17 and computed EFPC 3209.9. Figure 32 provides visual information about the close match between observed and computed mercury concentration at Station 17 (EFK 23.4). Figure 33 showcases measured discharges and mercury concentration as a function of time in an attempt to identify trends among the two.

Based on the simulation results, it appears that the majority of the mercury in the creek is in the adsorbed form. As shown in Figure 34, approximately 75.2% of the total mercury is in the adsorbed form and 24.8% is estimated to be present in the dissolved mercury form. A more focused time-series graph is shown in Figure 35. highlighting fluctuations for the year 2000. These results are not only consistent with findings from the Y-12 micro-scale model but are also confirmed by field investigations performed by ORNL in previous years.

This pattern emphasizes the importance of suspended particles and its direct connection to the total mercury concentration in the creek. As shown in Figure 34 and Figure 35. , the streambed pore water within the reach contains very high concentrations of dissolved mercury often exceeding 100 ppt. Dissolved mercury in sediment pore water contributes to the high mercury concentration in the creek water through diffusive transport and pore-water recirculation. This occurs as higher flow in the river suspends both the mercury-laden particulates and the highly contaminated trapped water in sediment pores to the creek water. These findings are consistent with studies that associate floodplain with wet weather, high flow events, as oppose to the headwater flux which seem to occur under base-flow conditions [6].

Figure 31. Computed mercury concentrations downstream EFPC and BC for various model nodes (EFPC 3209.9, EFPC 20731.6, BC 20731.6, BC 8728.87, BC 7700.06, and BC 6168.82).

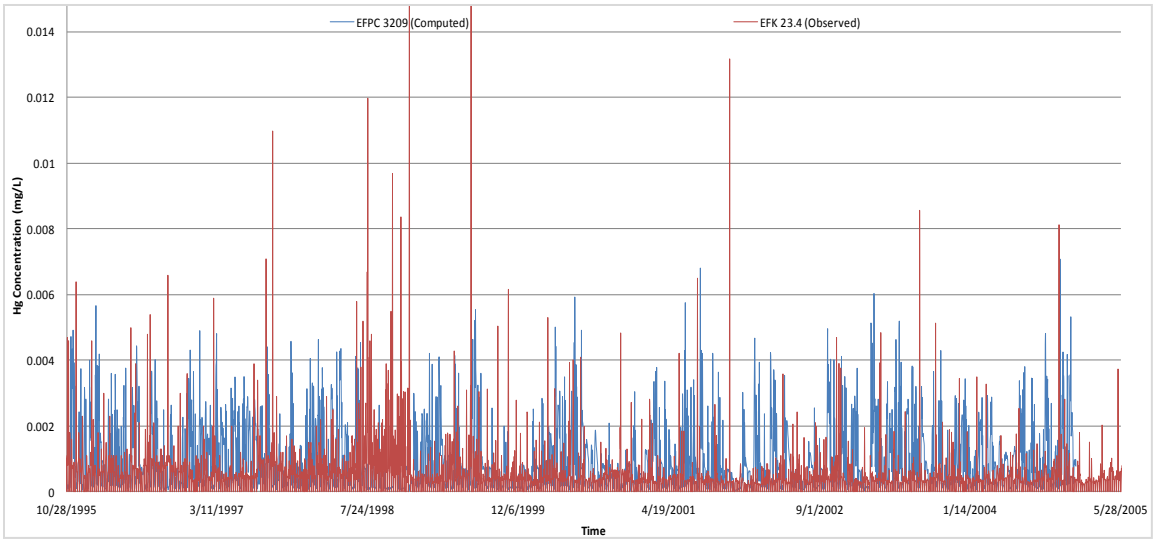

Figure 32. Comparison of mercury time-series at EFPC 3209.9 (computed) and EFK 23.4 (observed).

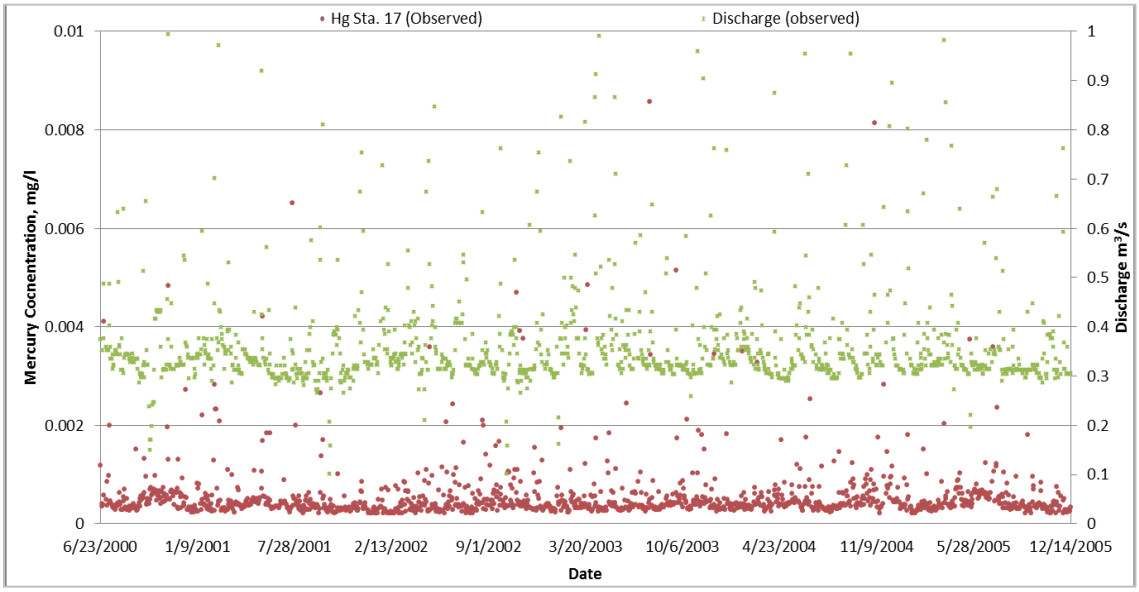

Figure 33. Measured mercury concentrations and discharges at Station 17.

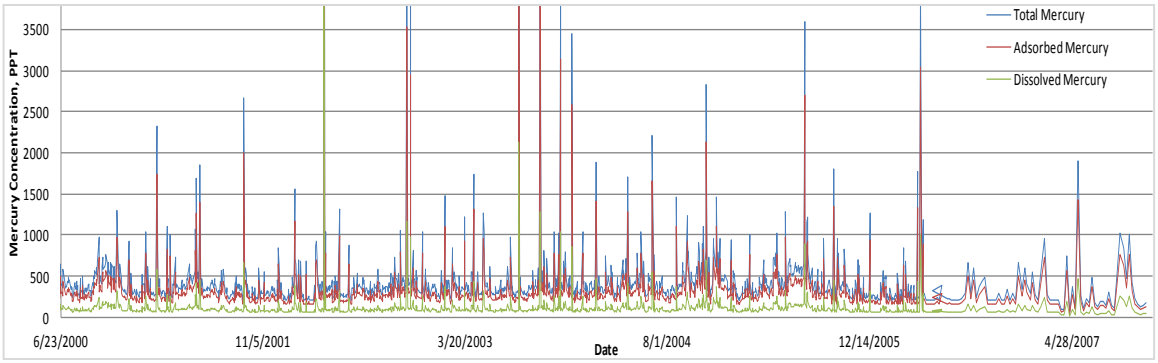

Figure 34. Total, adsorbed and dissolved mercury concentration time-series for the simulated time period starting at year 2000.

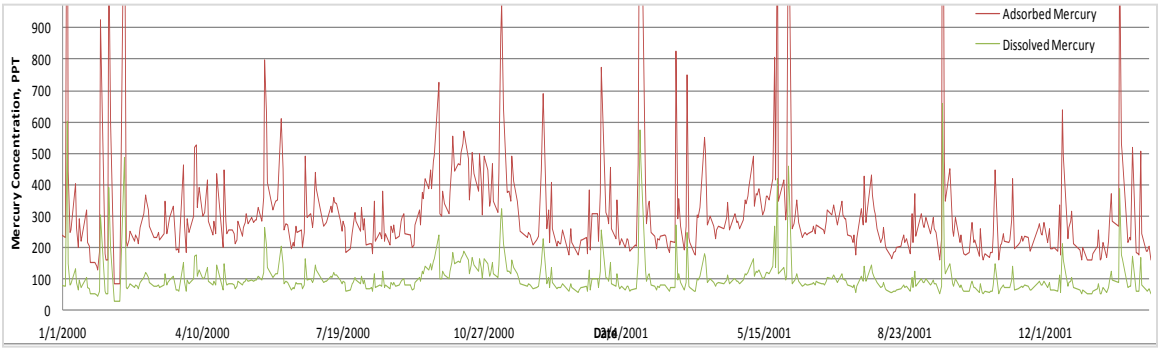

Figure 35. Simulated adsorbed and dissolved mercury concentration time-series for year 2000.

The sensitivity of the organic partition coefficient (K_d) within the water quality sorption processes was evaluated to establish how total mercury concentrations computed within the water quality module are impacted by variations of this parameter. The organic partition coefficient parameter was varied. The K_d values used include 0.001 m^3/g, 0.025 m^3/g, 0.050 m^3/g, 0.500 m^3/g, and 5 m^3/g. Figure 36 shows the variability caused by each K_d within the mercury concentration time-series for a 1-year period (2001 - 2002). As shown in the image, the pattern within the time-series is maintained yet the baseline mercury concentration and peak extent is accentuated. The relationship between the organic partition coefficient and the average daily load at Station 17 is best described as logarithmic (Figure 37).

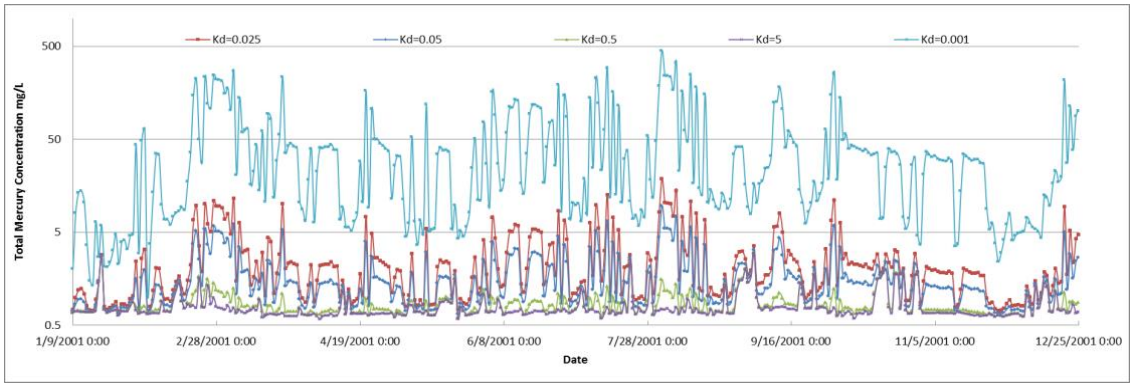

Figure 36. Total mercury time-series depicting sensitivity to organic partition coefficient (Kd) for various simulations.

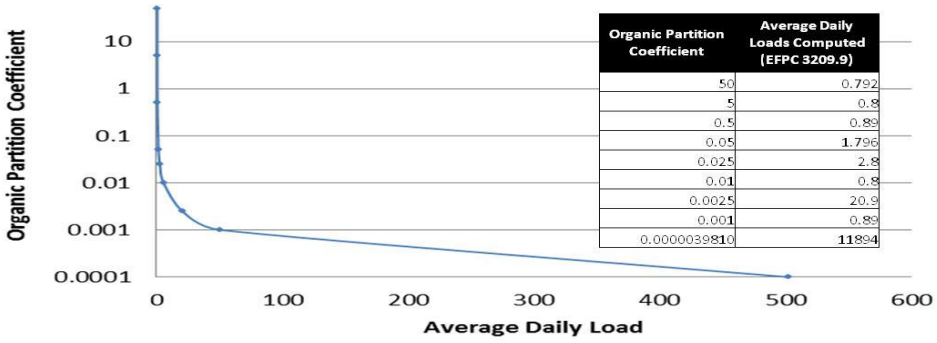

Organic Partition Coefficient	Average Daily Loads Computed (EFPC 3209.9)
50	0.792
5	0.8
0.5	0.89
0.05	1.796
0.025	2.8
0.01	0.8
0.0025	20.9
0.001	0.89
0.0000039810	11894

Figure 37. Observed trend between average daily loads and Kd.

Probability of exceedance curves are a classical way for regulators to understand the system in terms of the various flow regimes exhibited. Figure 38 shows the probabilities of exceedance for computed and recorded mercury concentrations prior to the implementation of mercury calibration efforts for EFPC 3209.9 and EFK 23.4. Similarly, Figure 38 depicts the post-calibration mercury concentration probabilities of exceedance for the same station. Figure 38 reveals a much better correlation between the field records and the simulated results at Station 17. As can be observed in Figure 39, the post calibration load was improved by orders of magnitudes.

The daily flow rates and observed concentration were used to obtain daily load estimates in an attempt to identify seasonal trends, compare one location to another, and serve as a future tool for the development of water quality goals. Computed and observed load duration curves (LDCs)

were thus created for the previously discussed field records and model stations. These images are shown in Figure 39 through Figure 43. The LDC for model station EFPC 3209.9 and field station EFK 23.4 provides a general trend consistent with the one previously reveal by the FDCs. For the loads, similarly to the discharges, the model is best able to simulate the observed for high flow, mid-range flow, and moist conditions. The mercury loads appear to be attenuated downstream EFPC (Figure 40). This pattern is not of significance at BC (Figure 41) as variations of load duration curves are minor throughout BC.

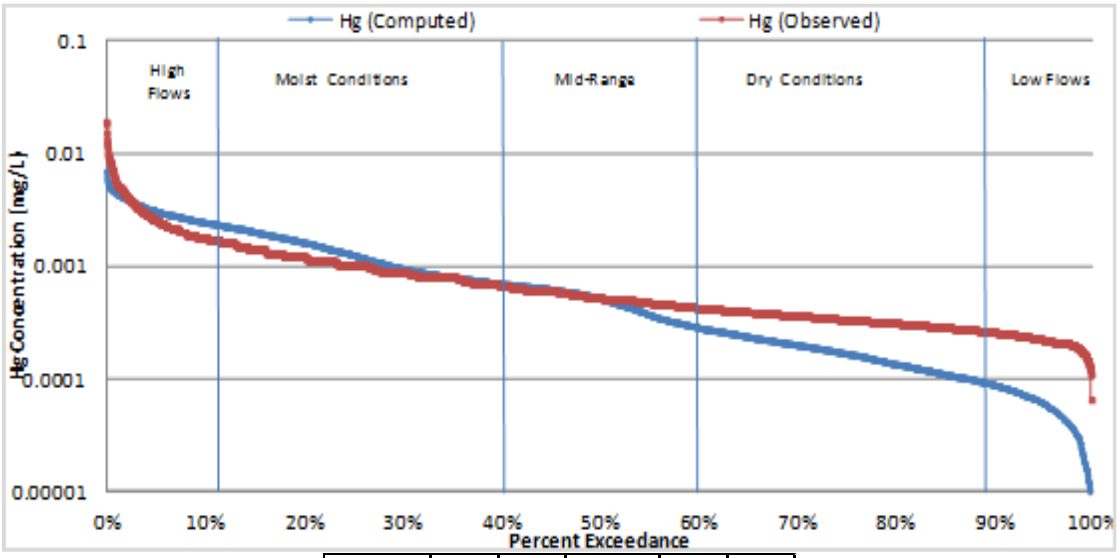

Average Concentration (mg/L)	High	Moist	Mid-Range	Dry	Low
Simulated	0.0033	0.0014	0.0005	0.0002	0.0001
Observed	0.0034	0.0011	0.0005	0.0003	0.0002
Averages Difference	0.0001	0.0003	0.0000	0.0001	0.0001

Figure 38. Comparison mercury concentration probability of exceedance for EFPC 3209.9 (computed) and Station 17 (observed).

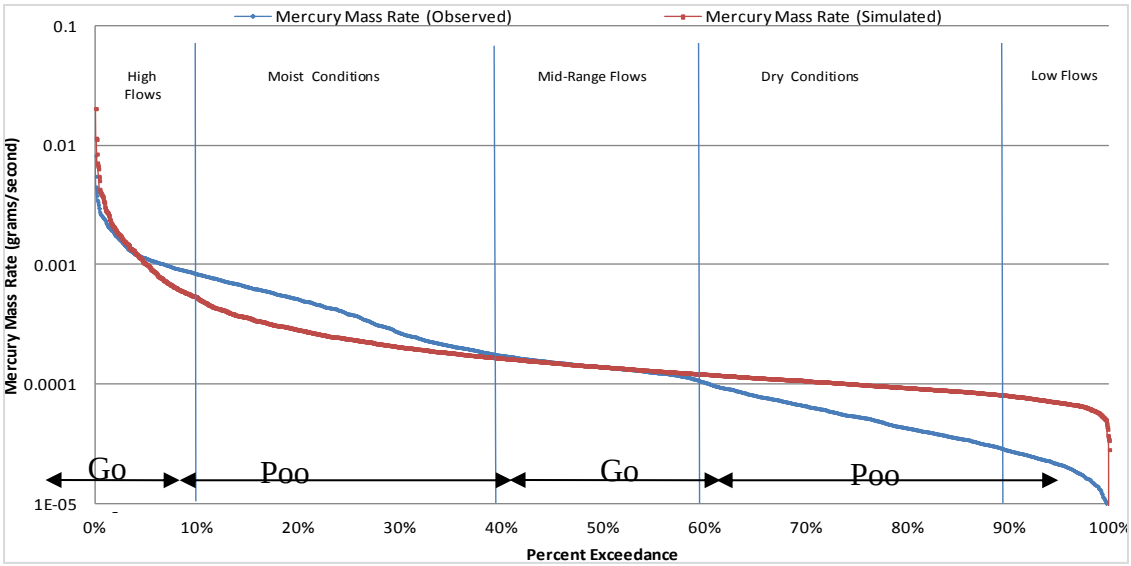

Figure 39. Comparison of load duration curves for EFPC 3209.9 (computed) and EFK 23.4 or Sta. 17 (observed).

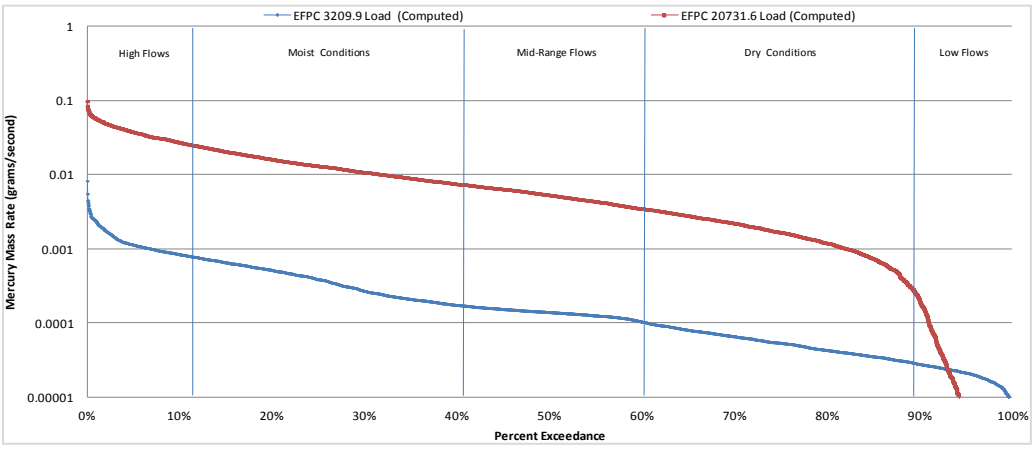

Figure 40. Comparison of load duration curves for computed model stations EFPC 3209.9 and EFPC 20731.6.

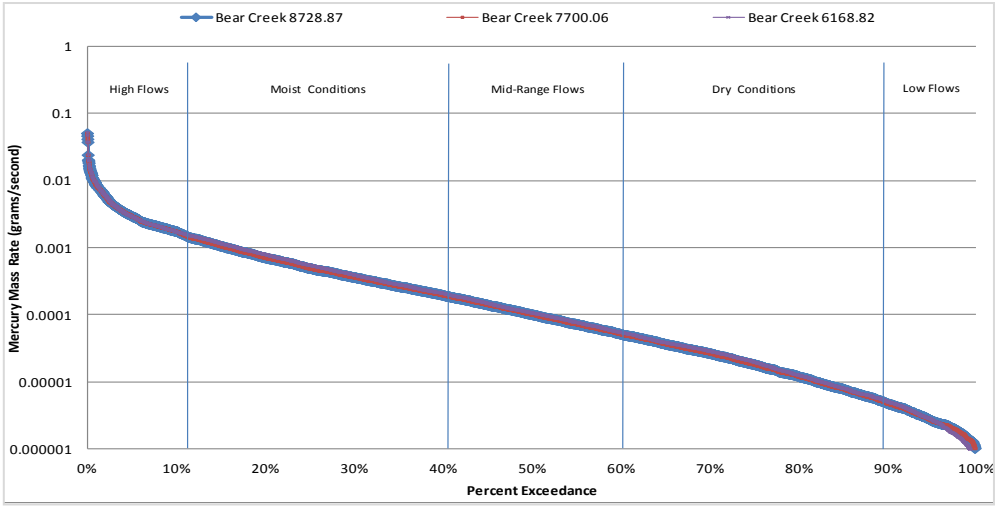

Figure 41. Load duration curves downstream BC.

Total suspended solids patterns were also investigated for Station 17. The same process applied for analyzing the flow and mercury time-series, generating probabilities of exceedance curves, and LDCs were implemented when evaluating total suspended solids. Figure 42 compares recorded and computed TSS and mercury load duration curves for different flow conditions and reiterates the observation established by Figure 34 and Figure 35. The resuspension of mercury-laden fine particulates during high flow conditions (i.e., the wet seasons) plays a significant role in the enhancement of local concentration of mercury along the creek.

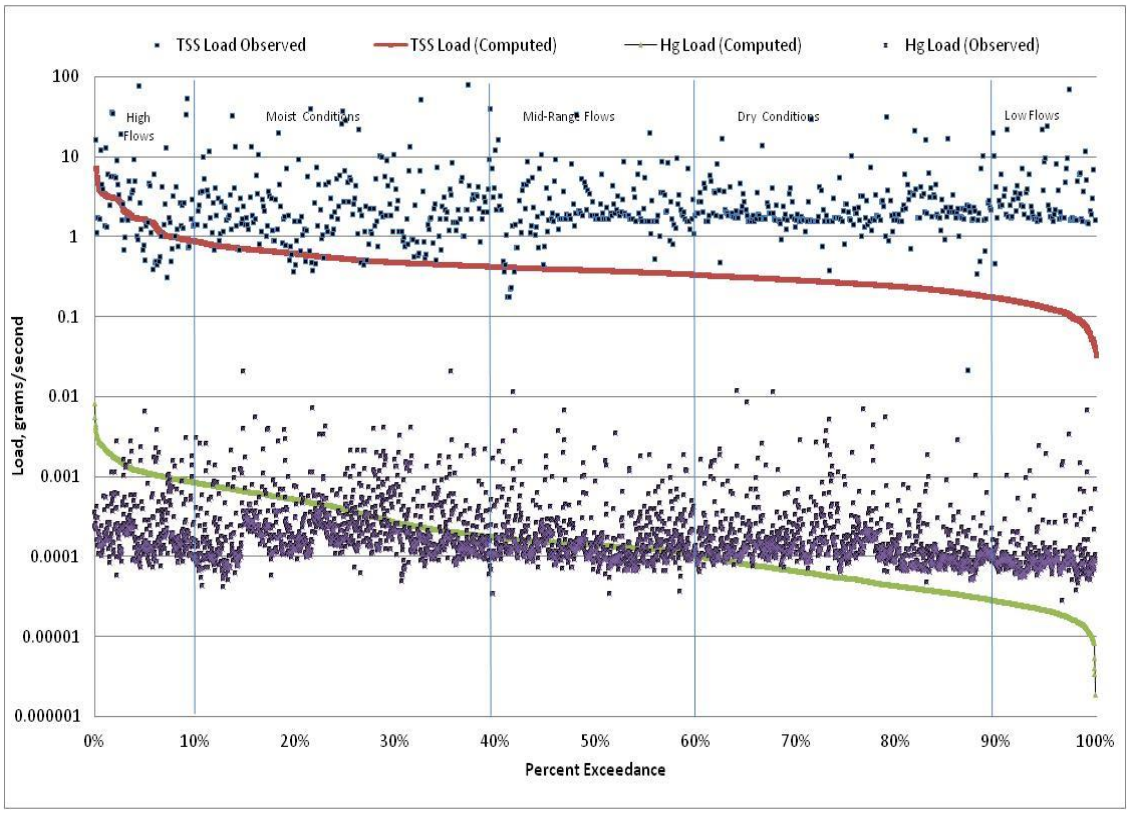

Figure 42. Observed and computed TSS and mercury concentration load for Station 17.

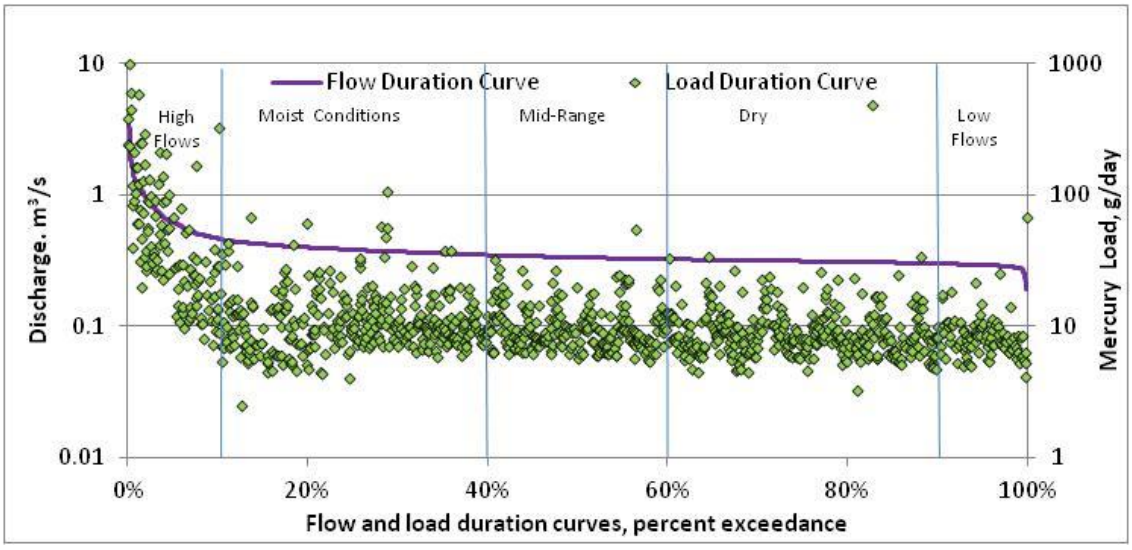

Figure 43. Comparison of flow and load duration curves at Station 17.

Profiles were also generated for the major streams (East Fork Poplar Creek, BC, Gum Hallow Branch, Mill Branch, and Pinhook Branch) in addition to evaluating mercury concentrations and mercury loads downstream EFPC and BC. The profiles were used to analyze fluctuations in mercury concentrations as a function of time and identify how these fluctuations relate to hydrologic events. The graphs portray the simulated mercury concentrations downstream EFPC per corresponding hydrological event for time-step November 11, 1995 and January 6, 1996. The maximum mercury concentration reached within the simulated period is shown in red. A comparison of the mercury profile downstream the selected branch with the precipitation pattern, reveals that during high flood events mercury concentration decreases due to dilution. However, post hydrological events, the mercury concentration levels increase. At this point, simulation results reveal rainfall as a facilitating agent in the exchange of mercury and its movement through hydrologic zones. The attenuation of mercury concentrations downstream of EFPC is consistent with previous studies.

The target for the TMDL analyses is the numeric water quality criterion for the pollutant of concern; mercury in this case, for the specified EFPC waterbody. The target concentration was summarized based on the detailed description of water uses and regulations established by EPA, DOE, and TDEC. These numeric water quality targets were translated into TMDLs through the loading capacity or as defined by EPA "the greatest amount of loading received without violating water quality standards." Several target load-duration curves were generated for EFPC by applying the mercury target concentration of 51, 200, and 770 ppt to each ranked flows used to generate the flow duration curve. These target mercury load duration curves are shown in the figure below. The mercury target maximum load corresponding to each ranked daily mean flow was computed by multiplying the recreation use water quality criterion (51 ppt) by the flow and by the appropriate unit conversion factor. The same calculation was performed for the ROD designated target concentration of 200 ppt and water quality criterion of 770 ppt established to sustain fish and aquatic life.

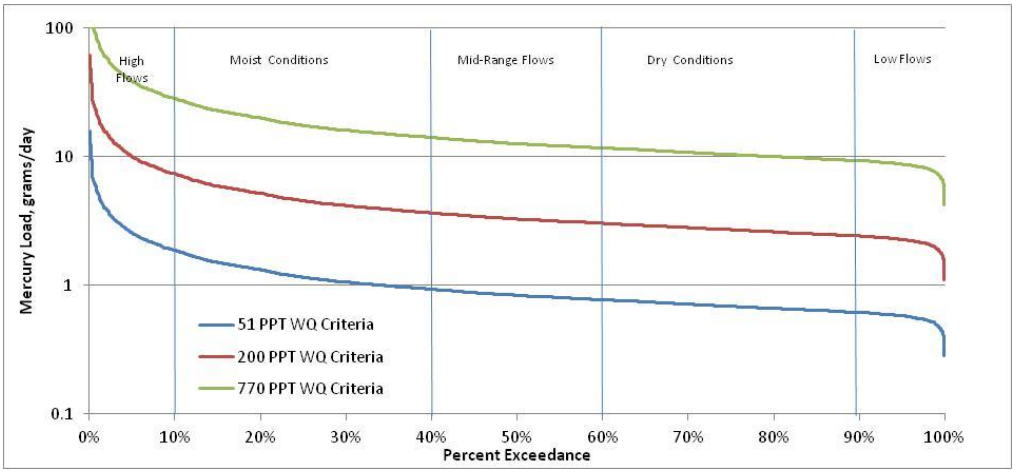

Figure 44. Target mercury load duration curves for 51, 200, and 770 ppt water quality criterion.

Available water quality data for station 17; encompassing a 10 year period, was utilized to compute the percent reduction required to decrease the concentration from the observed mean considering a 95 percent confidence interval (CI) to the desired target level. A total of 2,286 samples were considered. All recorded values were converted to parts per trillion (ppt). All recorded values exceeded the mercury concentration of 51 ppt necessary to meet the recreational use classification. Only 203 of the 2286 samples; in other words, 8.89% of the samples exceeded the 770 ppt criterion required to sustain fish and aquatic life but the majority of the mercury concentrations recorded exceeded the 200 ppt established by the DOE ROD.

Table 5 summarizes the statistical parameters such as the mean, minimum, standard deviation and 95% and 90% confidence interval used in calculating the percent reduction required. The percent reduction was calculated as the difference between the mean and the water quality criteria; considering a confidence interval, and divided by the mean with the incorporated confidence interval. This relationship is shown by below by Equation 60.

Table 5. Target TMDL percent reductions at Station 17.

No. of Samples	Minimum	Mean	Standard Deviation	Criterion 1	Criterion 2
2286	66.10	495.25	668.91	51	770
No. of Samples Exceeding Criterion 1	**No. of Samples Exceeding Criterion 2**	**95% CI**	**Mean + 95% CI**	**90% CI**	**Mean + 90% CI**
All	203	27.42	522.67	23.01	518.26

$$\%\,\mathrm{Re}\,duction = \frac{(Mean + Confidence\_Interval) - (Criterion)}{(Mean + Confidence\_Interval)} \qquad \text{(Equation 60)}$$

Based on the equation above, a 90.24% reduction in mercury loading is required at Station 17. Figure 45 shows how the probability of exceedance for mercury loading computed from observed flows and mercury concentrations compare to the standard target mercury loading. The average loading at each flow regime is also shown as the dashed red line. Figure 46 also shows the standard water quality criteria compared to the simulated mercury loading for which the required percent reduction was applied. As can be observed from Figure 46 the percent reduction applied places the simulated loading within the range of the 51 ppt water quality criteria and below the 200 ppt standard mandated by the DOE record of decision.

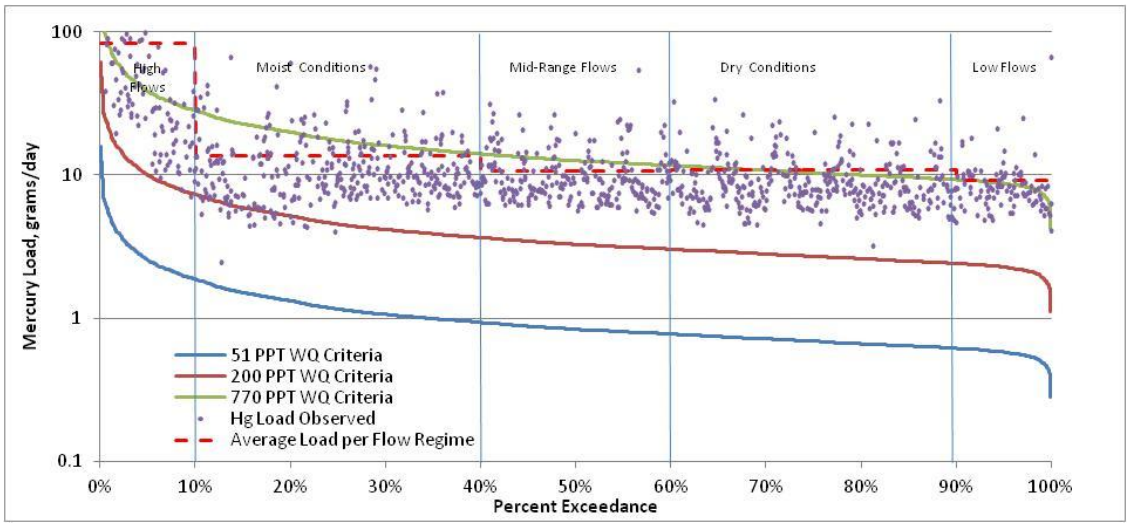

Figure 45. Comparison of target TMDLs and recorded mercury load at Station 17.

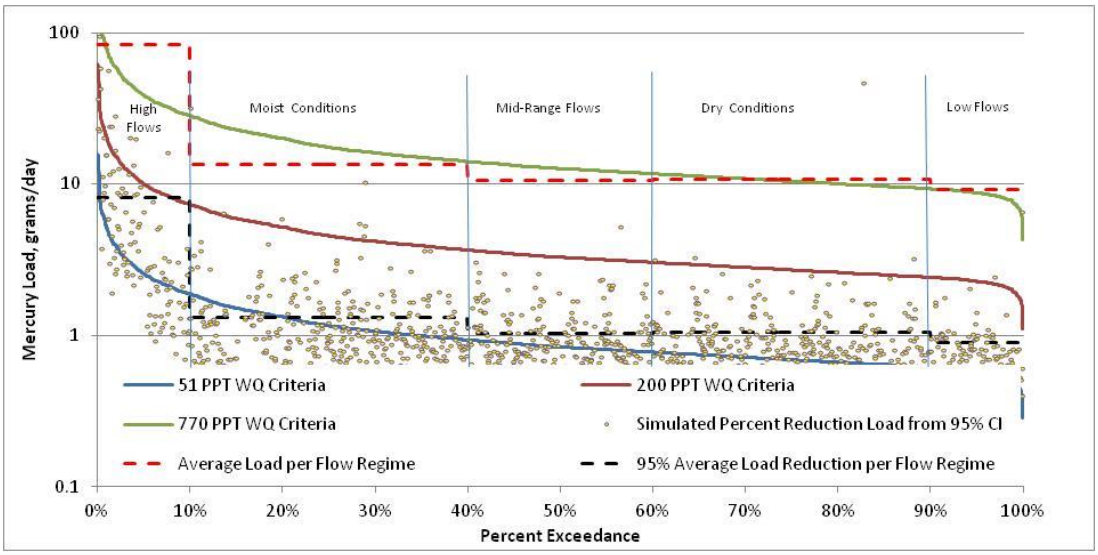

Figure 46. Comparison of simulated mercury loading with applied percent reduction and target TMDLs.

THERMODYNAMIC MODELING

Exposure to Hg in any of its forms under different circumstances may cause serious health problems, such as nervous system damage, immune system damage, chromosome damage and neurobehavioral disorders (Clarkson and Magos, 2006; Zahir et al., 2005). One of the worst disasters caused by mercury contamination is the Minamata disease. The contamination of Minamata Bay, Japan, occurred due to the releases of mercury from a chemical manufacturing plant during 1950 to 1971. This resulted in mercury poisoning, causing an epidemic scale illness in fish and humans (Matsuyama et al. 2011; Tsuda et al. 2009). Since then, many other concerns related to Hg have come up.

Hg in the environment comes from two major sources. First, it is from the earth's crust. Second, it is from anthropogenic activities (e.g. manufacturing industry, fossil fuel power plant industry, etc.) (Fitzgerald, 2014; Pacyna 2002). These activities have resulted in the release of both forms of Hg (i.e. inorganic and organic forms) into the environment (Pacyna, 2002; Wang et al., 2004; Appelo and Postma, 2005). The Hg is transported to aquatic environments by soil erosion and discharge from anthropogenic activities (Wang et al., 2004; Appleo and Postma, 2005). There are different forms of Hg present in natural water, including elemental mercury (Hg^0), ionic mercury (Hg^+, Hg^{2+}) and organic mercury [e.g., (CH_3Hg^+, $(CH3)_2Hg$]. Organomercury compounds are of concern because of their toxicity and ability to concentrate in the biota. These compounds are released into the environment as biocides, but can also be produced by enzymatic methylation of cations or due to reactions with biogenic methylation agents (Southworth et al., 2001; Ravichandran, 2004; Morel et al., 1993). The high animal tissue affinity of organomercury compounds, allows bioaccumulation and biomagnification of MeHg in aquatic organisms (e.g., fish) and humans to occur easier than other Hg species (Ravichandran, 2004; Dong et al., 2010).

Similarly to other metals, the fate of Hg in aquatic systems depends on its speciation, which is a function of the following processes (Facemire et al., 1995 Ravichandran, 2004; Morel et al., 1993):

- Precipitation and dissolution of minerals;
- Dissolution and dissociation of weakly acidic gases;

- Complexation with inorganic (e.g., OH^-, CO_3^-, SO_4^{2-}) and organic (e.g., DOC constituents, such as humic and fulvic acids) ligands;
- Sorption on solids; and
- Biological activity.

Complexation, sorption and biological activity could be considered at thermodynamic equilibrium or under kinetic conditions, which may affect speciation. In addition, speciation also depends on the mixture of metals and complexing agents, pH, temperature, redox, salinity, major ion composition and sorbing solids (Arias et al., 2004; Wang et al., 1991; Wnalin et al., 2007).

In the atmosphere, Hg occurs from natural and anthropogenic sources in its neutral or elemental state. Hg^0 can be converted to an oxidized form of Hg(II) (Ravichandran, 2004; Dong et al., 2010). Hg(II) is transferred to the watersheds and water bodies through wet and dry deposition (Ravichandran, 2004). Reddy and Aiken (2001) reported that, in oxic/aerobic water, Hg(II) is bound to inorganic and organic ligands, hydroxide and chloride ligands, which depends on pH and chloride concentration, resulting in $Hg(OH)^+$, $Hg(OH)_2$, $Hg(OH)_3^-$, $HgCl^+$, $HgCl_2$, $HgCl_3^-$, HgClOH and Hg-Humates (humic acid). Zhong and Wang, (2009) found that, in anoxic environments, inorganic and organic sulfides play an important role and bind mercury strongly, resulting in HgS_0, $Hg(S_2H)^-$, $Hg(SH)_2$ and $Hg(RS)^+$ species (Zhong and Wang, 2009; Harmon et al., 2004; Jay et al., 2002; Karlsson and Skyllberg, 2003; Qian et al., 2002). The activity of sulfate-reducing bacteria (SRB) in the presence of mercury–sulfur compounds, promotes the methylation of mercury (Zhong and Wang, 2009; Harmon et al., 2004). The MeHg, that is produced by the bacteria in anoxic zones, transports to surface water and binds with inorganic and organic ligands to be eventually transferred and accumulated in biota through the food chain (Harmon et al., 2004; Bengtsson and Picado, 2008; Hill et al., 2010; Hintelmann et al., 1997). The study of Li et al. (2010) indicated that MeHg can be converted to a volatilized mercury form (Hg^0) through photodegradation (Li et al., 2010).

Hg has also been found to be in high concentration in sediment, from high absorption in clay (Arias et al., 2004; Reddy and Aiken, 2001); transport of Hg can thus occur through its attachment to sediment (Lui et al., 2008). The latter implies that site stratigraphy, sediment type,

and distribution coefficient (K_d) are important factors for estimating Hg transport in sediment (Reddy and Aiken, 2001).

Because Hg fate and transport processes in an aquatic system are very complex, the study of these processes requires multiple disciplines of science including, geological, hydrological, chemical, biological and microbiological studies (Mackay et al., 1995; Parkhurst and Appelo, 1999; Appelo and Postma, 2005). The Hydro-geochemical model, PHREEQC, is a tool to integrate the processes affecting the fate and transport of the contaminants in an aquatic system. The PHREEQC model was selected for this study to assess the fate and transport of Hg. This chemistry and transport integrated model, which allows modelers to simulate the change of Hg chemical processes simultaneously with its transport in aquatic environment. However, it is recognized that there are many factors other than chemical processes (e.g., biological, microbiological processes) that can affect the fate of Hg in aquatic environments. For example, the activities of some bacteria and the effect of sunlight can transform Hg from one form to another (Li et al., 2010). This study emphasizes the chemical processes of Hg, while its biological and microbiological processes are not considered. Use of PHREEQC model is a cost effective way for assessing the fate and transport of Hg in aquatic environments and for developing management plans for the reduction of Hg exposure in such systems. However, in order for the PHREEQC model to best represent the fate and transport of Hg, further development of the model is needed. There are many challenges involved in developing PHREEQC model, which include the enhancement of Hg database of the model and testing and confirmation of the developed model.

The combining of equilibrium and kinetic chemical reactions with the transport processes in models such as PHREEQC, improves the accuracy of predictions of the fate and transport of chemicals of interest in aquatic environments. Thus, a great variety of reactive transport problems and boundary conditions of interest to researchers and practitioners can now be addressed for aquatic systems. Because of the versatile capabilities and the reliability of the PHREEQC model, it has been used widely in geochemical research area by many researchers. It is definitely of great benefit to use this robust geochemical-transport model to predict and address the fate and transport of Hg in aqueous systems. However, in order to use PHREEQC to

predict the fate and transport of Hg, its Hg database needs to be improved. Although the model includes a database with Hg thermodynamic data, it only contains limited Hg species data. Therefore many desired speciation calculations are not possible. In addition, it does not have data for adsorption processes that play a major role in the fate and transport of Hg in an aquatic system. Limited Hg species and no adsorption processes result in this database being very limited for our purposes in modeling Hg at ORR.

The two objectives, for this task which were achieved, were:

1. To develop, expand, and confirm the Hg database of the hydrogeochemical model "PHREEQC" to enhance its capability to simulate the fate of Hg species in the presence of complexing constituents and natural sorbents, under different conditions of pH, redox, salinity and temperature.
2. To apply and evaluate the new database in flow and transport scenarios, at two field test beds: Oak Ridge Reservation, Oak Ridge, TN and Everglades National Park, FL, where Hg is present and of much concern.

Two important questions were answered at the completion of this research effort:

1. Can the enhanced database describe the difference in behavior of the various partitioning species when subjected to processes, such as dissolution/precipitation, ion exchange, and surface complexation?
2. Can the enhanced PHREEQC model be used in site applications to best understand the fate and transport of Hg in aquatic environments?

In this study, the two test beds: Oak Ridge Reservation (ORR) at Oak Ridge, is selected. The high Hg contamination in East Fork Poplar Creek (EFPC) located in the ORR area at Oak Ridge, TN, has raised concern among researchers due to the accidentally discharged and spilled Hg from the Y-12 Plant into the surrounding environment in the 1950s (Southworth and Brooks, 2011). Dong et al. (2010) reported high concentration of MeHg in EFPC and found that neither total Hg nor dissolved inorganic Hg concentrations correlate with MeHg concentration in EFPC water. This suggests that speciation, mobility, and accumulation of Hg in EFPC are controlled by site aquatic, and geochemical characteristics, and conditions (Dong et al., 2010).

The further development of data for the database containing Hg thermodynamic data for the PHREEQC coupled-transport model enhanced the model capability to predict the Hg fate and transport in different aquatic environments. The enhanced model is now a valuable tool to study the Hg behavior, fate and transport in selected test-beds. The approach used to enhance and develop the PHREEQC coupled transport model is described in this section. The research deliverable is also listed.

Model Background and Theory

This section describes the currently available hydrogeochemical models at the time this study was conducted. The best hydrogeochemical models, PHREEQC and PHAST, were selected based upon their capabilities to simulate the Hg chemical and transport processes. The governing equations of the models are also described in this section.

Hydrogeochemical modeling helps in understanding and predicting the difficult combination of chemical and mineral interrelated processes that control the fate of chemical species as well as the transport in aquatic environments. Hydrogeochemical models have developed in recent years to simulate the geochemical processes only (geochemical model) and to also simulate both geochemical processes and transport (i.e., flow and transport model). Geochemical models include GEMS, MINEQL+, MINTEQA2, and Visual MINTEQ, among others. Flow and transport models that have just become available in the very recent years are PHREEQC and PHAST models.

Geochemical models are mostly used to simulate chemical equilibrium with thermodynamic databases of the elements of environmental interest. Equilibrium models assume that all reactions have completed and are in equilibrium with one another. The models have common capabilities in calculating speciation, sorption, and precipitation of aquatic chemical components. The model capabilities are described as follows.

GEMS: GEM-Selektor (GEM-Selektor Geochemical Software) was developed by Paul Scherer Institute in Switzerland. It is an interactive thermodynamic modeling of heterogeneous aquatic geochemical systems. The model uses the method of Gibbs Energy Minimization to calculate the multi-speciation at the equilibrium. It has capabilities to calculate aqueous-solid solution equilibrium, adsorption and ion exchange. It includes a built-in (default) thermodynamic database of common aqueous elements. The model provides the option for extension and modification of its database by the modeler.

MINEQL+: It was first developed at MIT, by John Westall and Francois Morel. It has abilities to perform the calculation of equilibrium aqueous speciation, of dissolved and solid phases, adsorption and ion exchange, at low temperature (0-50 °C) and low to moderate ionic strength (< 0.5 M). The MINEQL+ version 3 is available for the DOS operating system and is free for use, while version 4.6 is available for the window operating system, but at a cost to the modeler (MINEQL+, Geochemical Software).

MINTEQA2: This program is sponsored by the US Environmental Protection Agency (USEPA). It is an equilibrium speciation model, alike other geochemical models. MINTEQA2 has capabilities to calculate dissolved and solid phases and adsorption. The thermodynamic database in MINTEQA2 is well developed, including common aqueous elements. MINTEQA2 is a free and robust geochemical model that has been used by researchers. It is available for the DOS operating system (MINTEQA2, Geochemical Software).

Visual MINTEQ: It is a development of MINTEQA2; it has been maintained by Jon Petter Gustafsson at KTH, Sweden, since 2000. It has capabilities to calculate aqueous equilibrium reactions as MINTEQA2. The difference with MINTEQ is that Visual MINTEQ is available for the windows operating system (Visual MINTEQ).

PHREEQC and PHAST models are models that handle the kinetics of chemical reactions, reverse reactions and link the concentrations of species to simulations of 1-dimensional (PHREEQC) and 3-dimensional (PHAST) transport scenarios (U.S. Geological Survey, 1999 and 2010).

PHREEQC: It is a product of the US Geological Survey (USGS), developed by Parkhurst and Appelo in 1999. It is designed to perform low-temperature aqueous geochemical calculations. It is similar to other geochemical models having capabilities to calculate speciation, saturation index, batch reaction, surface complexion, adsorption and ion exchange at equilibrium. In addition, PHREEQC also has capabilities to simulate reversible reactions, kinetic reactions, with rate expressions defined by the modeler and one dimensional (1-D) transport simulations. Its databases contain those from MINTEQA2 and other USGS's models (i.e., WATEQF4). All these capabilities make PHREEQC more complete and advanced model than others. The coupling of geochemical and transport processes in PHREEQC allows the studying the behavior of aqueous components under flow and transport conditions at sites of interest. The model can link the chemical equilibrium (i.e., batch-reaction) calculations to simulations of flow and transport under two types of boundary conditions (i.e., flux or third-type boundary and the Dirichlet or surface or first-type - see Appendix B1 for details of PHREEQC model's capabilities and limitations) and various time conditions.

PHAST: It is an integrated computer program between Geochemical model (PHREEQC) and the flow model (HST3D). PHAST is designed to simulate multicomponent, reactive solute transport in 3-dimensional flow system. The calculations of flow and transport are based on a developed HST3D model (Parkhurst et al., 2010) while the geochemical reactions are simulated with the geochemical model PHREEQC (Parkhurst, 1995; Parkhurst and Appelo, 1999). The PHREEQC model is embedded in PHAST (see Appendix B2 for details of PHAST model's capabilities and limitations). Current hydrogeochemical model capabilities are summarized in Table 1.

Table 6. The Main Features and Capabilities of Available Hydrogeochemical Models

Models	Hg database	Expandable database	Saturation Index calculation	Precipitation Calculation	Sorption processes	Inverse model	Transport processes	System
GEMS	A	G	G	G	A	Na	na	Windows
MINEQL	A	L	G	G	A	Na	na	DOS
MINTEQA2	A	L	G	G	G	Na	na	DOS
Visual MINTEQ	A	L	G	G	A	Na	na	

								Windows
PHREEQC	A	G	G	G	G	G	G	Windows
PHAST	A	G	G	G	G	G	G	DOS

A: Average-comparable to other models; G: Good-better than other models; L: Limited; na: not available

All of the Hg databases available in PHREEQC and PHAST models are for speciation calculations of common inorganic Hg species, but they lack organic complexation, ion exchange and sorption stability constants.

PHREEQC and PHAST are thus the chosen models to support this research because of their various capabilities (Appelo and Postma, 2005; Halim et al., 2005; Parkhurst and Appelo, 1999; Tiruta-Barna, 2008). It is foreseen that, once the databases are enhanced, it will allow a more objective assessment and analysis of the fate of Hg, in flow and transport conditions, at the two applications test beds, namely, EFPC and ENP, where Hg is present and of concern.

The combined implementation of these models, products of the USGS, offers a mathematical framework to perform a wide variety of low-temperature aqueous geochemical calculations and to simulate dispersion (or diffusion) and stagnant zones in 1D-transport (PHREEQC) and 3D-transport calculations. It was mentioned earlier that PHREEQC model is embedded in PHAST

and used to calculate the geochemical reactions. The geochemical reactions (aqueous, exchange, and surface species at equilibrium) in both PHREEQC and PHAST are calculated using the activities and mass-action equations of an aqueous chemical system. The transport of substances of interest in the system is predicted by the advection-reaction-dispersion equations.

The activity and mass-action relation for each species in the models can be defined by the modeler. Models then derive the unknown mole of the species (*i*) from the mass-action relation. The mole of *i* in the system is then calculated by differentiation of equations derived with respect to *i* (Parkhurst and Appelo, 1999).

PHREEQC calculates the aqueous species at the thermodynamic equilibrium. However disequilibrium in the initial solution is allowed. For each aqueous species *i*, the unknowns: activity, a_i, activity coefficient, γ_i, molality, m_i , and moles in solution, n_i will be calculated by PHREEQC. The following relationship $a_i = \gamma_i m_i$ and $n_i = m_i W_{aq}$ apply for all aqueous species (W_{aq} is the mass of solvent water in an aqueous solution) (Parkhurst and Appelo, 1999). For example, the association reaction of the aqueous species is $Hg(OH)_2 + 2H^+ = Hg^{2+} + 2H_2O$. The log K for this reaction at 25 °C is 6.09, which results in the mass-action equation:

$$10^{6.09} = \frac{[Hg^{2+}]}{[Hg(OH)_2][H^+]^2} \qquad \text{(Eq. 1)}$$

In general, mass-action equations can be written as equation 2.

$$K_i = a_i \prod_m^{Maq} a_m^{-C_{m,i}} \qquad \text{(Eq. 2)}$$

where: K_i = a temperature-dependent equilibrium constant

$c_{m,i}$ = the stoichiometric coefficient of master species m in the species i, the value can be positive or negative

M_{aq} = the total number of aqueous master species

From mass-action expression, the mole of aqueous species *i* can be derived as equation 3

$$n_i = m_i W_{aq} = K_i W_{aq} \frac{\prod_{m}^{Maq} a_m^{c_{m,i}}}{\gamma_i} \quad \text{(Eq. 3)}$$

PHREEQC then uses the Newton-Raphson method to differentiate the total number of moles with respect to an unknown (see equation 4).

$$dn_i = n_i \left[d\mathrm{In}(W_{aq}) + \sum_{m}^{Maq} C_{m,i} d\mathrm{In}(a_m) - \frac{\partial}{\partial \mu} \mathrm{In}(\gamma_i) dI \right] \quad \text{(Eq. 4)}$$

The activity coefficient γ_i is expressed as a function of ionic strength, I (Davies equation). The relationship between γ_i and I of aqueous species in PHREEQC is defined as equation 5. The partial derivatives of the activity coefficient equation with respect to ionic strength are shown in equation 6 (Parkhurst and Appelo, 1999).

$$\log \gamma_i = -Az_i^2 \left(\frac{\sqrt{I}}{1+\sqrt{I}} - 0.3I \right) \quad \text{(Eq. 5)}$$

$$\frac{\partial}{\partial I} \mathrm{In}\gamma_i = -\mathrm{In}(10) \left(\frac{Az_i^2}{2\sqrt{I}\left(Ba_i^0\sqrt{I}+1\right)^2} + b_i \right) \quad \text{(Eq. 6)}$$

where A is constant which is only dependent on temperature, and z_i is the ionic charge of aqueous species i.

In PHREEQC, the modeler will need to define and input the chemical equation for the mole-balance and mass-action expressions, the log K, ΔH, and the activity coefficient parameters for each aqueous species. PHREEQC will then calculate the aqueous species using equations 1-6 (Parkhurst and Appelo, 1999).

PHREEQC calculates the ion-exchange at equilibrium using mass-action expressions based on half-reactions between aqueous species and an unoccupied exchange site (Appelo and Postma, 2005) for each exchanger *e*, The unknowns of each exchange species i_e of exchanger *e* that will be calculated by PHREEQC are the activity, a_{i_e}, and the moles, n_{i_e}. PHREEQC defines a_{i_e} to be the equivalent fraction times an activity coefficient γ_{i_e}. The equivalent fraction is the moles of sites occupied by an exchange species ($b_{e,i_e} n_{i_e}$ where b_{e,i_e} is the number of equivalents of exchanger *e* occupied by the exchange species i_e) divided by the total number of exchange sites (T_e). The a_{i_e} thus can be expressed as equation 7 (Parkhurst and Appelo, 1999).

$$a_{i_e} = \gamma_{i_e} \frac{b_{e,i_e} n_{i_e}}{T_e} \qquad \text{(Eq. 7)}$$

The mass-action for exchanged species is required in PHREEQC. For example, the association reaction for the exchange species HgX_2 is $Hg^{2+} + 2X^- = HgX_2$ where X^- is the exchange master species in the default database. The log K for Hg half-exchange reaction derived from literature is -1.39, thus the mass-action reaction can be written as equation 8 (Parkhurst and Appelo, 1999).

$$10^{-1.39} = \frac{[HgX_2]}{[Hg^{2+}][X^-]^2} \qquad \text{(Eq. 8)}$$

In general, mass-action equations can be written as equation 9.

$$K_{i_e} = a_{i_e} \prod_m^M a_m^{-C_{m,i_e}} \qquad \text{(Eq. 9)}$$

where:

K_{i_e} = half-reaction selectivity constant

C_{m,i_e} = the stoichiometric coefficient of master species m in species i_e, the value can be positive or negative

From mass-action expression, the mole of species i_e can be derived as equation 10.

$$n_{i_e} = K_{i_e} \frac{\prod_m^M a_m^{C_{m,i_e}}}{\gamma_{i_e}\left(\frac{b_{e,i_e}}{T_e}\right)} \quad \text{(Eq. 10)}$$

PHREEQC then calculates the total derivative of the moles of species i_e with respect to the master unknowns as in equation 11 (Parkhurst and Appelo, 1999).

$$dn_{i_e} = n_{i_e}\left[\sum_m^M C_{m,i_e} d\ln(a_m) - \frac{\partial}{\partial I}\ln(\gamma_{i_e})dI\right] \quad \text{(Eq. 11)}$$

PHREEQC requires the modeler to define and input the chemical equation for the mole-balance and mass-action expressions, the log K, ΔH, and the activity coefficient parameters for each exchange species. PHREEQC will then calculate the unknowns of each exchange species i_e using equations 8-11.

The differences between the surface complexation and the ion exchange defined in PHREEQC are that the surface reactions are not half-reactions and surface species may be anionic, cationic, or neutral. PHREEQC calculates the surface complexation processes using the theory proposed by Dzombak and Morel (1990). This theory assumes that the number of active sites, T_s, the specific area, A_s (m^2 /g), and the mass, S_s (g), of the surface are defined. PHREEQC assumes the activity of a surface species to be equal to the mole fraction of a given surface-site type that is occupied. This means that a surface species has an activity of 1 when it completely covers a given kind of surface site (Parkhurst and Appelo, 1999).

In the default PHREEQC database the surface of ferrihydrite is defined as “Hfo”. Hfo_s represents a high affinity or a strong site while Hfo_w is a week site. In PHREEQC the neutral surface species at weak and strong sites of ferrihydrite are defined as “Hfo_wOH” and “Hfo_sOH” and the surface association reaction with Hg (for a weak site) can be written as

Hfo_wOH + $Hg(OH)_2$ + H^+ = Hfo_wOHg^+ + $2H_2O$. The mass-action can be expressed as equation 12 (Parkhurst and Appelo, 1999).

$$K_{\text{int}} = \frac{[Hfo\_wHg^+]}{[Hfo\_wOH][Hg(OH)_2][H^+]} e^{-\frac{F\psi_s}{RT}} \quad \text{(Eq. 12)}$$

where K_{int} is the intrinsic equilibrium constant, F is the Faraday's Constant (96,493.5 Coulombs/equivalent), ψ_s is the potential at the surface (volts), R is the gas constant (8.3147 J mol $^{-1}$ K^{-1}), T is temperature (Kelvin) and the term $e^{-\frac{F\psi_S}{RT}}$ is a factor that indicates the work involved in moving a charged species (H^+) away from a charged surface (Parkhurst and Appelo, 1999).

In general, mass-action equations can be written as equation 13:

$$K_{\text{int},i(s_k)} = \left(a_{i(s_k)} \prod_m^M a_m^{-C_{m,i(s_k)}} \right) e^{\frac{F\psi_S}{RT}\Delta Z_{i(s_k)}} \quad \text{(Eq. 13)}$$

where the subscript (s_k) indicates the parameter for surface-site type k (weak or strong in Dzombak and Morell, 1990) in surface s, and $\Delta Zi_{(s_k)}$ is the net change in surface charge due to the formation of the surface species (Parkhurst and Appelo, 1999).

The derived equation for the total mole of surface species $i_{(s_k)}$ is shown in equation 14:

$$n_{i(s_k)} = K_{i(s_k)} T_{s_k} e^{\left(\frac{F\psi_S}{RT}\Delta Z_{i(s_k)}\right)} \prod_m^M a_m^{C_{m,i(s_k)}} = K_{i(s_k)} \frac{T_{s_k}}{b_{i(s_k)}} a_{\psi_s}^{-2\Delta Z_{i(s_k)}} \prod_m^M a_m^{C_{m,i(s_k)}} \quad \text{(Eq. 14)}$$

PHREEQC calculates the total derivative of the moles of the species $i_{(s_k)}$ with respect to the master unknowns using equation 15:

$$dn_{i_{(s_k)}} = n_{i_{(s_k)}}\left[\sum_{m}^{M} C_{m,i_{(s_k)}}\, d\mathrm{In}a_m - 2\Delta z_{i_{(s_k)}}\, d\mathrm{In}a_{\psi_s}\right] \qquad \text{(Eq. 15)}$$

Modelers are required to input the chemical equation for the mole-balance and mass-action expressions, the log K, ΔH, and surface properties (surface area, surface type, and the number of equivalents of each site type). PHREEQC then calculates the unknown of surface species *i* using equations 12-15.

PHREEQC has the capability to calculate and combine all the chemical reactions with transport processes. The transport processes that can be simulated by PHREEQC include diffusion, advection, advection and dispersion, and advection and dispersion with diffusion into the stagnant zone (Parkhurst and Appelo, 1999).

The 1D-transport processes in PHREEQC are governed by the Advection-Reaction-Dispersion (ARD) equation. PHREEQC makes availability for the equation to be used for both ground and surface water flow simulations by modeler defined parameters (i.e., velocity). Equation 16 is used to simulate the groundwater flow while equation 17 is for surface water flow.

$$\frac{\partial C}{\partial t} = -v\frac{\partial C}{\partial x} + D_L\frac{\partial^2 C}{\partial x^2} - \frac{\partial q}{\partial t} \qquad \text{(Eq. 16)}$$

$$\frac{\partial C}{\partial t} = -u\frac{\partial C}{\partial x} + D_L\frac{\partial^2 C}{\partial x^2} - \frac{\partial q}{\partial t} \qquad \text{(Eq. 17)}$$

where *v* is the average pore water flow velocity (m/d), u is the average stream velocity (m/d), *x* is the distance (m), *C* is concentration in water (mol/L), D_L is the dispersion coefficient [m^2/d, $D_L = \alpha_L v + D^*$ is for groundwater flow, while $D_L = \alpha_L u + D^*$ is for surface water flow, where α_L is longitudinal dispersive (m), and D* is the diffusion coefficient (m^2/d)], and *q* is the concentration in a solid phase (mol/L). The first term on the right hand-side of the earlier equations, $-v\frac{\partial C}{\partial x}$ and $-u\frac{\partial C}{\partial x}$ represent advection, the second term $D_L\frac{\partial^2 C}{\partial x^2}$ represents

dispersion, and $\frac{\partial q}{\partial t}$ represents the change in concentration due to a reaction (e.g., sorption, ion exchange, etc.). Equation 17 was recognized and successfully used by a number of researchers (Fried, 1991; Tradiff and Goldstein, 1991) to calculate the change of chemicals and substances in the stream flow.

The governing equation of flow and transport in the PHAST model includes advection, dispersion, and the reactions. The PHAST model also can be used to calculate both ground and surface water flows. Groundwater flow can be calculated using equation 18, in which the Darcy velocity (v) and porosity (ε) of the media are important parameters and defined by the modeler.

$$\frac{\partial}{\partial t}(\varepsilon\rho c_i) = \nabla \bullet \varepsilon D \nabla \rho c_i - \nabla \bullet \varepsilon v \rho c_i - \sum_{e=1}^{N_E} \upsilon_{i,e}^{E} \frac{\partial}{\partial t}(\varepsilon\rho \bar{c}_e) + \sum_{k=1}^{N_K} \upsilon_{i,k}^{K} \varepsilon\rho R_k + q\varepsilon\rho \hat{c}_i \quad \text{(Eq. 18)}$$

According to Parkhurst et al. (2010) and Parkhurst and Appelo (1999), "where $v = -\frac{K}{\varepsilon}\nabla h$, K is hydraulic conductivity, ∇h is potentiometric head (m); c_i is the total aqueous concentration of component i (mol/kgw); D is the dispersion-coefficient tensor (m^2/s); N_E is the number of heterogeneous equilibrium reactions; $\upsilon_{i,k}^{K}$ is the stoichiometric coefficient of component i in heterogeneous equilibrium reaction e (unitless); $\bar{c}_e$ is the concentration of solid reactant e (mol/kgw); N_K is the number of kinetic reactions; $\upsilon_{i,k}^{K}$ is the stoichiometric coefficient of component i in kinetic reaction k (unitless); R_k is the rate of kinetic reaction k (mol kgw^{-1} s^{-1} [moles per kilogram of water per second]); $\bar{c}_i$ is the total aqueous concentration of component i in the source water (mol/kgw); and N_c and is the number of chemical components in the system".

Substitution of v in equation 18 by $-\frac{K}{\varepsilon}\nabla h$ produces Equation 19, which indicates that K and ε must be defined by the modeler for groundwater flow simulation.

$$\frac{\partial}{\partial t}(\varepsilon\rho c_i) = \nabla \bullet \varepsilon D \nabla \rho c_i - \nabla \bullet K \nabla h \rho c_i - \sum_{e=1}^{N_E} \upsilon_{i,e}^{E} \frac{\partial}{\partial t}(\varepsilon\rho \bar{c}_e) + \sum_{k=1}^{N_K} \upsilon_{i,k}^{K} \varepsilon\rho R_k + q\varepsilon\rho \hat{c}_i \quad \text{(Eq. 19)}$$

In case of surface water flow, the following considerations are made: 1) the ε is constantly equal to 1, where the volume of void space is the total volume ($V_d/V_T = 1$). This is when the sediment is present in the stream bed but does not affect the stream velocity; and 2) the density of water (ρ) is constant. With these assumptions, the ε and ρ in equation 19 can be cancelled, and average stream velocity u can be substituted. Thus, the equation for surface water flow is written as equation 20:

$$\frac{\partial}{\partial t}c_i = \nabla \bullet Dc_i - \nabla \bullet uc_i - \sum_{e=1}^{N_E} \upsilon_{i,e}^{E} \frac{\partial}{\partial t}(\bar{c}_e) + \sum_{k=1}^{N_K} \upsilon_{i,k}^{K} R_k + q\hat{c}_i \qquad \text{(Eq. 20)}$$

Equation 20 is the simplified advection-dispersion-reaction equation, where the first term on the right-hand side represents advection, the second term represents dispersion and the rest is the change within concentration C due to the reactions and input.

There are two boundary types that can be considered for the transport: 1) constant, and 2) flux conditions.

The constant boundary condition is expressed by equations 21-24. The error function, A, for groundwater flow is calculated using equation 23, while equation 24 is for surface water flow.

at x = 0; $$C(0,t) = C_0 \qquad \text{(Eq. 21)}$$

at x > 0; $$C(x,t) = C_i + \frac{1}{2}(C_0 - C_i)A \qquad \text{(Eq. 22)}$$

$$A = erfc\left(\frac{x - vt/R}{\sqrt{4\alpha_L vt/R}}\right) + \exp\left(\frac{x}{\alpha_L}\right) erfc\left(\frac{x + vt/R}{\sqrt{4\alpha_L vt/R}}\right) \qquad \text{(Eq. 23)}$$

$$A = erfc\left(\frac{x - ut/R}{\sqrt{4\alpha_L ut/R}}\right) + \exp\left(\frac{x}{\alpha_L}\right) erfc\left(\frac{x + ut/R}{\sqrt{4\alpha_L ut/R}}\right) \qquad \text{(Eq. 24)}$$

where *x* is the distance (m), t is time (s), *v* is velocity (m/s), α_L is longitudinal dispersion (m), and *R* is the retardation that is caused by the media CEC in the case of groundwater flow (Eq. 23) and sediment CEC in surface water flow (Eq. 24) ($1+\frac{CEC}{C}$, where *CEC* is expressed in mol/L and *C* is the concentration in mol/L).

The flux boundary condition is shown in equations 25-28. The error function B for groundwater flow is expressed in equation 27, while equation 28 is for surface water flow.

Flux boundary condition:

at x = 0; $$C(0,t) = C_0 + \frac{D_L}{v}\frac{\partial C(x_{end},t)}{\partial x}$$ (Eq. 25)

at x > 0; $$C(x,t) = C_i + \frac{1}{2}(C_0 - C_i)B$$ (Eq. 26)

$$B = erfc\left(\frac{x - vt/R}{\sqrt{4\alpha_L vt/R}}\right) + \sqrt{\left(\frac{x}{\pi\alpha_L}\right)}\exp\left[-\frac{(x-vt/R)^2}{4\alpha_L vt/R}\right] - \frac{1}{2}\left(1 + \frac{x}{\alpha_L} + \frac{vt/R}{\alpha_L}\right)\exp\left(\frac{x}{\alpha_L}\right)erfc\left(\frac{x+vt/R}{\sqrt{4\alpha_L vt/R}}\right)$$ (Eq. 27)

$$B = erfc\left(\frac{x - ut/R}{\sqrt{4\alpha_L ut/R}}\right) + \sqrt{\left(\frac{x}{\pi\alpha_L}\right)}\exp\left[-\frac{(x-ut/R)^2}{4\alpha_L ut/R}\right] - \frac{1}{2}\left(1 + \frac{x}{\alpha_L} + \frac{ut/R}{\alpha_L}\right)\exp\left(\frac{x}{\alpha_L}\right)erfc\left(\frac{x+ut/R}{\sqrt{4\alpha_L ut/R}}\right)$$ (Eq. 28)

The retardation R in equation 33 is caused by the CEC of the transport media for ground water flow, while R in equation 34 is caused by CEC in the case of streambed sediment.

This section describes the model development, including Hg thermodynamic properties used for database enhancement and model confirmation.

In this section, the model database input method and the model language are described. The Hg thermodynamic data collected from the literature are also added into the model database for all aqueous, ion exchange, and surface species.

In order to calculate the aqueous species, PHREEQC requires all master species to be defined in the "MASTER SOLUTION_SPECIES" block in the PHREEQC database. Hg master species is defined under this block as $Hg(OH)_2$ species. As shown below, the alkalinity and the element gram formula weight of Hg are also required in this data block.

SOLUTION_MASTER_SPECIES

Element name	Master Species	Alkalinity	Element gram formula weight
Hg	$Hg(OH)_2$	0.0	200.59

The chemical reaction, log K, and ΔH of each Hg aqueous species must be defined in "SOLUTION_SPECIES" data block. The collected aqueous thermodynamic data can be added. However, the reactions must be written with $Hg(OH)_2$ species since it is defined as the master species for the Hg element in the database. The Hg thermodynamic and log K data collected from the literature are Hg^{2+} related reactions. However, since the $Hg(OH)_2$ is defined as the master species for Hg, the collected thermodynamic data must be converted to $Hg(OH)_2$ related reactions and log K prior to adding into the PHREEQC database. The example of a conversion is shown next and in equations 29-32.

The relationship between $Hg(OH)_2$ and Hg^{2+} is:

$$Hg(OH)_2 + 2H^+ = Hg^{2+} + 2H_2O$$

$$\text{Log K} = 6.19 \quad \text{(Eq. 29)}$$

and the reaction related to Hg^{2+} is:

$$Hg^{2+} + HPO_4^{3-} = (HgHPO_4)^-$$

$$\text{Log K} = 9.5 \quad \text{(Quarfort-Dahlman 1975)}$$

The above reactions (including Log K) can be combined to become a new reaction related to $Hg(OH)_2$ (equation 30), as shown next:

The combined equation is then:

$Hg(OH)_2 + 2H^+ + Hg^{2+} + HPO_4^{3-} = Hg^{2+} + 2H_2O + (HgHPO_4)^-$

Log K = 15.69 (Eq. 30)

However, since "Hg^{2+}" appears on both sides of the combined equation (equation 30), it can be subtracted from both sides. The final combined reaction (and Log K), which relates to $Hg(OH)_2$, is shown in equation 31:

$Hg(OH)_2 + 2H^+ + HPO_4^{3-} = (HgHPO_4)^- + 2H_2O$

Log K = 15.69 (Eq. 31)

The Hg aqueous species data related to $Hg(OH)_2$ added into the PHREEQC database, are shown in Appendix C.

In the PHREEQC database, the master exchanger *X* with one negative valence number (X^-), which represents the negative charge of typical soil and sediment, is defined under EXCHANGE_MASTER_SPECIES block.

EXCHANGE_MASTER_SPECIES

Element name	Master Species
X	X^-

The exchange half-reaction must be defined under the EXCHANGE_SPECIES block. As it was mentioned earlier, the Hg exchange species data is not available in the PHREEQC database, therefore, the Hg exchange species and their exchange coefficients obtained from Khan and Alam (2004) were inputted into the PHREEQC database (under EXCHANGE_SPECIES block) and are exemplified in equations 32-34.

For instance, the exchange equation Hg^{2+}/Na^{+} was obtained from Khan and Alam (2004):

$$Hg^{2+} + 2Na - X \leftrightarrow Hg - X_2 + 2Na^{+}$$

$K_{Hg/Na} = 0.04$, $\log (K_{Hg/Na}) = -1.39$ (Eq. 32)

One half-reaction for Na^{+} defined in PHREEQC is:

$$Na^{+} + X^{-} \leftrightarrow Na - X$$

Log K = 0 (Eq. 33)

Thus the second half-reaction of equation 32 is:

$$Hg^{2+} + 2X^{-} \leftrightarrow Hg - X_2$$

$$\text{Log K} = -1.39 \quad \text{(Eq. 34)}$$

The completed ion exchange between Hg^{2+} and other cations and their exchange coefficients are shown in Appendix C.

Similarly to aqueous and ion exchange species, the master surface species must be defined under the SURFACE_MASTER_SPECIES block. The PHREEQC database contains the surface species of $Fe(OH)_3$ for weak (Hfo_w) and strong (Hfo_s) sites with the hydroxide with ≡Hfo_wOH and ≡Hfo_sOH representing its surface master species. The new surface species data collected from the literature are Fe-Oxide (≡Feox), Hematite (≡Hem), Quartz (≡Sio), Gibbsite (≡Aloh), and Kaolinite (≡Sial) with their hydroxide group representing their master species.

SURFACE_MASTER_SPECIES

Element name	Master Species
≡Hfo_w	≡Hfo_wOH
≡Hfo_s	≡Hfo_sOH
≡Amo	≡Amo_OH
≡Hem	≡Hem_OH
≡Sio	≡Sio_OH
≡Aloh	≡Aloh_OH
≡Sial	≡Sial_OH

The surface species and log K data can be defined under the SURFACE_SPECIES block.

Under the SURFACE block, the surface name, number sites, specific area per gram (m^2/g), and mass (g) of the surface species must be defined. These data were obtained from the literature except the surface mass, which can be defined by the modeler. An example of the input file for $Fe(OH)_3$ and Quartz surface species that are defined under the SURFACE block is shown below.

SURFACE

Surface Name	Number of Surface Site (mole)	Surface Area (m^2/g)	Surface Mass (g)
≡Hfo_w	0.2	600	Modeler defined
≡Aloh	$1.023X10^{-4}$	4.15	Modeler defined

The completed new surface species data that was added into the PHREEQC database are shown in Appendix C.

Hg Thermodynamic Properties

The Hg speciation in aquatic environments is governed by a number of factors: pH, temperature, DO, presence of inorganic and organic ligands, among others. The existing Hg database in PHREEQC, which was obtained and validated by a vast number of studies (Parkhurst and Appelo, 1999), is shown in Table 2 for Hg reactions and Table 3 for Hg solubility reactions.

Table 7. Reaction Equilibrium Constants of Hg Available in PHREEQC (Parkhurst And Appelo, 1999)

Reactions	Log K
$Hg(OH)_2 + Cl^- + 2H^+ = HgCl^+ + 2H_2O$	12.85
$Hg(OH)_2 + 2Cl^- + 2H^+ = HgCl_2 + 2H_2O$	19.22
$Hg(OH)_2 + 3Cl^- + 2H^+ = HgCl_3^- + 2H_2O$	20.12
$Hg(OH)_2 + 4Cl^- + 2H^+ = HgCl_4^{2-} + 2H_2O$	20.53
$Hg(OH)_2 + Cl^- + H^+ = HgClOH + H_2O$	9.31
$Hg(OH)_2 + F^- + 2H^+ = HgF^+ + 2H_2O$	8.08
$Hg(OH)_2 + I^- + 2H^+ = HgI^+ + 2H_2O$	18.89
$Hg(OH)_2 + 2I^- + 2H^+ = HgI_2 + 2H_2O$	30.10
$Hg(OH)_2 + 3I^- + 2H^+ = HgI_3^- + 2H_2O$	33.79
$Hg(OH)_2 + 4I^- + 2H^+ = HgI_4^{2-} + 2H_2O$	35.78
$Hg(OH)_2 + H^+ = HgOH + H_2O$	2.70
$Hg(OH)_2 + H_2O = Hg(OH)_3^- + H^+$	15.00
$Hg(OH)_2 + 2HS^- = HgS_2^{2-} + 2H_2O$	31.24
$Hg(OH)_2 + 2HS^- + 2H^+ = Hg(HS)_2 + 2H_2O$	43.82
$Hg(OH)_2 + SO_4^{2-} + 2H^+ = HgSO_4 + 2H_2O$	7.49

Table 8. Hg Solubility Reaction Equilibrium Constants Available in PHREEQC (Parkhurst and Appelo, 1999)

Solubility Reactions	Log K	ΔH (kJ)
$HgS + 2H_2O = Hg(OH)_2 + H^+ + HS^-$	-45.69	253.76
$HgS + 2H_2O = Hg(OH)_2 + H^+ + HS^-$	-45.09	253.72
$HgO + H_2O = Hg(OH)_2$	-3.64	-38.9
$Hg(OH)_2 = Hg(OH)_2$	-3.49	-0
$HgCl_2 + 2H_2O = Hg(OH)_2 + 2Cl^- + 2H^+$	-21.26	107.82

However, as it was mentioned earlier, the existing Hg databases in PHREEQC are limited and thus inadequate to effectively represent all possible Hg speciation that may occur in an aqueous system. Therefore, the aim of this literature review was to obtain the thermodynamic properties of Hg (speciation, sorption process, etc.). These properties were added into the PHREEQC database. Then the model predictions were confirmed by simulating and comparing the Hg speciation to experimental reported results that were identified in the literature. The comparison between the literature results and those estimated by the enhanced database and model produced quite comparable results thus confirming the prediction capability of PHREEQC.

An illustration of the procedure is the case of the experimental work of Gårdfeldt et al. (2003), who conducted experiments to study the various mercuric acetate complexes in equilibrium at various pH values. The mercuric acetate species and their thermodynamic properties from Gårdfeldt et al. (2003) study (Table 4) were added to the enhanced PHREEQC database.

Table 9. Thermodynamic Properties of Hg-Acetate Obtained from Gårdfeldt et al. (2003)

Mercury species	Reactions	Log K
$[Hg(CH_3COO)]^+$	$Hg^{2+} + CH_3COO^- = [Hg(CH_3COO)]^+$	4.3
$Hg(CH_3COO)_2$	$Hg^{2+} + 2CH_3COO^- = Hg(CH_3COO)_2$	7.0
$[Hg(CH_3COO)_3]^-$	$Hg^{2+} + 3CH_3COO^- = [Hg(CH_3COO)_3]^-$	13.3
$[Hg(CH_3COO)_3]^{2-}$	$Hg^{2+} + 4CH_3COO^- = [Hg(CH_3COO)_4]^{2-}$	17.1

The results obtained from Gårdfeldt's experimental works are shown in Figure 1.

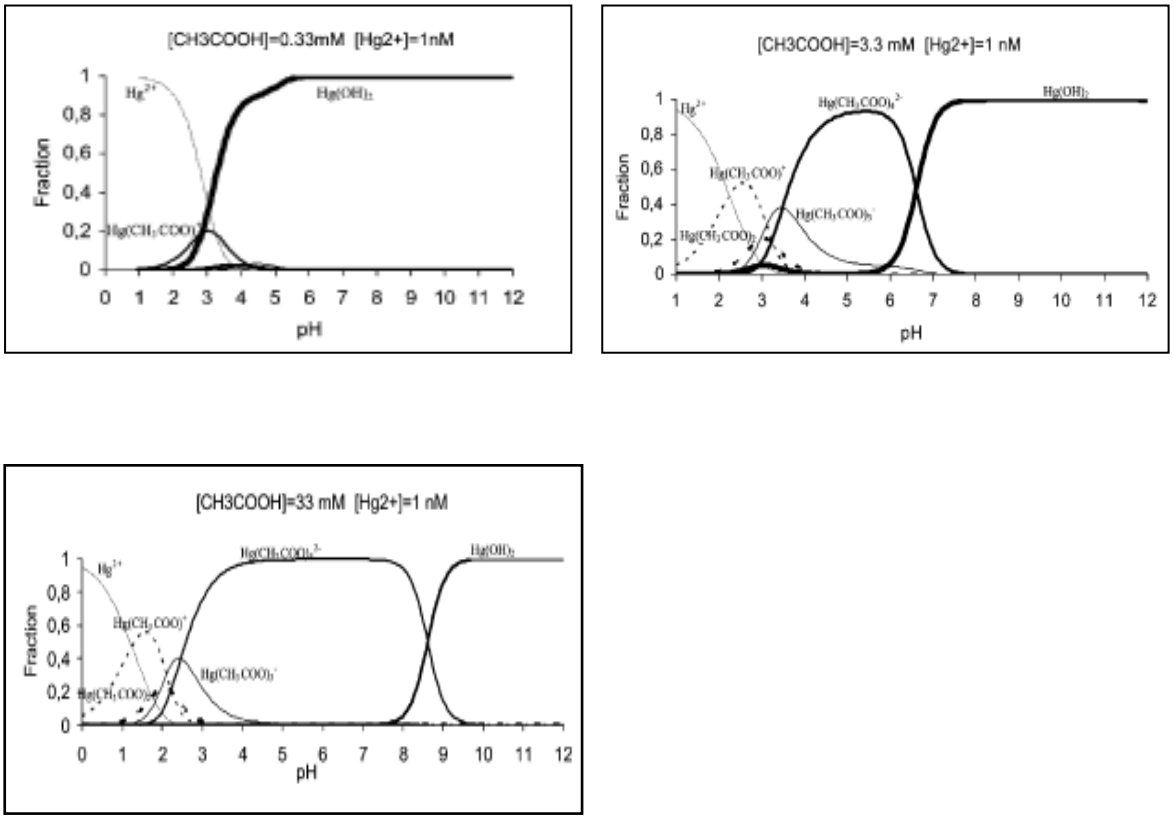

Figure 47. Gårdfeldt et al. (2003) study of mercuric acetate complexes over a wide pH.

Gårdfeldt et al. (2001) conducted experimental work to study the complexation of MeHg at various pH using phosphate buffer. They reported that the complexation of MeHg obtained from their experimental work (Figure 2) was quite consistent with hand calculations using the thermodynamic data in Table 5. Consequently, the thermodynamic data of Table 5 were also added to enhance the database of the PHREEQC model.

Table 10. Hg Reaction Equilibrium and Solubility constants (Gårdfeldt et al., 2001)

Reactions	Log K	References
$CH_3Hg^+ + HPO_4^{2-} = (CH_3Hg\ HPO_4)^-$	5.0	Schwarzenbach and Schellenberg (1965)
$CH_3Hg^+ + OH^- = CH_3Hg\ OH$	9.4	Schwarzenbach and Schellenberg (1965)
$2CH_3Hg^+ + OH^- = [(CH_3Hg)_2OH]^+$	2.4	Libich and Robenstein (1973)
$Hg^{2+} + OH^- = HgOH^+$	10.6	Dyrssen and Tyrell (1961)
$Hg^{2+} + 2OH^- = Hg(OH)_2$	21.9	Dyrssen and Tyrell (1961)
$Hg^{2+} + 3OH^- = (Hg(OH)_3)^-$	20.9	Garett and Hirschler (1938)
$2Hg^{2+} + OH^- = (Hg_2OH)^+$	10.7	Ahlberg (1962)
$Hg^{2+} + HPO_4^{3-} = (Hg\ HPO_4)^-$	9.5	Quarfort-Dahlman (1975)
$3Hg^{2+} + PO_4^{3-} + 3OH- = (HgOH)_3PO_4(s)$	21.4	Quarfort-Dahlman (1975)
$Hg^{2+} + 2OH^- = Hg(OH)_2(s)$	25.4	Dyrssen and Tyrell (1961)
$3Hg^{2+} + PO_4^{3-} = Hg_3(PO_4)_2(s)$	49.4	Gårdfeldt et al. (2003)
$Hg^{2+} + HPO_4^{2-} = HgHPO_4(s)$	13.1	Haitzer et al. (2002)
$Hg^{2+} + H_2O = HgO(s) + 2H^+$	-2.45	Hietanen and Hogfeldt (1976)

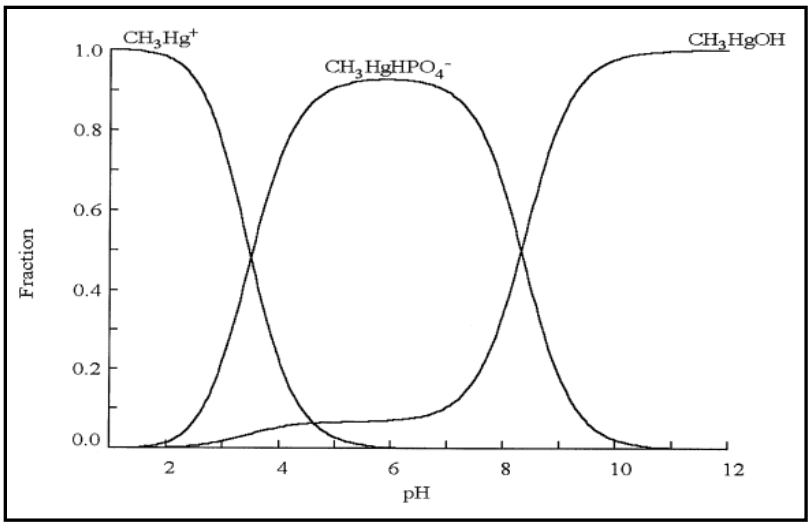

Figure 48. MeHg species as function of pH; Gårdfeldt et al. (2001).

Hg(II) is generally bound to the acid site of organic matter (i.e., carboxylic acid, phenols, ammonium ions, alcohols, and thiols) (Ravichandran, 2004);carboxylic acid and phenol groups are the acidic functional groups that contain up to 90% of DOM (dissolved organic matter). However, mercury is found to preferentially bind to thiol groups (RS^-), which constitute a small percentage of DOM compared to oxygen or nitrogen-containing functional groups (RO^- and RN^-). The study of Xia et al. (1999) also confirmed that Hg(II) preferably binds to RS^- groups over RO^- in DOM. The relationship between DOM and reduced sulfur concentration in DOM (equation 1) was proposed by Dong et al. (2010). Thus, concentration of reduced sulfur in DOM can be estimated using equation 35.

$$[Sred] = [DOM] \times F_1 \times F_2/W \qquad \text{(Eq. 35)}$$

where:

[Sred] is the concentration of reduced sulfur in DOM

F_1 is fraction of total sulfur content in DOM

F_2 is fraction of reduced sulfur

W is atomic weight of sulfur

Ravichandran (2004) reported that the total sulfur content in DOM was found to be approximately 1% (wt% of DOM), while reduced sulfur was 50% of total sulfur (wt% of total sulfur). However, not all of reduced sulfur is reactive for binding with Hg(II). Amirbahman et al. (2002) and Haitzer et al. (2002 and 2003) reported that only a small fraction, approximately 2%, of reduced sulfur, was available for binding with Hg(II). Moreover, the study of Skyllberg et al. (2006), which used EXAFS, an Extended X-Ray Absorption Fine Structure, to study the complexation of Hg(II) in soil organic matter, indicated that 20-30% of reduced sulfur is involved in the Hg-Thiol group. Furthermore, these studies indicate that around 2-30% of reduced sulfur content in DOM is reactive and is available for Hg(II) binding. The logs of stability constants (log K) between Hg and RS^- were reported in a wide range (log K = 20 – 40), the actual value depending on the conditions of the experimental study. The reaction constants of Hg-RS^-, Hg-RO^-, and Hg-RN^- are shown in Table 6.

Table 11. Reaction equilibrium constants of Hg and reactive functional groups in DOM [thiol group (RS^-), oxygen- or nitrogen-containing functional group (RO^- and RN^-)]

Type of DOM	Reaction	Log K
DOM isolates from Florida Everglades (Haitzer et al., 2003)	$Hg^{2+} + RS^- + RX^- =$ Hg(RS)(RX)	28.7±0.1
	$RXH = RS^- + H^+$ (X =O, N, S)	-6.3
	$SRH = RS^- + H^+$	-10.3
DOM from California natural waters (Black et al., 2007)	$Hg^{2+} + RS^- = Hg(RS)^+$	29.9 – 33.5
	$SRH = RS^- + H^+$	-9.96
DOM from Texas estuarine (Han and Gill, 2005)	$Hg^{2+} + RS^- = Hg(RS)^+$	26.1 – 26.9
	$SRH = RS^- + H^+$	-10

DOM from fresh and sea waters (Lamborg et al., 2003)	$Hg^{2+} + RS^{-} = Hg(RS)^{+}$	21 - 24
DOM isolates from Florida Everglades (Haitzer et al., 2002)	$Hg^{2+} + RS^{-} = Hg(RS)^{+}$ $RSH = RS^{-} + H^{+}$	28.5 -10
Peats and DOM from Florida Everglades (Drexel et al., 2002)	$Hg^{2+} + RS^{-} = Hg(RS)^{+}$ $RSH = RS^{-} + H^{+}$	25.8 – 27.2 -10
DOM isolates from Florida Everglades (Benoit et al., 2001)	$Hg^{2+} + RS^{-} = Hg(RS)^{+}$ $RSH = RS^{-} + H^{+}$	20.6 – 23.8 -10

Ion exchange is one of the important mechanisms that play a major role in the transport of Hg in aquatic environments. The difference between sorption and exchange mechanisms is that "sorption" indicates that the chemical is taken up into the solid, while "exchange" involves replacement of one chemical for another one at the solid surface (Appelo and Postma, 2010). The ion exchange for all solid surfaces in aquatic environments is related to the soil Cation Exchange Capacity (CEC) and ion exchange coefficients.

CEC indicates the amount of cations that can be attached to the negative charge sites of soil. CEC is commonly expressed as milli-equivalents of hydrogen (H^{+}) per 100 g of dry soil or meq/100g_{soil}. CEC values of common soils and sediment materials reported by several researchers (Appelo and Postma, 2005; Bergaya and Vayer, 1997) are shown in Table 7.

Table 12. CEC of common soil and sediment materials (Appelo and Postma, 2005; Bergaya and Vayer, 1997)

Soil and Sediment Materials	CEC meq/kg
Allophane	~700
Bentonite	1000-1200
Glauconite	50-400
Goethite	~800
Halloysite	50-100
Hematite	~700
Illite	200-500
Kaolinite	30-150
Montmorillonite	800-1200
Quartz	6-53
Shale	100-410
Vermiculite	1000-2000

The ion exchange coefficient is a coefficient that defines the amount of one chemical that replaces another chemical on the sediment's exchange site. For the ion exchange reaction of Hg(II) for any cation, I^i, can be written as equation 36, while its ion exchange coefficient can be obtained from the law of mass action as shown in equation 37.

Reaction: $$\tfrac{1}{2}Hg^{2+} + \tfrac{1}{i}\cdot I - X_i \leftrightarrow \tfrac{1}{2}\cdot Hg - X_2 + \tfrac{1}{i}I^{i+} \quad \text{(Eq. 36)}$$

Ion exchange coefficient: $$K_{Hg/I} = \frac{[Hg - X]^{1/2}[I^{i+}]^{1/i}}{[I - X_i]^{1/i}[Hg^{2+}]^{1/2}} \quad \text{(Eq. 37)}$$

where X is the exchange sites, and the square brackets in the equation represent the activities. The exchange coefficients are commonly used and their values depend upon the type of exchanger present in the soil.

The PHREEQC database contains ion exchange coefficients of various elements that are related to Na^+. This is because Na^+ is a common ion that is contained in soils. The existing PHREEQC database is shown in Table 8; M in Table 8 represents any cation, while the numbers in parentheses are the given ranges that present many measurements from different soils and for different clay minerals (Appelo and Postma, 2005; Bruggenwert and Kamphorst, 1979; Parkhurst and Appelo, 1999).

Although, many ion exchange coefficients that relate to Na are provided in the PHREEQC database, there is no data available for Hg.

Khan and Alam (2004) reported the ion exchange coefficients of Hg(II) for various ions as shown in Table 9. The ion exchange coefficients provided in Table 9 were then added and used in the PHREEQC database by converting them in values relative to Na^+. The exchange coefficients between other pairs of cations can be obtained by combining two reactions.

Table 13. PHREEQC existing database of ion exchange coefficients relative to Na^+ (Appelo and Postma, 2005; Bruggenwert and Kamphorst, 1979; Parkhurst and Appelo, 1999)

Ions	Ion exchange coefficients $K_{Na/M}$	Ions	Ion exchange coefficients $K_{Na/M}$
Li^+	1.2 (0.95-1.2)	Mn^{3+}	0.55
K^+	0.2 (0.15-0.25)	Fe^{2+}	0.6
NH_4^+	0.25 (0.2-0.3)	Co^{2+}	0.6
Rb^+	0.1	Ni^{2+}	0.5

Cs^{+}	0.08	Cu^{2+}	0.5
Mg^{2+}	0.5 (0.4-0.6)	Zn^{2+}	0.4 (0.3-0.6)
Ca^{2+}	0.4 (0.3-0.6)	Cd^{2+}	0.4 (0.3-0.6)
Sr^{2+}	0.35 (0.3-0.6)	Pb^{2+}	0.3
Ba^{2+}	0.35 (0.2-0.5)	Al^{2+}	0.7 (0.5-0.9)

Table 14. Ion exchange coefficients for various ions related to Hg(II) (Khan and Alam, 2004)

Ions	Ion exchange coefficients $K_{Hg/M}$
Na^{+}	0.04
K^{+}	0.03
Mg^{2+}	0.02
Co^{2+}	0.04
Ni^{2+}	0.02
Cu^{2+}	0.03
Mn^{2+}	0.03
Zn^{2+}	0.02
Pb^{2+}	0.07
Al^{3+}	0.01
Fe^{3+}	0.05

PHREEQC uses the surface complexation model that was proposed by Dzombak and Morel (1990) to calculate the sorption of metals onto the surface of minerals. Dzombak and Morel (1990) have obtained the database for surface complexation on hydrous ferric oxide or ferrihydrite [$Fe(OH)_3$] (Dzombak and Morel, 1990; Schlüter, 1995; Schlüter and Gäth 1997). Dzombak and Morel's complexation reaction model was defined for two sites on ferrihydrite, a weak site (≡Hfo_sOH) and a strong site (≡Hfo_wOH). The equilibrium constants for surface complexation of Hg are shown in Table 10 (Dzombak and Morel, 1990; Yasunaga and Ikeda, 1986; Hayes and Leckie, 1986). The surface complexation for other iron oxide minerals (Goethite, Amorphous Fe-Oxide, and Hematite) can also be calculated using Dzombak and Morel's model. Nevertheless, the sorption capability of the minerals mainly depends on their surface area properties (Arias et al., 2004; Miretzky et al., 2005; Martell and Smith, 2001) (Table 11).

Table 15. Dzombak and Morel (1990)'s sorption-reaction constant database for Hg

Reactions	Log K
≡Hfo_sOH + $Hg(OH)_2$ + H^+ = ≡Hfo_sOHg^+ + $2H_2O$	13.95
≡Hfo_wOH + $Hg(OH)_2$ + H^+ = ≡Hfo_wOHg^+ + $2H_2O$	12.64

Table 16. Surface property of iron oxide minerals (Arias et al., 2004; Miretzky et al., 2005; Martell and Smith, 2001)

Iron Oxides	Weak Sites (mol/mol	Strong Sites	Surface Area	Point of Zero
Ferrihydrite	0.2	0.005	600	8.11
Amorphous Fe-Oxide	0.075	0.0018	222.7	7.23
Goethite	0.02	0.0005	63.1	8.82
Hematite	0.003	0.00009	10.9	8.5

Sarkar et al. (1999) studied and conducted the experiments on the adsorption of Hg(II) on the surface of quartz (SiO_2) and gibbsite [$Al(OH)_3$], using the solid properties (Table 12)

documented in various studies (Elliott and Huang, 1981; Meng and Letterman, 1993; Riese, 1982; Singh and Mattigod, 1992). The surface complexation and the intrinsic equilibrium constants (log K_{int}) for quartz (≡Sio) and gibbsite (≡Aloh) used in this study are shown in Tables 13 and 14 respectively.

Table 17. Quartz and gibbsite properties used in Sarkar et al. (1999)

Parameter	Quartz	Gibbsite
Surface area, m^2/g	4.15	3.5
Site density, n/m^2	4.5	8.0
Total surface sites (x 10^{-4} mol/L)	1.023	1.534

Table 18. The surface complexation and the intrinsic equilibrium constants (log K_{int}) of Hg(II) adsorption on quartz (≡Sio) (Sarkar et al., 1999)

Parameter	Log K_{int}
≡Sio_OH + H^+ = ≡Sio_OH_2^+	2.77
≡Sio_OH = ≡Sio_O^- + H^+	-6.77
≡Sio_OH + Na^+ = ≡Sio_Na^+ + H^+	-6.21
≡Sio_OH + Hg^{2+} + H_2O = ≡Sio_OHgOH + $2H^+$	-2.19
≡Sio_OH + Hg^{2+} + $2H_2O$ = ≡Sio_$OHg(OH)_2^-$ + $3H^+$	-7.75
≡Sio_OH + Hg^{2+} + Cl^- + H_2O = ≡Sio_$OHgOHCl^-$ + $2H^+$	2.14
≡Sio_OH + Hg^{2+} + PO_4^{3-} + H_2O = ≡Sio_$OPO_2Hg(OH)_2^{2-}$ + H^+	11.61

Table 19. The surface complexation and the intrinsic equilibrium constants (log K_{int}) of Hg(II) adsorption on gibbsite (≡Aloh) (Sarkar et al., 1999)

Parameter	Log K_{int}
$\equiv Aloh\_OH + H^+ = \equiv Aloh\_OH_2^+$	4.7
$\equiv Aloh\_OH = \equiv Aloh\_O^- + H^+$	-8.7
$\equiv Aloh\_OH + Na^+ = \equiv Aloh\_Na^+ + H^+$	-7.0
$\equiv Aloh\_OH + Hg^{2+} + H_2O = \equiv Aloh\_OHgOH + 2H^+$	-2.6
$\equiv Aloh\_OH + Hg^{2+} + 2H_2O = \equiv Aloh\_OHg(OH)_2^- + 3H^+$	-10.2
$\equiv Aloh\_OH + Hg^{2+} + Cl^- + H_2O = \equiv Aloh\_OHgOHCl^- + 2H^+$	-0.5
$\equiv Aloh\_OH + Hg^{2+} + PO_4^{3-} + H_2O = \equiv Aloh\_OPO_3Hg(OH)_2^{2-} + H^+$	12.5

Zachara et al. (1988) studied the chromate adsorption by kaolinite [$Al_2Si_2O_5(OH)_4$] and proposed that the ideal structure of kaolinite consists of the ionization of quartz (≡Sio) and gibbsite (≡Aloh), which controls the surface charge. The result of their study concluded that the total site density (n_s) of kaolinite consists of equal contribution of ≡Sio and ≡Aloh sites (i.e., n_s = [≡Sio] + [≡Aloh], and [≡Sio] = [≡Aloh]). Sarkar et al. (2000) applied this principle in their model study of adsorption of Hg(II) by kaolinite, then verified the model results with experimental results. The kaolinite solid properties used in Sarkar et al. (2000) study are shown in Table 15 (Riese, 1982).

Table 20. Kaolinite properties used in Sarkar et al. (2000)

Parameter	Kaolinite
Surface area, m^2/g	12.3
Site density, n/m^2	6.0
Total surface sites (x 10^{-4} mol/L)	2.02

The modeling of adsorption of Hg(II) by kaolinite was conducted, using the surface complexation and the intrinsic equilibrium constants (log K_{int}) of Hg(II) adsorption onto quartz and gibbsite (see Tables 13 and 14). Sarkar et al. (2000)'s modeling and experimental results were comparable. This supports the Zachara et al. (1988)'s conclusion on the ideal structure of kaolinite. Zhu et al. (2012) studied the transport and interactions of kaolinite and mercury in saturated sand media, using the ideal kaolinite structure proposed by Zachara et al. (1988) and the Hg sorption thermodynamic data on quartz and gibbsite proposed by Sarkar et al. (2000) studies. Their model and experimental results were in good agreement, which confirmed Zachara et al. (1988) and Sarkar et al. (2000) studies.

Sorption isotherm is the relation between sorbed and dissolved solute concentration at a fixed temperature. The Langmuir and the Freundlich isotherms, which are shown in equations 38 and 39, are often used to describe the relation.

Langmuir Isotherm; $$S = \frac{K_L S_m C}{1 + K_L C}$$ (Eq. 38)

Freundlich Isotherm; $$S = K_F \cdot C^n$$ (Eq. 39)

where:

S = the amount of solute retained per unit weight of the adsorbent (mmol/kg)

C = the equilibrium concentration of the solute remaining in the solution (mmol)

K_L = constant related to the energy of adsorption (L/mmol)

S_m = the maximum adsorption capacity of the sample (mmol/g)

K_F and n = adjustable coefficients

The sorption with Freundlich equation extends infinitely as concentrations increase, which is not realistic since a limited number of sorption sites are expected. The sorption with the Langmuir

equation shows that the sorbed concentration S increases linearly with solute concentration C, if $C << K_L$. However, when the concentration is very high, $C >> K_L$, then the surface becomes saturated and $S = S_{max}$, which indicates the limitation of the sorption site.

Cruz-Guzman et al. (2003) studied the sorption isotherm of Hg(II) on Ferrihydrite [Ferrih], Humic acid (HA) and Montmorillonite (SW). The mixtures (binary and ternary sorbents) between the sorbents were also performed to test their Hg(II) sorption capabilities. For the single model sorbent, the Hg(II) sorption capabilities are following the sequence of HA > $Fe(OH)_3$ > SW. The sorption isotherms of Hg(II) on all model sorbents (single, binary, and ternary sorbents) showed a strong Langmuir-character with $R^2 > 0.98$ (Figures 3 and 4). The isotherms indicated a limited number of sorption sites exist and it became more difficult for the sorbing species to find a vacant site available when more sites in the sorbent were occupied.

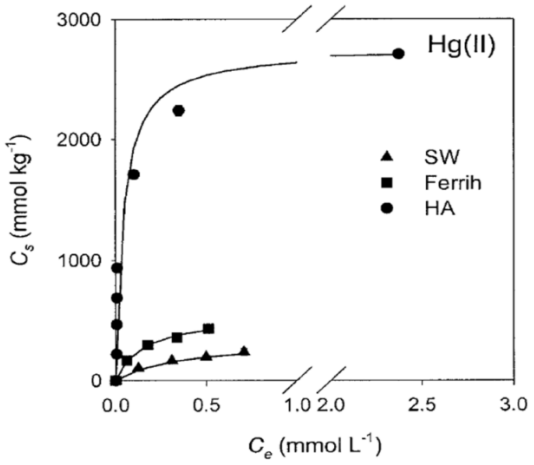

Figure 49. Hg(II) sorption isotherm on single model sorbent (Cruz-Guzman et al., 2003).

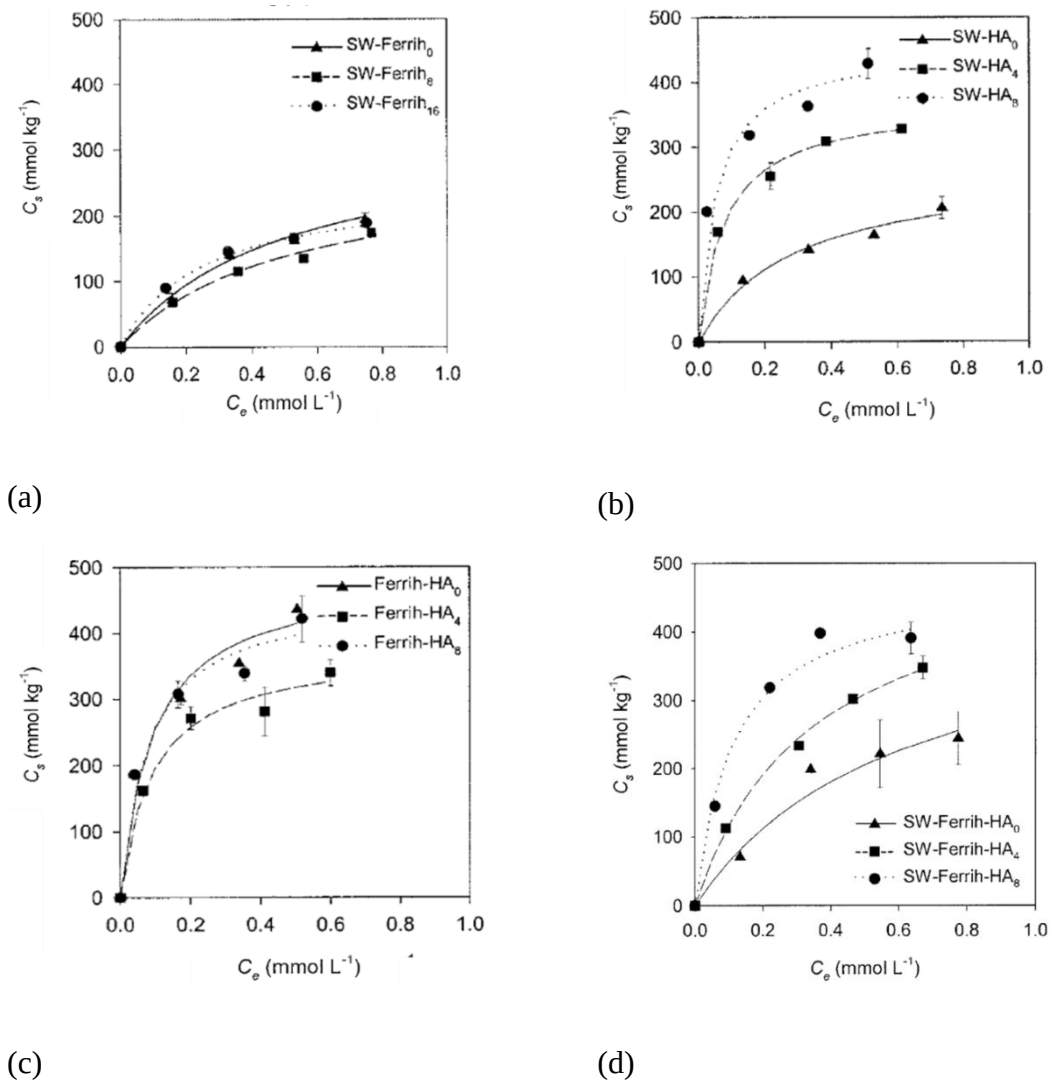

Figure 50. Hg(II) sorption isotherms on binary (a), (b) and (c) and ternary (d) model sorbents (Cruz-Guzman et al., 2003).

The characteristic of the sorbents used in Cruz-Guzman et al. (2003) study and the Langmuir isotherm results for Hg(II) sorption on all the model sorbents are shown in Table 16.

Table 21. The characteristic of the model sorbents and Langmuir Isotherm for Hg(II) sorptions Cruz-Guzman et al. (2003)

Model sorbents		Sorbent Composition (%)			Langmuir Parameters for Hg(II) sorption		
		SW	Ferrih	HA	S_m mmol/kg	K_L L/mmol	R^2
Single model sorbents	SW	100	0	0	319	4	0.99
	Ferrih	0	100	0	536	7	0.99
	HA	0	0	100	2750	23	0.99
Binary model sorbents	SW-Ferrih$_0$	100	0	0	331	2	0.96
	SW-Ferrih$_8$	92.7	7.3	0	275	2	0.95
	SW-Ferrih$_{16}$	86.3	13.7	0	246	4	0.99
	SW-HA$_0$	100	0	0	273	3	0.96
	SW-HA$_4$	95.7	0	4.3	369	13	0.99
	SW-HA$_8$	93.3	0	6.7	454	19	0.98
	Ferrih-HA$_0$	0	100	0	490	11	0.97
	Ferrih-HA$_4$	0	96.4	3.7	376	11	0.98
	Ferrih-HA$_8$	0	93.1	6.9	459	13	0.97
Ternary model sorbents	SW-Ferrih-HA$_0$	85.2	14.8	0	462	2	0.82
	SW-Ferrih-HA$_4$	82.5	14.6	2.9	525	3	0.99
	SW-Ferrih-HA$_8$	81.0	13.5	5.5	474	9	0.98

Liang et al. (2013) studied the sorption of Hg(II) on Goethite, Hydrous Manganese Oxides, and Birnessite in freshwater (salinity = 0‰) and marine water (salinity = 33‰). This was in order to study the effect of Cl^- on the Hg(II) sorption isotherms. They found that the sorption isotherms

can be well described by Langmuir isotherms as shown in Tables 17 (freshwater) and 18 (marine water).

Table 22. Langmuir parameters for Hg(II) sorption isotherm on Goethite, Hydrous Manganese Oxides, and Birnessite in freshwater (0‰ salinity, Liang et al., 2013)

Sorbents	Langmuir Parameters		
	S_m	K_L	R^2
	mmol/mol Fe or Mn	L/mmol	
Goethite	1.4	0.36	0.92
Hydrous Manganese Oxides	5.9	2.65	0.98
Birnessite	0.4	9.46	0.97

Table 23. Langmuir parameters for Hg(II) sorption isotherm on Goethite, Hydrous Manganese Oxides, and Birnessite in marine water (33‰ salinity, Liang et al., 2013)

Sorbents	Langmuir Parameters		
	S_m	K_L	R^2
	mmol/mol Fe or Mn	L/mmol	
Goethite	0.013	0.047	0.99
Hydrous Manganese Oxides	0.007	0.045	0.99
Birnessite	0.006	0.071	0.99

Liang et al. (2013) also found that the Langmuir isotherm parameters S_m and K_L were significantly higher in freshwater (Table 17) compared to marine water (Table 18). This indicated that the increase of salinity inhibited adsorption of Hg(II) on Goethite, Hydrous Manganese Oxides, and Birnessite. This is because the high reaction constant between Hg and Cl

leads to high formation of a stable, non-sorbing aqueous $HgCl_2$ complex in the solution, which limits the amount of free Hg(II) available to sorb.

Yin et al. (1997) studied the kinetics of Hg(II) adsorption on different soils which have different characteristic as shown in Table 24.

Table 24. Soil characteristics in Yin et al. (1997)

soil no	soil name	% sand	% silt	% clay	pH	OC (g/kg)	surface area (m^2/kg)
1	Freehold sandy loam	92	2	6	5.22	1.2	2040
2	Sassafras sandy loam	45	37	18	5.78	3.5	5310
3	Dunellen sandy loam	56	30	14	5.57	11	5210
4	Rockaway stony loam	54	30	16	4.69	28	8620

The kinetic sorption of Hg(II) on the soils can be described by the first order kinetic equation (equation 40)

$$\frac{dC}{dt} = -k_m\left(C_t - \frac{S_t}{k_d}\right) \qquad \text{(Eq. 40)}$$

where:

dC/dt is the reaction rate (µg/L min),
k_m is a mass transfer coefficient (min^{-1}),
C_t is Hg(II) concentration (µg/L),
S_t is the sorbed concentration (µg/g soil), and
k_d is the distribution coefficient (L/g)

The kinetic sorption parameters k_d and k_m for each soil obtained from the Yin et al. (1997) study are shown in Table 25.

Table 25. The kinetic sorption parameters of Hg(II) on different soils (Yin et al., 1997)

soil no	soil name	k_m (min^{-1})	k_d (L/g)
1	Freehold sandy loam	6.93E-05	0.033
2	Sassafras sandy loam	7.40E-05	0.179
3	Dunellen sandy loam	9.25E-05	0.822
4	Rockaway stony loam	1.07E-04	2.100

Krabbenhoft et al. (2007) conducted experiments on the Hg and MeHg kinetic adsorption on the Floridan aquifer bedrocks, for both aerobic and anaerobic conditions. The study aimed to investigate the possible changes to total Hg and MeHg concentrations in the Upper Floridan aquifer during operation of an ASR project. The kinetic experimental data for the first-order kinetic reaction (equation 41) was obtained. The kinetic parameters of Hg and MeHg sorption on Florida bedrock are shown in Table 26.

$$\frac{dS}{dt} = kS_t \qquad \text{(Eq. 41)}$$

where:

S_t is sorption at time t (ng of Hg/kg of bedrock),
k is the sorption rate constant (day^{-1})

Table 26. Sorption kinetic parameters for the Hg and MeHg on the Floridan aquifer bedrocks (Krabbenhoft et al., 2007)

Condition	Hg k (day^{-1})	MeHg k (day^{-1})
Aerobic	0.039	0.069
Anaerobic	0.061	0.070

Drexel et al. (2002) studied the Hg(II) sorption of two Everglades peats collected at different locations in the Everglades: Water Conservation Area 2A (WCA2A) and Conservation Area 2B (WCA 2B). The Hg(II) sorption isotherms showed the competition for Hg(II) between peat and DOM released from peat. DOM and the Everglades peat consist of two sorption sites: a weak site and a strong site. The binding constants for weak and strong sites of both peat and DOM are shown in Table 27.

Table 27. Equilibrium binding constants (Drexel et al., 2002)

Reactions	WCA 2A	WCA 2B
Single site		
K_{peat}	$10^{12.0\pm0.1}$	$10^{11.6\pm0.1}$
K_{dom}	$10^{12.8\pm0.1}$	$10^{9.0\pm2.6}$
Double site		
$K_{peat, s}$	$10^{22.0\pm0.1}$	$10^{21.8\pm0.1}$
$K_{peat, w}$	$10^{11.8\pm0.1}$	$10^{11.5\pm0.1}$
$K_{dom, s}$	$10^{23.2\pm0.1}$	$10^{22.8\pm0.1}$
$K_{dom, w}$	$10^{7.3\pm4.5}$	$10^{8.7\pm3.0}$

The K_d value of Hg(II) in the Everglades peat reported by Drexel et al. (2002) varies between $10^{4.1}$ to $10^{5.7}$ L/kg depending on the Hg(II) concentration. These K_d values are similar to the values that were reported by Hurley et al. (1998).

Data and Site Study Selections

The data used in this study were obtained from many sources including literature, technical reports of specific sites, and database websites (e.g., OREIS, DBHYDRO, SFWMD, etc.).

Data from selected research contributors were used to confirm the model estimation capability for Hg. In order to confirm the model capability, the Hg experimental conditions obtained from the literature were set for the model. Then the model results were verified by the results from the literature. The model confirmation using the literature data was made for Hg-species, ion-exchange, and surface complexation processes.

Data from technical reports of the specific sites and related websites, including site geology, water quality data, flow characteristics, etc., were used for 2 purposes: 1) model confirmation; and 2) model application. The model confirmations are explained in sections 4.6 and 4.7. The model application for Hg geochemical and transport processes are documented in Chapter 6.

In this study, two test-beds, Oak Ridge Reservation (ORR) at Oak Ridge, TN, was selected for the development and evaluation of Hg geochemical processes, and also for the application in fate and transport of the enhanced model.

ORR, Oak Ridge, TN consists of three large industrial production facilities constructed as part of the World War II-era Manhattan Project: the Oak Ridge National Laboratory (formerly known as the X-10 Site), K-25 Site, and the Y-12 National Security Complex or Y-12 Plant. The accidental spill and discharge of Hg to the surroundings of Y-12 plant was reported during the Y-12 operation time, 1950-1963 (Brooks and Southworth, 2011). Studies have also shown that Hg accumulated in the soil, rock, and groundwater of the site consequentially became sources of contamination to nearby rivers and creeks, such as the East Fork Poplar Creek (EFPC) located downstream from the Y-12 plant (Figure 51). Many cleanups have been attempted for ORR sites.

Y-12 is divided into the Bear Creek Valley Watershed and the Upper East Fork Poplar Creek (UEFPC) Watershed (Figure 51). Later on as part of this study, applications of the enhanced model of this research to understand the transport of Hg were made for Bear Creek Valley and EFPC within the Y-12 complex area.

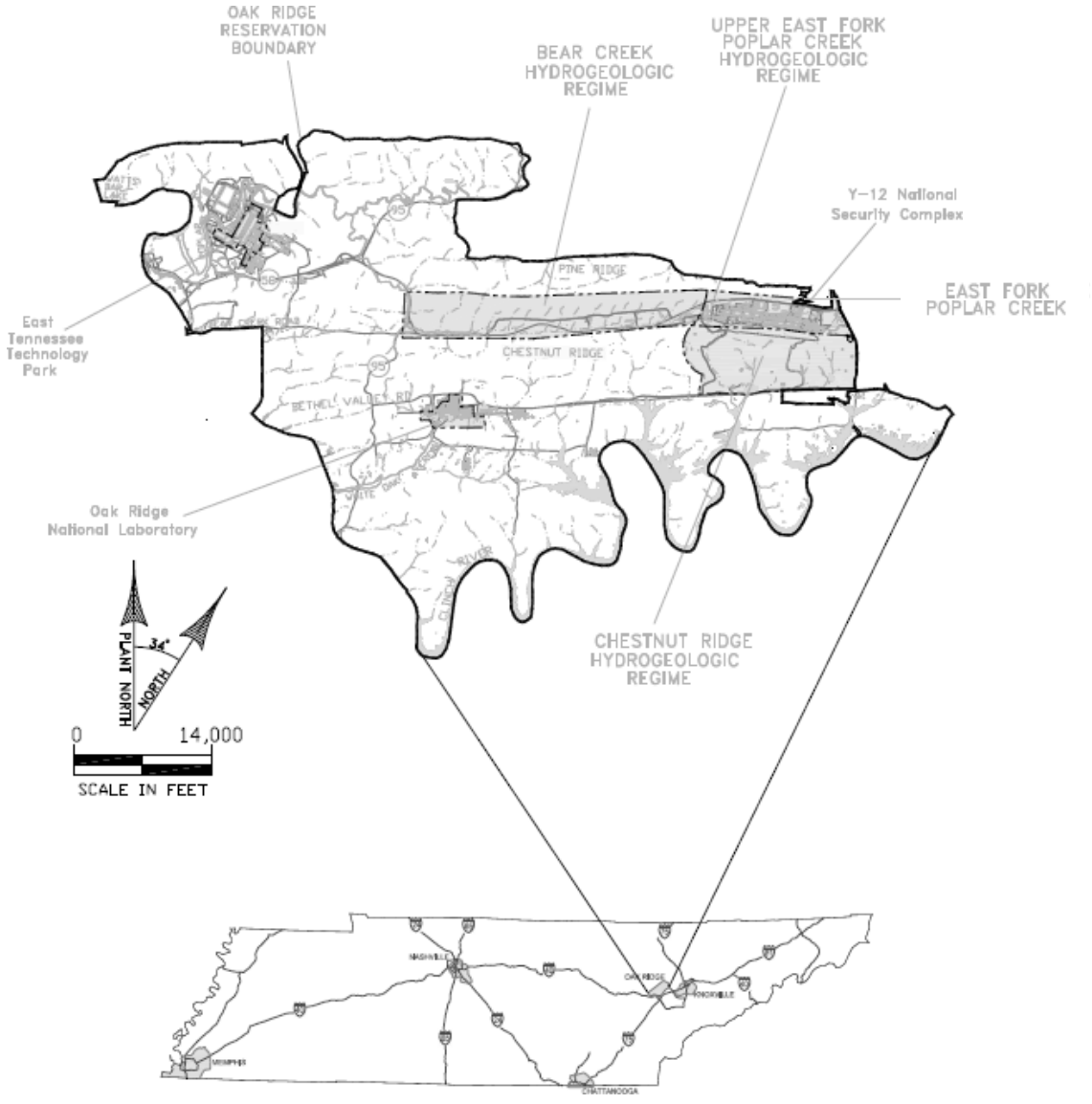

Figure 51 Oak Ridge Reservation Map (modified after www.esd.ornl.gov)

Model Confirmation in Batch Mode – Lab Scale

This section presents the tests of the model capability to simulate speciation, dissolution and precipitation, ion-exchange, surface complexation, and 1-D transport simulations. The model prediction was confirmed with both literature and field data for Hg and other species. The model capability tests were mostly done using data from the literature, for no field data is available for Hg fate as function of speciation, ion-exchange and surface complexation. However, field data were available to test the ability of the enhanced model to predict major ions such as Ca, Mg, Na, Cl, and SO_4, which are usually present in aqueous environments.

The Hg speciation prediction capability of PHREEQC with the enhanced database was satisfactorily compared with the experimental study of Gårdfeldt et al. (2003), which conducted experiments to define complexation of mercuric acetate at various pH values. Testing was done by simulating in PHREEQC the experimental conditions that Gårdfeldt et al. (2003) used in their study. The Gårdfeldt et al. (2003) study was conducted for 3 scenarios. The water conditions used in scenario 1 are shown in Table 23.

Table 28. Scenario 1 water condition in the Gårdfeldt et al. (2003) study used for model confirmation

Parameter	Unit	Value
Hg(II)	nmol	1.0
Acetic acid (CH_3COOH)	mmol	0.33
NaOH	mole	(to adjust pH)
Temperature	˚C	20

The comparison between the results from Gårdfeldt et al. (2003) and PHREEQC prediction using the enhanced database is shown in Figure 52.

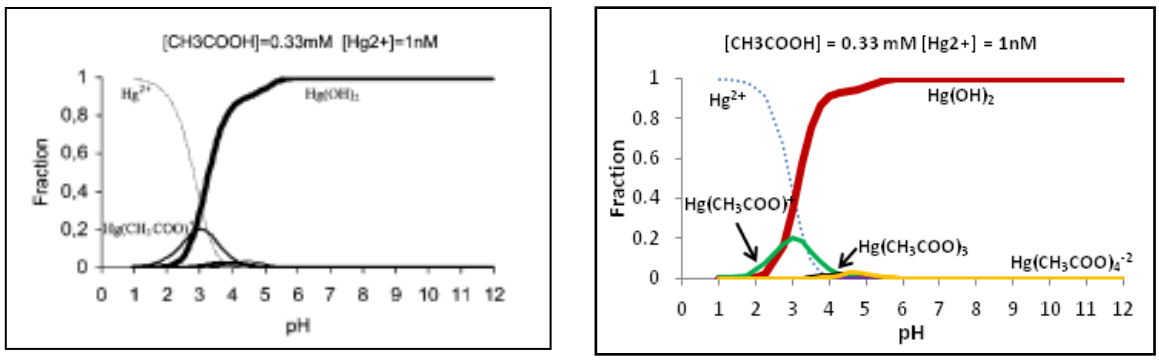

(a) (b)

Figure 52. Model speciation prediction capability testing; scenario 1 (Hg : CH_3COOH = 1 nmol : 0.33 mmol) result obtained from Gårdfeldt et al. (2003) (a) and enhanced PHREEQC model (b).

PHREEQC matches well the results of Gårdfeldt et al. (2003); the prediction showed Hg^{2+} to be dominant at pH=1 before a sharp decrease between pH 1-4. $Hg(OH)_2$ increased sharply between pH 2-5 and reached its maximum, being dominant at pH 6-12, while $Hg(CH_3COO)^-$ peaks at pH 3.

The water conditions used for the scenario 2 in the Gårdfeldt et al. (2003) study are shown in Table 24.

Table 29 Scenario 2: water condition in the Gårdfeldt et al. (2003) study used for model confirmation

Parameter	Unit	Value
Hg(II)	nmol	1.0
Acetic acid (CH_3COOH)	mmol	3.3
NaOH	mole	(to adjust pH)
Temperature	˚C	20

The comparison between the results of the Hg-CH_3COOH complexation, that is scenario 2 of the Gårdfeldt et al. (2003) experiments and the enhanced PHREEQC prediction results is shown in Figure 53.

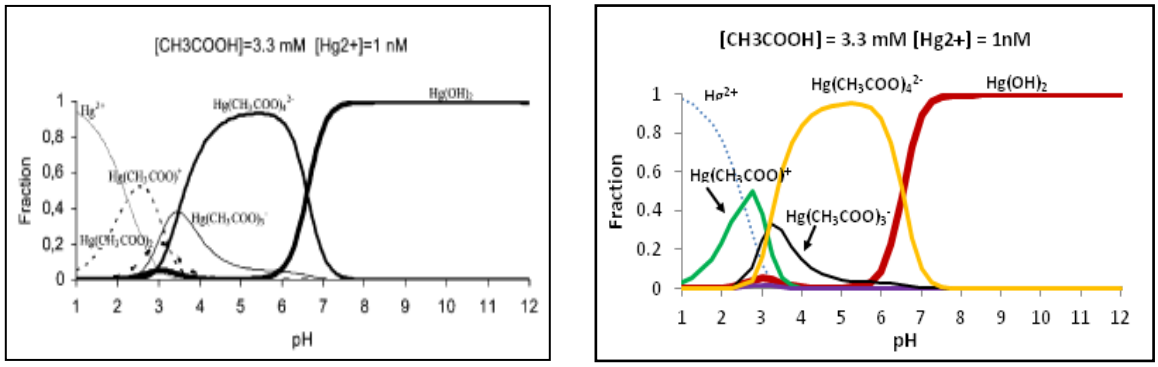

(a) (b)

Figure 53. Model speciation prediction capability testing; the scenario 2 (Hg : CH_3COOH = 1 nmol : 3.3 mmol) result obtained from Gårdfeldt et al. (2003) (a) and enhanced PHREEQC model (b).

PHREEQC predictions trace well Gårdfeldt et al. (2003) experimental results of the Hg-CH_3COOH species distribution for all pH values. A decrease in Hg^{2+} is predicted between pH 1-3, while $Hg(CH_3COO)^+$ and $Hg(CH_3COO)_3^-$ showed their peak concentrations at pH 2.8 and 3.2, respectively. $Hg(CH_3COO)_4^{2-}$ was the dominant species between pH 4-6 with a sharp decrease at higher pH values. An increase in the concentration of $Hg(OH)_2$ species occurred between pH 6-7, which then peaked at pH 8, being the only the dominant species between pH 8-12.

The water conditions used for scenario 3 are shown in Table 30.

Table 30. Scenario 3: water condition in the Gårdfeldt et al. (2003) study used for model confirmation

Parameter	Unit	Value
Hg(II)	nmol	1.0
Acetic acid (CH_3COOH)	mmol	33
NaOH	mole	(to adjust pH)
Temperature	˚C	20

The comparison between PHREEQC predictions of Hg-CH_3COOH complexation and that for scenario 3 in the Gårdfeldt et al. (2003) study is shown in Figure 54.

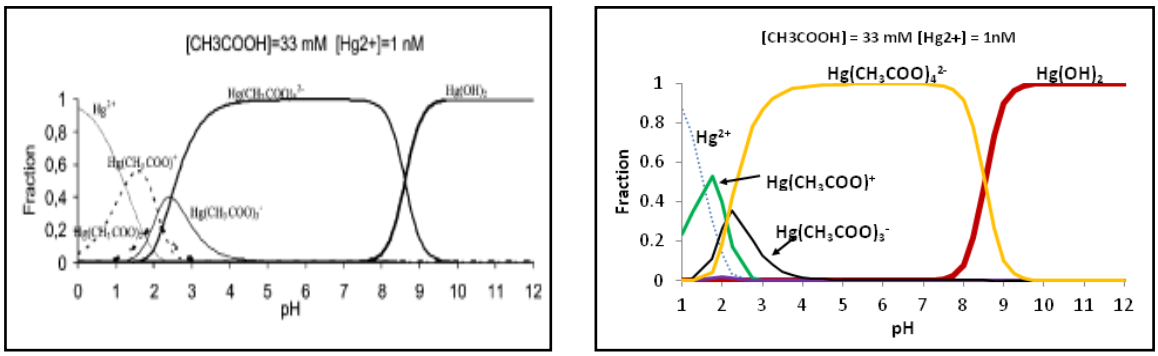

(a) (b)

Figure 54. Model speciation prediction capability testing; the scenario 2 (Hg : CH_3COOH = 1 nmol : 33 mmol) result obtained from Gårdfeldt et al. (2003) (a) and enhanced PHREEQC model (b).

Figures 9 (a) and (b) respectively depict the results of Gårdfeldt et al., 2003 (a) and the prediction with the enhanced PHREEQC model (b); the predictions are quite comparable. Hg^{2+} was estimated to be dominant at pH 1 before a sharp decrease in concentration at pH 2. The $Hg(CH_3COO)^+$ and $Hg(CH_3COO)_3^-$ peak concentrations shifted to lower pH values compared to

the previous scenarios. Increase in CH_3COOH in the solution promoted the complexation of $Hg(CH_3COO)_4^{2-}$, as dominant in concentration between pH 3-8, replacing $Hg(OH)_2$ as the dominant species in comparison to previous scenarios. The $Hg(OH)_2$ species dominated between pH 9-12.

The testing of PHREEQC for its capability to calculate the complexation of MeHg at various pH values was conducted with the enhanced PHREEQC model by comparing it to Gårdfeldt et al. (2001) experimental conditions as shown in Table 26.

Table 31. Scenario 4: water condition in Gårdfeldt et al. (2001) study used for model validation for MeHg complexation

Parameter	Unit	Value
DI Water	L	1.0
CH_3HgCl	ppb	25
PO_4^{3-}	mole	(to adjust pH)
Temperature	˚C	20

The results obtained from both the Gårdfeldt et al. (2001) experiments study and the enhanced PHREEQC model are shown in Figure 55 side by side.

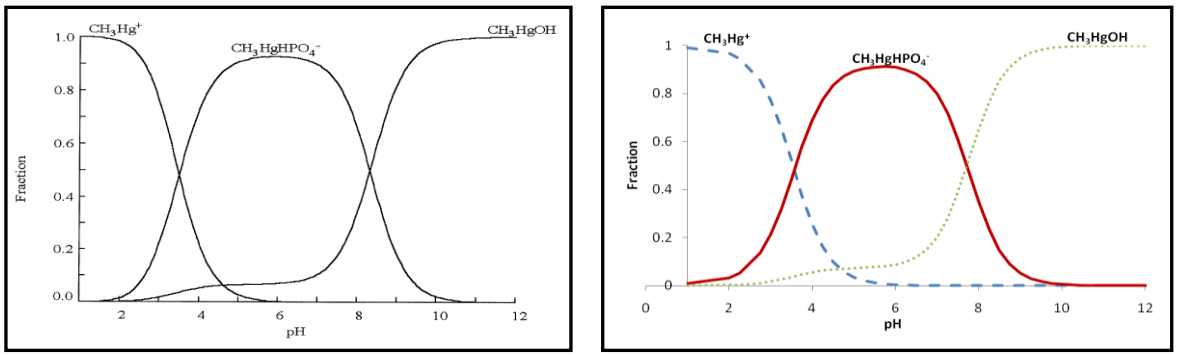

(a) (b)

Figure 55. Model speciation prediction capability testing; the scenario 4 MeHg complexation result obtained from Gårdfeldt et al. (2001) (a) and enhanced PHREEQC model (b).

Figure 55 shows that the enhanced PHREEQC model reproduces well the MeHg complexation and its speciation distribution for all pH values at the experimental conditions of Gårdfeldt et al. (2001). The CH_3Hg^+ shows dominant between pH 1-2, then has a sharp decrease in its concentration between pH 2-5 and goes to very low concentrations beyond pH 6. The dominated species at pH 4-8 was $CH_3HgHPO_4^-$, while CH_3HgOH dominates within pH 8-12.

Process Confirmation in Batch Mode – Lab Scale

The enhanced PHREEQC model surface complexation calculation capability for the Hg(II) surface complexation on $Fe(OH)_3$ was tested in reference to the experiments by Cruz-Guzman et al. (2003) study (Table 27).

Table 32. Scenario 1: sorption experimental condition in the Cruz-Guzman et al. (2003) study used for model confirmation for Hg(II) surface complexation on $Fe(OH)_3$

Parameter	Unit	Value
Fe $(OH)_3$ Sorbent	mg	10
$Hg(NO_3)_2$	mmol/L	0.25 - 1
Temperature	˚C	20
pH	-	3.0±0.3

The PHREEQC model was used to calculate the Hg(II) sorption by surface complexation with $Fe(OH)_3$ using the specific surface area characteristics of $Fe(OH)_3$ and the thermodynamic data added to the model. The model result was then compared with the experimental sorption data obtained by Cruz-Guzman et al. (2003) (Figure 56).

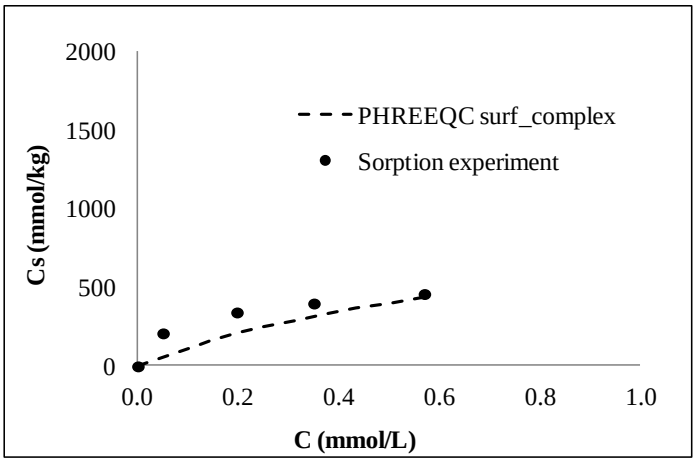

Figure 56. The model surface complexation prediction capability testing for scenario 1: Hg(II) surface complexation on $Fe(OH)_3$, sorption experimental result Cruz-Guzman et al. (2003) (dot); the enhanced PHREEQC model (dashed line).

Figure 56 shows the plot between the concentration of Hg in $Fe(OH)_3$ (C_s) and in water (C) as estimated by the model and the experimental data Cruz-Guzman et al. (2003); the values are within the same range and trend comparably. The comparison indicates that the concept, mathematics of surface complexation and the needed thermodynamic data added into PHREEQC are quite appropriate to represent the sorption of Hg(II) on $Fe(OH)_3$ surface.

In this scenario, the enhanced PHREEQC model was used to test its capability to predict the sorption of Hg(II) on Humic Acid (HA), using the added thermodynamic database obtained from Yin et al. (1997). The sorption experimental conditions obtained in the Cruz-Guzman et al. (2003) study (Table 28) were used to assess the model predictive performance.

The same experimental condition in Table 28 was used to compare PHREEQC simulation of sorption with the Cruz-Guzman et al. (2003) sorption experimental result (Figure 57).

Table 33. Scenario 2: sorption experimental condition in the Cruz-Guzman et al. (2003) study used for model confirmation for Hg(II) sorption of Humic Acid

Parameter	Unit	Value
HA Sorbent	mg	10
$Hg(NO_3)_2$	mmol/L	0.25 - 5
Temperature	˚C	20
pH	-	3.0±0.3

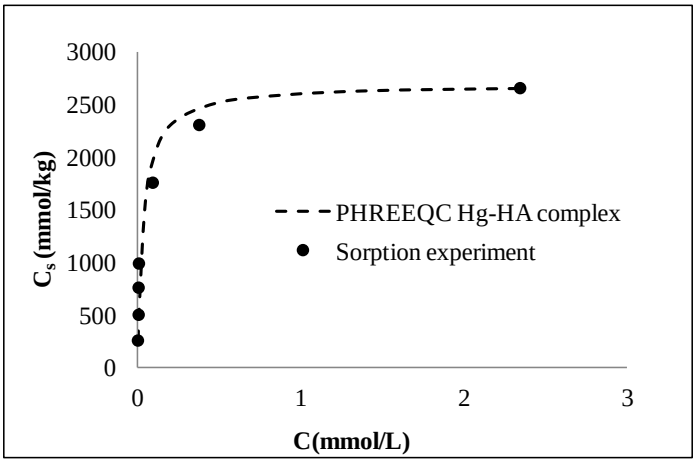

Figure 57. The model Hg-HA complexation prediction capability testing for scenario 2: sorption experimental result Cruz-Guzman et al. (2003) (dot); enhanced PHREEQC model (dashed line).

The results of Hg-HA sorption isotherm obtained from both the enhanced PHREEQC model and the experimental study were quite comparable. The comparison of both results in Figure 12 confirmed that the concept, mathematics and thermodynamic database of Hg-HA surface complexation that was added to enhance the PHREEQC model reproduces well the from experimental results of the reference, adding confidence to the use of the enhanced PHREEQC model for the prediction of Hg(II) sorption on the HA.

The model was tested for its capability to calculate the kinetic sorption of Hg and MeHg on the Florida aquifer bedrocks at both aerobic and anaerobic conditions using the first-order kinetic rate equation, $\frac{dS}{dt} = kS_t$, and rate parameters shown earlier in Table 26. The sorption experimental conditions in the Krabbenhoft et al. (2007) study were used for the model simulations (Table 29).

Table 34. Scenario 3: water condition used to test the model capability for Hg and MeHg kinetic sorption on Floridan aquifer bedrock (Krabbenhoft et al., 2007)

Parameters	Unit	Value
Aquifer bedrock Sorbent	kg	1
Water solution	mmol/L	0.2 – 5.0
pH	-	7.4
Temp	˚C	23
Alkalinity	mg/L	150
Calcium	mg/L	53
Magnesium	mg/L	12.1
Potassium	mg/L	6.8
Sodium	mg/L	45.3
Chloride	mg/L	87
Sulfate	mg/L	28.7
Hg	ng/L	2.1
MeHg	ng/L	0.09

The kinetic sorption results calculated by the model were then compared with the experimental results of Krabbenhoft et al. (2007). The comparison is shown in Tables 30 and 31 for Hg(II) and MeHg, respectively.

Table 35. Scenario 3: Comparison results of Hg kinetic sorption on Floridan aquifer bedrock between Krabbenhoft et al. (2007) study and kinetic model calculation

Condition	Time	Experiment Dissolved Hg, ng/L	Experiment Sorbed Hg, ng/kg	Model Sorbed Hg, ng/kg
Initial	2/4/2004	2.14	0	0
Aerobic Condition	2/4/2004	2.14	0	0
	2/18/2004	1.74	0.39	0.21
	3/17/2004	0.67	1.47	1.40
	4/15/2004	0.33	1.81	1.79
	5/13/2004	0.16	1.97	1.98
Anaerobic Condition	2/4/2004	1.45	0.68	0.71
	2/18/2004	0.75	1.39	1.12
	3/17/2004	0.55	1.58	1.65
	4/15/2004	0.24	1.89	2.00
	5/13/2004	0.13	2.01	2.20

Table 36. Scenario 3: Comparison results of MeHg kinetic sorption on Floridan aquifer bedrock between Krabbenhoft et al. (2007) study and kinetic model calculation

Condition	Time	Experiment Dissolved MeHg, ng/L	Experiment Sorbed MeHg, ng/kg	Model Sorbed MeHg, ng/kg
Initial	2/4/2004	0.090	0.0	0.0
Aerobic Condition	2/4/2004	0.085	0.005	0.005
	2/18/2004	0.024	0.066	0.064
	3/17/2004	0.009	0.081	0.094
	4/15/2004	0.005	0.085	0.102
	5/13/2004	0.006	0.084	0.102
Anaerobic Condition	2/4/2004	0.090	0.0	0.0
	2/18/2004	0.028	0.062	0.061
	3/17/2004	0.023	0.067	0.076
	4/15/2004	0.014	0.076	0.079
	5/13/2004	0.015	0.075	0.079

The kinetic sorption results calculated from the model and plotted against the experimental results are shown in Figure 58.

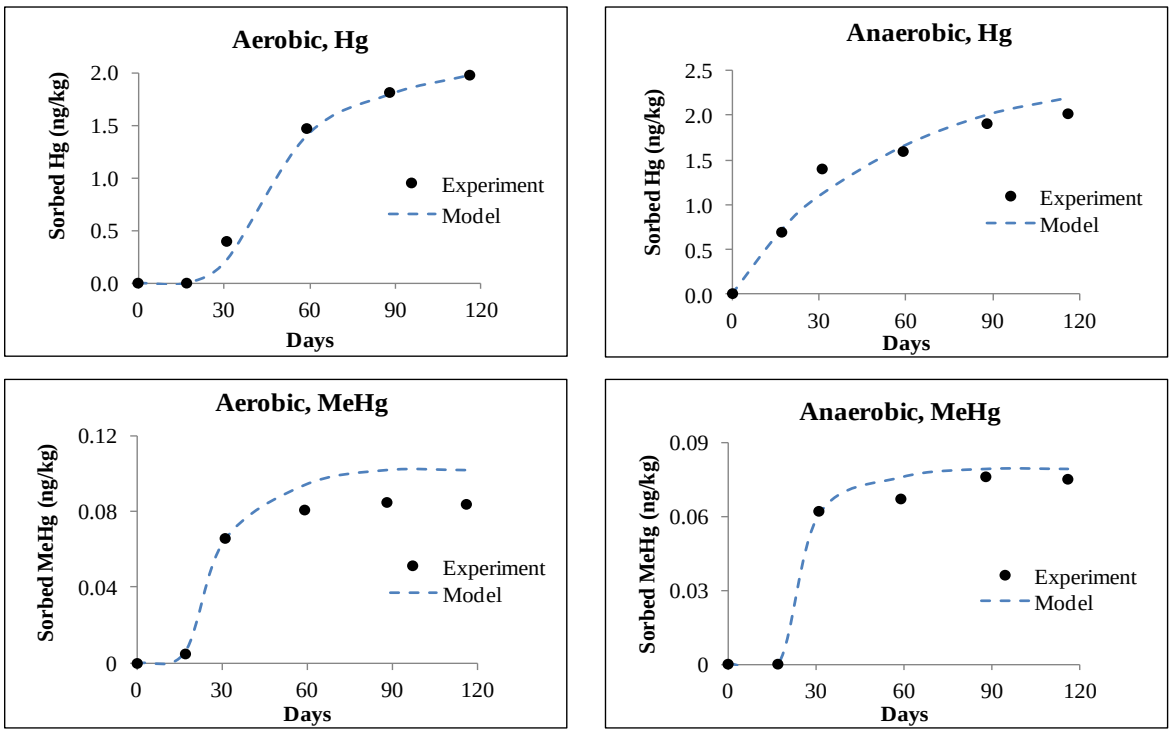

Figure 58. The model kinetic sorption prediction capability testing for scenario 3: Hg and MeHg kinetic sorption on Floridan aquifer bedrock experimental result Krabbenhoft et al. (2007) (dot); enhanced PHREEQC model (dashed line).

Tables 30 and 31 and Figure 13 show that the model provided similar sorption kinetic trends to those of the experimental results for both Hg and MeHg. This reaffirms that the model is capable of calculating the kinetic sorption for Hg and MeHg in the Florida aquifer bedrock.

Mathematical Model Confirmation in Batch Mode – Field Scale

In this section, the model was tested for its capability to predict the change in dissolution and precipitation of major ions (i.e., Ca^{2+}, Mg^{2+}, K^{+}, Na^{+}, Cl^{-} and SO_4^{2-}), which are the main constituents in the groundwater of the Floridan aquifer, with the effect of salinity caused by the intrusion of seawater (Price et al., 2003). This testing will also help to confirm that the model can be used for a wide range of ionic strengths of water (*I* is less than 0.02 for freshwater, and ~ 0.7 for seawater). In order to test the model prediction capability, a series of model simulations,

mixing saline with freshwater, were carried out within assumptions. Then the comparison between model results and water quality data obtained from over 30 monitoring wells in the central to south Florida regions were made. The average freshwater and seawater water quality data, during the years 2005-2006, obtained from the DBHYDRO database website were used for the model testing. The freshwater monitoring well locations are shown in Table 32.

Table 37. The location of the selected freshwater water quality monitoring stations (DBHYDRO)

Parameter	S332BES	S332CWD	S332CWS	S332DES
S332BES	253254.185	803343.98	Miami-Dade	East Coast Buffer
S332CWD	253053.735	803429.21	Miami-Dade	Everglades National Park
S332CWS	252809.954	803427.64	Miami-Dade	Everglades National Park
S332CWS	252809.954	803427.64	Miami-Dade	Everglades National Park
S332DES	252717.076	803421.91	Miami-Dade	East Coast Buffer

The average freshwater and seawater water quality data for the major ions, including Ca, K, Na, Mg, Fe, DO, Cl, SO_4, and Alkalinity, are shown in Tables 33 and 34, respectively.

Table 38. Freshwater water quality used for the fresh-seawater mixing model, unit in mg/L for major ion and °C for temperature (DBHYDRO)

Parameter	S332BES	S332CWD	S332DWS	S332DES	S332CWS	Average
pH	7.0-7.6	6.8-7.2	6.9-7.4	6.7-7.3	6.8-7.3	7.15
Temp	23.0-28.8	25.9-23.3	22.8-30.1	25.1-26.9	23.1-29.4	25.78
Alkalinity	205-224	202-221	194-226	198-220	203-221	209.39

Ca	66.2-77.0	71.2-77.2	66.1-74.9	74.3-77.6	66.7-76.1	73.1
K	2.8-7.0	1.8-2.7	1.5-2.8	2.1-2.9	1.5-2.8	2.47
Na	32.2-45.5	29.7-37.0	19.7-34.2	22.0-30.7	27.0-40.5	31.39
Mg	8.2-10.1	6.1-7.4	5.0-8.3	5.1-5.7	5.5-8.3	6.95
Fe	0.24-0.30	0.18-0.45	0.22-0.33	0.55-0.84	0.22-0.45	0.39
DO	0.12-0.19	0.09-0.14	0.06-0.18	0.06-0.35	0.08-0.35	0.13
Cl	49.5-68.1	43.8-58.2	29.8-53.2	40.7-47.3	40.2-61.7	47.53
SO_4	0.7-5.8	0.3-1.7	0.5-3.7	0.1-0.4	0.1-2.7	1.12

Table 39. Seawater water quality used for the fresh-seawater mixing model (DBHYDRO)

Parameter	Unit	Value
pH	-	8.2
pe	-	8.4
density	mg/L	1.0
Temperature	℃	25
Ca	mg/L	412.3
Mg	mg/L	1291.8
Na	mg/L	10768
K	mg/L	399.1

Cl	mg/L	19353
Alkalinity	mg/L	141.7
SO_4	mg/L	2712

The simulation for the fresh-seawater mixing model was divided into 2 steps. In order for the model to represent the Floridan aquifer geochemistry, the freshwater was firstly equilibrated with calcite under the assumption that the freshwater in the Florida aquifer equilibrates with calcite bedrocks (simulation step 1). The fresh groundwater saturated with calcite was then called "carbonate groundwater" (Barlow and Richard, 2010; Tibbals, 1990). The carbonate groundwater was then mixed in fresh-seawater model simulation (simulation step 2).

- Step 1: Carbonate groundwater simulation

The first step of simulation represented the equilibrium dissolution of calcite bedrock by the fresh groundwater. Geologically, the groundwater in this area underlies the calcite bedrocks. Upon their contacting, the dissolution of calcite by groundwater occurs, and become carbonate groundwater. The reaction equation of calcite dissolution/precipitation used in the model is shown in equation 42.

$$CO_2(g) + H_2O + CaCO_3 \leftrightarrow Ca^{2+} + 2HCO_3^- \quad \text{(Eq. 42)}$$

The carbonate groundwater simulation was defined by equilibrating freshwater (the average value in Table 33) with calcite (to yield the saturation index of calcite, $SI_{cc} = 0$). Equation 42 indicates that an increase of CO_2 results in dissolution of $CaCO_3$. When removing CO_2 from the water, the reaction goes to the left (Eq. 42), which causes the precipitation of $CaCO_3$. For this simulation, it was assumed that the partial pressure of carbon dioxide (P_{CO_2}) in groundwater was 10^{-2} atm. (Plummer and Sprinkle, 2001). The output represented the carbonate groundwater and was used for the mixing simulation in step 2.

- Step 2: Carbonate groundwater-seawater mixing simulation

The carbonate groundwater in step 1 was then used to mix with different seawater proportions varying from 0-100% in the mixtures. PHREEQC calculates the concentration in mixtures by multiplying the concentration of each element in each solution with its mixing fraction (Parkhurst, 1995), summing these numbers, and dividing by the sum of mixing fractions. For instance, Na concentration in solution 1 is 0.1 mol/L, and is 0.5 mol/L in solution 2. If the solutions 1 and 2 are mixed in the proportion of 0.2:0.8, then the Na concentration in the new solution is (0.1 x 0.2 + 0.5 x 0.8)/1 = 0.42 mol/L. The temperature and other intensive properties of the mixture were calculated the same way as the concentration. The model calculates the change of ionic concentrations and saturation indexes (i.e. Calcite, Aragonite, Dolomite, Gypsum, etc.), as a function of ionic strength caused by seawater in the mixture.

The results obtained from the mixing model simulations were then used to compare with the observed Coastal Floridan aquifer data collected from over 30 monitoring stations during the years 2005 and 2006. The model results of major ion concentrations, as a function of salinity, were plotted against the observed data in Figure 59. The complete observed Coastal Floridan aquifer quality database and the selected monitoring station locations are shown in Appendix D.

In Figure 59 the observed data are represented by blue circles; the model results are shown in black lines. Figure 14 clearly shows that the salinity and major ion concentrations are linearly related, for both observed data and model results, with the coefficient of determinations, R^2, greater than 0.8. The model results for Na, Mg, K and Cl ions showed similar trends and correlation to the observed data; lower R^2 were obtained for the Ca and SO_4 ions.

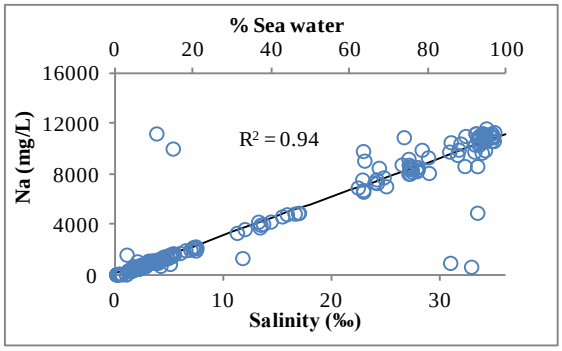

(a)

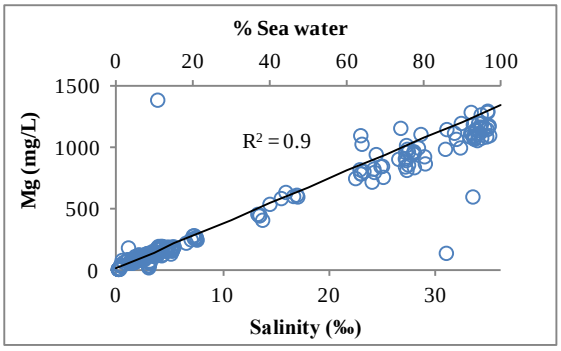

(b)

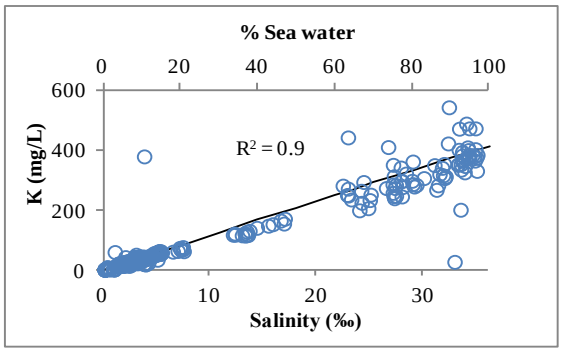

(c)

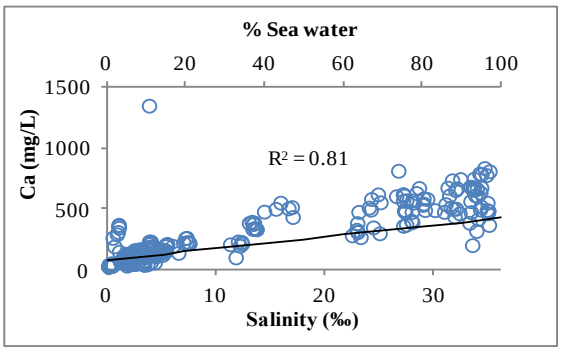

(d)

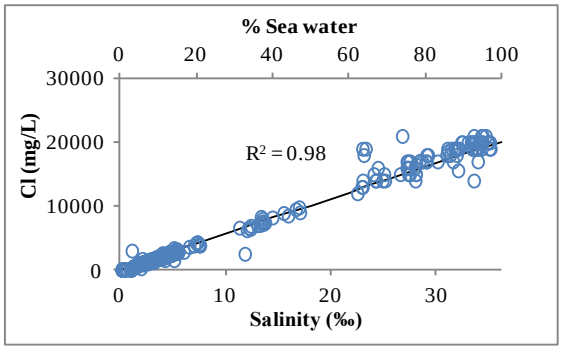

(e)

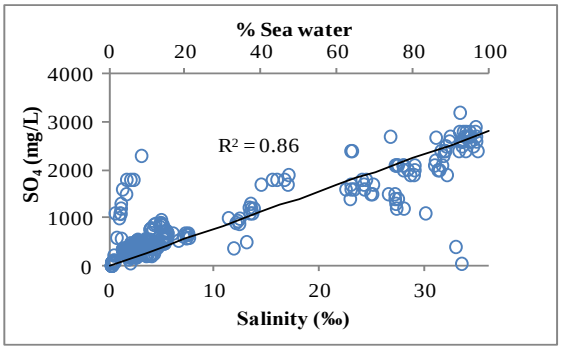

(f)

Figure 59. Comparison of major ion concentrations as a function of salinity in the mixtures between observed data collected from DBHYDRO (dots) and model results (lines); (a) Na, (b) Mg, (c) K, (d) Ca, (e) Cl and (f) SO_4.

A P_{CO_2} = 10^{-2} was assumed for the mixing model. P_{CO_2} in groundwater is one of the important factors that influences the change in water pH and the dissolution and precipitation of carbonate minerals. Assuming P_{CO_2} = 10^{-2} simulated a water pH that was comparable to the observed value the low seawater percentages (Figure 60). However, the water pH decreased at higher percentage of seawater, which did not match as well as in the case of the lower salinity fractions. A possible explanation is that ion-exchange occurs at high seawater percentages (refer to Ca concentration in Figure 60) which releases vast Ca^{2+} into the solution. Some of the Ca^{2+} may react with HCO_3^- causing $CaCO_3$ and CO_2 (g), thus, the water pH decreases.

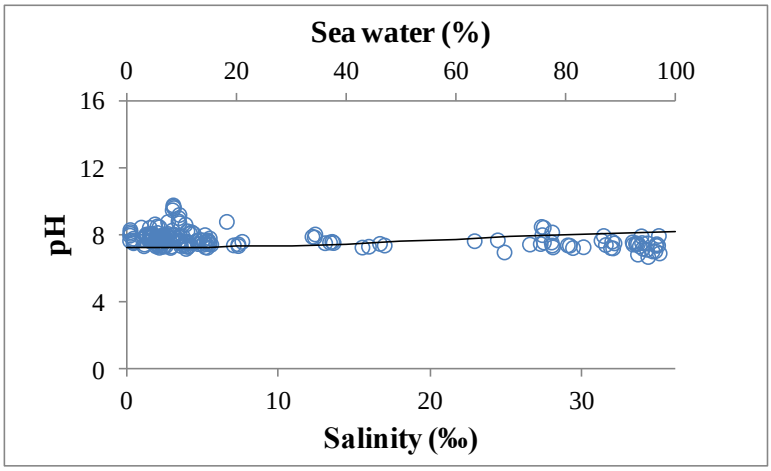

Figure 60. Water pH in the Floridan aquifer (open circles) for the sample collected during 2005 and 2006. The theoretical water pH (solid line) was calculated by PHREEQC model.

The PHREEQC model was used to calculate the saturation indexes of Aragonite ($CaCO_3$), Calcite ($CaCO_3$), Dolomite ($CaMg(CO_3)_2$), Halite (NaCl), Gypsum ($CaSO_4$), and Magnesite ($MgCO_3$) of the ground-seawater mixing process. The results from the model were plotted against the seawater proportion and salinity in the mixture and compared to the calculated saturation indexes of observed data (Figure 61).

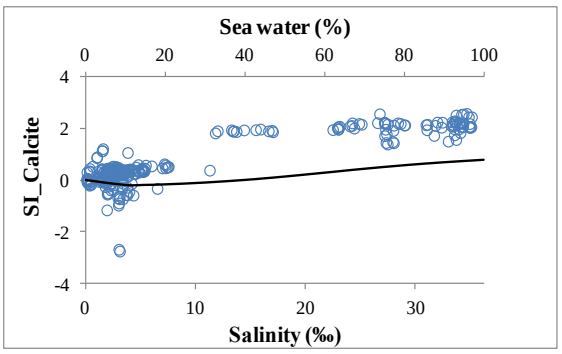

(a)

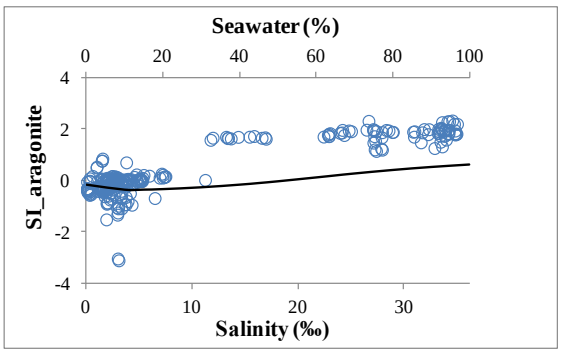

(b)

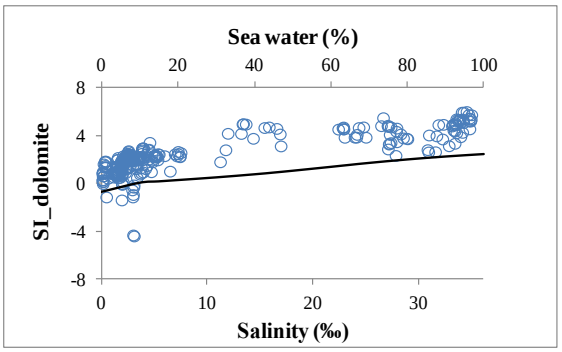

(c)

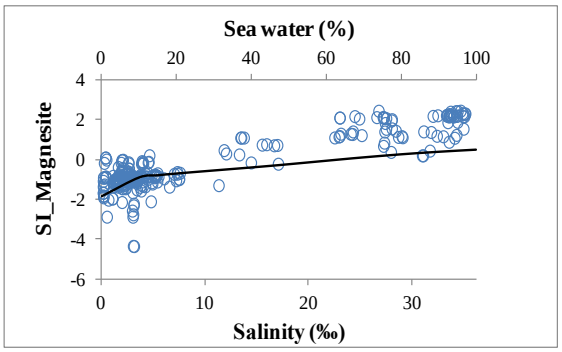

(d)

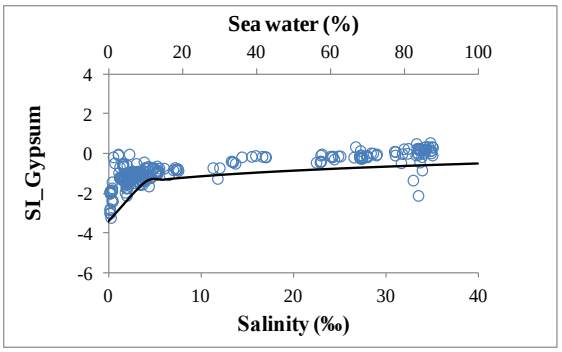

(e)

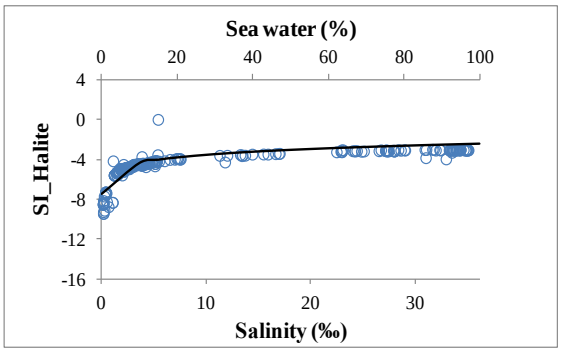

(f)

Figure 61. Various minerals saturation indexes (a) Calcite; (b) Aragonite; (c) Dolomite; (d) Magnesite; (e) Gypsum; (f) Halite, observed data (dots) and model result (lines).

The mixing model results of calcite and aragonite saturation indexes in Figure 61 show the SI < 0 for the mixture containing 10-20% of seawater. This indicates that there is dissolution of these minerals. The model results were comparable with the observed data at this point (<20% seawater). Differences between the observed data and the model predictions of saturation indexes occurred at seawater percentages greater than 20%; the model underpredicted, for those minerals were not as oversaturated as expected from observed data. An explanation is non-conservative behavior of calcite dissolution, ion-exchange, and CO_2 flux (Stoessell et al., 1989; Price et al., 2006).

The saturation state of dolomite and magnesite showed similar behavior to calcite and aragonite; big differences between observed data and the model results occurred for seawater proportion greater than 20%. However, the oversaturation of dolomite was found for all seawater percentages, while the under-saturation of magnesite is found in the mixtures containing seawater less than 20%. In reality the deposit of dolomite is kinetically favored, which also depends on the ratio of [Mg]:[Ca] and the change of P_{CO_2} (Pulido-Leboeuf, 2004). One basic condition that is required for the occurrence of dolomite deposition is that the ratio of [Mg] to [Ca] should be greater than 1(Margaritz et al., 1980), which was found for all the seawater proportion in Floridan aquifer. Nevertheless, the dolomitization is very much influenced by P_{CO_2}. Change in CO_2 flux by the respiration or the microbial metabolism affect the dolomitization. Thus the dissolution and precipitation of dolomite in Floridan aquifer may not happen thermodynamically as in Figure 16. A further investigation on dolomitization in Floridan aquifer is needed.

Gypsum saturation indexes in Figure 61 showed the same trends for both the observed data and the model results. Both results indicated the undersaturation of gypsum for all seawater proportions. Nevertheless, the saturation index of observed data was found slightly higher than that from the theoretical model. This indicated the presence of SO_4 sources other than seawater. Samborska and Halas (2010) reported that the sources of SO_4 in carbonate aquifers could be from the de-dolomitization process (equation 43) (Plummer et al., 1990) and the dissolution of pyrite (equations 44-45) (Stumm and Morgan, 1996, Banks et al., 1996).

$$1.8CaSO_4 + 0.8CaMg(CO_3)_2 = 1.6CaCO_3 + Ca^{2+} + 0.8Mg^{2+} + 1.8SO_4^{2-}$$ (Eq. 43)

$$FeS_2 + 7/2\,O_2 + H_2O = Fe^{2+} + 2SO_4^{2-} + 2H^+$$ (Eq. 44)

$$FeS_2 + 15/4\,O_2 + 7/2\,H_2O = Fe(OH)_3 + 2SO_{4-}^{2--} + 4H^+$$ (Eq. 45)

The co-existence of gypsum in carbonate rocks indicates the de-dolomitization that causes the dissolution of gypsum and dolomite and precipitation of calcite. Consequently, this process increases the concentrations of Ca, Mg and SO_4 ions in the solution, which could be a reason for the concentrations of these ions exceeding those predicted by the theoretical model. One possible source of SO_4 ion could be from the dissolution of pyrite which cannot be rejected, since there are some studies (Pichler et al., 2011) that reported the occurrence of pyrite dissolution in Floridan aquifer.

Halite saturation indexes from both observed and model results showed the under-saturation in the mixtures with all seawater proportions. However, the model gave slightly overestimated SI, especially at seawater percentages greater than 20%. This could be because of the non-conservative dissolution of carbonate rocks that lead to changes in ionic strength. Thus, it affects the dissolution of halite.

The model provided good predictions on major ion concentrations as a function of salinity with $R^2 > 0.9$ for Na, Mg, K and Cl. For Ca and SO_4 concentrations, the correlation of $R^2 > 0.8$, is obtained. It leads to the possible presence of Ca and SO_4 sources other than seawater and their minerals. The prediction of saturation indexes is comparable to observed data. Overall, the enhanced model shows good potential to be used to calculate the major ion reactions in wide ranges of ionic strength. This confirms that the enhanced model is capable and can be employed to predict the Hg reactions in water.

Process Confirmation in Transport Mode – Field Scale

This section presents the testing of enhanced PHREEQC model capability to simulate geochemical processes and coupling them to flow and transport settings. The purpose was to explore the potential of the model to assess the fate and transport of a group of heavy metals in a groundwater field site; the site is located at the Y-12 National Security Complex (NSC) in Oak Ridge, Tennessee. Historical data shows that more than 200 tons of Hg from this Y-12 atomic plant was released into the surrounding environment during operations in the 1950s (Brooks and Southworth, 2011). Studies have also shown that metals accumulated in the soil, rock, and groundwater of the site consequentially became sources of contamination to nearby rivers and creeks (e.g., East Fork Poplar Creek, Bear Creek) (AJA Technical Services, Inc. 1998). For instance, mercury (Hg), zinc (Zn), cadmium (Cd) and lead (Pb) have been found and reported on the site groundwater (Brooks and Southworth, 2011; Dong et al., 2010; Loar et al., 2011; and Stewart et al., 2009). The site is reported to have a Ca-Mg-HCO_3 groundwater type.

In this study, ion exchange and surface complexation reactions were hypothesized to be the dominant reactions of the study of metals in groundwater transport at this site. A previous study documented that ion exchange and precipitation were the major reactions that affected the change of ionic species, along with rock weathering, for this site (Toran and Saunders, 1999). The approach herein uses the enhanced PHREEQC model to couple the geochemical and transport components to verify the possible role of ion exchange and surface complexation in the groundwater transport of the selected metals by comparison to observed concentrations.

The geology and hydrology as well as the groundwater quality data at Oak Ridge Y-12 plant were obtained from five existing core holes (GW 131 to GW 135). These core holes were instrumented with multiport monitoring systems at depths of 60–300 m below land surface within Bear Creek Valley (Dreier et al., 1993). Four of the core holes (GW-132 through GW-135) are along Bear Creek Valley and Chestnut Ridge on the western end of the Y-12 plant. The fifth core hole, GW-131, is located along the geologic strike with GW-135 on Chestnut Ridge near the eastern end of Y-12 plant (Figure 62). The prevailing direction of the groundwater flow

along the valley is from the west to the east (Figure 63, from GW-135 to GW-131) (Dreier et al., 1993). The distance between GW-135 and GW-131 is 2414 ft. or 736 m.

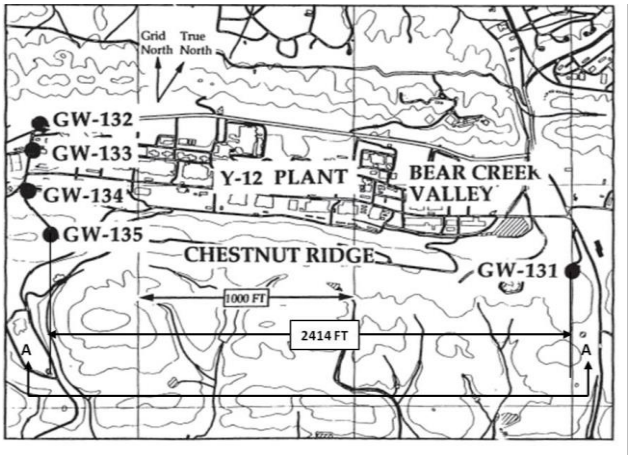

Figure 62. Study area location of the five core holes and of the section A-A between GW-131 and GW-135 at Y-12 plant, Oak Ridge, Tennessee (Dreier et al., 1993).

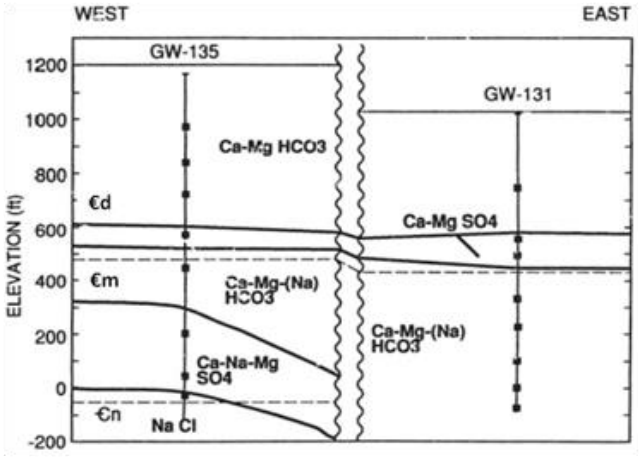

Figure 63. Profile, is strike-parallel section, shows hydrology and geology for core holes GW-131 and GW-135 where €d is Copper Ridge Dolomite, €m is Maynardville Limestone, and €n is Nolichucky Shale (obtained from Dreier et al., 1991; and Toran and Saunde, 1999).

The study focuses on the flow in the saturated zone, between the water table and intermediate intervals level (depths of about 300 ft. or 91.5 m.) (Jago et al., 1995). At these depths, the groundwater lay on the Copper Ridge Dolomite where the background water is classified as Ca-Mg HCO_3 water type (Toran and Saunders, 1995; Dreier et al., 1993). The water quality at GW-

135 is shown in Table 40 and was input to define the groundwater quality background characteristics.

Table 40. Analysis of groundwater at core hole GW-135, Oak Ridge, TN (Dreier et al., 1993)

Parameters	Units	Value
pH	-	8.0 - 8.4
Temperature	^{o}C	20.2
K	mg/L	0.61 - 0.88
Na	mg/L	0.37 – 0.58
Mg	mg/L	17 - 22
Ca	mg/L	28 - 33
Cl	mg/L	1 - 2
SO_4	mg/L	2 - 6
NO_3	mg/L	0.5 - 1
Fe	mg/L	0.1 – 0.3
Hg	mg/L	0.00086 - 0.0066
Pb	mg/L	0.004 – 0.006
Zn	mg/L	0.013 - 0.022
Cd	mg/L	0.0031- 0.059

The geochemical model PHREEQC coupled to a one-dimensional (i.e.,1-D) transport algorithm was used to assess the heavy metal contaminations fate and transport from a starting core hole (GW-135) to the destination point (GW-131) (Figures and Figure 63).

The travel distance between GW-135 and GW-131 is 736 m (or 2414 ft.). The average groundwater pore velocity was reported to be up to 0.66-1.00 m/day (Jago et al., 1995). An average velocity of 0.66 m/day and a dispersion coefficient D_L of 0.066 m^2/d were judged appropriate to be used in the transport simulations at the depths of interest (Jago et al., 1995).

Initial conditions were defined by the water quality characteristics at core hole GW-135 for major ions, heavy metals of concerns, pH and temperature. A constant-flux type-three boundary condition was used to define as the boundary condition at GW-135 in the simulations. PHREEQC then calculated the change in aqueous chemistry (dissolution-precipitation, speciation, ion exchange, and sorption) along the travel distance based on an ion-association model for two scenarios: a) ion-exchange only (with major cations) and b) ion-exchange with sorption reaction on $Fe(OH)_3$.

At this site, the exchange capacity (CEC) of the dolomite and quartz rich sediment is about 39 meq/kg (Appelo and Postma, 2005; and Vertacnik et al., 1997), while the bulk density (ρ_b) and the porosity (θ) of the used in this paper are, respectively, 1.67 g/cm^3 and 0.5 (Dreier et al., 1993). Converting CEC to a constant volume (mmol/kg to mmol/L) facilitates comparison with the quantities of elements in the pore solution and mass transfer associate with reaction and transport through the groundwater. The CEC of 39 meq/kg soil can be converted to 130 mmol/L of pore water using equation 46 (Appelo and Postma, 2005):

$$CEC\left(\frac{meq}{kg}\right) \text{x } \frac{\rho_b}{\theta}\left(\frac{g}{cm^3}\right) = CEC\left(\frac{meq}{L}\right) \qquad \text{(Eq. 46)}$$

The exchange reaction equations used in this study included Ca and Mg, which were assumed to occupy 100% of all exchanged sites. The exchange reactions for *Ca-I* and *Mg-I*, where I represents any cation with i valence state, are presented in equations 47 and 48.

$$Ca^{2+} + \frac{2}{i} I - X_i^- \leftrightarrow Ca - X_2 + \frac{2}{i} \cdot I_i^+ ; K_{Ca/I} \qquad \text{(Eq. 47)}$$

$$Mg^{2+} + \frac{2}{i} I - X_i^- \leftrightarrow Mg - X_2 + \frac{2}{i} \cdot I_i^+ ; K_{Mg/I} \qquad \text{(Eq. 48)}$$

The exchange reactions and exchange coefficients relative to Ca^{2+} and Mg^{2+} after the Gaines-Thomas convention (Bruggenwert and Kamphorst, 1979) are shown in Table 41.

Table 41. Exchange reaction equations and coefficients for Ca and Mg (Appelo and Postma, 2005; Bruggenwert and Kamphorst, 1979; and Stumm and Morgan, 1996)

Reaction	Coefficients (K)
$\mathbf{Ca^{2+} + Hg\text{-}X_2 \leftrightarrow Ca\text{-}X_2 + Hg^{2+}}$	$K_{Ca\backslash Hg} = 0.25$
$\mathbf{Ca^{2+} + Zn\text{-}X_2 \leftrightarrow Ca\text{-}X_2 + Zn^{2+}}$	$K_{Ca\backslash Zn} = 1.00$
$\mathbf{Ca^{2+} + Pb\text{-}X_2 \leftrightarrow Ca\text{-}X_2 + Pb^{2+}}$	$K_{Ca\backslash Pb} = 0.75$
$\mathbf{Ca^{2+} + Cd\text{-}X_2 \leftrightarrow Ca\text{-}X_2 + Cd^{2+}}$	$K_{Ca\backslash Cd} = 1.00$
$\mathbf{Ca^{2+} + Mg\text{-}X_2 \leftrightarrow Ca\text{-}X_2 + Mg^{2+}}$	$K_{Ca\backslash Mg} = 1.25$
$\mathbf{Mg^{2+} + Hg\text{-}X_2 \leftrightarrow Mg\text{-}X_2 + Hg^{2+}}$	$K_{Mg\backslash Hg} = 0.20$
$\mathbf{Mg^{2+} + Zn\text{-}X_2 \leftrightarrow Mg\text{-}X_2 + Zn^{2+}}$	$K_{Mg\backslash Zn} = 0.80$
$\mathbf{Mg^{2+} + Pb\text{-}X_2 \leftrightarrow Mg\text{-}X_2 + Pb^{2+}}$	$K_{Mg\backslash Pb} = 0.60$
$\mathbf{Mg^{2+} + Cd\text{-}X_2 \leftrightarrow Mg\text{-}X_2 + Cd^{2+}}$	$K_{Mg\backslash Cd} = 0.80$
$\mathbf{Mg^{2+} + Ca\text{-}X_2 \leftrightarrow Mg\text{-}X_2 + Ca^{2+}}$	$K_{Mg\backslash Ca} = 0.80$

PHREEQC offers a surface complexation model to calculate the sorption of heavy metals on a mineral, which can define the mineral (i.e., ferric oxide), the available sorption sites, and the sorption equilibrium constant (K). This study used the Linear Free Energy Relations (LFER) method to calculate the sorption reaction constant for each metal of interest (Dzombak and Morel, 1990) and used a complexation reaction on $Fe(OH)_3$ for two types of sites, a strong site type (i.e., Hfo_sOH) and a weak type site (i.e., Hfo_wOH) (Stumm and Morgan, 1996; and Dzombak and Morel, 1990). Properties of hydrous ferric oxide were used for the model

calculations. The sorption reactions and their sorption constants used in the model are presented in Table 42 (Farley et al., 1984; Stumm and Morgan, 1996; and Dzombak and Morel, 1990).

Table 42. Equations and constants of sorption reactions of ions on $Fe(OH)_3$ (Farley et al., 1984; Stumm and Morgan, 1996; and Dzombak and Morel, 1990)

Reactions	Log K_{ads}
$Hfo\_sOH + Ca^{+2} = Hfo\_sOHCa^{+2}$	4.97
$Hfo\_wOH + Ca^{+2} = Hfo\_wOCa^{+} + H^{+}$	-5.85
$Hfo\_wOH + Mg^{+2} = Hfo\_wOMg^{+} + H^{+}$	-4.6
$Hfo\_sOH + Cd^{+2} = Hfo\_sOCd^{+} + H^{+}$	0.47
$Hfo\_wOH + Cd^{+2} = Hfo\_wOCd^{+} + H^{+}$	-2.9
$Hfo\_sOH + Zn^{+2} = Hfo\_sOZn^{+} + H^{+}$	0.99
$Hfo\_wOH + Zn^{+2} = Hfo\_wOZn^{+} + H^{+}$	-1.99
$Hfo\_sOH + Pb^{+2} = Hfo\_sOPb^{+} + H^{+}$	4.65
$Hfo\_wOH + Pb^{+2} = Hfo\_wOPb^{+} + H^{+}$	0.3
$Hfo\_sOH + Hg^{+2} = Hfo\_sOHg^{+} + H^{+}$	7.98
$Hfo\_wOH + Hg^{+2} = Hfo\_wOHg^{+} + H^{+}$	5.87

The concentrations of dissolved metals along the travel distance, when the effect of cation exchange capacity on the heavy metals retention is considered are shown in Figure 64. The dissolved concentrations of Zn, Pb, and Cd are predicted to decrease sharply within the first 100 m, sorbing in trace amounts beyond 100 m, while the Hg concentration remains quite constant over most of the entire distance between core holes but showing a decreasing trend around GW-131. The pattern of transport and the differences among the metals of interest may be explained by the lower exchange coefficients of Hg to Ca and Mg ($K_{Ca\backslash Hg}$ = 0.25, and $K_{Mg\backslash Hg}$ = 0.20) than those of the other metals (i.e., Zn, Pb, and Cd) to Ca and Mg Table 41. Additional analyses also indicate that Ca and Mg occupy most of the exchanged sites in the rock matrix (~60% for Ca and ~40% for Mg), a dolomite bedrock (Toran and Saunders, 1999), where dissolution should yield

high concentrations of Ca and Mg in the groundwater (i.e., Ca-Mg-HCO_3 background water type).

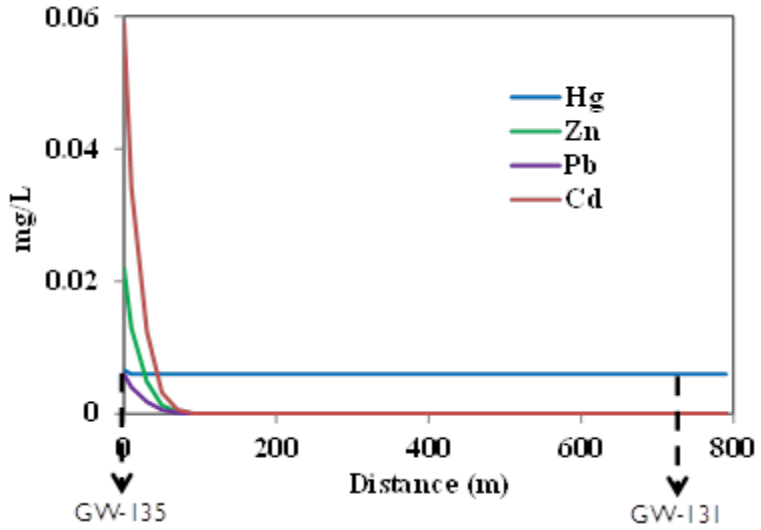

Figure 64. Effect of ion exchange on metal concentration along the distance between core holes.

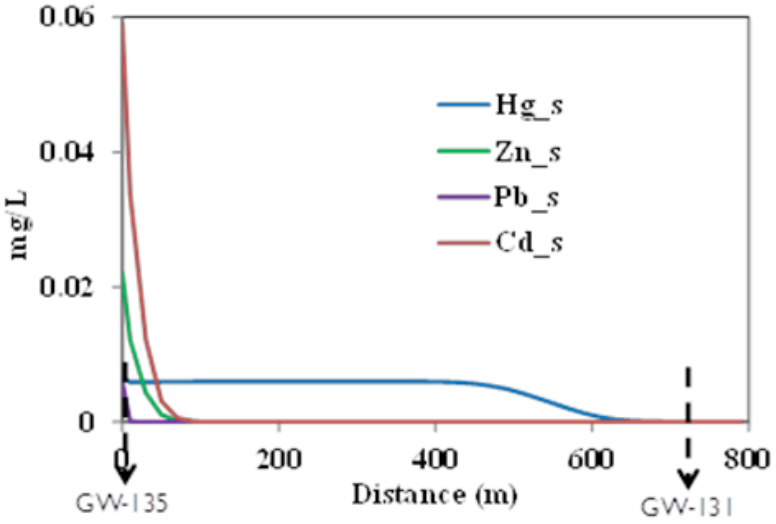

Figure 65. Effect of ion exchange and sorption on dissolved metal concentration along the distance between core holes.

Figure 65 shows the concentration of heavy metal along the travel distance when ion exchange is simulated simultaneously with the sorption on the precipitated $Fe(OH)_3$.The results show that the presence of precipitated $Fe(OH)_3$ may trigger more sorption on its surface of Hg and Pb than of Zn and Cd; Figure 66 shows, with more detail, the comparison between the possible role of ion exchange only and that of simultaneous ion exchange and sorption for Hg and Pb along the distance between the core holes.

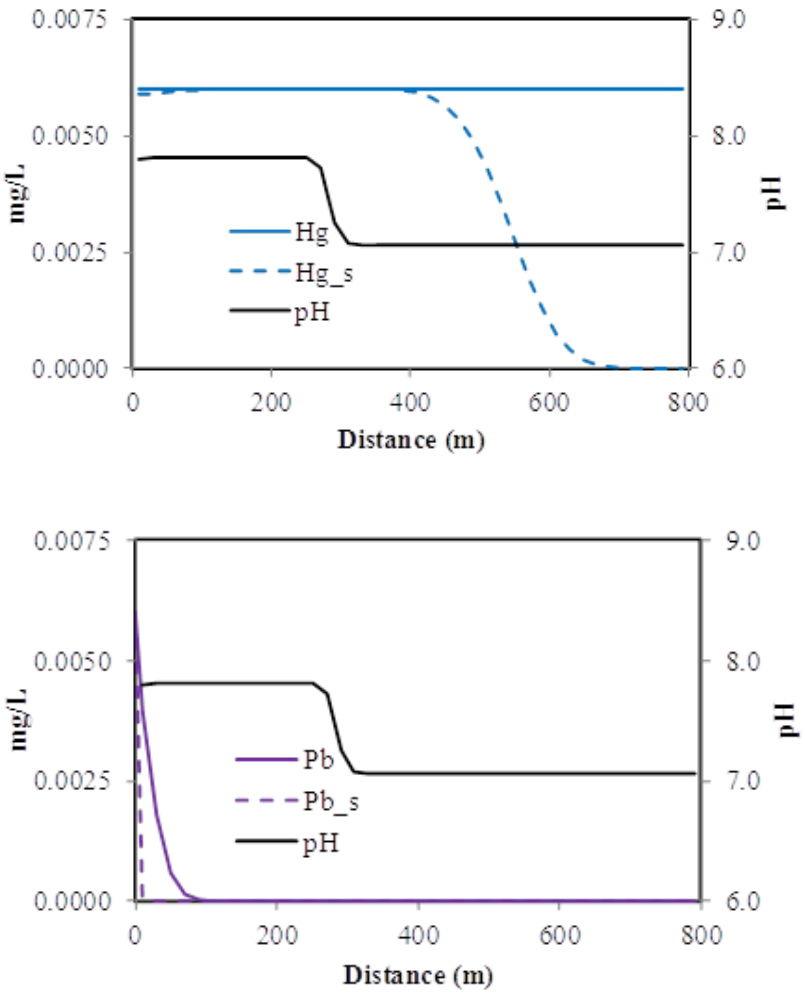

Figure 66. Dissolved metal concentrations, (a) Hg; and (b) Pb and pH profiles along the distance between core holes: only ion exchange model (dashed line) and ion exchange with sorption on $Fe(OH)_3$ (solid line).

The lower predicted concentrations of Zn and Cd may be explained by their much smaller sorption-reaction constants on $Fe(HO)_3$ (i.e., log K is 0.99 for Zn and 0.47 for Cd) than those of Hg (log K = 7.98) and Pb (log K = 4.65) (Zhu, 2002; and Morel and Hering, 1993). The latter difference is expected to specially occur when limited amounts of sorbent are available, which results in competition between metals with high sorption constants, such as those of Hg and Pb, and those with low constants such as Zn and Cd.

An attempt was made to verify the role of ion exchange and sorption, for the initial and boundary conditions of the simulations, using limited water quality data at GW-131 (Dreier et al., 1993). The estimated change in dissolved metal concentrations, with distance between GW-135 and GW-131for the case of simultaneous ion exchange and sorption, and the available water quality measurements at GW-131 are tabulated in Table 43.

The predictions of dissolved concentrations at the location of core hole GW-131 are found to be, within reported ranges, for all major ions, below limits of detection for the metals of interest, and for pH. Available measurements are however not sufficient to satisfactorily verify the hypothesized scenarios of process dominance in the field setting, but they do provide an encouraging indication of the potential of the modeling approach to simulate field conditions. Clearly, an appropriate plan for measurements of both flow and transport parameters and water quality constituents is needed to enhance the opportunity for reasonable field verification. A reasonable verification should provide a tool that can be used for that site with a higher level of confidence.

Table 43. Predicted and measured groundwater quality between core holes GW-135 and GW-131, Oak Ridge, TN (concentrations in mg/L)

Distance (m)	Observed data at GW 135	Calculated Data				Observed data at GW 131
	0[a]	50	250	500	736	736[a]
Parameters						
pH	8.0 - 8.4	7.54	7.4	7.3	7.1	7.0 - 7.9
K	0.61 - 0.88				0.82	0.73 – 9.9
Na	0.37 – 0.58	0.57	0.32	0.38	0.37	0.1 - 110
Mg	17 - 22	18.4	17.6	18.7	20	18 - 110
Ca	28 - 33	29.8	29	30.04	33	30 - 190
SO_4	2-700	183	163	142	155	4 – 170
NO_3	1-10	5.01	4.02	4.38	4.43	2-10
Hg	$8.6x10^{-4}$ - $6.6x10^{-3}$	0.0059	0.0059	0.0042	$1.3x10^{-6}$	< 0.0002[b]
Pb	0.004 – 0.006	$3.3x10^{-10}$	$5.5x10^{-19}$	$7.1x10^{-23}$	~0.00	< 0.004[b]
Zn	0.013 - 0.022	0.001	$7.1x10^{-19}$	$2.4x10^{-22}$	~0.00	< 0.002[b]
Cd	0.0031- 0.059	0.003	$2.08x10^{-15}$	$3.0x10^{-21}$	~0.00	< 0.002[b]

[a]Data obtained from Dreier et al. (1991)

[b]The limited detection values

The approach herein used couples geochemical and transport components in an attempt to verify the role of ion exchange and surface complexation in the transport of the selected metals with emphasis on Hg in the groundwater setting at Oak Ridge, TN. Overall the simulated dissolved concentrations fall within the ranges of the reported water quality measurements, supporting previous findings that concluded ion exchange to be an important fate process at this site (Toran and Saunders; 1999). The hypothesized roles prove the capability of the enhanced PHREEQC coupled-transport model is a tool that can be used to simulate the hydrogeochemical transport of Hg in groundwater setting.

FUNDAMENTAL SCENARIOS AND ANALYSIS

The objectives of this Chapter are to describe and utilize the enhanced model to assess the chemical and physical (fate and transport; advection, dispersion) processes of Hg in different scenarios. The fundamental process simulations are described herein sections 5.1 and 5.2, respectively. The model was then used to simulate the processes in transport (i.e., the coupling between chemical processes and transport) in section 5.3.

Hg chemical processes for which the thermodynamic database has herein been improved include solution and precipitation, ion-exchange, and surface complexation. These processes are described in this section.

PHREEQC assumes that the dissolved species are in thermodynamic equilibrium. The model then calculates the species using the added thermodynamic database. For example, the association reaction of the aqueous species is $Hg(OH)_2 + 2H^+ = Hg^{2+} + 2H_2O$. The log K for this reaction at 25 °C is 6.09. This can be written in the form of mass-action equation (recall equation 1):

$$10^{6.09} = \frac{[Hg^{2+}]}{[Hg(OH)_2][H^+]^2} \qquad \text{(Eq. 1)}$$

PHREEQC calculates the solubility and precipitation processes based on the added thermodynamic database. It then assumes the activity of pure phase to be one and calculates the solubility and precipitation using the mass-action equation. For example, the solubility reaction of cinnabar is $HgS = Hg^{2+} + S^{2-}$ with log K at 25 °C of -53, thus, mass-action equation is $10^{-53} = a_{Hg^{2+}} a_{S^{2-}}$. The simple schematic in Figure 67 helps to understand that at equilibrium, the model can simulate the speciation-distribution, solubility, and precipitation.

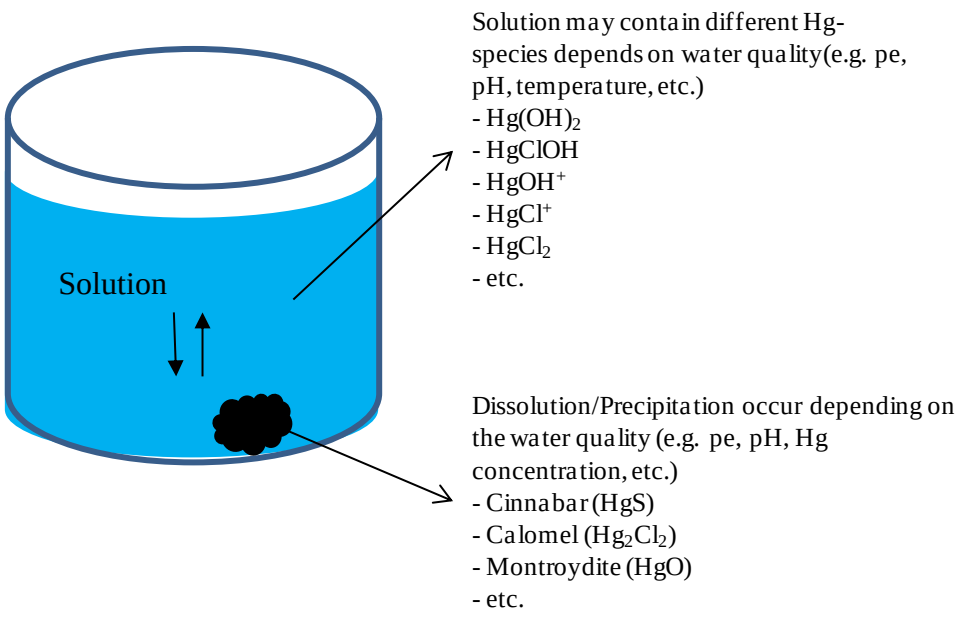

Figure 67. PHREEQC solution and precipitation process.

However, the occurrence of solubility and precipitation, as well as the presence of each dissolved species, depend on many factors (e.g., pe, pH, temperature, etc.). The sensitivity analysis of these factors with respect to the Hg processes is described in section 5.3.

Ion exchange is a replacement process of one ion by another on the exchanger. Ion exchange is one form of sorption by which one substance becomes attached to another through the exchange of ions. The other sorption mechanisms are adsorption (the process in which the ion attaches onto the surface of a solid) and absorption (the process in which the ion attaches into the solid). For the typical aqueous environment, some examples of exchangers are soil, clay and rocks (Figure 68).

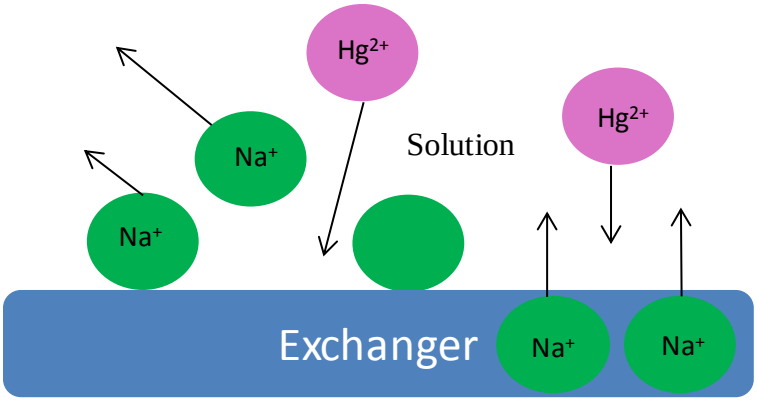

Figure 68. Ion-exchange process.

PHREEQC calculates the ion-exchange species at equilibrium using the added thermodynamic database, which is expressed in the mass-action equation. For example, the association reaction for the exchange species HgX_2 is $Hg^{2+} + 2X^- = HgX_2$ with log K of -1.39.

$$10^{-1.39} = \frac{[HgX_2]}{[Hg^{2+}][X^-]^2} \qquad \text{(Eq. 49)}$$

From the mass-action equation of HgX_2, the model calculates and solves for the amount of HgX_2.

It has been mentioned earlier in this study that surface complexation is the process whereby an ion sorbs on the surface of solid surfaces. The solids are minerals, soils, rocks, etc. Figure 69 shows the surface complexation process where the ions sorb onto the solid surface. The difference between surface complexation and ion exchange processes is that surface complexation is not a replacement of ion by another ion unlike the ion exchange process.

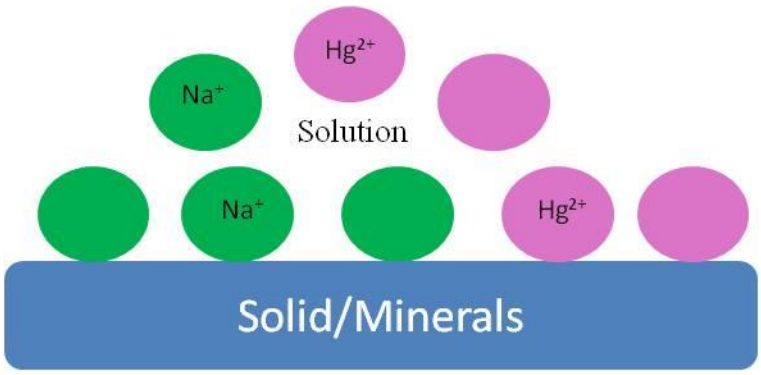

Figure 69. Surface complexation process.

PHRREQC calculates the surface complexation species at equilibrium from the mass-action equation using the added thermodynamic data. For example, the ferrihydrite surface association reaction with $Hg(OH)_2$ species is ≡Hfo_wOH + $Hg(OH)_2$ + H^+ = ≡Hfo_wOHg^+ + $2H_2O$ with log K of 12.6. The mass-action can be expressed as equation 12 (recall Eq. 12).

$$10^{12.6} = \frac{[Hfo\_wOHg^+]}{[Hfo\_wOH][Hg(OH)_2][H^+]} e^{-\frac{F\psi_S}{RT}} \qquad \text{(Eq. 12)}$$

The amount of ≡Hfo_OHg^+ species is calculated by the model using Equation 12.

The physical or transport process in PHREEQC consists of 2 main transport mechanisms:

1) Advection is a transport process in which flowing water transports the substances or the pollutants. The process depends on the 1) water flow velocity, and 2) direction of water flow.
2) Dispersion is a transport process that occurs as a result of concentration variations. Only the dispersion in the direction of flow or longitudinal dispersion is considered here. Dispersion coefficient is the sum of mechanical dispersion ($\alpha_L v$) and diffusion (D*).

PHREEQC calculates the transport of a dissolved chemical by coupling chemical and physical process calculations based on the mass conservation principle (Figure 70).

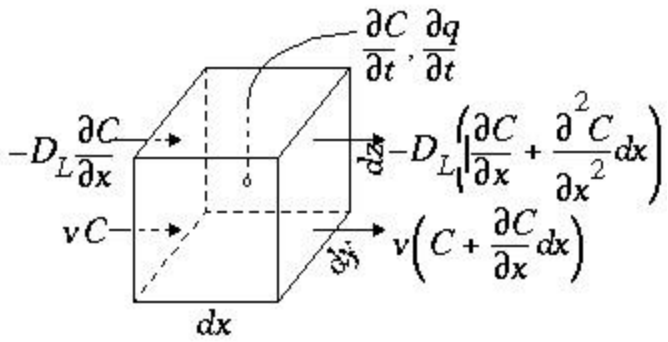

Figure 70. Mass conservation for transport process (Parkhurst and Appelo 1999).

Figure 70 graphically depicts that the mass enters the cube from the right side (x direction). As mentioned before, the mass is transported by advection and dispersion. Mass balance in the system is expressed as:

$$\frac{\partial C}{\partial t} = C_{In} - C_{out} - C_{reaction} \qquad \text{(Eq. 50)}$$

$$\frac{\partial C}{\partial t} = vC - D_L \frac{\partial C}{\partial x} + D_L\left(\frac{\partial C}{\partial x} + \frac{\partial^2 C}{\partial x^2} dx\right) - v\left(C + \frac{\partial C}{\partial x} dx\right) - \frac{\partial q}{\partial t} \qquad \text{(Eq. 51)}$$

Equation 51 can be reduced to:

$$\frac{\partial C}{\partial t} = -v\frac{\partial C}{\partial x} + D_L \frac{\partial^2 C}{\partial x^2} - \frac{\partial q}{\partial t} \qquad \text{(Eq. 52)}$$

Equation 52 is called the Advection-Reaction-Dispersion equation (previously described). Figure 71 shows the simple schematic of the transport process in the PHREEQC computational code, in which the flow is divided into cells. Each cell consists of solid particles that can interact with the

chemicals that may speciate and also can be subjected to processes such as ion-exchange and surface complexation, all together causing changes in chemical concentration.

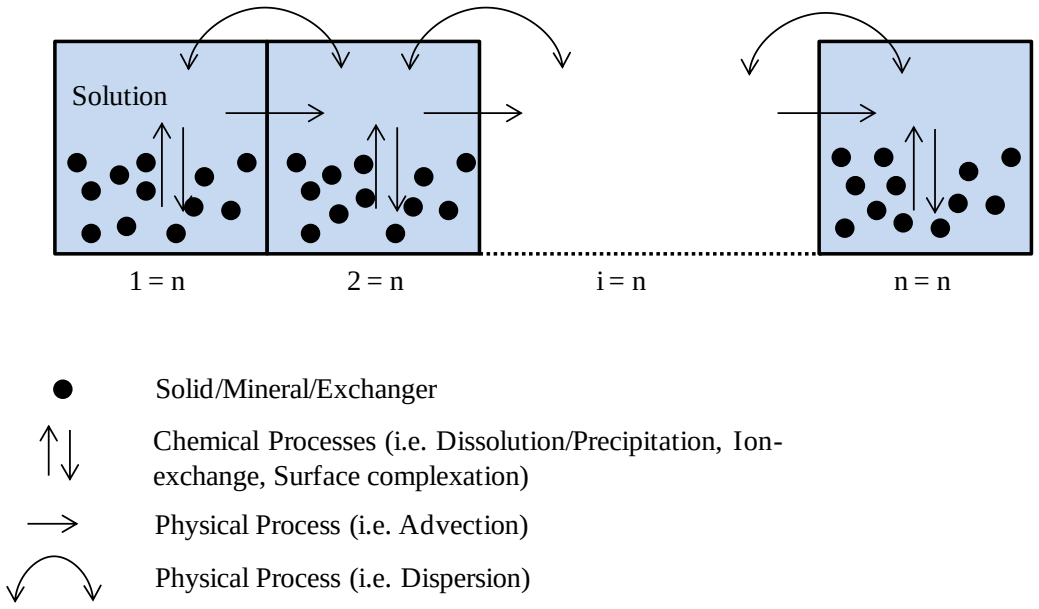

Figure 71. Coupling processes in PHREEQC to transport process calculations.

This transport process (equation 52), involving advection and dispersion, is solved using finite difference method (using elemental time step (Δt) and space (Δx), which is the distance between each cell). The chemical change for each element is the sum of all equilibrium and non-equilibrium reactions (solution and dissolution/precipitation, ion-exchange, and surface complexation) that are calculated separately from the transport computations for each time step (Δt) (Parkhurst and Appelo 1999).

In this section, the enhanced model PHREEQC coupled to transport calculations is used to assess the chemical and physical processes of Hg in different scenarios. For chemical processes, the simulations are conducted in batch mode. This mode is used to understand the fundamental Hg behavior at various water pe, pH, and temperatures, and in the presence of different exchangers

and sorbents (section 5.3.1), but in the absence of transport. The enhanced model is then further used to perform the simulation of Hg fate and transport. A sensitivity analysis of chemical (CEC and sorbents) and physical (v, D_L) parameters was conducted to study the effect of these parameters on the Hg fate and transport (section 5.3.2).

Simulations of Hg behavior at different scenarios were carried out using the water quality obtained from groundwater monitoring well 135 located in the ORR area (Table 39). The water quality data in Table 44 is used for all Hg chemical process simulations (sections 5.3.1.1 to 5.3.1.5).

Table 44. Water quality data obtained from groundwater well 135 located in ORR area (Dreier et al., 1993; Elvado Environmental LLC, 2009 and 2011)

Parameters	Value	Parameters	Value
pH	6.0 - 8.0	SO_4 (mg/L)	2 - 6
Temperature, °C	20.2	NO_3 (mg/L)	0.5 - 1
K (mg/L)	0.61 - 0.88	Fe (mg/L)	0.1 – 0.3
Na (mg/L)	0.37 – 0.58	Hg (mg/L)	0.00086 - 0.0066
Mg (mg/L)	17 - 22	Pb (mg/L)	0.004 – 0.006
Ca (mg/L)	28 - 33	Zn (mg/L)	0.013 - 0.022
Cl (mg/L)	1 – 2	Cd (mg/L)	0.0031- 0.059

The objective of this analysis is to assess the Hg-species distribution of various soluble and insoluble forms at various pe-pH values using the enhanced PHREEQC model. The pe-pH diagram shows in a comprehensive way how protons and electrons shift equilibrium and which species are present and dominant under any given condition of pe and pH.

In this study, the pe-pH diagrams of Hg-species were developed based on the redox stability of water, which are shown next in equations 53-54.

$$2H^+ + 2e = H_2(g) \qquad log\ K = 0 \qquad \text{(Eq. 53)}$$

$$O_2(g) + 4H^+ + 4e = 2H_2O \qquad log\ K = 83.1 \qquad \text{(Eq. 54)}$$

The pe-pH values associate with the partial pressure of H_2 and O_2, as shown in equations 55-56.

$$log\,p_{H_2} = 0 - 2pH - 2pe \qquad \text{(Eq. 55)}$$

$$log\,p_{O_2} = -83.1 + 4pH - 4pe \qquad \text{(Eq. 56)}$$

The above equations can be rewritten as equations 57-58, where pe is a function of pH.

$$pe = 0 - pH - \tfrac{1}{2} log\ p_{H_2} \qquad \text{(Eq. 57)}$$

$$pe = 20.78 - pH + \tfrac{1}{4} log\ p_{O_2} \qquad \text{(Eq. 58)}$$

The diagrams were produced using the enhanced database of the PHREEQC model, which allows modelers to assess the formation of Hg species; soluble and insoluble forms, at various pe-pH values. In addition to the capabilities of the existing PHREEQC model, the enhanced model is capable of estimating the pe-pH conditions that favor the sorption of Hg and the mobility of Hg. The water quality in Table 39 was selected for the Hg pe-pH diagram study. This is because the diverse presence of various chemical constituents in the water allows the possibility of the formation of several Hg-species for any given pe and pH conditions. Although the water quality used for the diagram study (Table 39) was groundwater quality data, however, the diagram study is not specific only for groundwater condition. The Hg pe-pH diagram study helps in describing the trend of Hg behavior in various aquatic environments depending on the given of pe-pH.

The simulations of Hg pe-pH diagrams were determined based on 3 different scenarios: 1) without sorbent; 2) with $Fe(OH)_3$ sorbent; and 3) Hg mobility with $Fe(OH)_3$.

Using the water chemical composition in Table 39, the pe-pH diagram of Hg species at various pe-pH values is shown in Figure 27. The diagram shows the thermodynamically stable species of Hg at different pe-pH, of which only 2 oxidation states (Hg^0 and Hg^{2+}) and one solid phase (cinnabar) are stable.

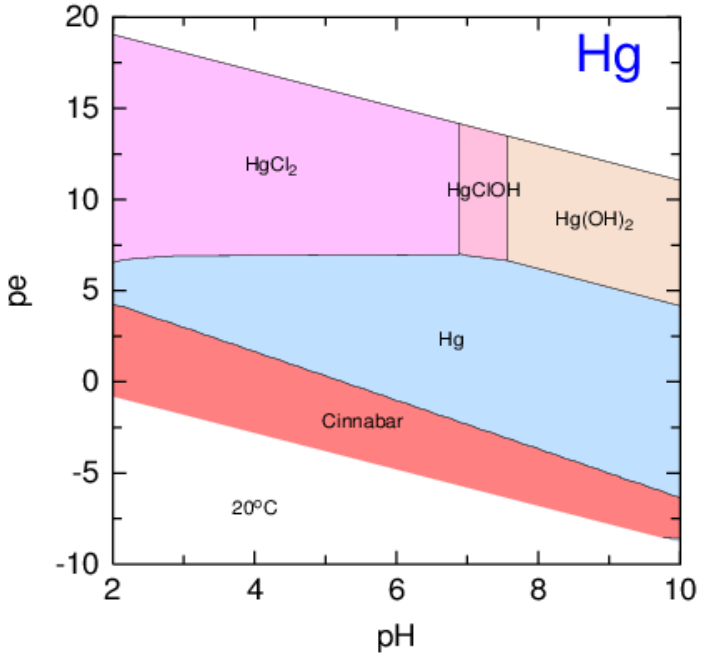

Figure 72. pe-pH diagram of Hg-species at temperature 20 °C.

In oxidation condition of water, Hg^{2+} complexes with inorganic ions: Cl ion at pH < 7, Cl-OH ion at pH ~ 7-7.5 and OH ion at pH > 7.5. The reaction between SO_4 ion and Hg is negligible in oxidizing water condition. However, in reducing water condition where S^{6+} is reduced to S^{2+}, the solid phase of HgS (cinnabar) is formed. This is because Hg has high affinity for sulfide. For such reducing water conditions, cinnabar is present at all pH of water. The result obtained from the model is consistent with various studies (Little, 2006; Chattopadhyay and Ickes, 2001; Davis et al., 1997; Cox et al. 1996; Sigels, 1997) that had developed the pe-pH diagrams of Hg using both geochemical models and analytical calculation. The results from some previous studies on Hg pe-pH diagram are summarized here (Figures 28-31). The result obtained using the PRHEEQC model is consistent with those from previous studies. It was confirmed that only two

oxidation states (Hg^0 and Hg^{2+}) and one solid phase (HgS or cinnabar) are thermodynamically stable in the pe-pH ranges considered here (pe = -10 to 20, pH = 2 to 10).

Sigel, A. and Sigel, H., 1997, Little, 2006 and Davis et al., 1997 developed pe-pH diagram of Hg using water conditions that consist of Cl, SO_4 and Hg. According to their studies, $HgCl_2$ is the dominant species at pH<7 while $Hg(OH)_2$ is present at pH>7 (Figures 28-30). Cox et al., 1996 developed the pe-pH diagram (Figure 31) using the water condition that consists of I, SO_4 and Hg. In this case, HgI_2 and Hg_2I_2 were observed under oxidizing conditions. The complexation of $HgSO_4$ was not obtained in oxidizing water. This can be attributed to its low thermodynamic constant (log K = 2.6 for $HgSO_4$, 14.2 for $HgCl_2$ and 24.8 for HgI_2 (Powell, et al., 2005; Martell and Smith 2001)). However, in reducing condition, Hg readily complexed with S (as sulfide) resulting in HgS (cinnabar), which is the dominant species in such water condition. This species was observed in all the previous studies.

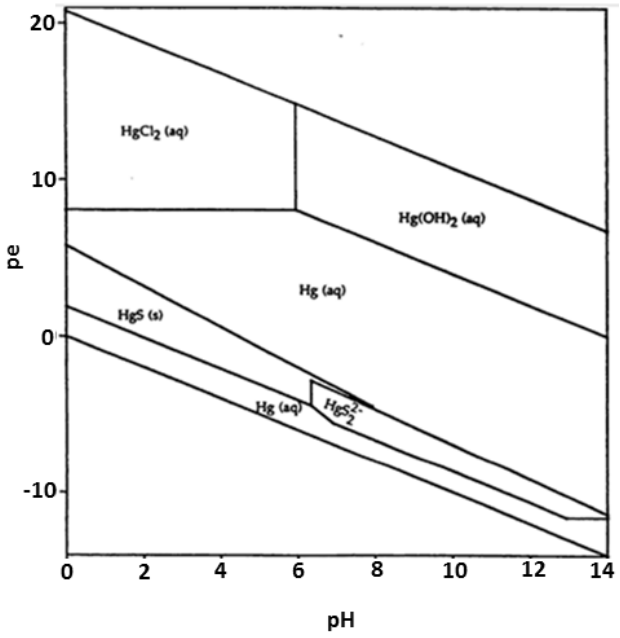

Figure 73. pe-pH diagram for mercury in a typical soil solution (total Hg of $5x10^{-11}$ M, Cl of $2 x 10^{-4}$ M and S of $6 x 10^{-4}$M) (Sigel, A. and Sigel, H., 1997).

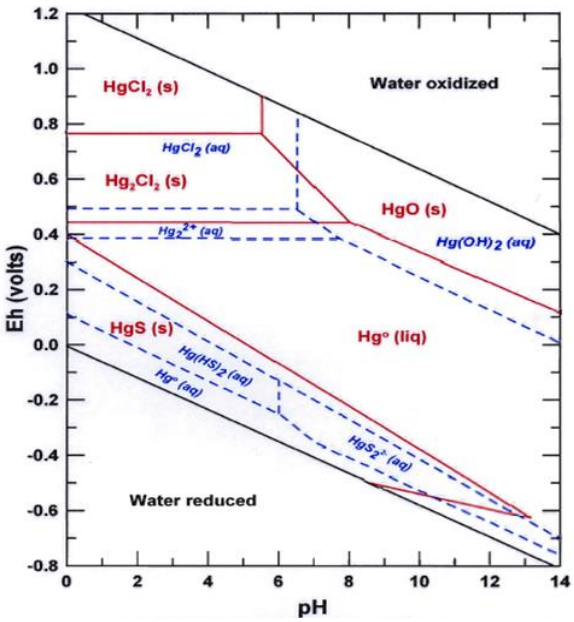

Figure 74. Eh-pH diagram for Hg at 25 °C and 1 atmosphere pressure. The dashed lines represent the stability field of aqueous species, and solid lines are for solid phases. System includes water containing 36 mg/L Cl, total S 96 mg/L as SO_4^{2-} (Little, M.E., 2006). On axis y, pe ranges from -13.5 to 20 (Eh to pe conversion is calculated using Eh-pe relationship: Eh (mV) = 59.2pe, obtained from Stumm and Morgan, 1996).

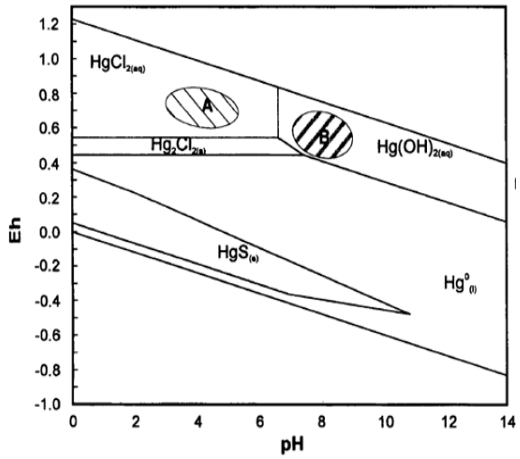

Figure 75 Davis et al., 1997 studied the ability of mercury to cross tissue membranes of the mouth, esophagus, stomach, and the small and large intestines. Figure shows Gastrointestinal tract pH-Eh conditions superimposed on mercury system, A = Stomach, and B = Small Intestinal conditions. Activity of Cl = 10^{-3} M, S = 10^{-5} M, Hg = 10^{-5} M. On axis y, pe ranges from -16 to 20 (Eh-pe conversion is calculated using Eh-pe relationship: Eh (mV) = 59.2pe, obtained from Stumm and Morgan, 1996)

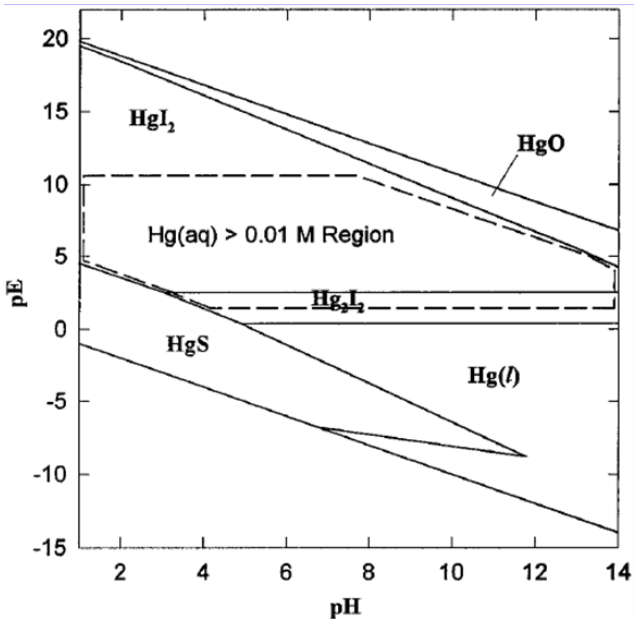

Figure 76. Stability diagram for Hg in the presence of 0.1 M total I and 0.001 M of S (Cox et al., 1996).

The result obtained from PHREEQC model (Figure 27) are comparable with the results obtained from previous studies (Figures 28-31). The difference is that the Hg database of PHEEQC model was enhanced by adding the thermodynamic data of HgClOH species. Thus in Figure 27, HgClOH is dominant approximately in the pH range of 7-7.5, in oxidizing water condition. It is to be noted here that the range of x and y axes in Figure 27 is a subset of the corresponding axes displayed in Figures 28-31. This made the comparison between the figures possible.

In this simulation, the enhanced model was used to assess the pe-pH values that favor the surface complexation between Hg and $Fe(OH)_3$ sorbent. It was assumed that the Fe concentration in solution was 20 mg/L (or log Fe_T = -3.4 mole). The water quality data employed in this simulation is shown in Table 44. The $Fe(OH)_3$ surface properties and the surface sorption constants for Hg of Tables 10 and 11 were used in all model calculations. The precipitation of $Fe(OH)_3$ and the Hg sorption on the precipitated $Fe(OH)_3$ were simulated for different pe-pH conditions. The results are shown in Figure 77.

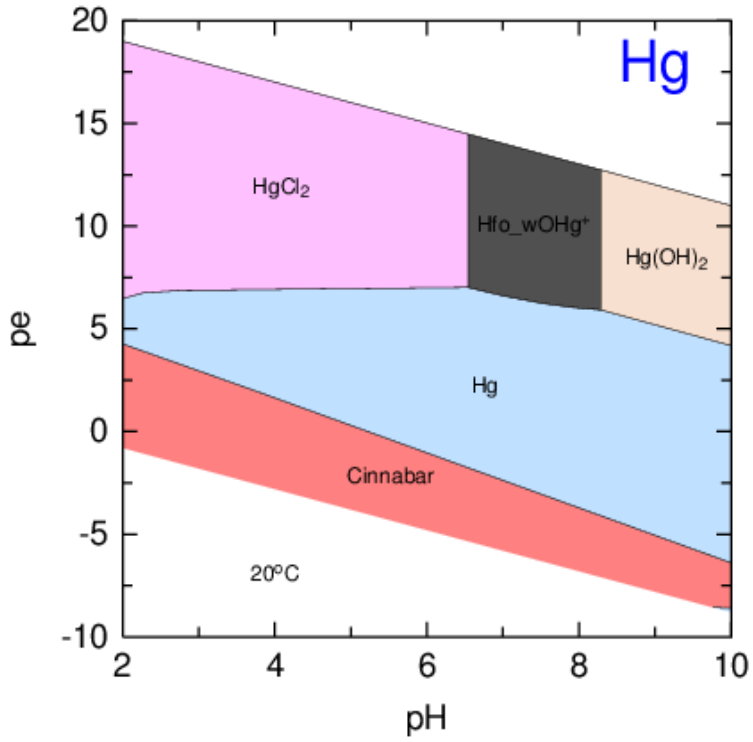

Figure 77. pe-pH diagram of Hg-species with Fe = 20 mg/L and at temperature 20 °C.

Figure 77 shows that, in oxidizing water condition, the precipitation of $Fe(OH)_3$ mineral occurred at pH 7-8. Hg simultaneously sorbed onto precipitated $Fe(OH)_3$ surface by forming surface complexes at these pH ranges. It can also be observed that Hg sorbed on the weak sorption sites of $Fe(OH)_3$ (Hfo_wOHg^+). This is due to the abundance of $Fe(OH)_3$ weak sorption sites (weak sites = 0.2 mol/mol Fe, strong sites = 0.005 mol/mol Fe) (Dzombak and Morel, 1990). It can be concluded that, at pH 7-8, $Fe(OH)_3$ dominates Cl^-OH ligand for Hg complexation.

Using the water quality conditions in scenario 2, the Hg phases (dissolved and solid phases) in Figure 77 also present the possibility of Hg to be mobilized in the water. In order to better describe the potential for mobilization, Figure 32 is redrawn into a Hg mobilization diagram that is shown in Figure 78.

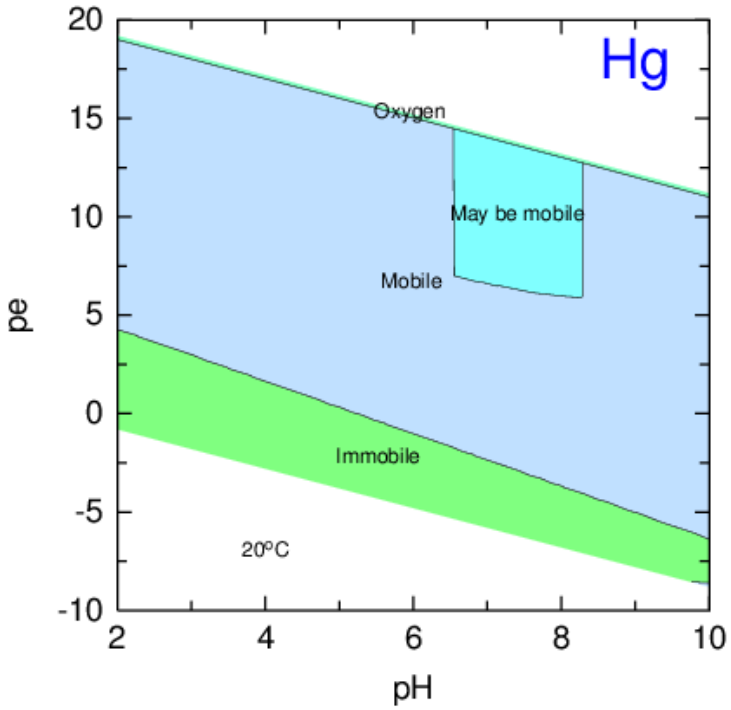

Figure 78. pe-pH diagram of Hg mobilization with Fe = 20 mg/L, temperature 20 °C.

The "mobile" section in the figure suggests that the dissolved Hg will be transported in the water while "immobile" indicates that cinnabar (i.e., solid phase) is immobilized. Of course, if the precipitated $Fe(OH)_3$ is present as fine particles then the sorbed Hg may be transported with water. Otherwise, it may settle down. Similarly, a "may be mobile" section is also depicted for pe-pH ranges, where Hg sorption occurs.

A sensitivity analysis was conducted using the water quality data in Table 44. The temperature was varied from 5 – 35 ℃ and water pH within 2 – 10. The results of the simulations analysis are shown in Figure 34.

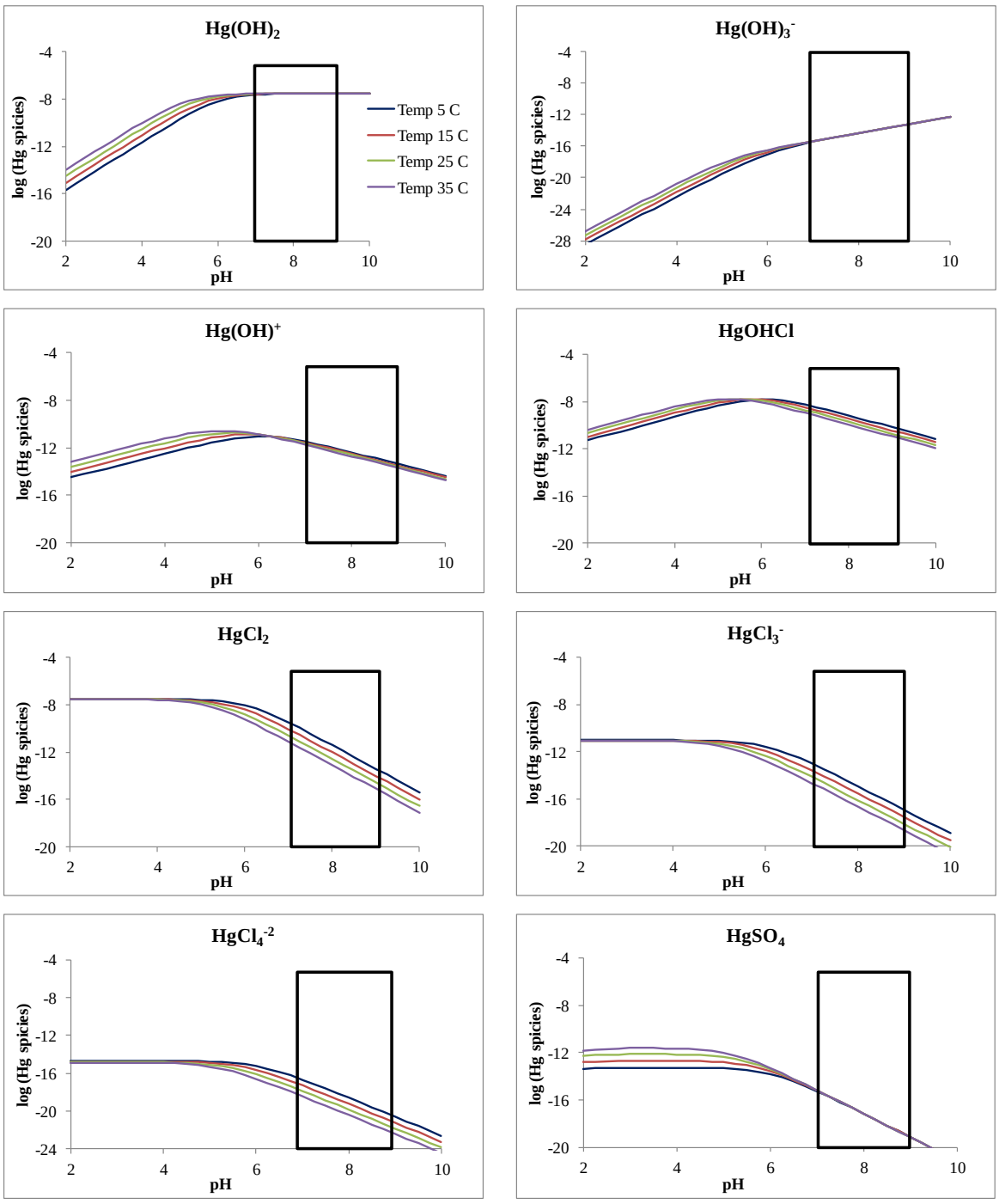

Figure 79. Hg species sensitivity to temperature (5-35 °C) and pH (2-10), black box shows groundwater pH range.

It can be observed in Figure 34 that the formation of Hg-OH species increases with increase in water temperature, while the temperature does not favor the formation of Hg-Cl species. Temperature favors the formation of $HgSO_4$ at pH 2-6. The effect of temperature is negligible for pH > 6. Increase in water pH also increases the formation of $Hg(OH)_2$ and $Hg(OH)_3^-$.However for $Hg(OH)^+$ and HgOHCl, the concentrations increase with water pH between 2-7; for pH > 7, their concentrations were observed to decline. Low water pH (pH 2-6) does not appear to have any influence on Hg-Cl concentrations, but , Hg-Cl

The sensitivity analysis using the water quality data in Table 44 was conducted for a range of water temperature (5-35 °C) and pH (2-10).

Figure 80 shows the effect of water temperature and pH on the SI of dominant minerals for the water condition in Table 44. From the figure, it can be seen that the SI of Ferrihydrite, Goethite, Magnesioferrite, Hematite, K-Jarosite, and Na-Jarosite increase with water temperature, while temperature does not affect the formation of $Fe(OH)_{2.7}Cl_3$ and Lepidocrocite. Increase in water pH favors the formation of all the above minerals, except for K-Jarosite and Na-Jarosite, whose SIs decrease at pH greater than 8. This analysis also indicates that at pH 7-9.2; temperature 25 °C, water is supersaturated with Ferrihydrite, Goethite, Magnesioferrite, Hematite, K-Jarosite, Na-Jarosite, $Fe(OH)_{2.7}Cl_3$, and Lepidocrocite.

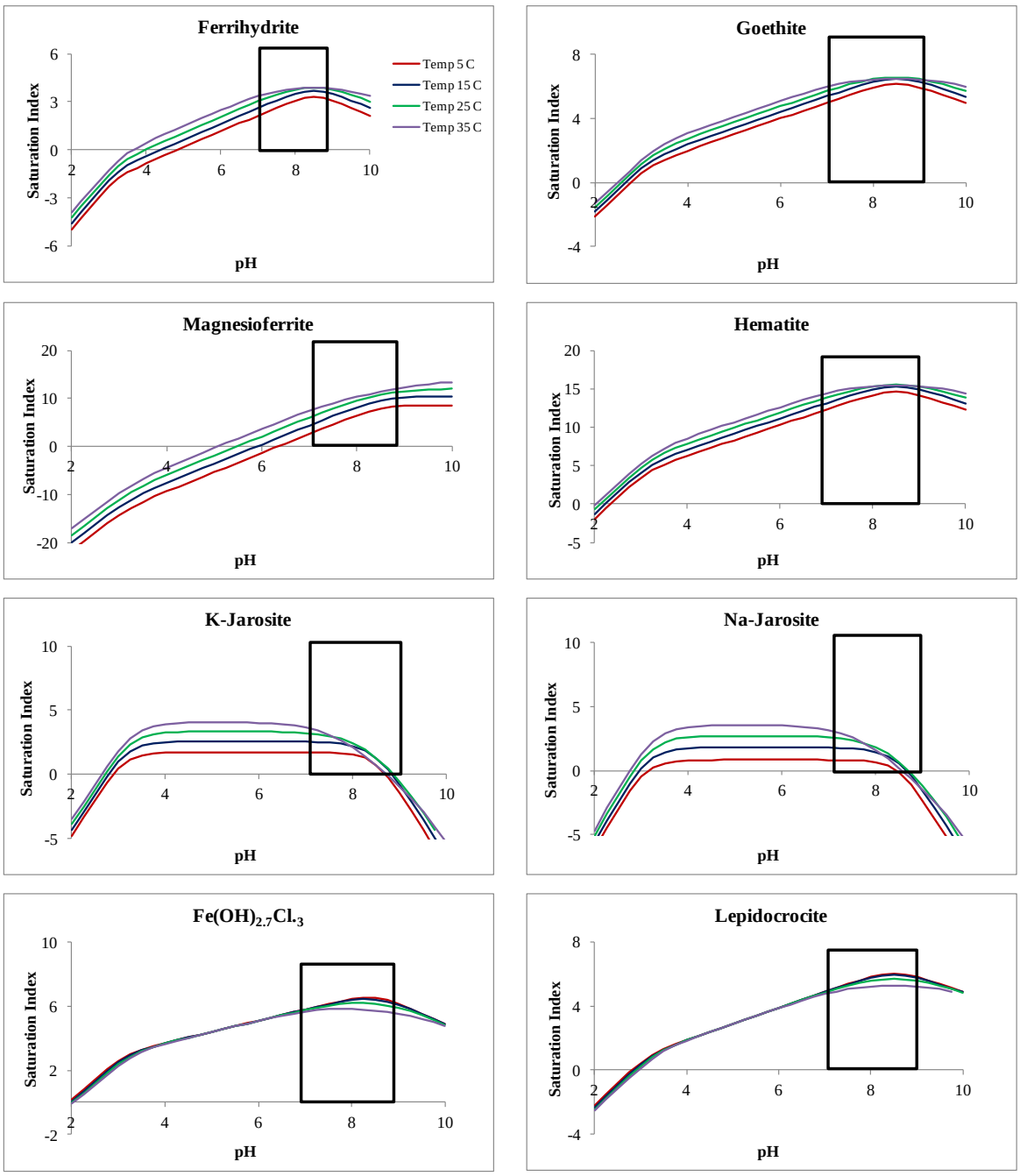

Figure 80. Sensitivity of the SI of minerals to water temperature and pH at oxidation water condition.

The effect of exchangers on Hg-species concentrations was investigated at a water temperature of 25 °C and pH 2-10 (Figure 36).

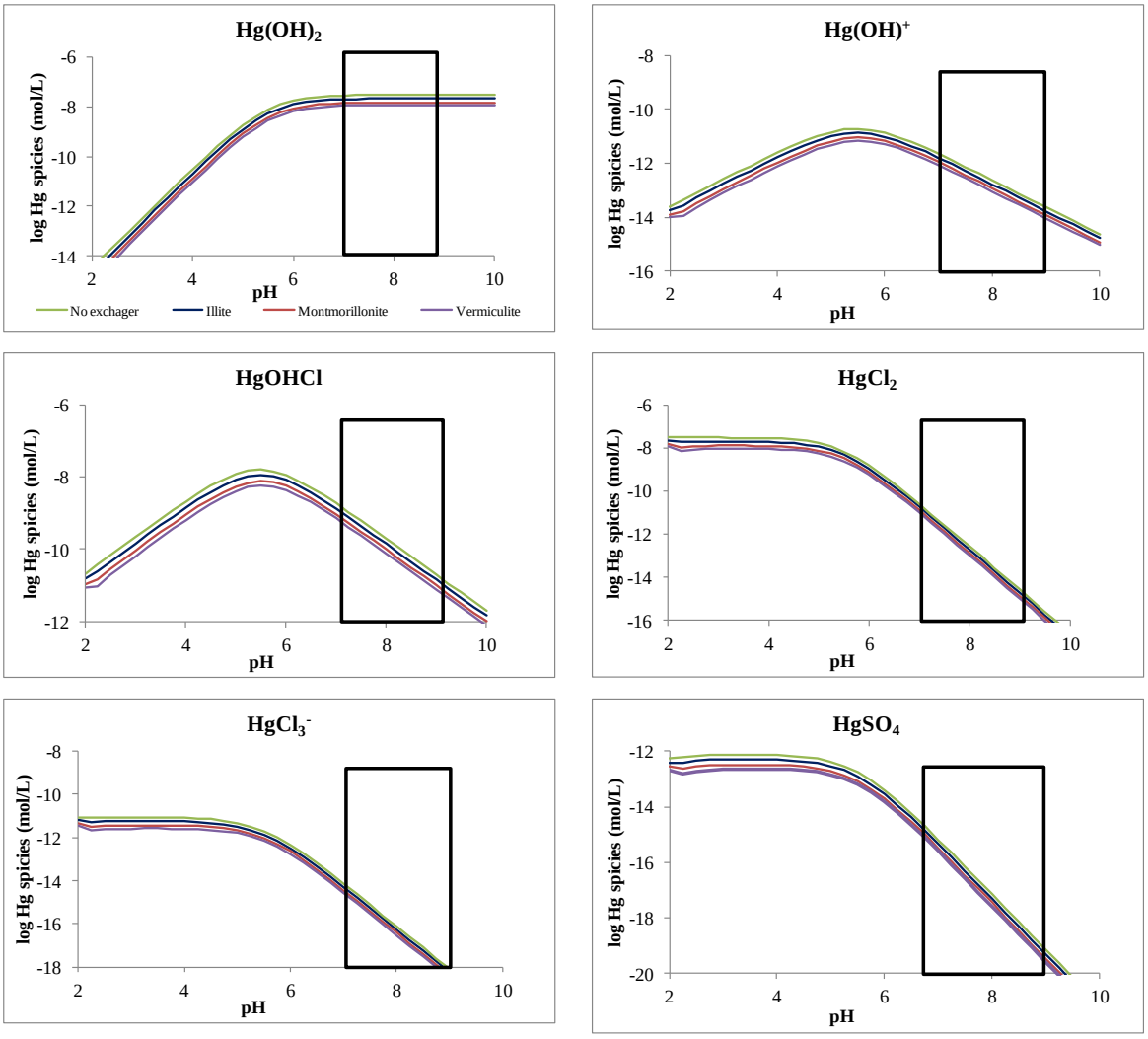

Figure 81. Sensitivity analysis of Hg-species concentration with respect to different exchangers (the effect of ion exchange); 1 kg/L of exchangers, temperature 25 °C, oxidation condition.

It should be noted that only the effect of ion exchange (no surface complexation) is considered here. The ion exchange simulations were conducted using 1 kg of exchangers with different CEC: Illite (CEC 6.5 mol/L), Montmorillonite (CEC 15 mol/L), Vermiculite (CEC 26 mol/L). Figure 36 shows that the exchange of Hg increases with CEC in the following order; Illite < Montmorillonite < Vermiculite.

It can also be observed in Figure 36 that the exchange reactions of $Hg(HO)_2$ and $Hg(OH)^+$ species occur at high pH. However, high pH does not favor the exchange reaction of $HgCl_2$, $HgCl_3^-$, and $HgSO_4$ species. Low pH favors formation of $HgCl_2$, $HgCl_3^-$, and $HgSO_4$, thus, the better exchange reaction of these species are obtained.

The effect of sorbents on Hg-species concentration was carried out at water temperature of 25 ℃, pH 2-10. It should be noted that only the effect of surface complexation is considered here (no ion exchange). The simulations were conducted using 1 g/L of $Fe(OH)_3$, Gibbsite, and Kaolinite.

It can be observed in Figure 82 that at pH 2-4 surface complexation does not occur. This is because at low pH the surface complexation of H^+ is dominant at high values log K of 7.29, 4.7, and 3.7 for $Fe(OH)_3$, Gibbsite and Kaolinite, respectively. These log K values are very high compared to those for surface complexation of $HgCl_2$, which is the dominant species at low pH. Therefore, it could be said that, at low pH, there is no available surface for Hg complexation. $Fe(OH)_3$ shows high surface complexation with all Hg-species at pH 4.5-8.5 compared to other sorbents. This is because of the high surface complexation constant (log K). However, the complexation cannot take place at pH > 8.5. This is due to the Point of Zero Charge (PZC) of $Fe(OH)_3$, which ranges between pH 8.5 – 9.3. Therefore, the surface complexation does not occur at this pH range. With Kaolinite and Gibbsite, the Hg surface complexation is obtained at pH > 5.

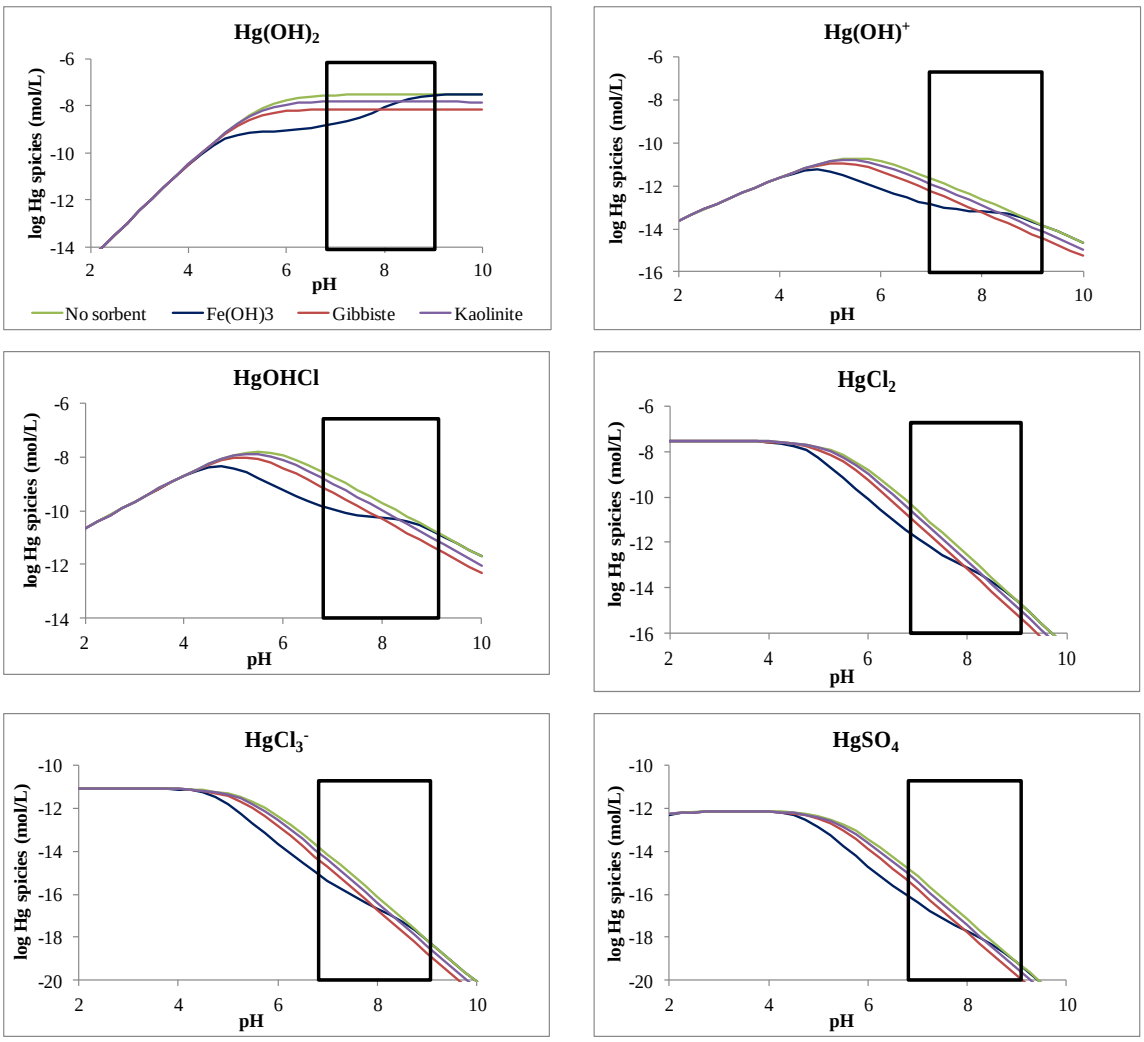

Figure 82. Sensitivity analysis of Hg-species concentration with respect to different sorbents (the effect of surface complexation) ; 1 g/L of sorbents, temperature 25 °C, oxidation condition.

It can also be seen that $Hg(OH)_2$, $Hg(OH)^+$ and HgClOH can complex with all sorbents better than $HgCl_2$, $HgCl_3^-$ and $HgSO_4$ species at pH 4.5-8.5. High formation of $Hg(OH)_2$, Hg(OH), and HgClOH species occurs at this pH range, while the formation of $HgCl_2$, $HgCl_3^-$ and $HgSO_4$ species decreases. Increase in $Hg(OH)_2$, $Hg(OH)^+$, and HgClOH formation makes surface complexation reactions possible, which results in a higher surface complexation of these species. The surface complexation reaction rate of Hg are in the following order: Kaolinite < Gibbsite < $Fe(OH)_3$. This result is consistent with previous studies (Sarkar et al., 1999 and 2000; Kim et al., 2004; Weerasooriya et al., 2007).

This section describes the utilization of the enhanced model to predict the fate and transport of Hg. Different scenarios were conducted to mimic the typical transport condition in aqueous environments. For all scenario simulations, it was assumed that the background water in the flow reach, with a length of 100 m, is the Ca-Mg-HCO_3 type, which is a typical background water type that can be found at ORR and South Florida areas. At the beginning of the flow reach, the groundwater (GW-135) consists of all elements, including Hg, as shown in Table 45, which is the water quality data used in section 5.3.1. Different scenarios were considered to study the effect of chemical processes (i.e. exchangers, sorbents) and physical processes (i.e., v, D_L) on Hg fate and transport.

Table 45. Water quality data used for Hg fate and transport simulations (Dreier et al., 1993; Elvado Environmental LLC, 2009 and 2011).

Parameters	Background water	GW-135
pH	8.5	6.0
Temperature, °C	20	20.2
K (mg/L)	-	0.88
Na (mg/L)	-	0.58
Mg (mg/L)	24	22
Ca (mg/L)	40	33
CO_3 (mg/L)	60	-
Cl (mg/L)	-	2
SO_4 (mg/L)	-	6
NO_3 (mg/L)	-	1
Fe (mg/L)	-	0.3
Hg (mg/L)	-	0.0066
Pb (mg/L)	-	0.006
Zn (mg/L)	-	0.022
Cd (mg/L)	-	0.059

The Hg fate and transport in a typical groundwater environment were investigated for 3 different scenarios: 1) without exchangers and sorbents; 2) with exchangers; and 3) with sorbents.

Figure 83 shows the simple schematic of this transport scenario, where the flow reach of 100 m long is divided into 10 cells for the coupled PHREEQC model's calculation. The water quality data in Table 45 and flow parameters in were used in the simulations.

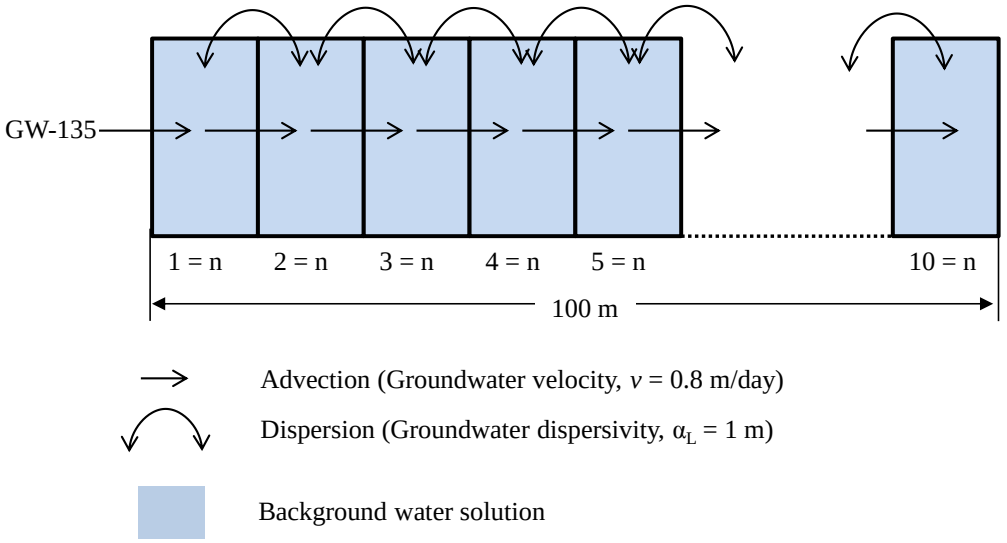

Figure 83. Model of Hg transport for a typical groundwater flow condition.

The GW-135 flows through the reach with Ca-Mg-CO_3 water type, with no interactions between Hg and the solid (exchanger/sorbent). PHREEQC calculated the Hg-species profile based on inputted water quality data and flow parameters (Figure 84).

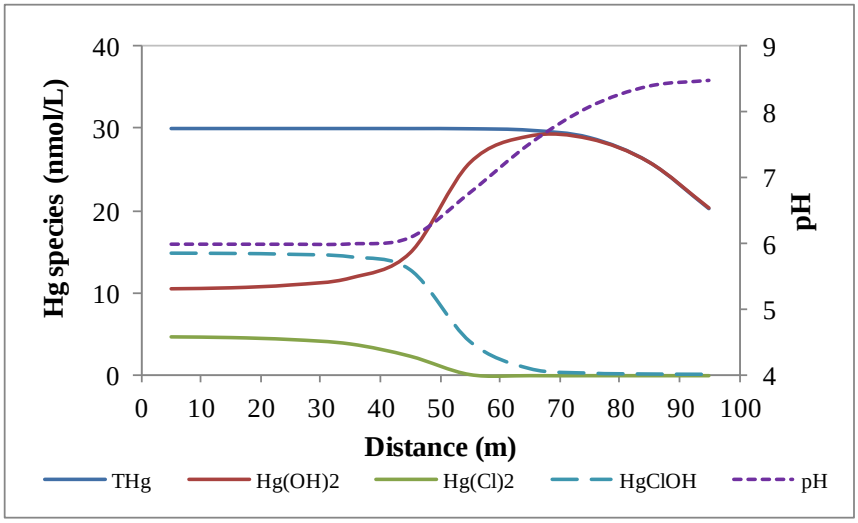

Figure 84. Hg-species flow profile in typical groundwater flow condition.

It can be seen in Figure 84 that the total Hg (THg) shows a conservative behavior and indicates the effect of dispersion at around the 70 m of distance from the start. The pH profile shows an increase at 50 m. This is due to the effect of flow parameters on the mixing of 2 solutions. At pH lower than 6.3, HgClOH is dominant with 50% of THg, while $Hg(OH)_2$ and $HgCl_2$ are 35% and 15% respectively. The sharp increase of pH at 50 m (from 6 to 8.4) affects the distribution of Hg-species. Thus, $Hg(OH)_2$ increases and reaches the maximum ($Hg(OH)_2$ = THg) at 70 m, while $HgCl_2$ and HgClOH decrease and disappear at 55 m and 70 m respectively. Using the typical groundwater flow condition, the travel time for the distance of 100 m is 125 days.

In this scenario, the water quality and flow parameters are kept as those in scenario 1; the water quality and flow parameters in Table 45 and 43 were used in the simulations. However, in this scenario, the exchangers (Illite, Montmorillonite and Vermiculite) were individually added into cells 4 and 5 of the flow reach (Figure 85). This was to examine the effect of each exchanger with the role of ion exchange on Hg fate and transport in a typical groundwater flow environment. Four simulations were made 1) with Illite, CEC of 6.5 mol/L, 2) with Montmorillonite, CEC of 15 mol/L, 3) with Vermiculite, CEC of 26 mol/L, 4) with Illite+Montmorillonite+Vermiculte, CEC of 47.5 mol/L.

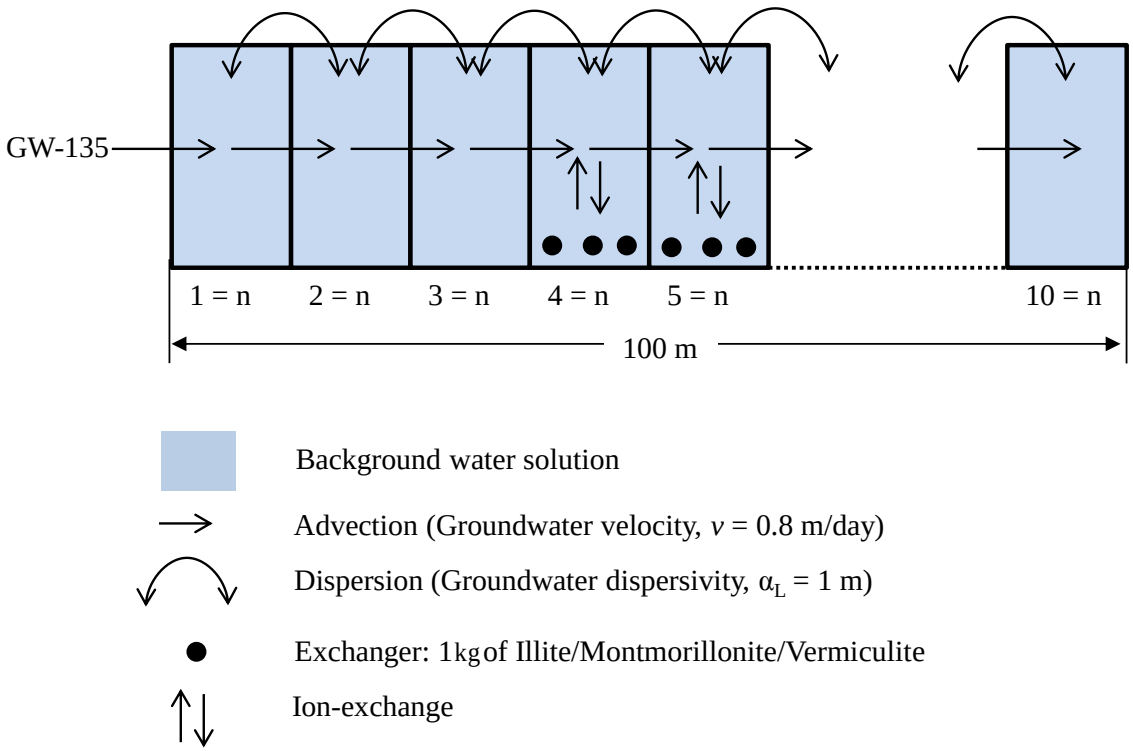

Figure 85. Model of Hg transport for a typical groundwater flow condition. Simulations were performed for each individual exchanger (Illite, Montmorillonite and Vermiculite).

Figure 86 (a) shows the comparison of dissolved THg concentration profiles, from which, it can be seen that dissolved THg concentration in cells 4 and 5 decrease with increase in CEC. In other words, the Hg sorption increases with CEC. Therefore, in this study, the exchange capacities (or sorption capacity) of the exchangers are in order of Vermiculite > Montmorillonite > Illite. The dissolved Hg-species profiles with Illite, Montmorillonite, and Vermiculite are shown in Figures 41 (b), (c), (d), respectively.

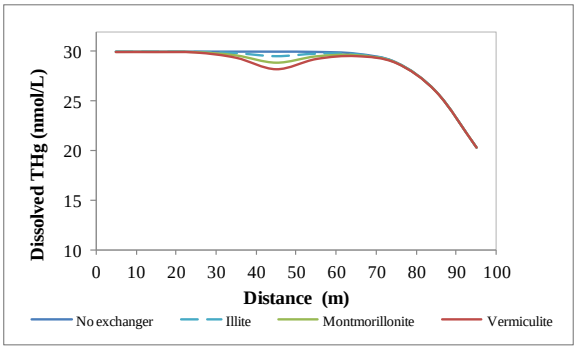

(a) THg with different exchangers

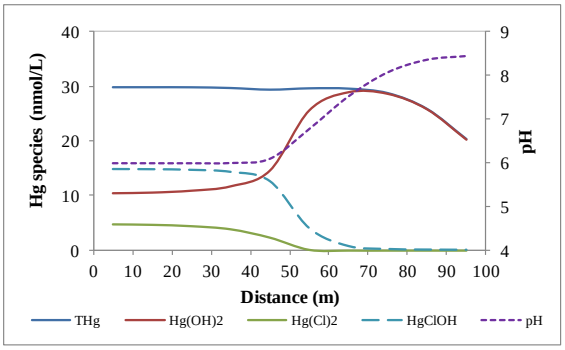

(b) Hg-species with Illite

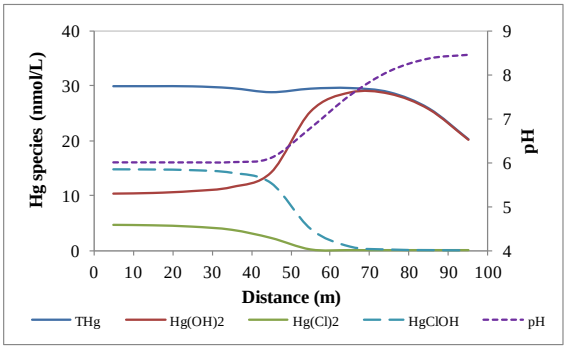

(c) Hg-species with 1 Montmorillonite exchanger

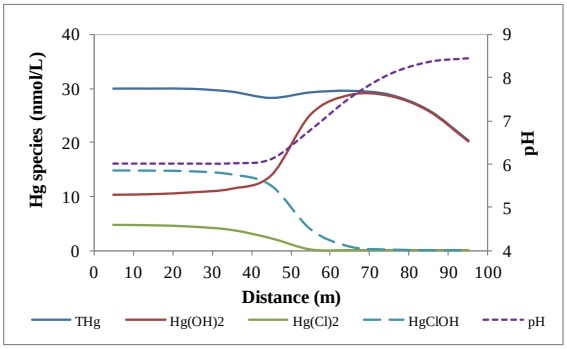

(d) Hg-species with Vermiculite exchanger

Figure 86. The effect of ion exchange on Hg-species flow profiles for different exchangers (Illite, Montmorillonite and Vermiculite). The exchangers were individually applied to cells 4 and 5 (40 and 50 m of flow distance).

The Hg profiles do not show significant change with the exchangers. This can be attributed to the low exchange constant ($Hg^{2+} + 2X^- = HgX_2$, log K = -1.39). $Hg(OH)_2$ is the main component that is sorbed by the exchangers. Water pH is not affected by the exchangers.

The water quality and flow parameters in this scenario were the same as those employed in scenarios 1 and 2. However, the different sorbents were individually added to cells 4 and 5 for

this scenario. The goal was to determine the effect surface complexation on the Hg fate and transport. The sorbents that were chosen for this study ($Fe(OH)_3$, Gibbsite, and Kaolinite) are typically found in groundwater bedrock and streambed sediment. The schematic of the PHREEQC transport model for this scenario is shown in Figure 87.

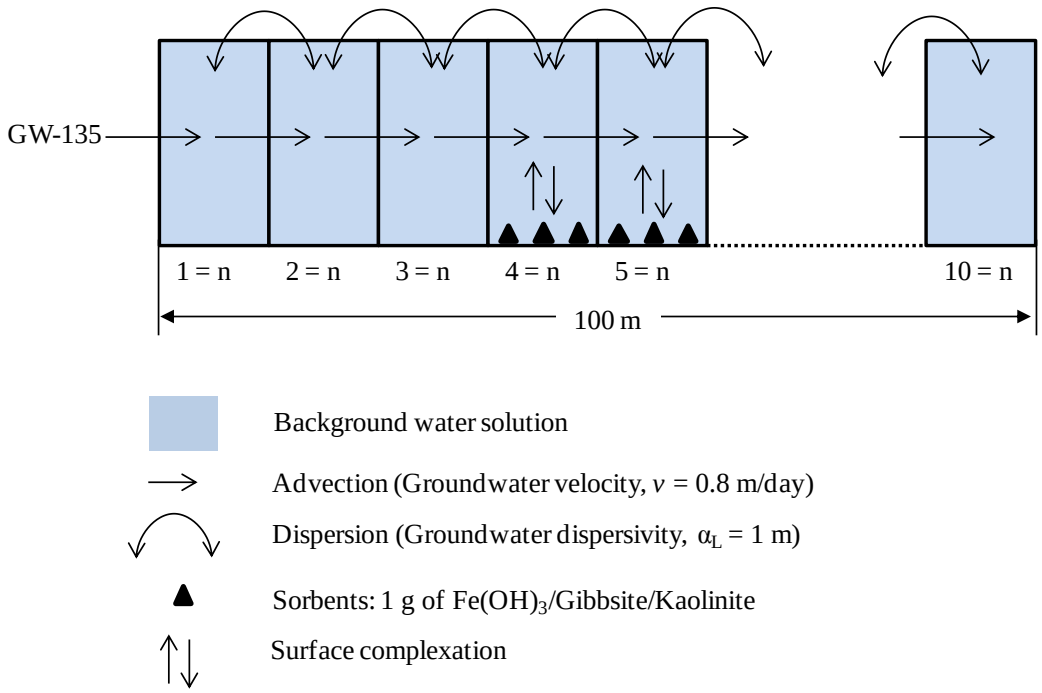

Figure 87. Model of Hg transport for a typical groundwater flow condition. Simulations were performed for each individual sorbents ($Fe(OH)_3$, Gibbsite and Kaolinite).

Figure 43 (a) shows the THg profile as a function of flow distance. With $Fe(OH)_3$ sorbent, THg shows the sharp decrease in its concentration at 40 m, where the surface complexation between Hg and $Fe(OH)_3$ occurs. The surface complexation between Hg and $Fe(OH)_3$ is so strong that most of Hg was sorbed and became negligible after 40 m. Adding more than one type of sorbents, which is more representative of typical conditions in aqueous environments, increases the sorption capacity. However, since $Fe(OH)_3$ has strong Hg sorption capability, the surface complexation between Hg and a combination of Kaolinite, Gibbsite, $Fe(OH)_3$ sorbents, is mainly influenced by the $Fe(OH)_3$.

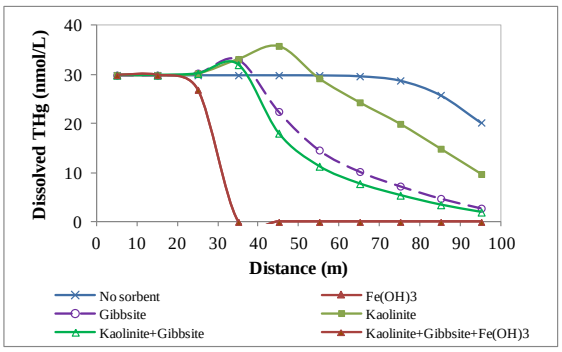

(a) THg profile with different sorbents

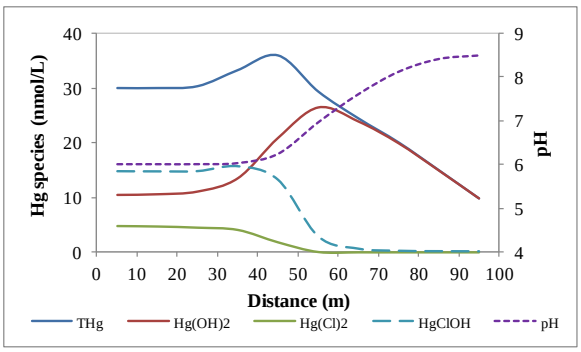

(b) Hg-species profile with 1 g of Kaolinite

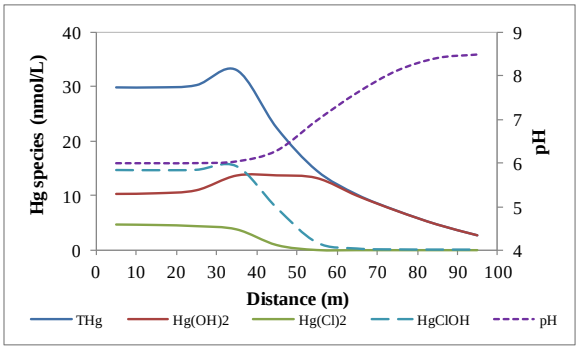

(c) Hg-species profile with 1 g of Gibbsite

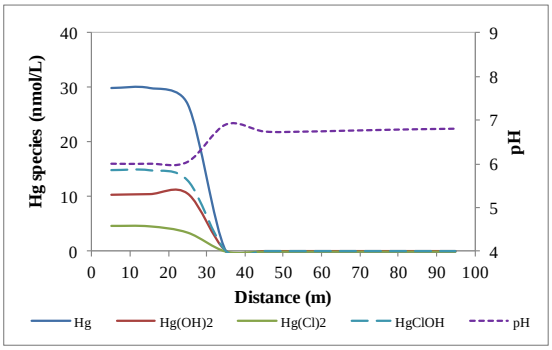

(d) Hg-species profile with 1 g of $Fe(OH)_3$

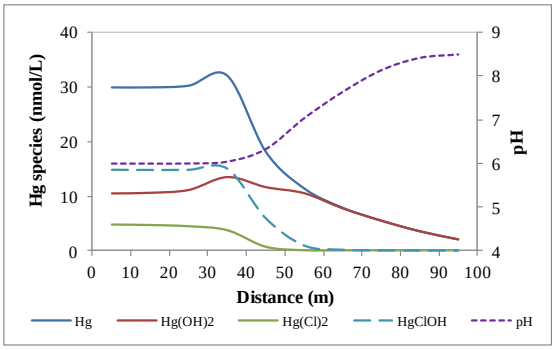

(e) Hg-species profile with 1 g of Kaolinite and Gibbsite

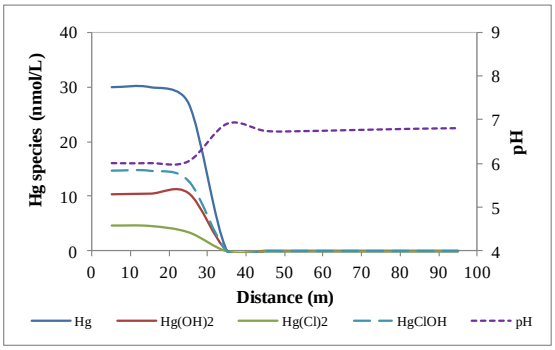

(f) Hg-species profile with 1 g of Kaolinite, Gibbsite, and $Fe(OH)_3$,

Figure 88. The effect of surface complexation on Hg-species flow profiles for different sorbents ($Fe(OH)_3$, Gibbsite and Kaolinite).The sorbents were applied to cells 4 and 5 (40 and 50 m of flow distance).

For this study, the sorption capacity of sorbents are in the order Kaolinite < Gibbsite < Gibbsite + Kaolinite < $Fe(OH)_3$ = $Fe(OH)_3$ + Gibbsite + Kaolinite. The Hg-species and pH profiles with each sorbent are shown in Figures 43 (b) to (f).

It can be seen from Figures 43 (b) and (f) that water pH increases sharply between 35-40 m. This is because of the effect of added $Fe(OH)_3$. The logarithm of the surface complexation reaction constant, log K, of the reaction between H^+ and $Fe(OH)_3$, (≡Hfo_sOH + H^+ = ≡Hfo_sOH_2^+) is 7.29. This implies that the pH of water should increase in the presence of $Fe(OH)_3$. However, after the surface complexation reaction between Hg and $Fe(OH)_3$, pH drops to a constant value of 7. This is because some of the H^+ is released back to the water when Hg complexes with $Fe(OH)_3$. In the presence of Kaolinite, $HgCl_2$ and HgClOH are sorbed and become negligible after 55 and 70 m respectively. The same happens at 50 and 60 m in the case of Gibbsite. Final THg concentrations at 100 m are 9.7, 2.8, 2.0 and 0 nmol/L in the presence of 1 g of Kaolinite, Gibbsite, Kaolinite + Gibbsite, and $Fe(OH)_3$, respectively.

This section describes the modeling performed on the Hg fate and transport in a typical surface water flow condition. The same water quality data used previously to study the groundwater condition (Table 45) were used here. The typical surface water flow parameters in Table 42, which were reported in literature, were used for the simulations in this section. The Hg fate and transport in a typical surface water condition were studied for 3 different scenarios: 1) without exchangers and sorbents; 2) with exchangers; and 3) with sorbents.

As previously mentioned, the flow parameters for a typical surface water flow condition were used for this study. The travel distance was chosen to be the same as that employed for the groundwater modeling. The flow reach was100 m long and was divided into 10 cells for PHREEQC calculation. The schematic of the Hg transport model for this scenario is shown in Figure 89.

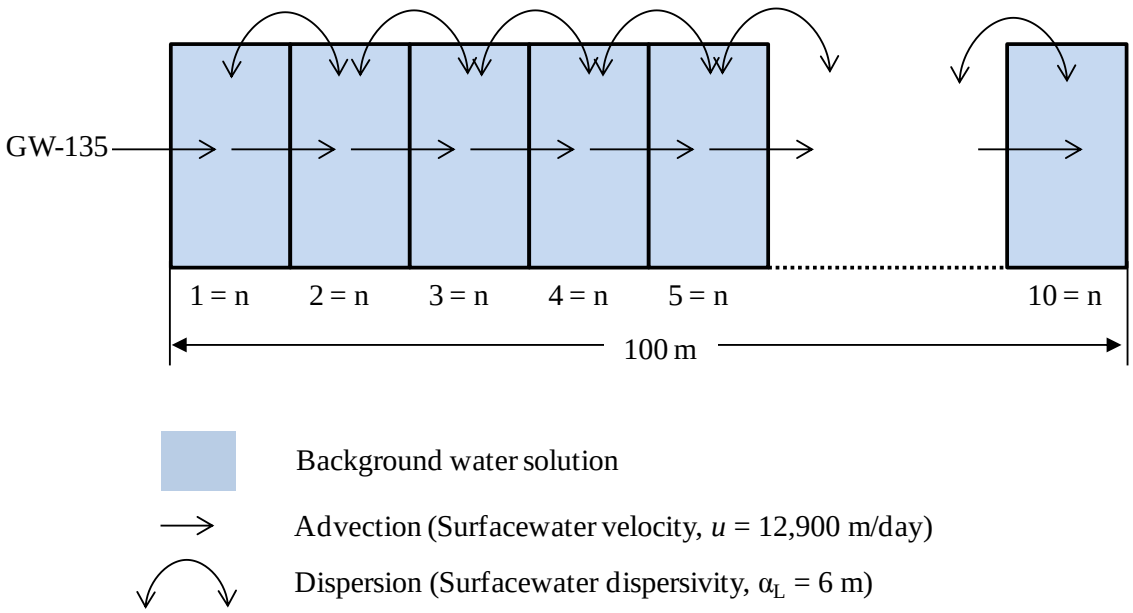

Figure 89. Model of Hg transport for a typical surface water flow condition.

The water flows from GW-135 through the reach without any interactions between Hg and the solid (exchanger/sorbent). PHREEQC calculated the Hg-species profile based on the water quality data and flow parameters that were provided (see Figure 90).

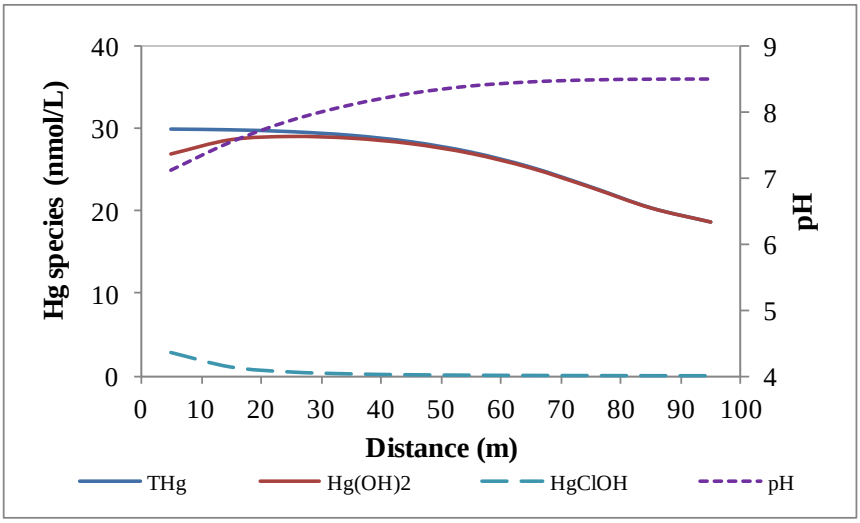

Figure 90. Hg-species flow profile in a typical surface water flow condition.

It can be inferred from Figure 90 that, with high velocity and dispersion, the Total Hg (THg) shows quite a conservative profile over the reach. The THg gradually reduces in concentration, presumably due to the effect of dispersion. There were only two Hg-species ($Hg(OH)_2$, HgClOH) that were observed throughout the flow distance. HgClOH was observed in the range of 10 to 30 m. but became negligible after 30 m. The travel time of 11 min (for 100 m distance) was considerably quicker when compared to the transport in the groundwater flow (i.e., 125 days).

The Hg fate and transport in a typical surface water flow environment was simulated with different exchangers (i.e., Illite, Montmorillonite and Vermiculite) that were individually added into cells 4 and 5 of the flow reach (Figure 46). This was to examine the effect of ion exchange of each exchanger on Hg fate and transport. The water quality and the travel distance were identical to scenario 1. The same type of exchangers and CEC used in the groundwater scenario were used for simulations herein. These were 1) Illite, CEC of 6.5 mol/L, 2) Montmorillonite, CEC of 15 mol/L, 3) Vermiculite , CEC of 26 mol/L and 4) Illite + Montmorillonite + Vermiculite, CEC of 47.5 mol/L. Four simulations with different exchangers were conducted. The schematic of the transport model is presented in Figure 91.

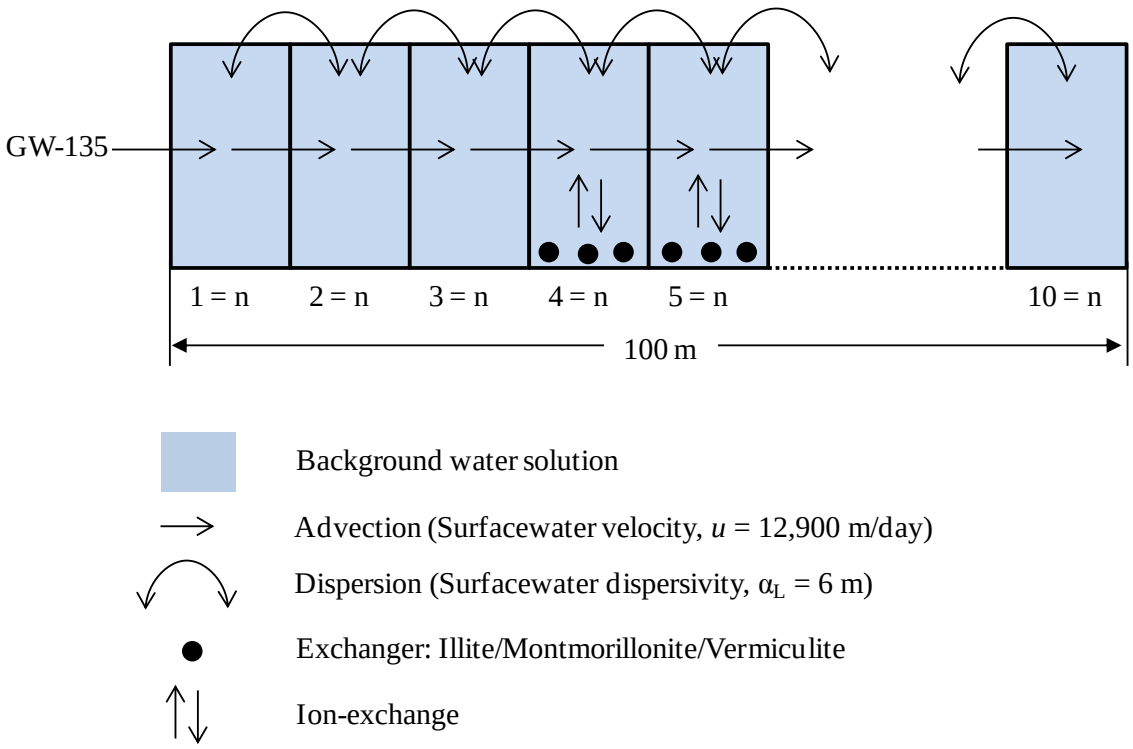

Figure 91. Model of Hg transport for a typical surface water flow condition. Simulations were performed for each individual exchanger (Illite, Montmorillonite and Vermiculite).

A significant difference was observed in the results obtained for surface water flow when compared to groundwater flow condition. The effect of dispersion on the concentration of Hg was more dominant when compared to the effect of ion exchange. There was no change in THg profiles when different exchangers were used along with the surface water flow condition of Table 42 (u = 12,900 m/day and α_L = 6 m). To further understand the effect of dispersion, a sensitivity analysis of Hg concentration to dispersivity along the travel distance was performed for 5 different conditions (

Table 46). This was performed only for Vermiculite exchanger (Vermiculite has higher CEC compared to the other exchangers).

Table 46. Conditions used for sensitivity analysis of dispersion to exchange reaction between Hg and Vermiculite

Condition	U (m/day)	α_L (m)	CEC of Vermiculite in cells 4 and 5 (mol/L)
1	12,900	No dispersion	No exchanger
2	12,900	2	26
3	12,900	6	26
4	12,900	20	26
5	12,900	100	26

Results in Figure 92 show that for condition 1, without dispersion and ion exchange, a constant concentration of THg, i.e., 30 nmol/L, is obtained throughout the travel distance. For condition 2, with 2 m of dispersivity and 26 mol/L of CEC, the dip in concentration of THg obtained at cells 4 and 5 (where the exchanger was added) is due to the ion-exchange reaction. The concentration also gradually reduces during 70-100 m due to dispersion.

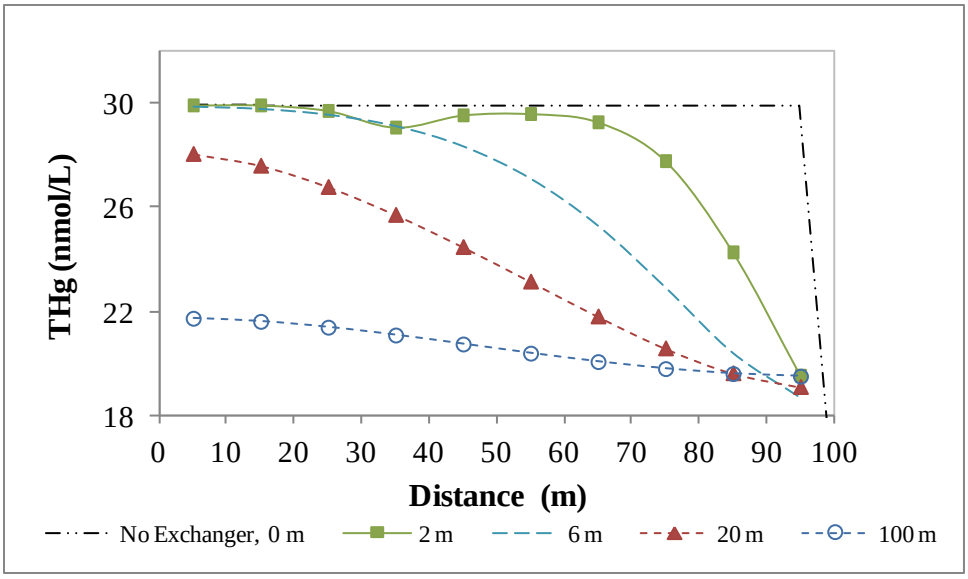

Figure 92. Effect of dispersion on the exchange reaction and Hg transport for surface water flow condition.

The THg concentration changes along the travel distance for conditions 3, 4, and 5, which were 26 mol/L CEC of Vermiculite and dispersivity of 6 m, 20 m, and 100 m. There was no dip in concentration in cells 4 and 5 (where ion exchange is expected to take place) unlike that observed in condition 2. It can be inferred that, keeping all the other parameters constant, lower dispersivity (~ 2 m) is required to see the effect of ion exchange under surface water flow condition. Since the dispersivity for typical surface flow condition is 6 m, it can be concluded that the Hg concentration as predicted by this model is dominated by dispersion instead of ion exchange.

The water quality and flow parameters in this scenario were the same as those employed in scenarios 1 and 2. The goal was to determine the effect surface complexation on the Hg fate and transport. One g/L of different sorbents: $Fe(OH)_3$, Gibbsite, and Kaolinite, were individually added into cells 4 and 5 of the flow reach. The schematic of the transport setting is shown in Figure 93.

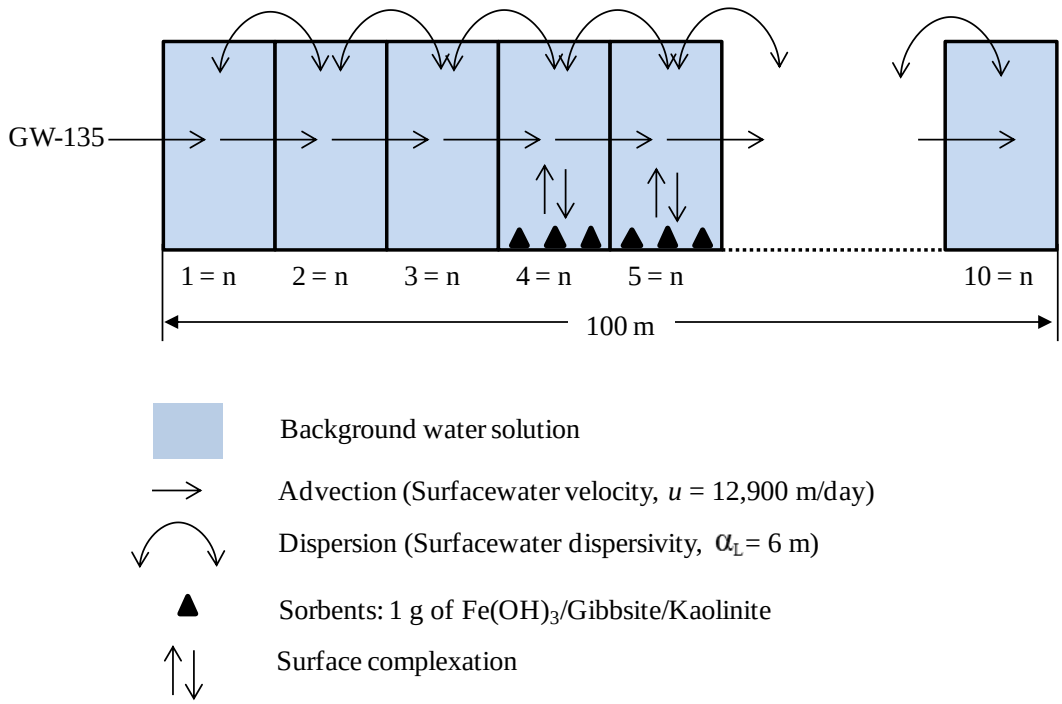

Figure 93. Model of Hg transport for a typical surface water flow condition. Simulations were performed for each individual sorbents ($Fe(OH)_3$, Gibbsite and Kaolinite).

Figure 94 (a) shows the THg profile along the flow distance. It was observed that the sorption capacity of sorbents is in the order Kaolinite < Gibbsite < Kaolinite + Gibbsite < $Fe(OH)_3$ = Kaolinite + Gibbsite + $Fe(OH)_3$. The Hg-species and pH profiles for each sorbent are shown in Figures 94 (b) to (f).

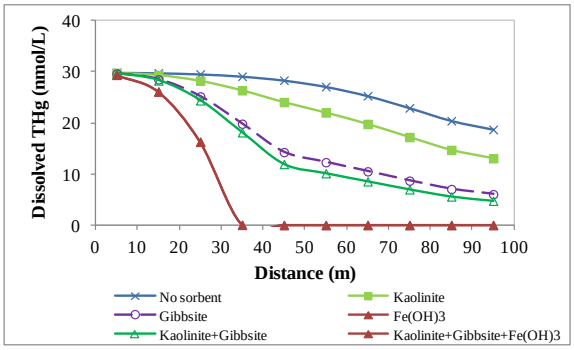

(a) THg profile with different sorbents

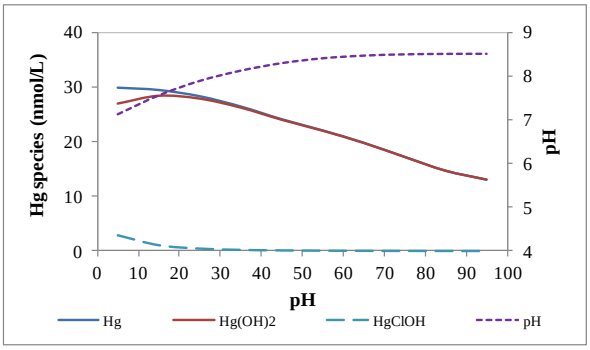

(b) Hg-species profile with 1 g of Kaolinite

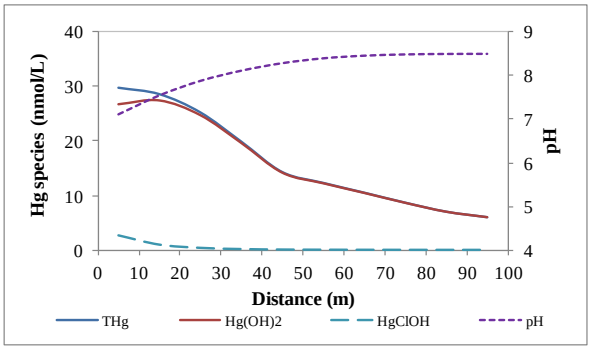

(c) Hg-species profile with 1 g of Gibbsite

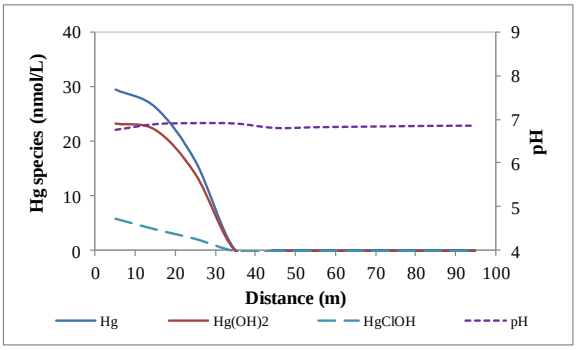

(d) Hg-species profile with 1 g of $Fe(OH)_3$

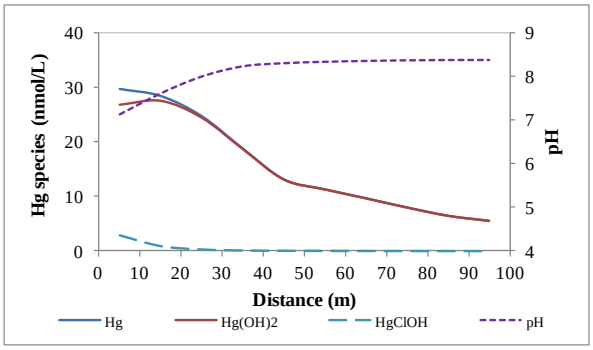

(e) Hg-species profile with 1 g of Kaolinite and Gibbsite

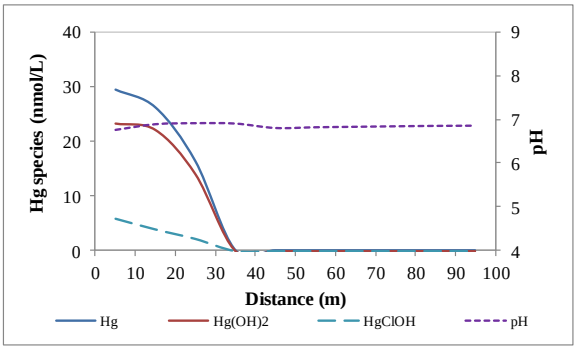

(f) Hg-species profile with 1 g of Kaolinite, Gibbsite, and $Fe(OH)_3$

Figure 94. The effect of surface complexation on Hg-species flow profiles for different sorbents ($Fe(OH)_3$, Gibbsite and Kaolinite).The sorbents were applied to cells 4 and 5 (40 and 50 m of flow distance).

The water pH in the presence of $Fe(OH)_{3,}$ as shown in Figures 49 (d) and (f), is expected to increase because of surface complexation of H^+ and $Fe(OH)_3$; but the reaction between Hg and $Fe(OH)_3$ reduces the pH, to a pH of 7 as shown in (d) and (f). A small drop in THg concentration was observed in the presence of Gibbsite, which is shown in (b) and (e). That could be due to the high surface complexation constant between Hg and Gibbsite. The surface complexation between Hg and $Fe(OH)_3$ is also very strong. This explains why the Hg complexation is influenced by $Fe(OH)_3$, when a mixture of Kaolinite + Gibbsite + $Fe(OH)_3$ is used. The reaction between HgClOH and Kaolinite is stronger than that between HgClOH and Gibbsite, while Gibbsite can complex with $Hg(OH)_2$ better than Kaolinite.

MODEL APPLICATIONS, RESULTS AND DISCUSSION

This section presents the application of the enhanced model to assess the geochemical processes, fate, and transport of Hg (ORR). Using specific water quality data obtained from each site, the sensitivity analysis to pH and temperature of Hg-species was conducted in batch mode. For ORR test-bed, Hg transport in groundwater (Bear Creek Valley Regime) and surface water (EFPC) were investigated. The results yielded a better understanding of the fate and transport of Hg in these settings thereby aiding the selection of suitable restoration.

ORR Test-Bed Simulations – Batch Mode

In this section, the improved PHREEQC model was used to simulate the behavior of Hg in EFPC water located in the ORR area. The distribution of Hg species, the sensitivity analysis of Hg-species and saturation index (SI) of minerals to water pH and water temperature were investigated. The simulations were conducted using the EFPC water quality data which is shown in Table 47 (Dong et al., 2010). The ORR and EFPC soil characteristics (physical and chemical properties) are described in Appendix E.

Table 47. EFPC water quality data (Dong et al., 2010)

Constituent	Range
pe	3.81
pH	7.0 – 9.2
Total Ca, mol/L	$7.7 \times 10^{-4} – 1.1 \times 10^{-3}$
Total Mg, mol/L	$4.5 \times 10^{-4} – 4.8 \times 10^{-4}$
Total Na, mol/L	$7.7 \times 10^{-4} – 1.1 \times 10^{-3}$
Total K, mol/L	$5.0 \times 10^{-5} – 9.0 \times 10^{-5}$

Total Fe, mol/L	2.6×10^{-8} - 2.8×10^{-8}
Total Cl, mol/L	2.2×10^{-4} – 6.5×10^{-4}
Total HCO_3, mol/L	2.0×10^{-3} – 2.1×10^{-3}
Total NO_3, mol/L	1.0×10^{-4} – 2.8×10^{-4}
Total PO_4, mol/L	2.5×10^{-6} – 1.2×10^{-5}
Total Zn, mol/L	1.6×10^{-7} – 2.6×10^{-7}
Total Cu, mol/L	1.2×10^{-8} – 2.8×10^{-8}
Total Cd, mol/L	5.2×10^{-8} – 1.3×10^{-9}
Total Pb, mol/L	6.1×10^{-10} – 1.3×10^{-9}
Total Hg, mol/L	4×10^{-11} – 4×10^{-10}

The Hg species distribution in EFPC using the improved PHREEQC model and the EFPC water quality data of Table 47 is shown in Figure 95.

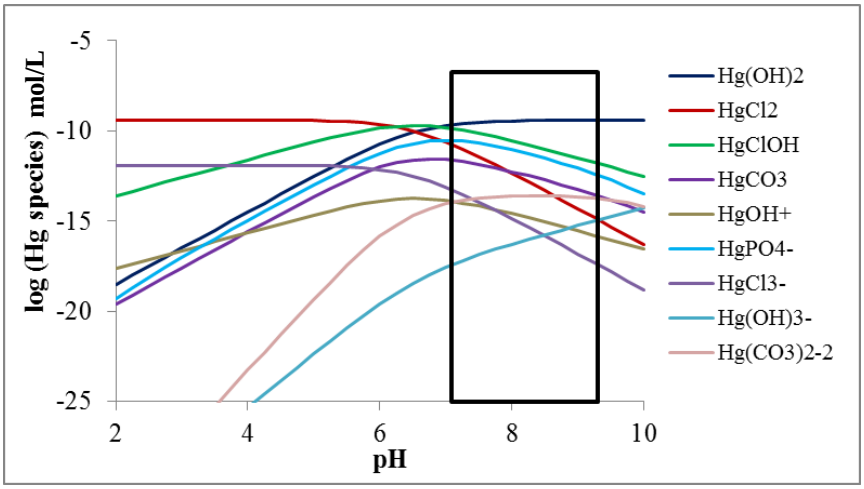

Figure 95.Hg species distribution in EFPC water.

The $Hg(OH)_2$ is the dominant species at typical EFPC water pH (black box shown in Figure 50, pH ~ 7.0 - 9.2). The second dominant species is HgClOH. $Hg(HO)_2$ concentration is low at low pH, while $HgCl_2$ dominates at low pH (0-6). The $Hg(OH)_2$ concentration increases with water pH (0-6), while $HgCl_2$ decreases. The higher concentration of $Hg(OH)_2$ at high pH is due to the increase in OH with the water pH.

The sensitivity of Hg speciation in EFPC to water temperature and pH was studied at temperatures in the range of 5-35 °C and pH 2-10 (Figure 96).

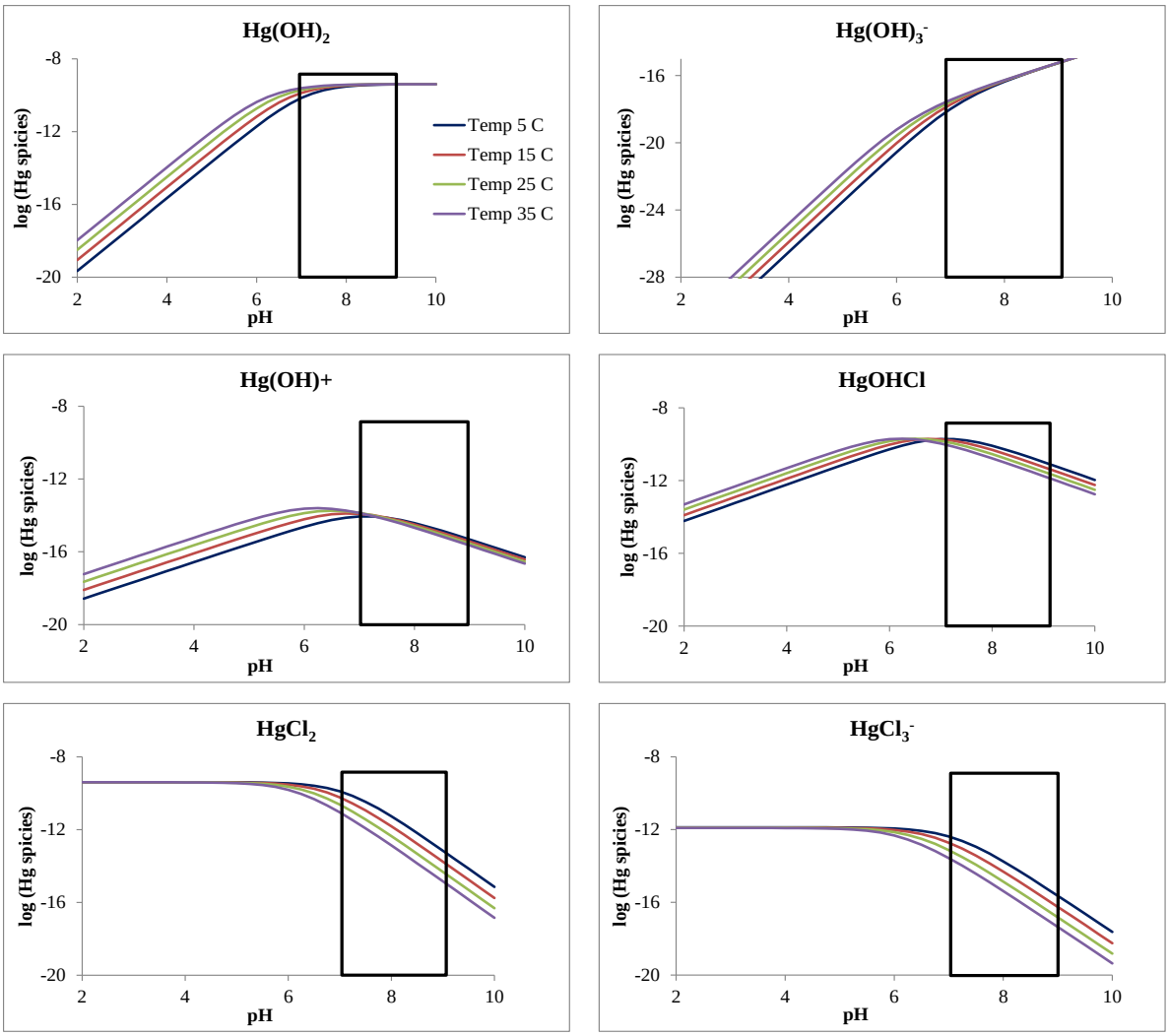

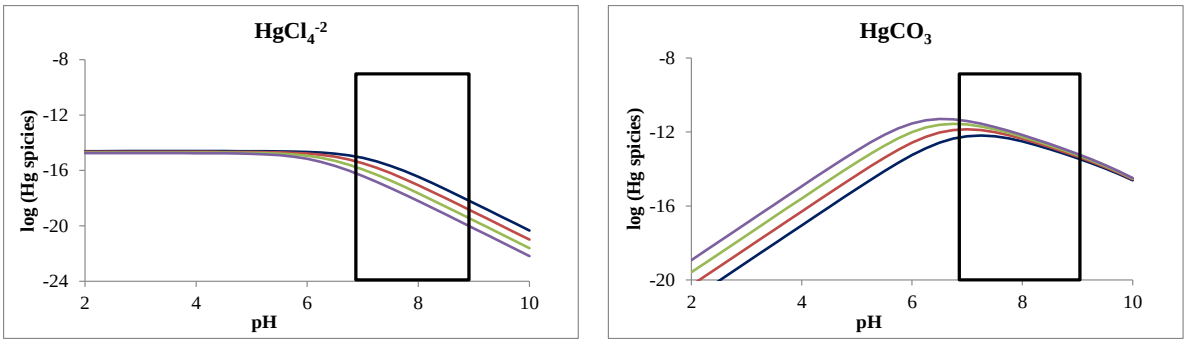

Figure 96. Hg species sensitivity to temperature (5-35 °C) and pH (2-10) (unit in log mol/L); black box shows EFPC water pH range under oxidizing condition.

It can be seen from Figure 96 that the formation of Hg-OH and Hg-CO_3 species increases with water temperature. An increase in water temperature does not favor the formation of Hg-Cl species. An increase in water pH increases the formation of $Hg(OH)_2$ and $Hg(OH)_3^-$. However, for $Hg(OH)^+$, HgOHCl, and $HgCO_3$, the concentrations increased with pH between 2-7 and declined for pH > 7. Low water pH (pH 2-6) does not have any influence on Hg-Cl concentration. However, a decrease in its concentration is observed for pH > 6.

The sensitivity analysis to water temperature and pH for the mineral precipitation at EFPC water conditions was conducted for temperature range of 5-35 °C and for pH of 2-10 (Table 47). Figure 97 shows the effect of water temperature and pH on the SI of dominant precipitated minerals in EFPC water. The SI of Ferrihydrite, Goethite, Magnesioferrite, and Hematite increases with water temperature. However, temperature does not affect the formation of FCO_3Apatite, Lepidocrocite, Hydroxylapatite, and Arogonite. Increase in water pH favors the formation of all the above minerals since their SI increases with water pH. Within the EFPC water conditions, pH 7.0-9.2 and temperature 25 °C, water is supersaturated with Ferrihydrite, Goethite, Magnesioferrite, Hematite, FCO_3Apatite, Lepidocrocite, and Hydroxylapatite. Hence these minerals are expected to precipitate at these conditions. At pH 8, the EPFC water becomes saturated with Arogonite and its precipitation takes place.

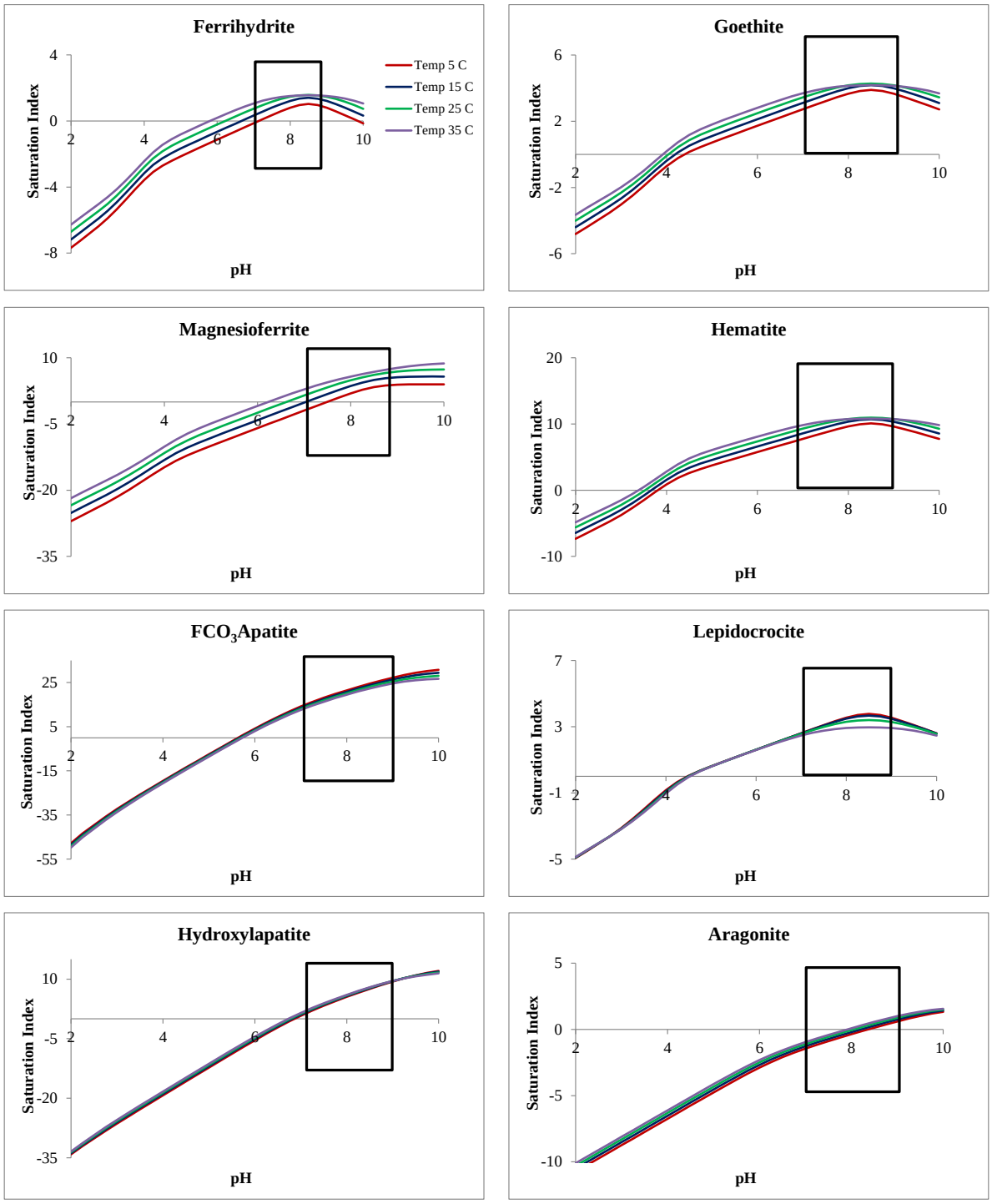

Figure 97. Sensitivity of mineral precipitation to water temperature and pH in EFPC water conditions.

ORR Test-Bed Simulation – Groundwater Transport Mode

Hg in Groundwater Transport: Bear Creek Valley

The transport of Hg in Bear Creek Valley, which is located in the ORR area is presented in this section. Data was collected from 4 monitoring wells: GW-916, GW-923, GW-363, GW-639. These wells were selected for the study because of 1) the availability of Hg data and 2) the wells were located in the main groundwater flow path as defined by the surface water table elevations. The locations of selected monitoring wells are shown in Figure 98.

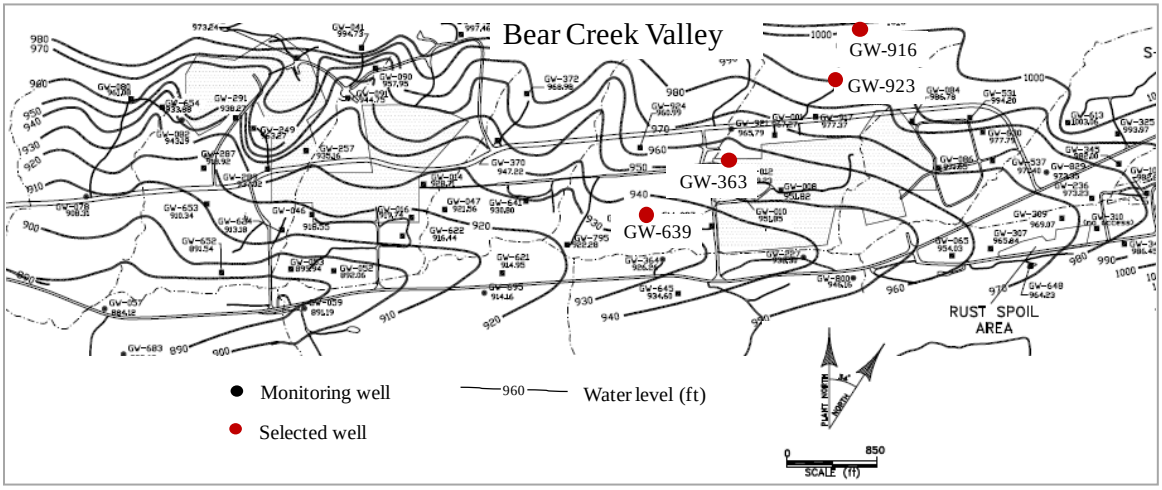

Figure 98. Location of selected wells for Hg transport in Bear Creek Valley, Oak Ridge, TN (modified after Elvado Environmental LLC, 2009).

The geology and soil bedrock of the site consist of shale, limestone, siltstone, and clay. The soil consists of different minerals, such as Ferrihydrite, Gibbsite, Geothite, Illite and Kaolinite, etc. (Atre and Carpenter, 2010; Driese et al., 2001) (See Appendix E for soil characteristics); the CEC of 130 mmol/L was reported. The background water is a Ca-Mg-HCO_3 water. The average

groundwater velocity of 0.66-1.0 m/day (Jago et al., 1995) and the dispersivity of 1 m (Stafford et al., 1998; Schulze-Makuch, 2005; Kelkar et al., 2006) were used in simulations herein. The water quality data at the selected wells and the flow parameters of the site that were used for the simulation are respectively shown in Tables 45 and 46.

Table 48. Water quality data used for Hg transport study in Bear Creek Valley (Elvado Environmental LLC, 2009 and 2011)

Parameter	GW-916	GW-923	GW-363	GW-639
Groundwater Elevation (ft)	998	983	953	930
Dissolved Oxygen (mg/L)	0.2 - 0.9	0.3 - 1.3	2.0 - 4.0	3.8
Oxidation/Reduction (mV)	-105 - 15	-10 – 19	31 - 127	78 – 98
Temperature (°C)	13.9-14.3	15.6 - 16.3	14.5 - 21.5	12.3 – 17
pH	7.1 – 8.0	7.2 - 6.2	8.6 - 9.3	8.0 – 9.0
Aluminum (mg/L)	-	-	26.6	28.0
Calcium (mg/L)	35.7-43.1	48.3 - 33.8	1.0 - 1.2	0.9 - 0.8
Magnesium (mg/L)	5.8-47.0	18.0 – 10.0	0.26 - 0.49	0.2 - 0.2
Sodium (mg/L)	24.6-32.0	26.4 - 4.1	1.04 - 1.18	1.9 - 2.1
Iron (mg/L)	1.3-1.6	1.7 - 28.3	0.05 - 0.07	0.1 - 0.2
Mercury (ng/L)	110 – 100	72 – 130	80 - 91	80 – 90
SI of Cinnabar	-9.6	5.9	-36.8	-41.8
SI of $Fe(OH)_3$	-1.2	-1.7	2.9	3.1
SI of Gibbsite	-	-	0.3	0.1

Table 49. Groundwater flow parameters used for Hg transport in Bear Creek Valley simulations (Jago et al., 1995; Kelkar et al., 2006)

Parameters	ORR area	Value used in this study
***v* (m/d)**	0.6-1.0 (Jago et al., 1995)	0.8
α_L (m)	1-2 (Kelkar et al., 2006)	1
D_L (m^2/d)	0.6 – 1.2 (calculated using DL= α_Lv	0.8
D* (m^2/d)	$3x10^{-9}$	3x10-9

The analysis performed on the water quality data in

Table 49 using the enhanced PHREEQC model indicates that the GW-923 water is supersaturated with Cinnabar (SI = 5.9). In other words, it supports the occurrence of deposited Cinnabar mineral at that location. This also indicates the potential that the dissolved Cinnabar can be released and become a source of Hg. The analysis also suggests that GW-363 and GW-639 waters are supersaturated with Gibbsite and $Fe(OH)_3$. In order to better understand the transport of Hg in the site, a number of simulations were made, which are explained next. These simulations were based on the following general assumptions:

1) Groundwater from well 916 (Table 48) flows through the Ca-Mg-HCO_3 background water type to well 639 over 975 m of travel distance.
2) The transport model in PHREEQC is divided in to 50 cells each of 20 m length.
3) The flow parameters in
4) Table 49 are used for the simulation.
5) The dissolution of Cinnabar at GW-923 constantly releases 120 ng/L of dissolved Hg.
6) A CEC of 130 mmol/L is the ion exchange capacity of the bedrock applied for all the cells to assess ion-exchange.
7) The $Fe(OH)_3$ and Gibbsite minerals are present at wells 363 and 639 (cells 34, 35 and 49), which is indicated by the SI of the minerals in Table 48. These minerals are considered as the sorbents that can complex with Hg by the role of surface complexation.

8) Simulation scenarios were conducted for 1) 1 g of the sorbents: $Fe(HO)_3$, Gibbsite, and Kaolinite in cells 34, 35 and 49 and 2) different combinations of sorbents $Fe(HO)_3$ and Gibbsite in cells 34, 35 and 49.

A schematic of the Hg transport situation for this site is shown in Figure 99.

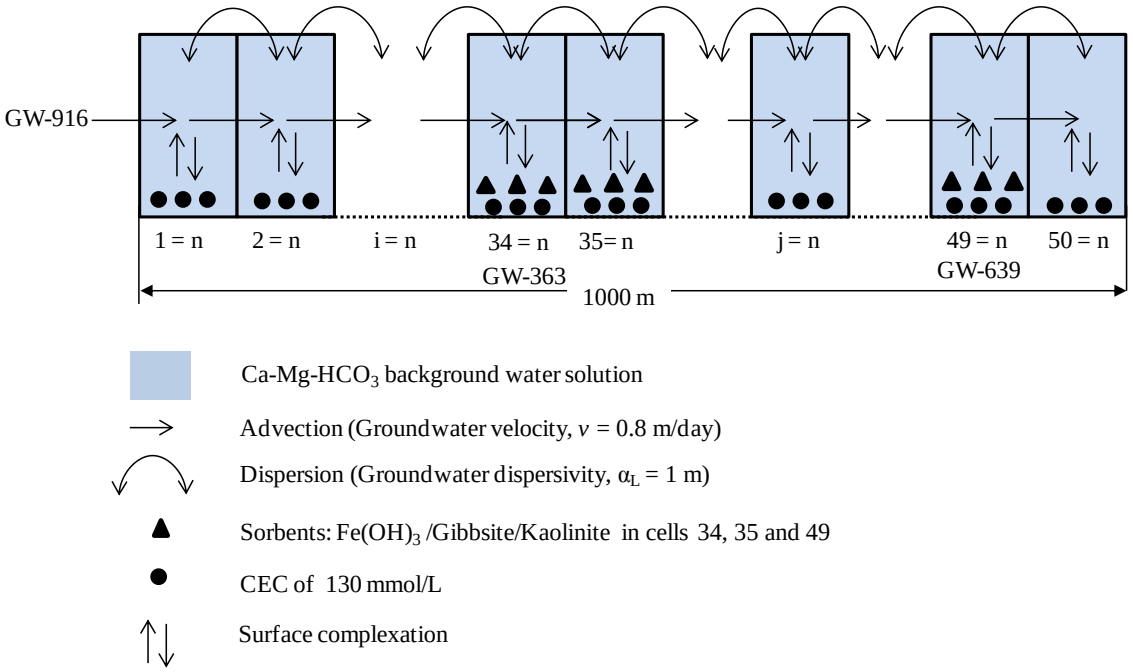

Figure 99. Hg transport model for Bear Creek Valley.

The results of the Hg transport simulations based on the assumptions mentioned earlier are shown in Figure 100. Without the presence of sorbent, the dissolved total Hg (THg) profile matches the concentration at wells GW-916 and 923. However, the measurements taken downstream (GW-363 and 639) are significantly lower than that predicted by the model (assuming no sorbent was present). It can be inferred that sorbents were present downstream which reduces the concentration of Hg in water. This simulation confirms, to a certain extent

(based on the good correlation obtained at the first two wells), the "validity" of the assumptions 4 and 5 (CEC value and rate of Hg release due to the dissolution of Cinnabar).

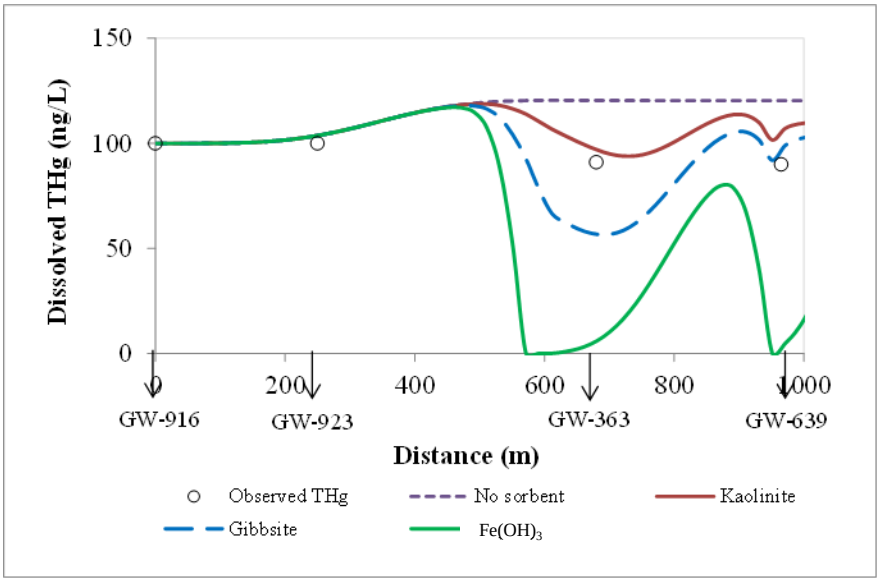

Figure 100. Dissolved THg transported in the presence of three different sorbents, individually present in cells 34, 35 and 49, at Bear Creek Valley.

It should also be noted that when the sorbents were added, strong surface complexation occurred between dissolved THg and $Fe(OH)_3$ and led to a reduction in concentration of Hg at GW-363 and GW-639. With 1 g of $Fe(OH)_3$ at cells 34, 35 and 49, the dissolved THg appears to be underestimated compared to the observed data. Applying 1 g of Gibbsite into those cells also indicates an underestimation of THg at GW-363, while over estimation is obtained at location of GW-639. With 1 g of Kaolinite in the same cells, the model shows a slight overestimation of THg at both wells GW-363 and GW-639.

A sensitivity study was also conducted for CEC. However, CEC did not show any significant effect on THg concentration. This seems to be because of the low exchange constant (log K) for Hg at low CEC values.

This scenario was conducted to determine the optimum amount of sorbents present at GW-363 and 639 that will give a good correlation between the simulation and observed data. The optimization was achieved by performing several simulations with different amounts and combinations of sorbents. The optimum amount of sorbents was found to be 4 and 5 mg of Gibbsite and $Fe(OH)_3$, respectively, at GW-363 and 1 g and 5 mg of Gibbsite and $Fe(OH)_3$, respectively, at GW-639. The results are shown in Table 50 and Figure 101.

Table 50. Optimum amount of sorbents at GW-363 and GW-639

Sorbents	Cells 34-35 (GW-363)	Cell 49 (GW-639)
Gibbsite	4 mg	1 g
$Fe(OH)_3$	5 mg	5 mg

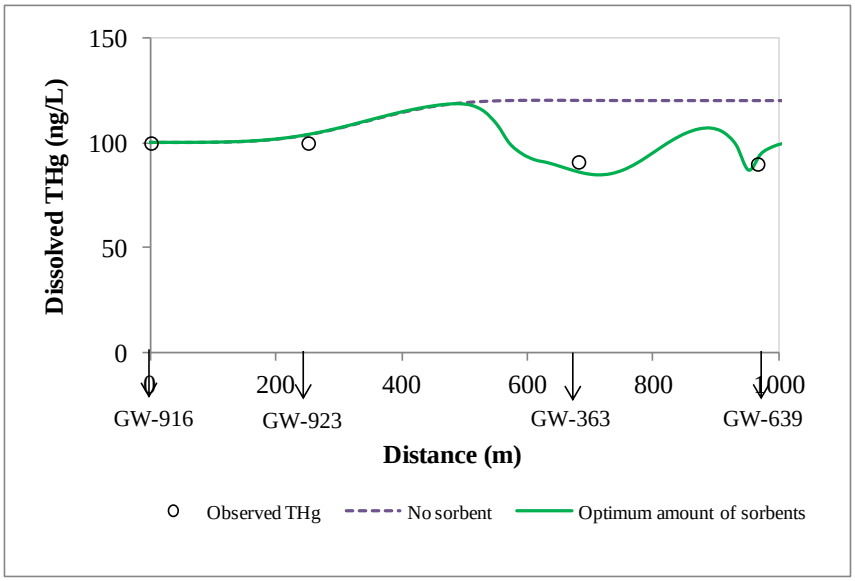

Figure 101. Dissolved THg transported in the presence of two different sorbents, simultaneously present in cells 34, 35 and 49, at Bear Creek Valley.

Figure 101 shows that THg concentration obtained for the enhanced model simulation, using optimized amounts of sorbents for surface complexation. The result provides a good match with observed data. With the optimum amount of sorbents, the enhanced model was then used to estimate the distribution of Hg-species along the main flow path. The comparison of Hg-species and pH profiles between the model results and observed data is shown in Figure 102.

It can be observed in Figure 102 that the model results match well with the observed data for most of the Hg-species and the pH profile along the flow distance. The difference in concentration between the Hg-species at each location is related to the pH of that location. At GW-923 where pH is neutral, $HgCl_2$ is dominant, while the second dominant species is HgClOH. With an increase in pH, $HgCl_2$ decreases. HgClOH shows its peak at pH 7.5 at a distance of 400 m. $HgCl_2$ and HgClOH become relatively low at a farther distance when pH is greater than 7.5, which favors the occurrence of $Hg(OH)_2$. $Hg(OH)_2$ is the dominant species at GW-363 and 639.

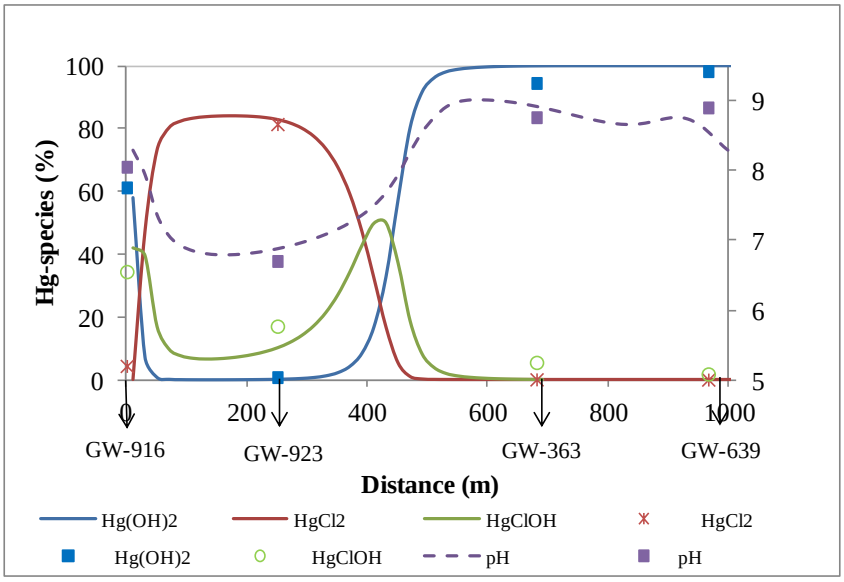

Figure 102. Comparison of Hg-species and pH profiles along the flow distance between the model results and observed data. The points represent observed data and the lines represent model results.

The model results show a peak of HgClOH species at 400 m. This is consistent with the pH value (7.5) observed at this location (HgClOH dominates other Hg species at pH = 7.5).

ORR Test-Bed Simulation – Surface Water Transport Mode

This section presents the Hg transport study in EFPC where the Hg contamination in the creek water has been of concern since the 1980s. The major cause of this contamination was the accidental spills and discharges of 128,000±35,000 kg Hg to the EFPC that occurred during the period of operation of the Y-12 plant (1950-1963) (Brooks and Southworth, 2011; Dong et al. 2010). Many attempts have been made since then to reduce the mercury concentration in EFPC. In 2011, an 85% decrease from ~2000 ng/L in 1980s was reported (Brooks and Southworth, 2011). However, throughout of EFPC, the Hg concentration was reported to be in excess of the 0.051 µg/L criterion (TDEC, 2008). The Hg concentrations obtained from the monitoring stations were 0.5 µg/L at EFK 23.4 located at the EFPC headwater, 0.3 µg/L at EFK 18.3 (~5 km downstream from EFPC headwater), and 0.25 µg/L at EFK 13.8 (~10 km downstream from EFPC headwater) (Brooks and Southworth, 2011; TDEC, 2008). EFK is an operational code used to identify and name monitoring stations along the creek.

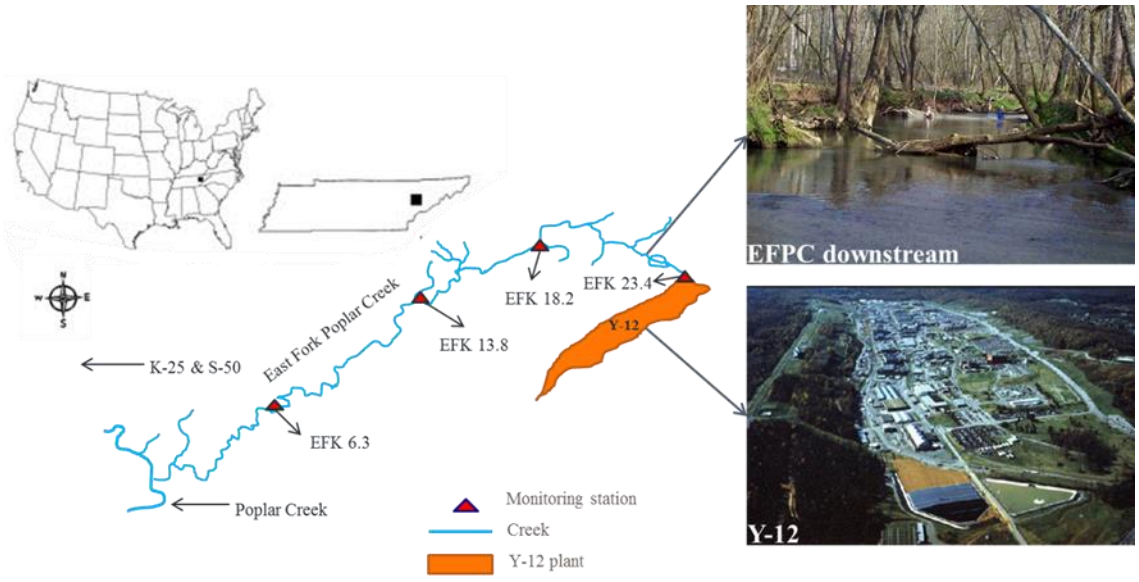

Figure 103. EFPC and Y-12 map (modified after www.esd.ornl.gov).

Hg in Surface Water Transport: Hg Reduction Load to EFPC

In order to achieve the concentration criterion, Hg daily load reduction strategy was used (Brooks and Southworth, 2011; Loar et al., 2011). The loading of total Hg to EFPC was estimated to exceed 100 g/day in 1985. Hg loading decreased to 15 g/day by 1993 (Brooks and Southworth, 2011; Loar et al., 2011) and 1-10 g/day by 2007 (TDEC, 2008). Therefore, in this section the simulations were conducted to test how long the Hg concentration in EFPC may take to reduce to the concentration criterion of 0.051 µg/L with respect to a range of Hg loadings (2.5 g/day, 1.5 g/day and 0.5 g/day). The PHAST integrated model and the developed PHREEQC database were used for the simulations. The EFPC is approximately 5-9 m wide and 30 km long (Loar et al., 2011) (Figure 103). However, the modeling domain in this study was a 5 m x 10 km (width x length) stretch, which covers the stations EFK 23.4, EFK 18.2, and EFK 13.8. The modeling domain was selected based on the availability of water quality data. The Hg transport was simulated with the following assumptions: 1) The head boundary (water level) at location EFK 23.4 was 1 m and 2) the flow occurs only in forward direction (from EFK 23.4 to EFK 13.8). The water quality data, at different locations (EFK 23.4, EFK 18.2, EFK 13.8), were collected from previous studies (Loar et al., 2011; Dong et al., 2010; Brooks and Southworth, 2011) and used in the model (Table 48). The surface complexation [1 mg/L of $Fe(OH)_3$] and ion-exchange (CEC = 0.01 mol/L) properties were applied to all the model domains. The flow parameters collected from Loar et al. (2011) and Vasquez (2008) studies were used in the model (Table 52).

Table 51. EFPC surface water quality at different monitoring stations (ion concentrations in mg/L) (Loar et al., 2011; Dong et al., 2010; Brooks and Southworth, 2011)

Parameters	Stations		
	EFK 23.4	EFK 18.3	EFK 13.8
Temperature, °C	25	25	25
pe	3.81	3.81	3.81
pH	7.0 – 9.2	7-9.2	7-9.2
Total Ca	44	37.4	30.8
Total Mg	11.66	11.29	10.93
Total Na	25.3	21.505	17.71
Total K	3.51	2.73	1.95
Total Fe	0.0015	0.0015	0.0015
Total Cl	23.01	15.399	7.788
Total HCO_3	128.1	125.05	122
Total NO_3	17.36	11.78	6.2
Total PO_4	1.1388	0.6880	0.23
Total Zn	0.0169	0.0137	0.0105
Total Cu	0.0017	0.0013	0.0008
Total Cd	0.0001	0.003	0.0058
Total Pb	0.0002	0.0002	0.0001
Total Hg	0.0005	0.0003	0.00025
CEC (mol/L)	0.01	0.01	0.01
Sorbent [mg of $(FeOH)_3$/L]	1	1	1

Table 52. Transport parameters used for Hg transport study in EFPC

Parameters	Values
Model Domain	10 km x 5 m
Velocity, m/d	12,960 (Vasquez, 2008; Loar et al., 2011)
Loading rate, cfs (cms)	11 (0.31) (Vasquez, 2008; Loar et al., 2011)
Dispersivity, m	6 (Loar et al., 2011)
Diffusivity, m^2/s	$1x10^{-9}$ (Loar et al., 2011)
Number of Grid in X axel	100
Number of Grid in Y axel	5
Number of Grid in Y axel	1
Grid size	0.1 km x 1 m
Grid for EFK 23.4 station (X_1, Y_1, Z_1: X_2, Y_2, Z_2)	0, 0, 0 : 50, 5, 1 it is associated with water quality from station EFK 23.4
Grid for EFK 18.3 station (X_1, Y_1, Z_1: X_2, Y_2, Z_2)	50, 0, 0, : 70, 5, 1 it is associated with water quality from station EFK 18.3
Grid for EFK 13.8 station (X_1, Y_1, Z_1: X_2, Y_2, Z_2)	70, 0, 0, : 100, 5, 1 it is associated with water quality from station EFK 13.8
Initial Hg concentration at EFK 23.4 station, µg/L	0.5
Initial Hg concentration at EFK 18.3 station, µg/L	0.3
Initial Hg concentration at EFK 13.8 station, µg/L	0.2
Ion-exchange: CEC 1 mmol/L	All domain
Sorbent: 1mg $Fe(OH)_3$/L	All domain

The transport model employed an EFPC average hydraulic retention time of 0.25 day. Figure 104 shows the model domain and the initial concentrations of Hg in EFPC at different locations. The Hg transport simulations were calculated at 3 different Hg loading rates (2.5 g/day, 1.5 g/day and 0.5 g/day). These rates were used to define a range of possible Hg pollution prevention strategies.

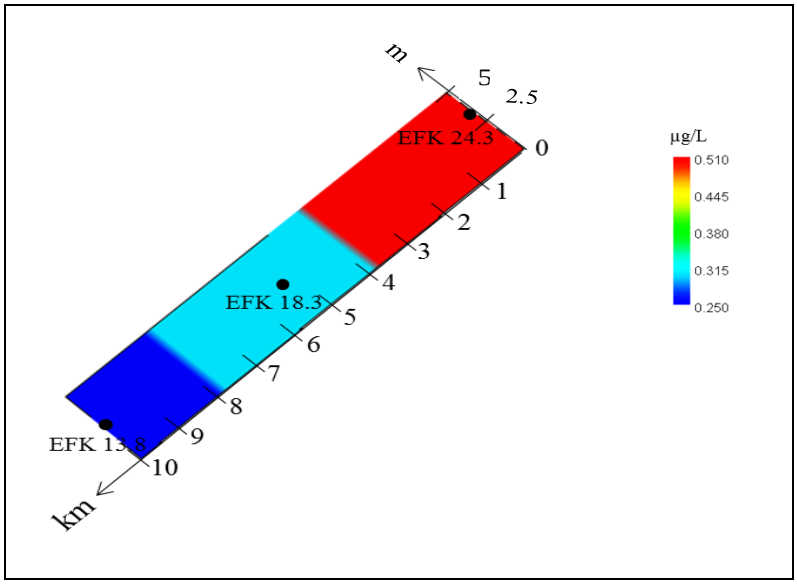

Figure 104. Initial concentration of Hg in EFPC water at different monitoring stations.

Simulation scenario 1 was made with a 2.5 g/day of Hg loading at the source (EFK 24.3) in the EFPC. The simulation was conducted to predict the time that takes to reduce the Hg concentration in the creek to meet the concentration criterion of 0.051 µg/L. The simulation was started with initial background Hg concentrations in the creek as 0.5 µg/L, 0.3 µg/L, and 0.2 µg/L at EFK 23.4, 18.3, and 13.8, respectively.

0 year

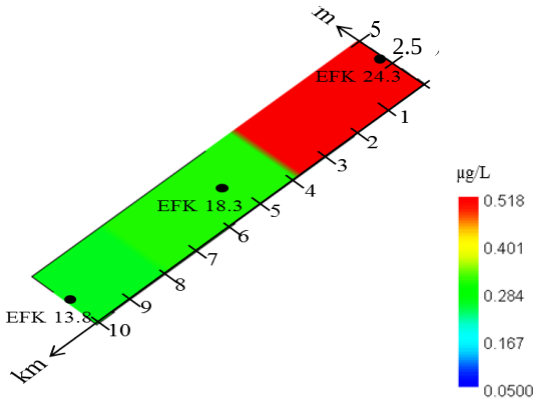

1 year

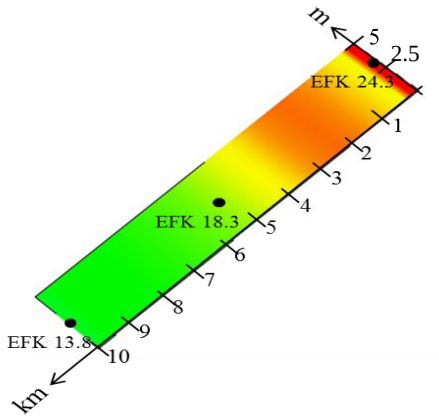

15 years

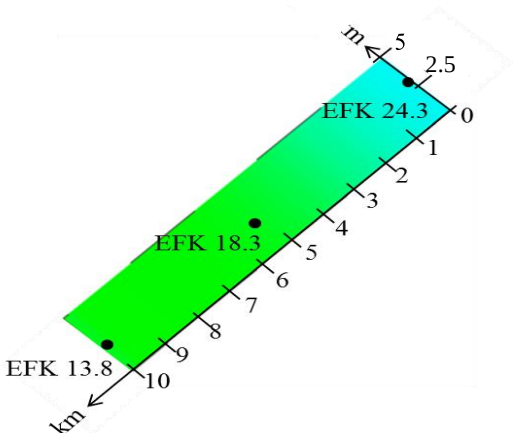

30 years

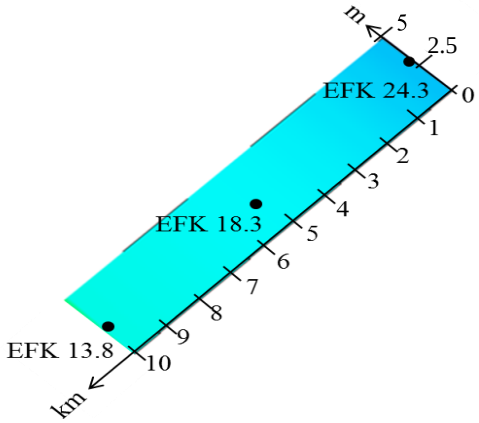

45 years

60 years

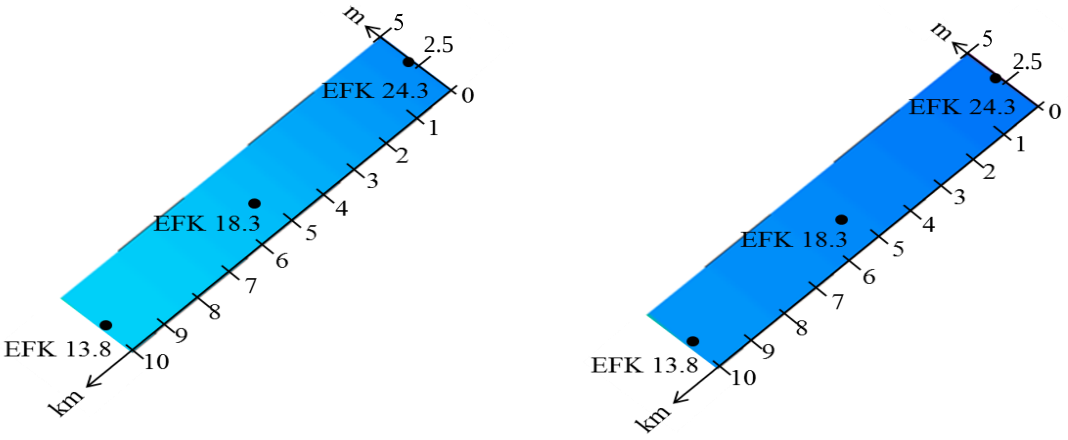

Figure 105. Transport of dissolved Hg in EFPC water with loading rate of 2.5 g/day (from EFK 24.3 to EFK 13.8).

In Figure 105, at a Hg mass loading of 2.5 g/day, (flow rate is 11 cfs, Hg concentration is 9.3 x 10^{-5} mg/L), the simulation shows that the concentration at EFK 24.3 becomes lower than the downstream concentrations (EFK 18.3 and 13.8) by year 13 (not shown in the Figure). By year 15, the total dissolved Hg concentration at EFK 24.3 decreased approximately to 0.15 µg/L (from an initial concentration of 0.5 µg/L). The concentrations at EFK 18.3 and EFK 13.8 did not show any significant change. However, a reduction in total dissolved Hg concentrations at EFK 18.3 and 13.8 are observed in year 30 (0.15 µg/L). Hg concentrations of less than 0.1 µg/L for the entire model domain are reached by year 45. These are 0.09, 0.09 and 0.1 µg/L at EFK 24.3, 18.3, and 13.8, respectively.

It also can be seen in Figure 106 that the total dissolved Hg concentration in the EFPC shows big reduction during years 10 and 25 (~100% reduction at EFK 24.3 and ~200% reductions, at EFK 18.3 and 13.8). However, the reduction slows down in the later years; in fact, reduction rates between years 35, 45, and 60 are very small. The result shows that the total dissolved Hg reaches a constant concentration of 0.08 µg/L by year 60. The model result also suggests that, with 2.5 g/day of Hg mass loading to the EFPC, the Hg concentrations will not meet the criteria of 0.051 µg/L.

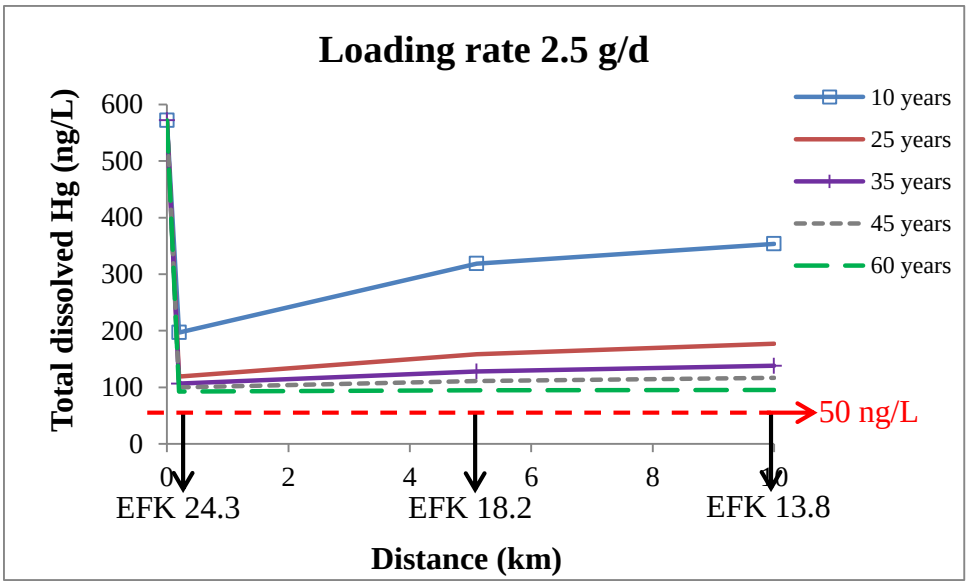

Figure 106. Total dissolved Hg concentration along the domain with Hg mass loading of 2.5 g/day.

In simulation scenario 2, the Hg mass loading rate to the EFPC was reduced to 1.5 g/day. The simulation was conducted to predict the time that took to reduce the Hg concentration in the creek to criteria concentration of 0.051 µg/L. The simulation started with initial background Hg concentrations in the creek of 0.5 µg/L, 0.3 µg/L, and 0.2 µg/L at EFK 23.4, 18.3, and 13.8, respectively.

The results from using a Hg mass loading to 1.5 g/day in the simulation (see Figure 107) showed that the dissolved Hg concentration at EFK 24.3 becomes lower than the downstream concentrations (EFK 18.3 and 13.8) by year 9 (not shown in the figure). By year 15, Hg concentrations at EFK 24.3 are predicted to be about 0.15 µg/L (from 0.5 µg/L), extending over a larger area compared to scenario 1 (0.5 km^2 for Scenario 1, and 1 km^2 for scenario 2). Total dissolved Hg concentrations at EFK 18.3 and EFK 13.8 did not show a significant change after 15 years. However, the reduction in total dissolved Hg concentrations at EFK 18.3 and 13.8 is expected in year 25 to reach 0.15 µg/L. Concentrations of less than 0.1 µg/L for the entire model domain are obtained by year 35; they are 0.06, 0.07 and 0.08 µg/L at EFK 24.3, 18.3, and 13.8,

respectively. It can also be noted in Figure 108 that the total dissolved Hg concentration in the EFPC shows a big reduction during years 10, 25, and 35; the reduction percentage of Hg concentrations at all stations, between years 10 and 25 is in the range 100% - 200%; and is the same for years between years 25 and 35 is in the range is 25% - 50%. The reduction rate slows down in later years. The reduction rate between years 45 and 60 is very low with similar concentrations. Results show that the total dissolved Hg reaches its constant concentration of 0.051 µg/L (EFPC criterion) by year 45. To summarize, with a 1.5 g/day of Hg loading to the EFPC, the total dissolved Hg concentration within the model domain is predicted to decrease, meeting the criteria of 0.051 µg/L by year 45.

0 year

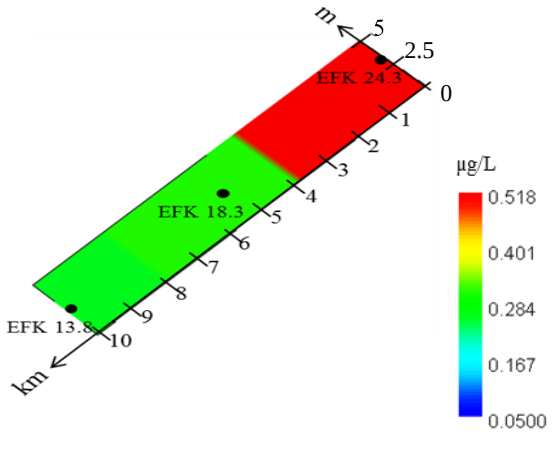

1 year

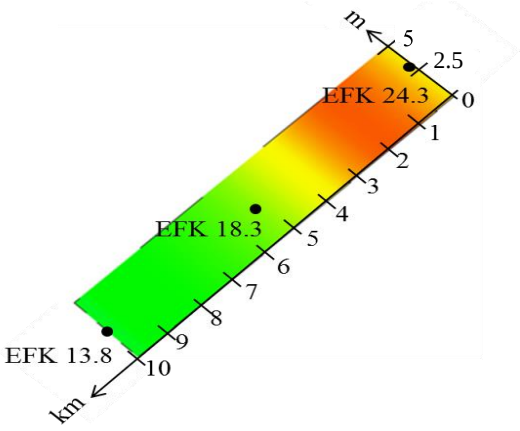

15 years

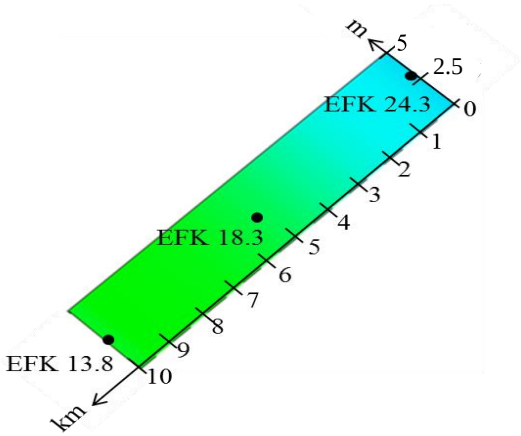

25 years

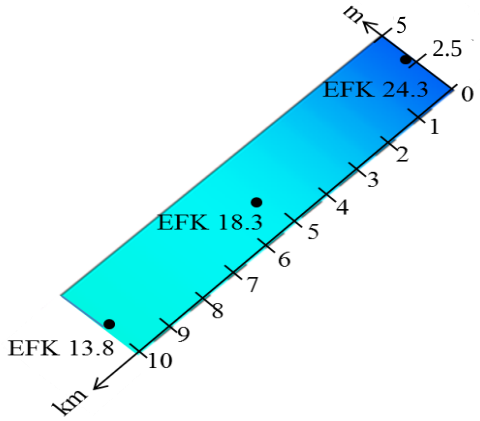

35 years

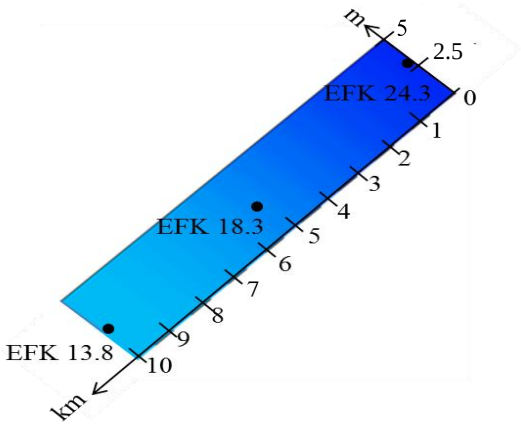

45 years

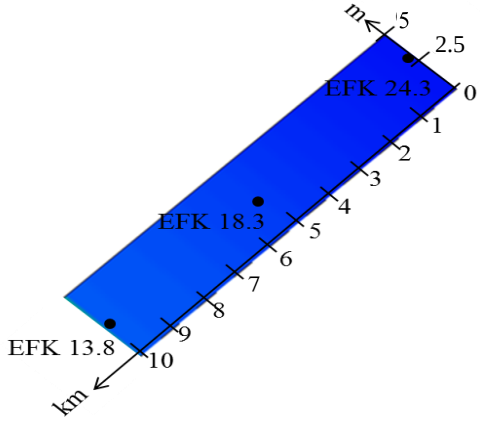

Figure 107. Transport of dissolved Hg in EFPC water with Hg mass loading of 1.5 g/day (from EFK 24.3 to EFK 13.8).

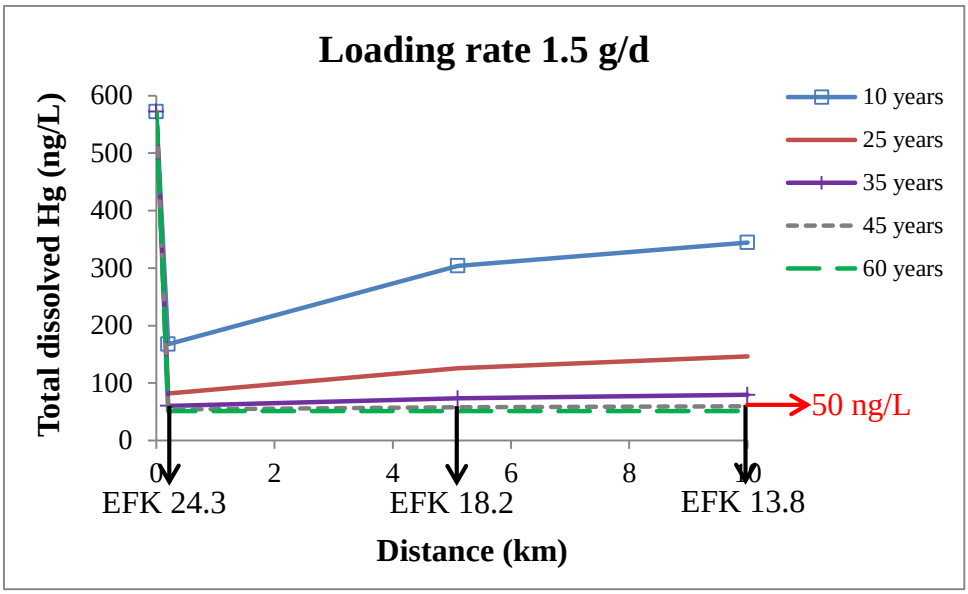

Figure 108 Total dissolved Hg concentration along the domain with Hg mass loading of 1.5 g/day

In simulation scenario 3, the Hg loading into the EFPC was set at 1.5 g/day. The simulation was conducted to predict the time that took to reduce the Hg concentration in the creek to criteria concentration 0.051 µg/L. The simulation started with initial background Hg concentrations in the creek, which were of 0.5 µg/L, 0.3 µg/L, and 0.2 µg/L at EFK 23.4, 18.3, and 13.8, respectively.

0 year

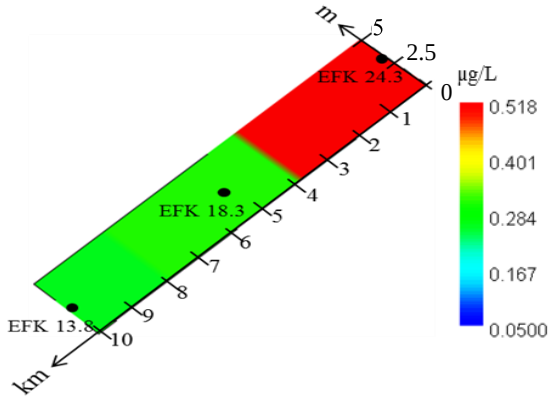

1 year

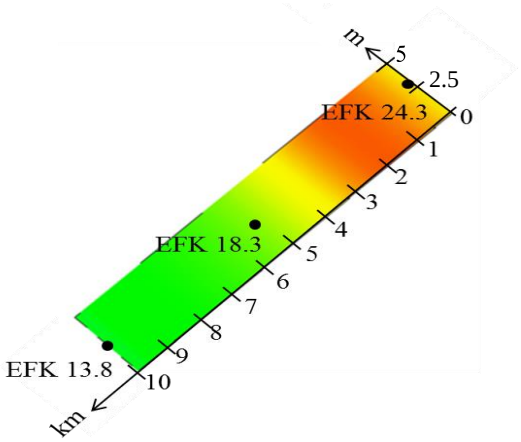

10 years

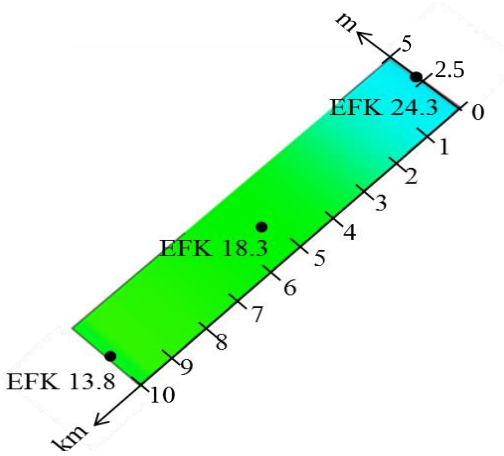

20 years

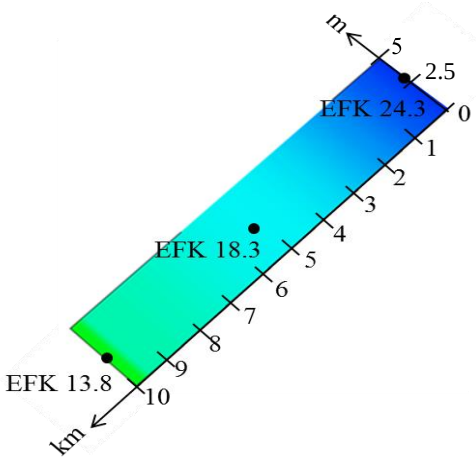

30 years

35 years

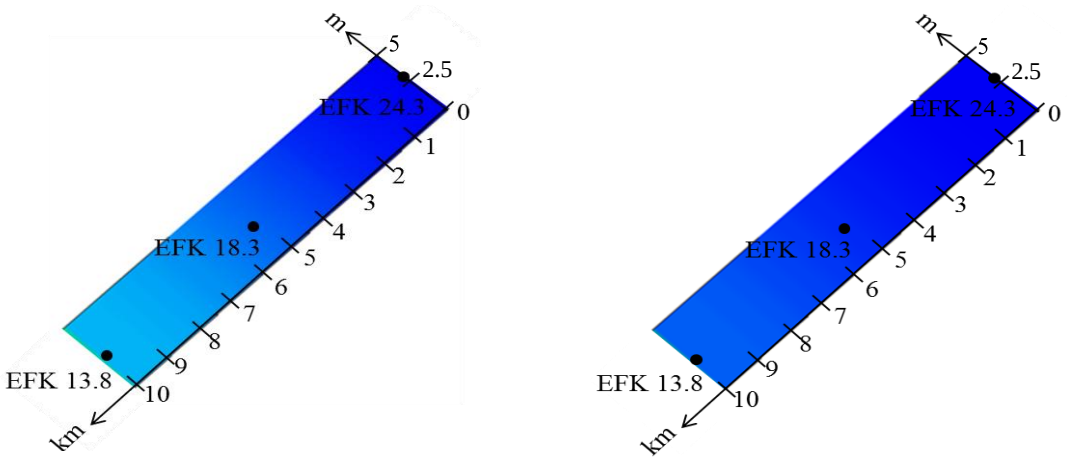

Figure 109. Transport of dissolved Hg in EFPC water with Hg mass loading of 0.5 g/day (from EFK 24.3 to EFK 13.8).

In Figure 64, with a Hg mass loading of 0.5 g/day, the simulation result showed that the concentration at EFK 24.3 is diluted and is lower than the downstream concentrations (EFK 18.3 and 13.8) by year 7 (not shown in the figure). In year 10 the total dissolved Hg concentration at EFK 24.3 reaches about 0.15 µg/L (from 0.5 µg/L), while the concentrations at EFK 18.3 and EFK 13.8 did not show any significant change with respect to the previous scenarios. However, the reduction in total dissolved Hg concentrations at EFK 18.3 and 13.8 reached 0.15 µg/L by year 20. Concentrations less than 0.1 µg/L for the entire model domain were estimated by year 30; they were 0.06, 0.07, and 0.08 µg/L at EFK 24.3, 18.3, and 13.8, respectively.

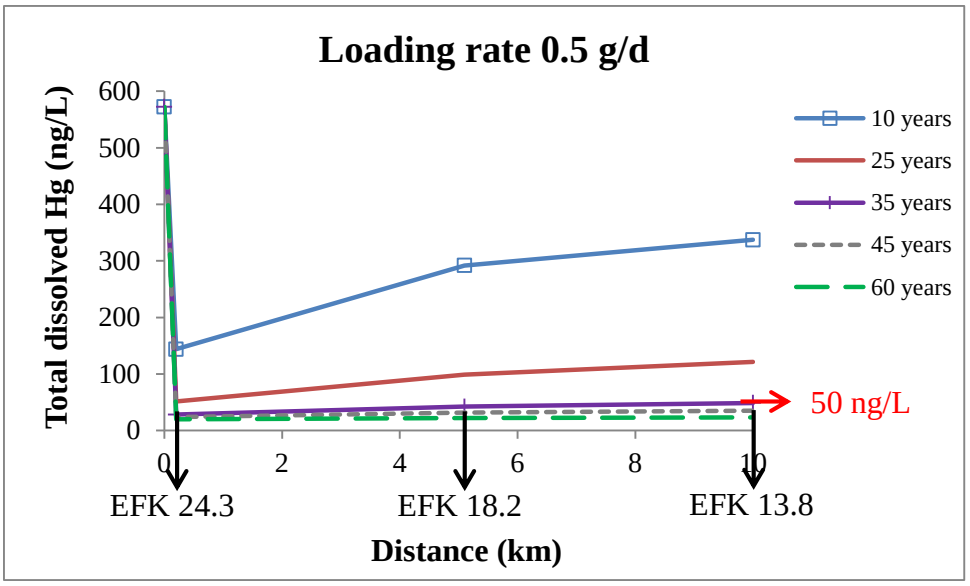

Figure 110. Total dissolved Hg concentration along the domain with Hg mass loading of 0.5 g/day.

Figure 110 shows a big reduction of total dissolved Hg concentrations during years 10, 25, and 35. The reduction percentage of Hg concentration at all stations, between years 10 and 25 is in the range 100% - 230%. The same reduction is predicted between 25 and 35 years, in the range of 25% to 70%. The reduction rate reduces in later years. The reduction rates between years 35, 45 and 60 are low, with similar concentrations. Results also show that the total dissolved Hg can reach its constant concentration of 0.051 µg/L (EFPC criterion) by year 35. It can be summarized that with a 0.5 g/day of Hg loading into the EFPC, Hg concentrations within the model domain should decrease and meet the criterion of 0.051 µg/L by year 35.

Although, various water chemical constituents were measured at this station, DOC data was not available. A vast number of studies indicated that, for ENP, DOC plays an important role on Hg fate. This is because of the abundance of existing of DOC in that setting and the strong binding constant of Hg with the Thiol ligand or the reduced sulfur ligand (RS^-) present in DOC. Therefore, DOC and its RS^- content must be considered and accounted for the Hg-speciation study with ENP waters. Although, there was no data available for DOC at P33 station, the DOC

concentrations in this study were calculated using a correlation between total suspended solid (TSS) and DOC using data obtained from Cai et al. (1999) (Figure 111).

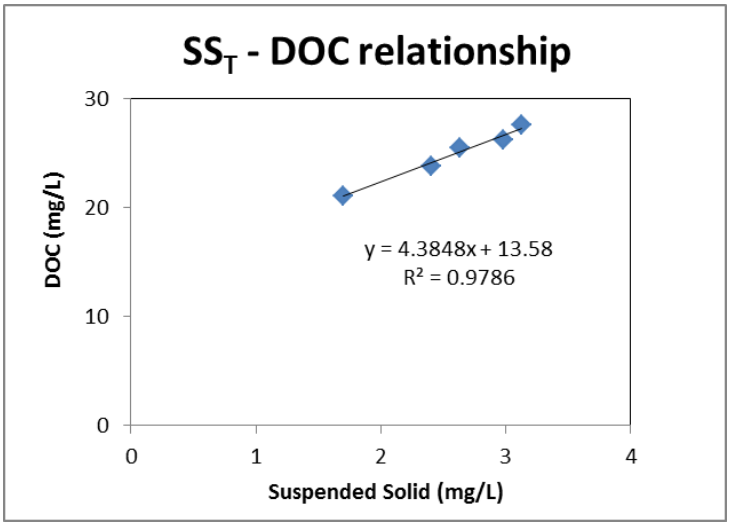

Figure 111. Relationship between the concentration of total suspended solid and DOM in (Cai et al., 1999).

The linear relationship between TSS and DOC, Y = 4.38X + 13.58 where Y is DOC (mg/L) and X is TSS (mg/L), calculated using data in Cai et al. (1999) was used to estimate the DOC concentration at station P33. With this relationship, the calculated DOC at P33 ranged between 17-153 mg/L. The average DOC concentration over 11 years was estimated to be 31 mg/L. The average DOC value (31 mg/L) was consistent with the data reported by Reddy and Aiken (2001) and this value was used for this study.

The calculated DOC concentrations were then used to calculate the RS- content in DOC using an equation proposed by Dong et al. (2010). The calculated RS- ranged between 7.3 – 24.2 x 10-5 mg/L, with an average of 8.6 x 10-5 mg/L. The average values of surface water quality data, including calculated DOC and RS-, used in this study are shown in Table 53.

Table 53. Surface water quality data at P33 station (during 2001-2011) (mg/L for concentration, °C for temperature) (DBHYDRO)

Constituents	Range	Average Value
Temperature	9.0-30.7	23.76
pH	7.0-8.1	7.47
DO	0.8-9.1	4.20
Alkalinity HCO_3^-	53-277	179.09
Total Ca	39.8-118.3	59.48
Total Cl	14.3-108	54.81
Total PO4	0.003-0.075	0.0079
Nitrate NO_3^-	0.005-0.127	0.029
Nitrite NO_2^-	0.002-0.011	0.0035
Total K	0.8-5.3	3.12
Total Na	10.3-66.6	36.26
Total Mg	3.9-17.1	10.48
Total SO_4	0.6-239	9.26
Total SS	1-32	3.98
DOC	17.96-153.89	31.05
$*RS^-$	7.3-24.2 x 10^{-5}	8.6 x 10^{-5}
Total Hg	0.7-5.9 x 10^{-6}	2.023x10^{-6}

*RS^- represents the reduced sulfur was estimated by the equation proposed Dong et al., 2010)

Hg Speciation Distribution

The surface water quality data shown in Table 50, was used in the simulations. The speciation distribution of Hg surface water is shown in Figure 67.

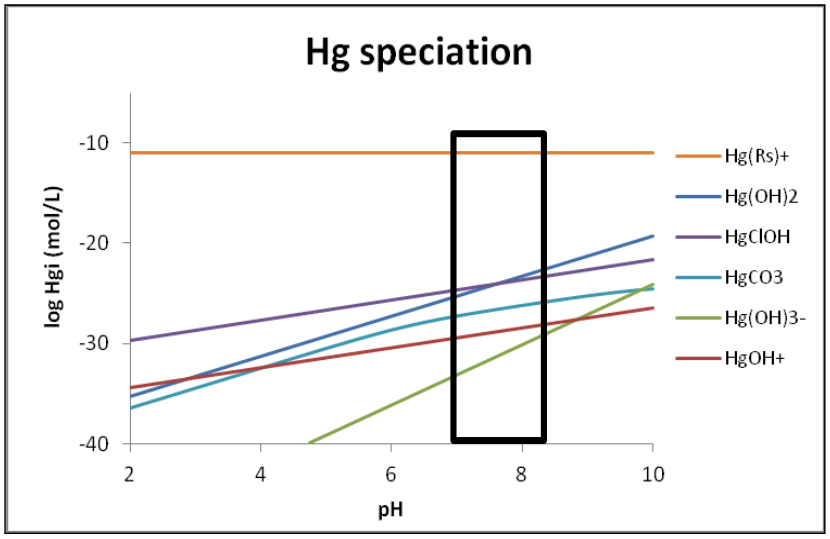

Figure 112. Hg speciation in surface water. The black box represents the pH range of surface water (pH 7.0-8.2)

It can be seen from Figure 67 that most of Hg(II) binds with the RS^- content in the DOC. The $Hg(RS)^+$ species is at least ten orders of magnitude higher than other inorganic Hg. This is because the reaction constant (log K = 28.5) of $Hg(RS)^+$ is higher than those of Hg-inorganic (Cl^-, OH^-, CO_3^-, SO_4^{2-}, etc.) complexation.

Sensitivity Analysis of Hg Species to Water Temperature and pH

The sensitivity of Hg species to water temperature and pH was studied for a range of temperatures (5-35 °C) and pH (2-10) (Figure 113).

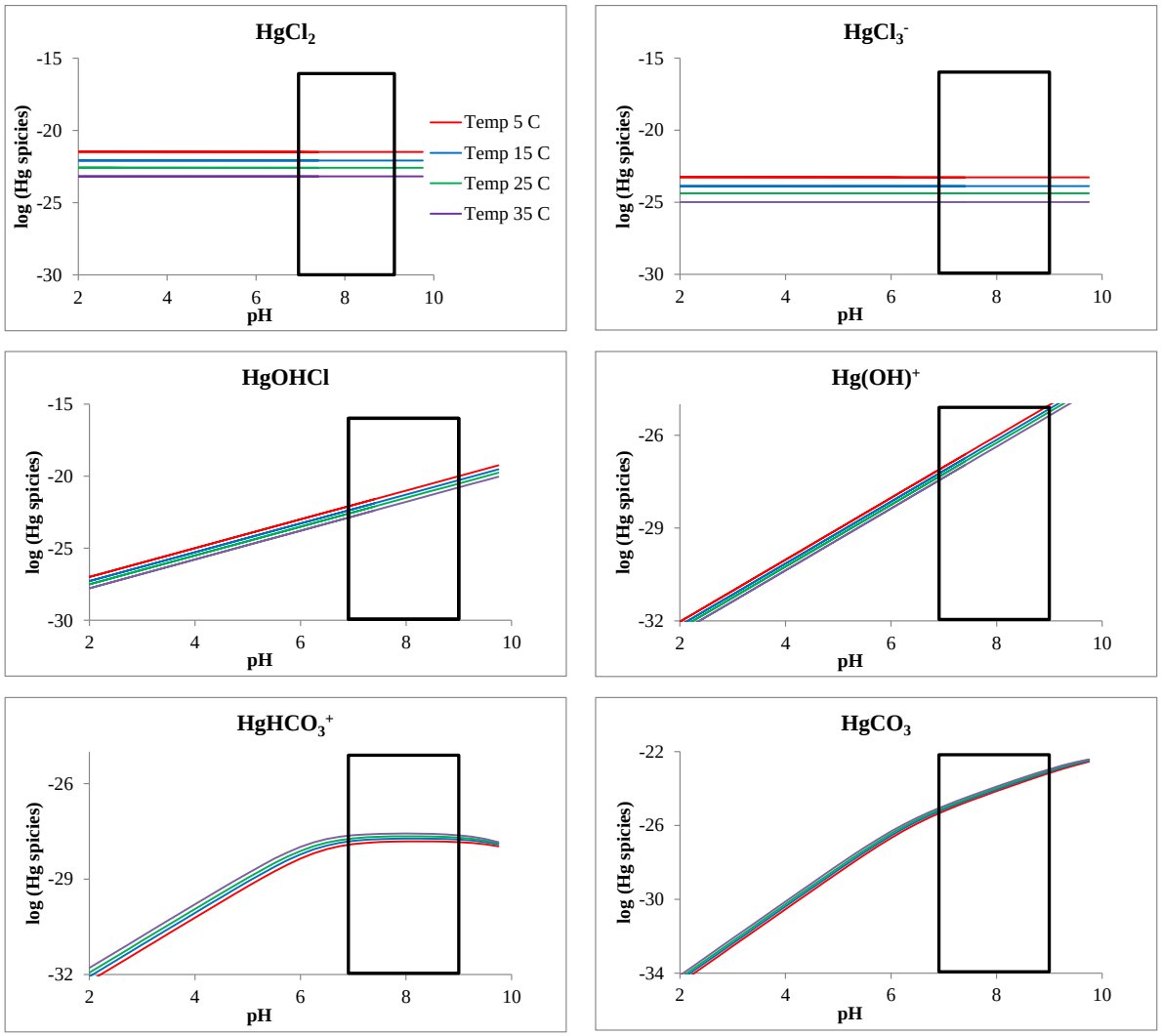

Figure 113. Hg species sensitivity to temperature (5-35 °C) and pH (2-10). The black box shows the water pH range

The formation of Hg-Cl and Hg-OH species decreases with increase in water temperature, while higher temperatures favor the formation of Hg-CO_3 species (Figure 68). The water pH does not affect the formation of Hg-Cl species; however, the concentration of Hg-OH species shows a steady increase with water pH. This is because higher pH promotes the formation of OH^- ion. The concentration of Hg-CO_3 species increases sharply between pH 2-6. The rate formation of $HgCO_3$ slightly decreases between pH 6-10. However, the dominant Hg species, $Hg(RS)^+$, did not show sensitivity to water pH and water temperature.

Sensitivity Analysis of Mineral Saturation Index to Water Temperature and pH

The sensitivity analysis of water temperature and pH on the mineral precipitation in surface water condition was conducted for temperature ranges of 5-35 °C and for water pH range of 2-10.

Figure 69 shows the effect of water temperature and pH on the SI of dominant minerals in water. The SI of Calcite, Aragonite, Dolomite, and Huntite increases with water temperature. However, temperature does not affect the formation of $Ca(PO_4)_3OH$ and Magnesite. The water pH favors the formation of all the above minerals since the SI increases with water pH. An increase in water pH increases the precipitation of CO_3 minerals (Calcite, Aragonite, Dolomite, Huntite, and Magnesite minerals). Formation of $Ca_5(PO_4)_3OH$ mineral also increases with pH because an increase in water pH favors the production of OH^+ ion. From Figure 114, it can be concluded that at typical water condition (i.e., pH 7-8.2 and temperature = 23.4 ℃), water is expected to be supersaturated with Calcite, Aragonite, Dolomite, and $Ca_5(PO_4)_3OH$ minerals.

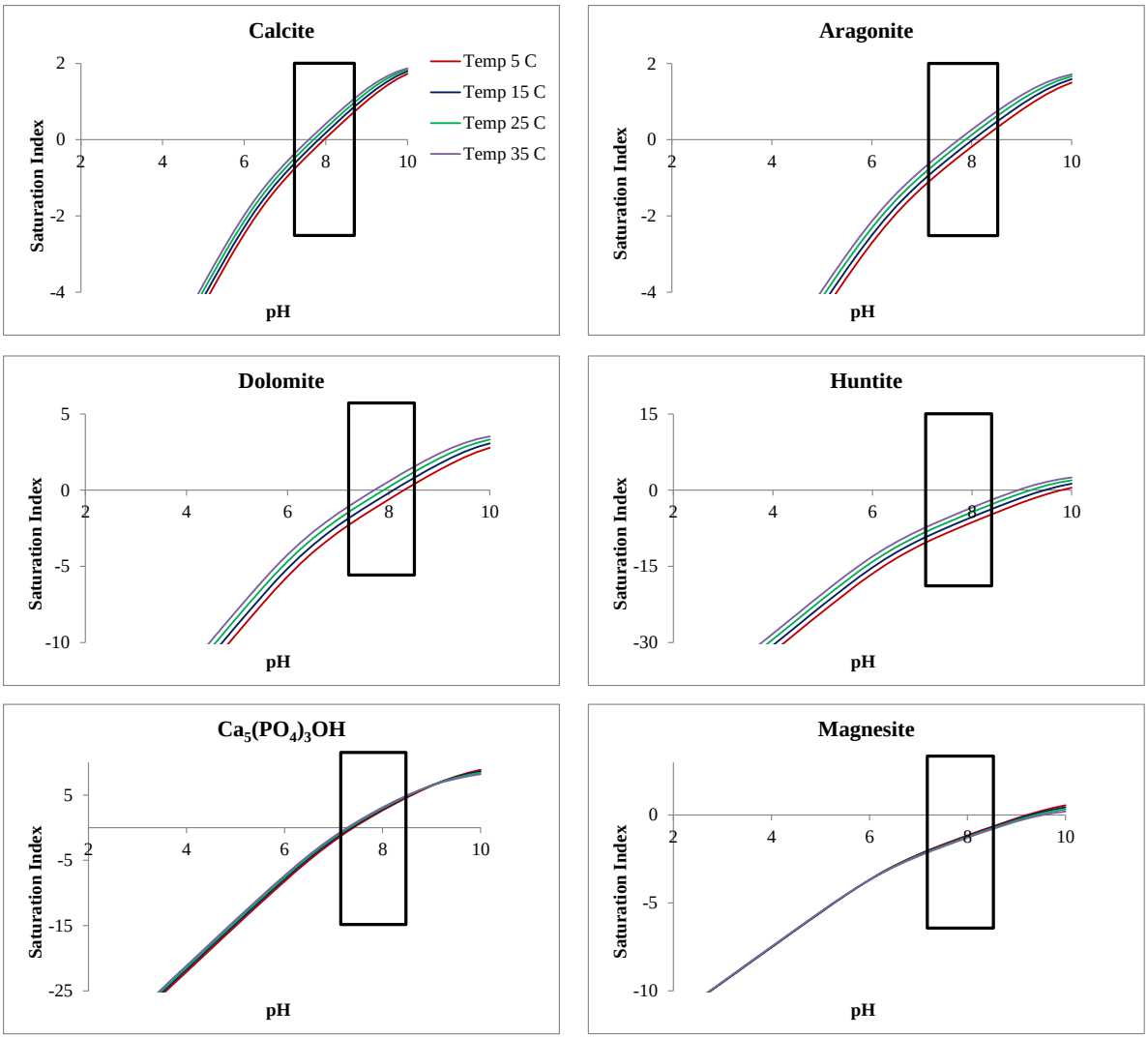

Figure 114. Sensitivity of the mineral precipitation for water with water temperature and pH.

Sensitivity to Salinity on Inorganic Hg Speciation

For test-bed, seawater intrusion becomes an important variable that can affect water quality. The fate of Hg and Hg-species distribution is expected to be affected by this variable as well. In this section, the sea and fresh water mixing model was used in order to predict and simulate the Hg-species distribution at various salinity contents (Bloom and Crecelius,1983; Conaway et al., 2003; Grassi and Netti, 2002). The freshwater water quality data collected from P33 station, in **Error! Reference source not found.**.

(without DOC) was used for analyzing the mixing with seawater. The typical seawater water quality data obtained from DBHYDRO, shown in Table 54, was used for the simulations. Simulations were conducted for various percentages of the seawater contents in the mixtures. The Hg complexation in the mixtures was then investigated.

Table 54. Seawater data (temperature in ˚C, ion concentration in mg/L) (DBHYDRO)

Constituent	Value
pH	8.2
Pe	8.4
Density	1.0
Temperature	25
Total Ca	412.3
Total Mg	1291.8
Total Na	10768
Total K	399.1
Total Cl	19353
Alkalinity as HCO_3^-	141.7
Total SO_4	2712

The Hg species distribution plotted against salinity content (‰) in the mixtures is shown in 1-D graphical plot (Figure 115). Figure 71 shows the 3-D graphical plots between concentration of Hg-species, salinity content (‰), and percentage of seawater content in the mixtures.

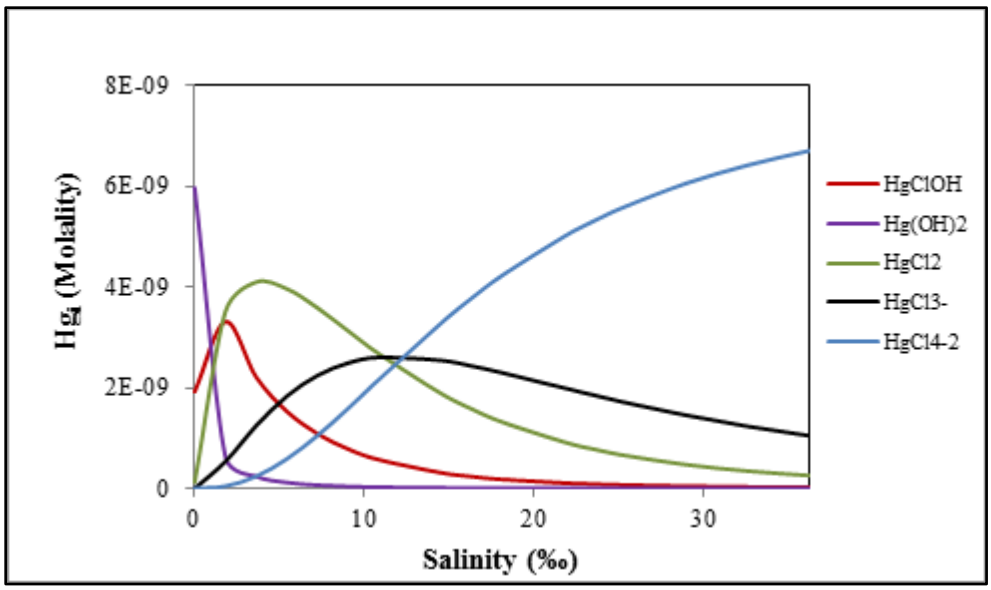

Figure 115. Distribution of Hg-species at various salinities (‰).

The mixing simulations of fresh and seawater yielded Figures 70 and 71, which describe the effect of salinity on the relative distribution of Hg-species. The figures depict how the different Hg-species are influenced by Cl^- concentration. At low salinity (i.e., low Cl^- concentrations) species formation is predicted to be dominated by $HgCl_2$; at higher salinities, $HgCl_2$ declined and $HgCl_3^-$ and $HgCl_4^{2-}$ increased. The overall implication of the above effect is that, salinity significantly impacts the relative distribution of Hg-species and thus the mobilization of Hg.

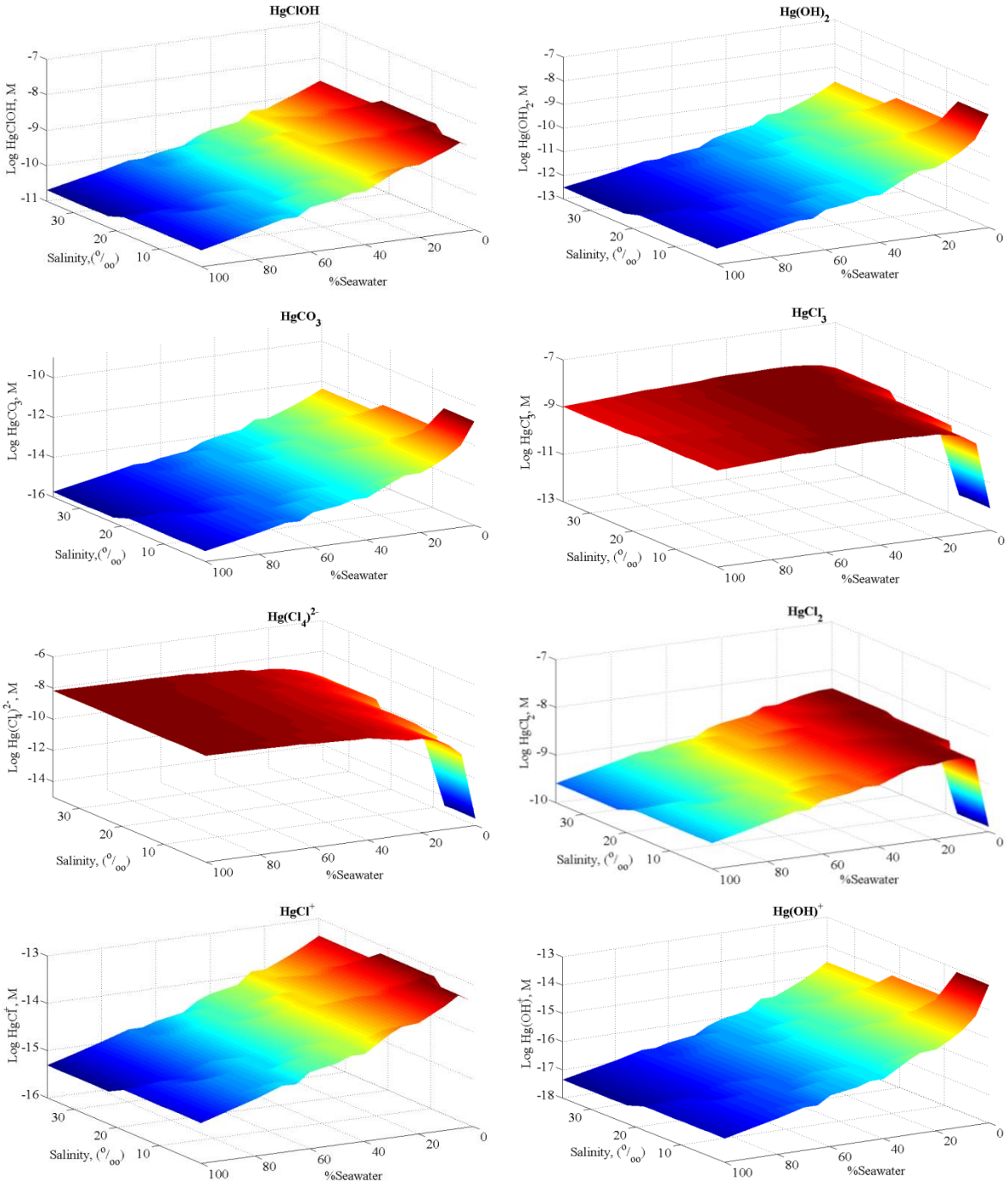

Figure 116. The 3-D graphical distribution of Hg-species as function of salinity (‰).

Hg-S Complexation and the Production of MeHg

It was mentioned earlier that Hg binds strongly with the RS^- content in DOC. The distribution of Hg species (Figure 117) that was estimated using the water quality data in Table 53.

Table 53 shows that Hg-DOC complexation (represented by $Hg(RS)^+$ species) is the dominant species. Many studies have also reported that the SO_4 content in water, especially in reducing water condition where S^{6+} is reduced to S^{2+}, is the parameter that triggers the production of MeHg (Bates et al., 2002; Jeremiason et al., 2006; Wang et al., 2009; Weaver et al., 2008; Wnalin et al., 2007). In order to understand the water quality conditions that favor the complexation between Hg and Sulfur, which can lead to the methylation of Hg, the Hg species distribution at various redox values in water was evaluated (using the water quality data at P33 station, which is shown in Table 53; the results are depicted in Figure 117.

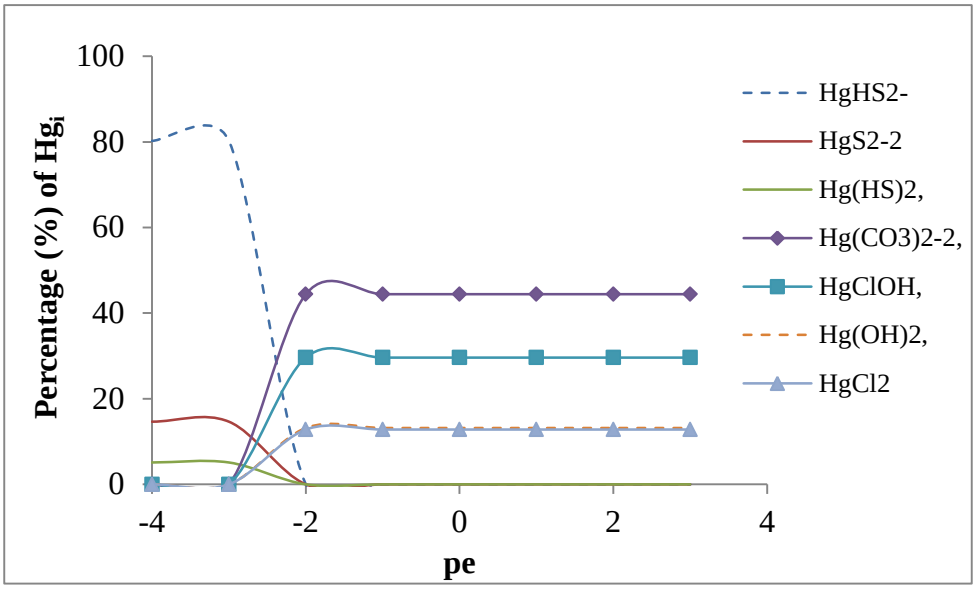

Figure 117. Hg species distribution at various redox potential (pE) in water.

Hg-DOC 0 year

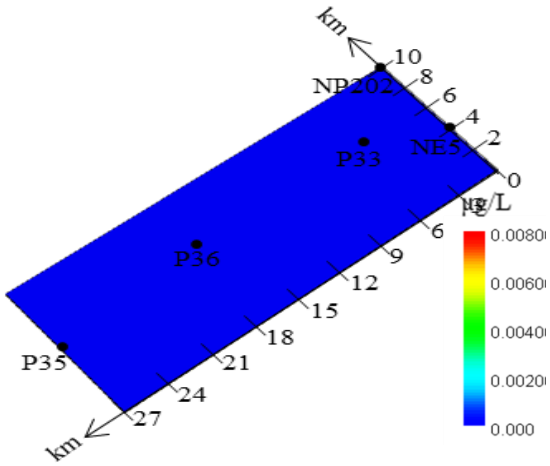

5 years

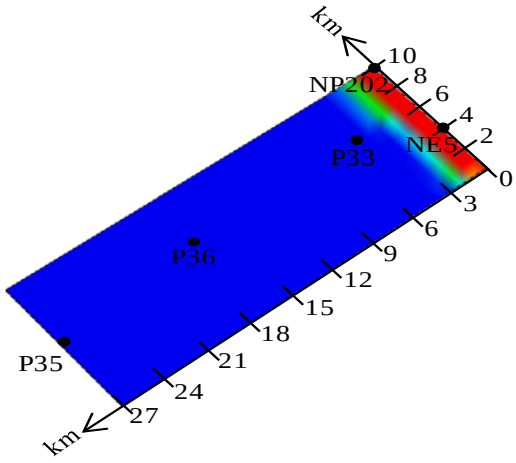

20 years

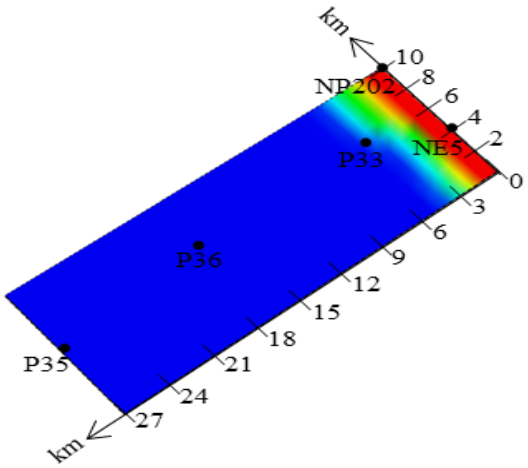

40 years

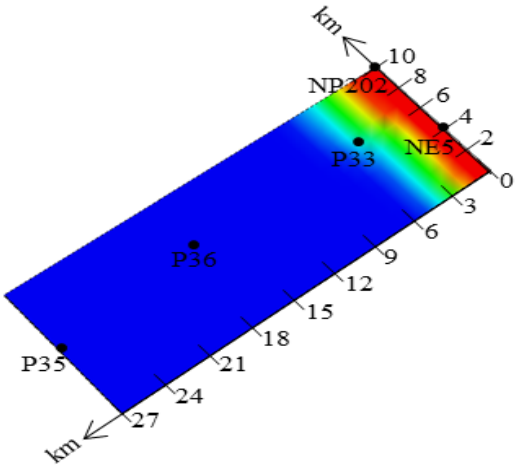

60 years

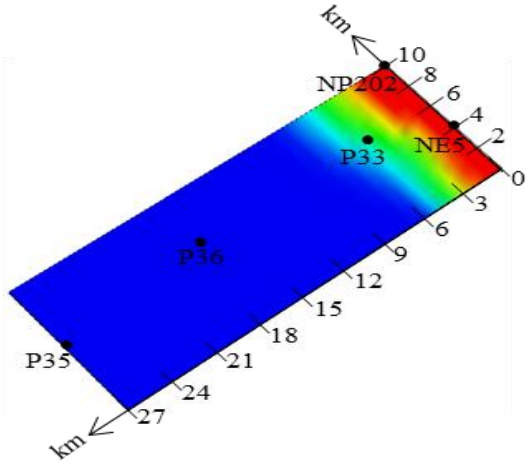

80 years

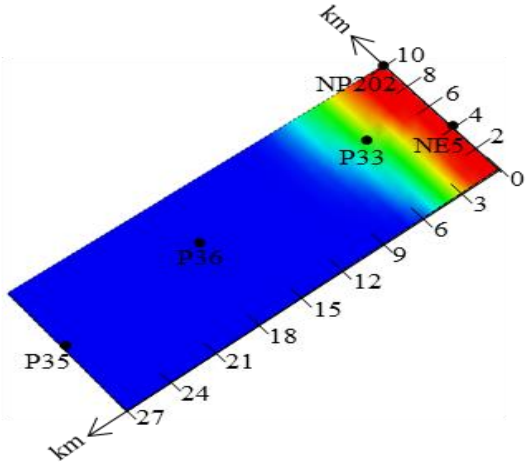

100 years

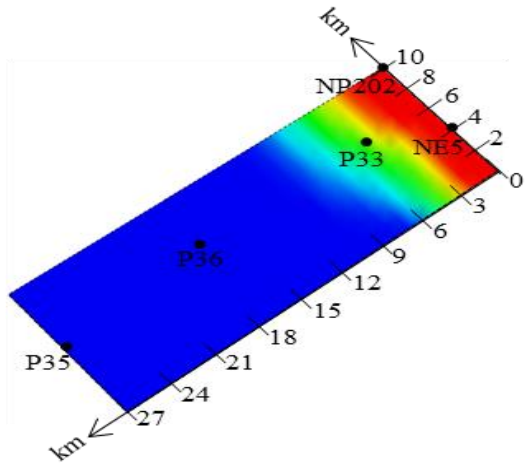

120 years

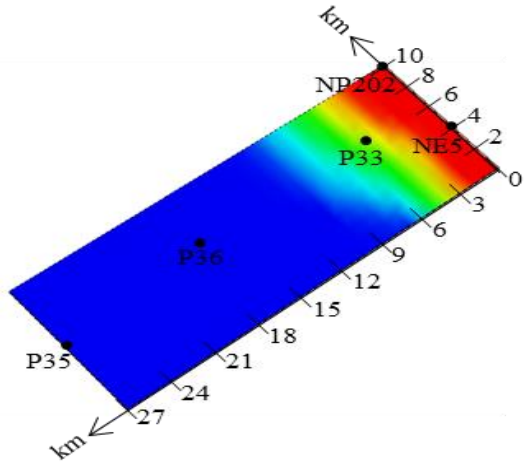

140 years

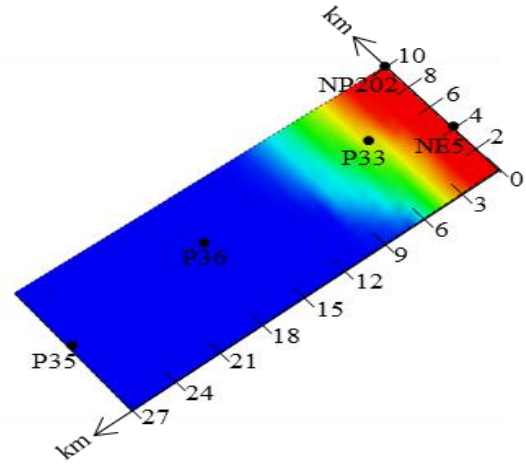

160 years

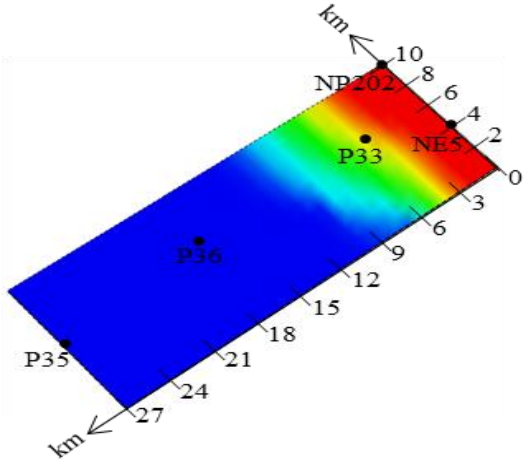

180 years

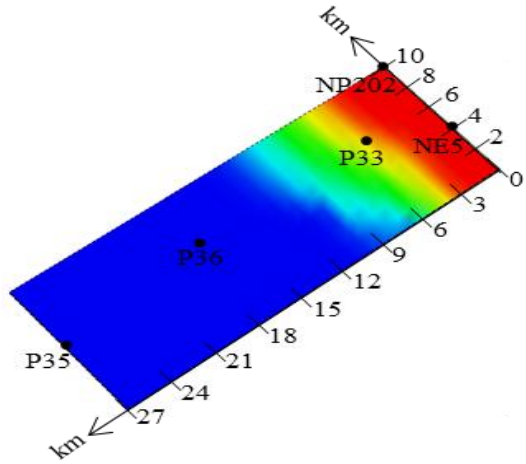

200 years

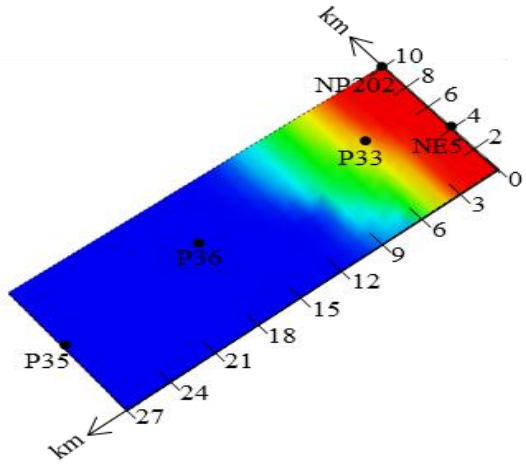

Figure 118. Hg-DOC species transport in Shark River Slough (0 – 200 years).

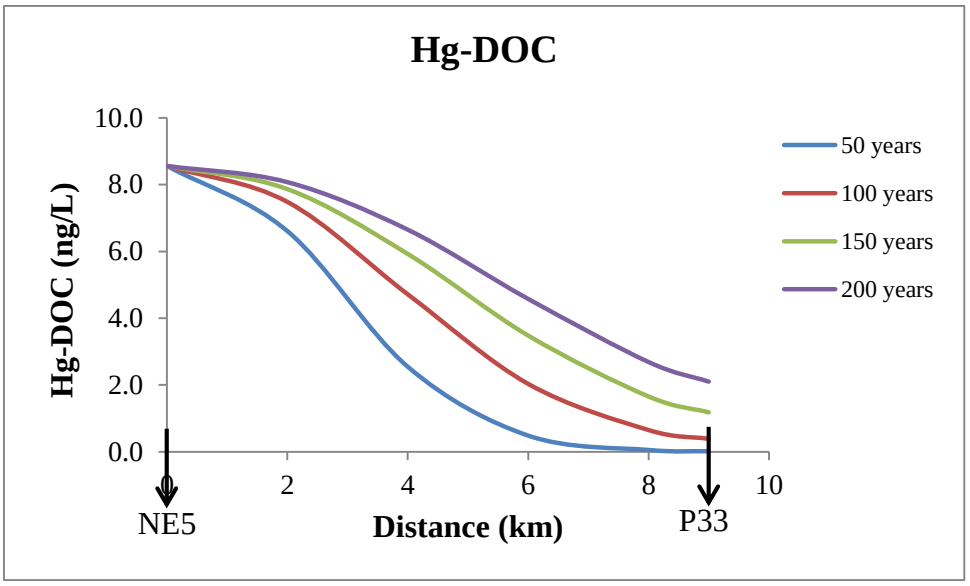

Figure 119. Hg-DOC concentration at different time periods.

Figure 120 depicts the effect of Hg retardation by peat sediments. With an average Hg-Peat log binding constant of 22 for a strong site and 11.8 for a weak site, an Hg-Peat concentration in Shark River Slough of 21.6 ng/L is obtained at the beginning of the modeling domain where Hg is introduced. This is about 73% of the initial Hg concentration. Although, the binding constant between Hg and peat is lower than those for Hg-DOC, the rich amount of peat water provides more sites for Hg to attach to peat.

Hg-Peat 0 year

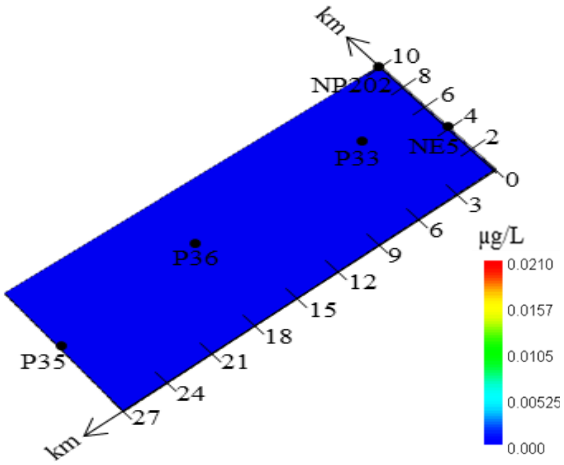

5 years

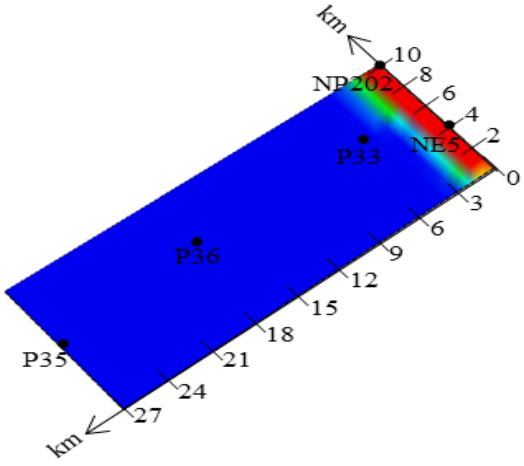

20 years

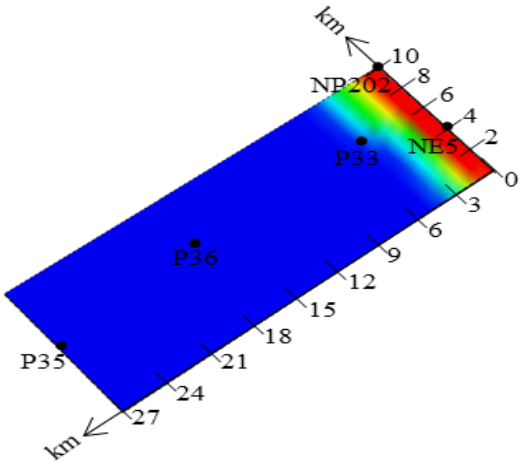

40 years

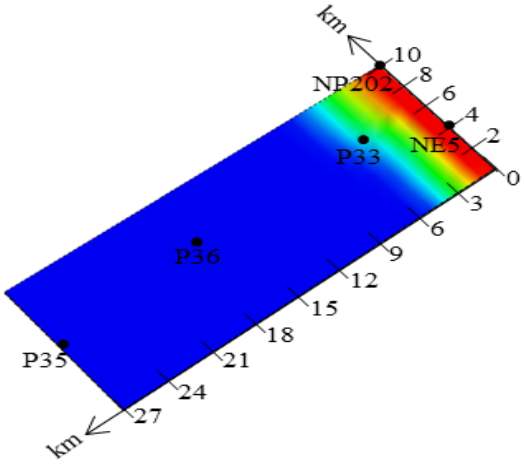

60 years

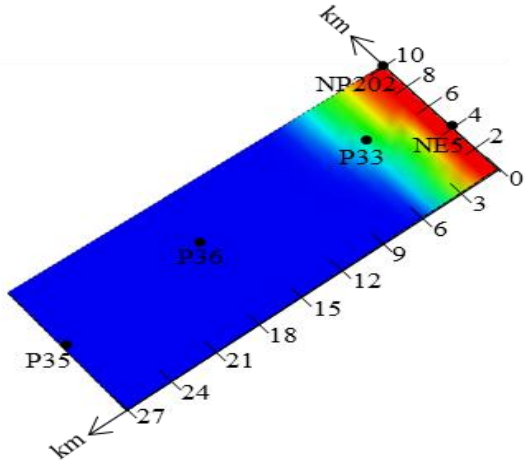

80 years

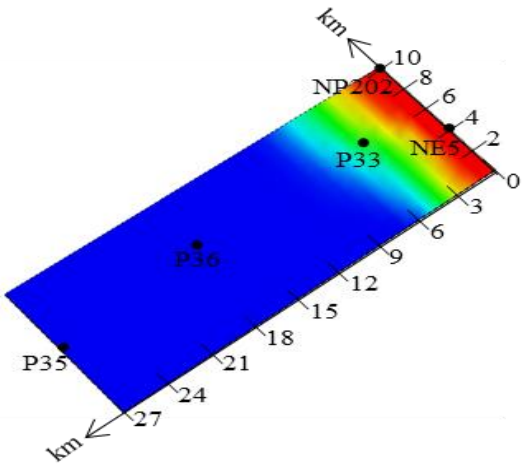

100 years

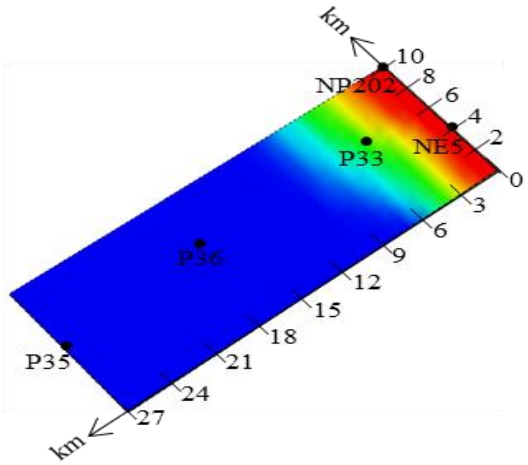

120 years

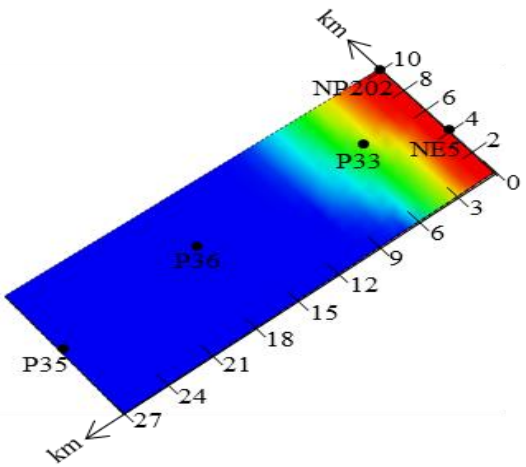

140 years

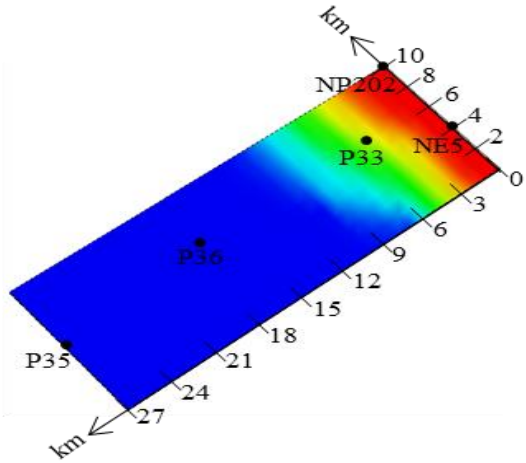

160 years

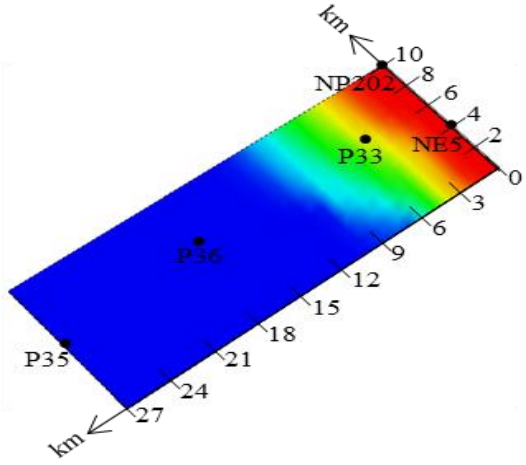

180 years

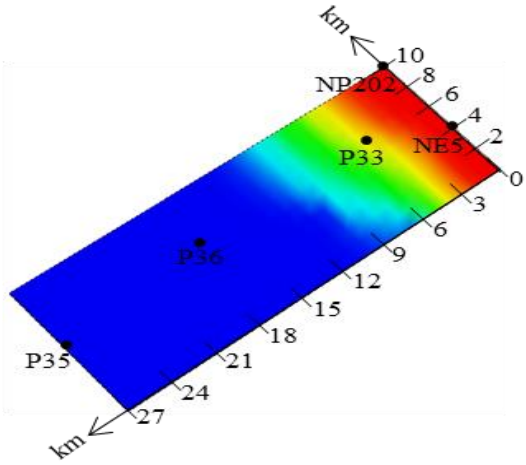

200 years

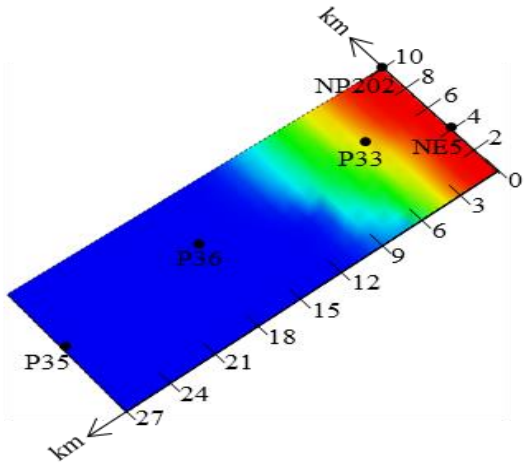

Figure 120. Hg-Peat complexation in Shark River Slough (0 - 200 years).

Figure 80 illustrates that the Hg-Peat concentration decreases with increasing distance and this may be attributed to the decrease in available free Hg along the travel distance. The Hg-Peat complex concentration, at any point (for instance P33) along the travel distance, is estimated to increase with time in relation to the water velocity. Hg attached on peat may most possibly be retained at the slough bottom and thus “immobilized”.

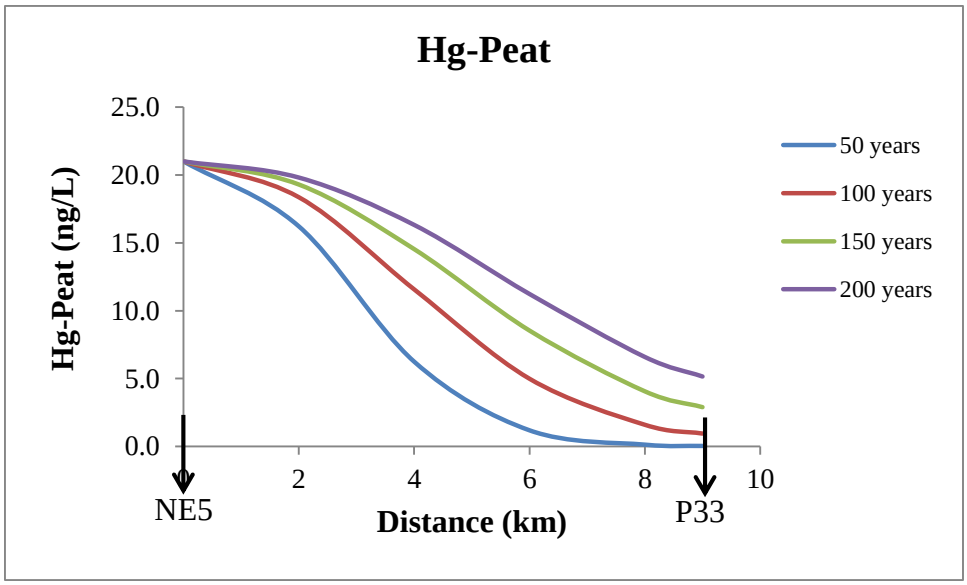

Figure 121. Hg-Peat concentration at different time periods.

The remaining trace amount of formed Hg, 6 x10^{-14} µg/L, moves with water. This amount is available to complex with inorganic ions (i.e., inorganic-Hg complexes). The transport of inorganic-Hg (0 – 200 years) in Shark River Slough is described in Figure 122.

Inorganic-Hg 0 year

5 years

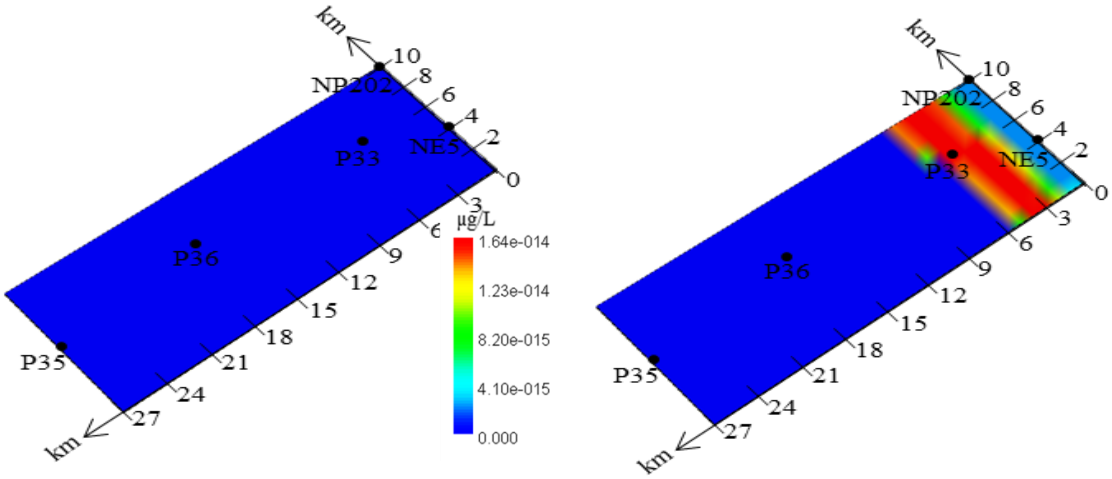

20 years

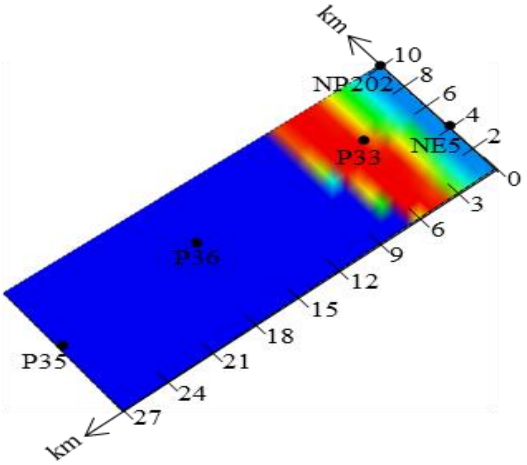

40 years

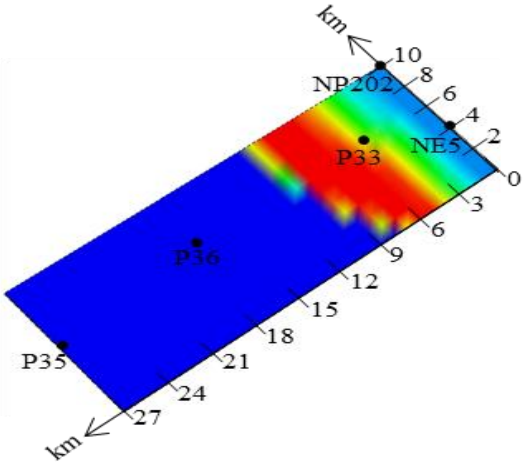

60 years

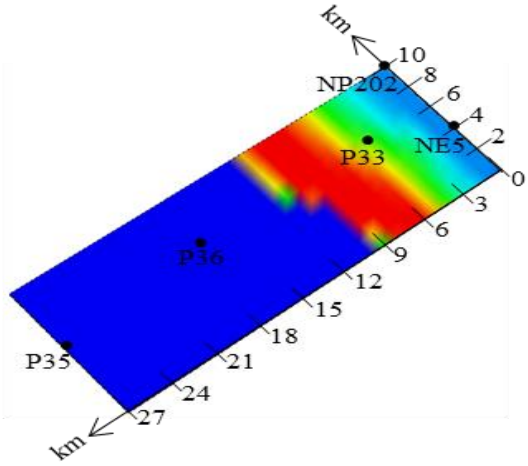

80 years

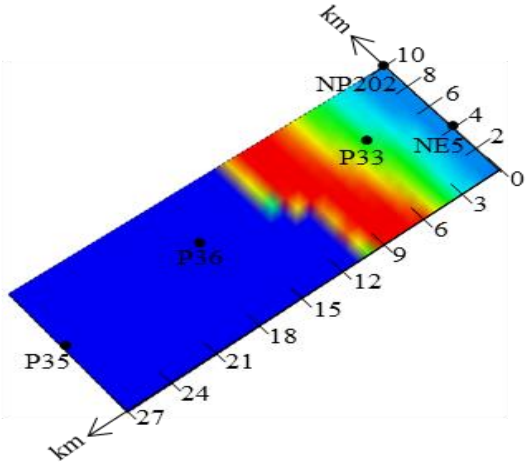

100 years

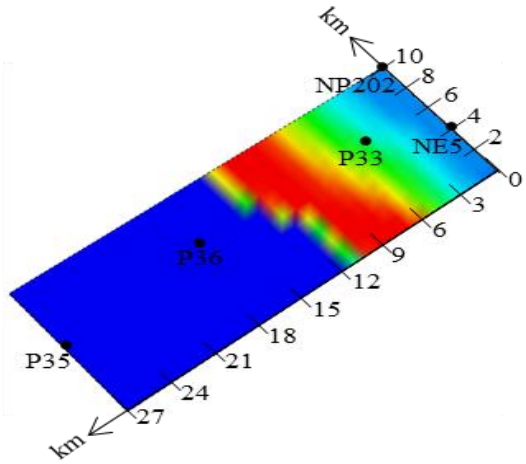

120 years

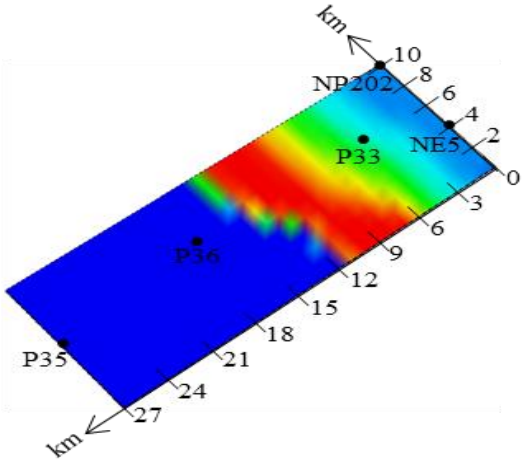

140 years

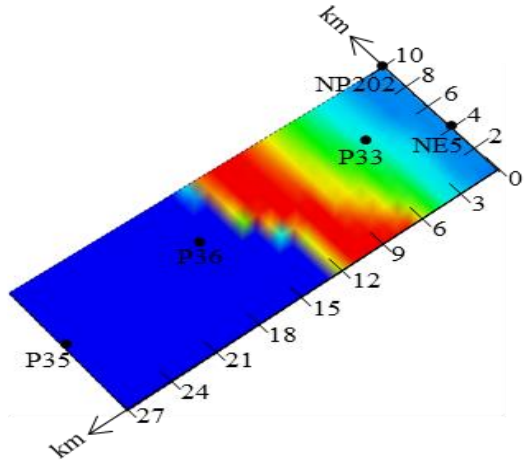

160 years

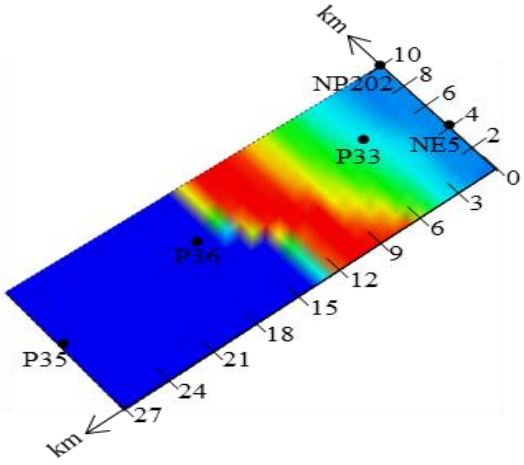

180 years 200 years

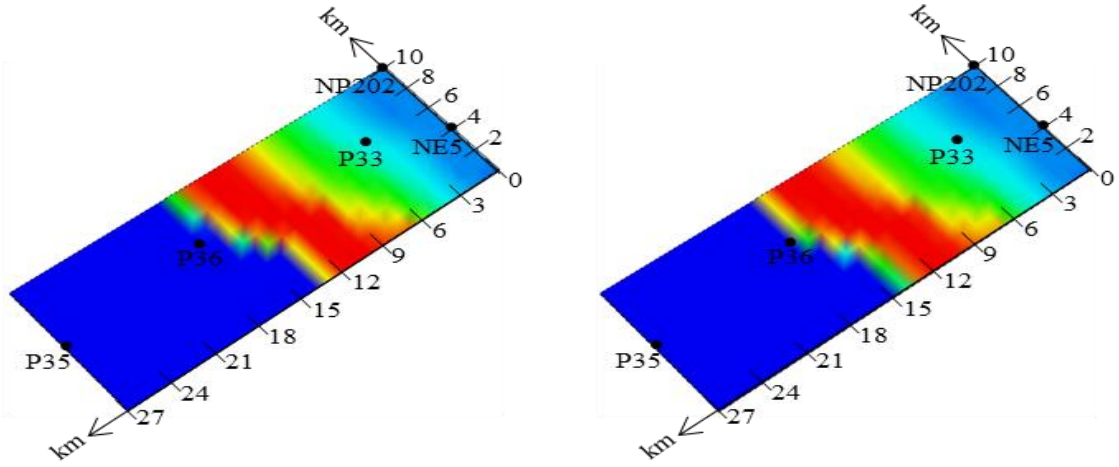

Figure 122. The transport of inorganic Hg in Shark River Slough (0 - 200 years).

Analysis of Figure 81 points out that when Hg is introduced it binds to DOC and peat; as a result, the inorganic-Hg complex fraction is expected to be low at the beginning. For the velocity of water considered here, inorganic-Hg is expected to cover 60 km^2 after 5 years and about 150 km^2 after 200 years. However, inorganic-Hg is much smaller, trace amounts, than the organic complexes to DOC and peat.

The PHREEQC model developed in this research, with a significantly enhanced Hg database, is capable of predicting the behavior of various Hg-species in a variety of processes. These include dissolution/precipitation, ion exchange, and surface complexation. In addition, the enhanced PHREEQC model, coupled with the transport model offers a computational tool to be used in site applications (specific site data input is required), to understand the fate and transport of Hg in the aquatic environments of interest.

The enhanced model was confirmed using documented experimental and field data. This strengthened the confidence in the model and its capability to simulate Hg processes and transport.

Using the experimental data documented in relevant literature, the enhanced model was tested to predict Hg species for a wide range of water pH conditions (2-10). Overall, the comparisons between the model results and those from literature were satisfactory.

The model was tested using SFWMD field data to study the capability to calculate major ions, which are typical constituents in all aqueous environments. The model prediction of major ions as function of salinity, were comparable with the observed data collected from over 30 monitoring wells in the SFWMD area. This indicates that: 1) the enhanced model is capable of simulating the geochemical processes for major ions, which are expected to interact with Hg in aqueous environments; and 2) the enhanced model is capable of capturing the effect of salinity on chemical processes.

An Hg transport simulation was conducted using the enhanced PHREEQC model in order to study the solute transport in a groundwater setting at Oak Ridge, TN. The goal was to determine the effects of ion-exchange and surface complexation on Hg transport. The model results compared well with the empirical data and proved the capability of the PHREEQC coupled-transport model. The enhanced model is an effective tool and can be used to simulate the hydrogeochemical transport of Hg in a groundwater setting. There is a lot of potential for the enhanced PHREEQC model as a tool in the screening, selection and monitoring of remediation technologies, for Hg contaminated groundwater sites, such as EFPC.

The enhanced model showed that the Hg species concentrations were influenced by the pe and pH of water. Under oxidizing conditions, $HgCl_2$, HgClOH and $Hg(OH)_2$ were the dominant species. HgCl2 was dominant in the pH range of 2.0-7.0 and HgClOH in the range of 7.0 – 7.5. $Hg(OH)_2$ was the dominant species for pH > 7.5. Cinnabar was the dominant species under reducing water conditions for all pH.

The enhanced model showed that the exchangers affected the Hg concentration in the water through the ion exchange process in the order of Illite < Montmorillonite < Vermiculite. The effect of ion exchange increased with the CEC of the exchanger. This result was consistent with the previous studies. The model results, with the improved Hg surface complexation database for $Fe(OH)_3$, Gibbsite, and Kaolinite, showed that the surface complexation process affected the Hg

concentration. These sorbents can complex strongly with Hg and hinder its transport. The effect of these minerals on Hg are in the order of Kaolinite < Gibbsite < $Fe(OH)_3$. The enhanced model also showed that $Hg(OH)_2$, $Hg(OH)^+$ and HgOHCl can complex with the minerals better than $HgCl_2$, $HgCl_3^-$ and $HgSO_4$ species for pH in the range 4.5-8.5.

The effect of ion exchange on Hg transport was observed to be low in the groundwater and surface water settings that were studied. This may be related to either the low exchange equilibrium constant or the low concentrations of exchangers or that both are expected in typical ground and surface water settings.

The effect of surface complexation on Hg transport was also estimated in both typical groundwater and surface water settings for Gibbsite, Kaolinite and $Fe(OH)_3$. Kaolinite was observed to have no effect on Hg transport in the studied surface water setting. This may be attributed to its low equilibrium constant or low expected concentrations or both.

At the typical conditions of the water at East Fork Poplar Creek (EFPC) (water pH 7.0 - 9.2 and temperature of 25 °C), the most dominant species, as predicted by the model, were $Hg(OH)_2$ and HgClOH. The formation of $Hg(OH)_2$ increased with water pH and temperature. For water pH between 2.0-7.0, an increase in water pH and temperature favored the production of HgClOH.

Simulation results predicted the water to be supersaturated with Ferrihydrite, Goethite, Magnesioferrite, Hematite, FCO_3Aptite, Lepidocrocite, Hydroxylapatite, and Arogonite. The formation of these minerals increased with the water pH. In addition, an increase in water temperature favored the precipitation of Ferrihydrite, Goethite, Magnesioferrite, and Hematite. However, temperature did not favor the formation of FCO_3Aptite, Lepidocrocite, Hydroxylapatite, and Arogonite.

The Hg transport in ORR groundwater (Bear Creek Valley) was investigated using the enhanced model. The result showed that the Hg transport was influenced by ion-exchange and surface complexation with $Fe(OH)_3$ and Gibbsite. The water quality at GW-923 showed that water was supersaturated with cinnabar. Thus, it was hypothesized that, at the test well, the dissolution of cinnabar became a source of Hg. The dominant Hg species at GW-923 was $HgCl_2$. This

indicated that, at this well location, the Cl-ligand promoted the mobilization of Hg. The presence of $Fe(OH)_3$ and Gibbsite at wells GW-363 and 369 reduced the Hg concentration in the solution and retarded the transport of Hg by surface complexation.

The enhanced model was employed to investigate the feasibility of using reduction in Hg loading as an Hg control strategy at EFPC. The model was used in the transport mode to assess the role of ion exchange and surface complexation in EFPC. Among other estimates, the application showed that the Hg concentration in EFPC can be reduced from 0.5 µg/L to about 0.08 µg/L within 60 years, if the Hg loading at the sources is reduced to 2.5 g/day. Furthermore, if the loading is further reduced to 0.15 g/day, Hg concentrations in the creek will reach 0.05 µg/L within 45 years.

CONCLUSIONS

This study has been able to enhance previous versions of the model by considering the most significant parameters and processes of flow and mercury transport for the study site and combining the processes of advection and dispersion with a sedimentation (ECO Lab) module at the EFPC Watershed scale. The objectives of the study were met through the successful integration and validation of this module to enhance the simulation of mercury transport and in the demonstration of the application of the model to the mercury TMDL analysis for the project site in the EFPC watershed.

Modeling software MIKE SHE, MIKE11, and ECO Lab were thus combined in a comprehensive package that models the flow and transport of mercury in exchange with sediment. The application of the enhanced models includes an analysis of spatial and temporal patterns stimulated by variations of selected properties of the sub domain. The impact of sedimentation on the fate of mercury was assessed through a series of simulations and using the sedimentation layer module (ECO Lab); this module addresses the dissolved mercury in the water, the adsorbed mercury concentration on suspended matter, the dissolved mercury in sediment pore water, and the adsorbed mercury in the sediment.

In the application of the model to the EFPC watershed, previous modeling efforts, which originally included only the upper portions of EFPC, were extended to include the entire EFPC watershed, down to station EFK 6.4 and the BC watershed. The model is capable of simulating the entire hydrological cycle. Water quality, transport, and sediment related parameters were updated based on DOE experimental reports and journal publications to include observed data of flow, stage, and mercury concentrations in soil, surface water, groundwater and sediments at Station 17 as well as the stations previously mentioned.

Simulations were executed for a range of input parameters to correlate stochastic hydrologic events with mercury distribution patterns and total suspended solids pattern at Station 17. The simulations were analyzed using a range of techniques, primarily comparative schematics of time-series plots, probability of exceedance curves, and load duration curves. The modeling was

intended to aid in the development of flow duration curves and mercury loads probabilities of exceedance for selected stations where applicable.

Based on the patterns exhibited throughout various observed and computed probability of exceedance curves for flow and mercury, it can be concluded that the model most accurately simulates discharges and mercury loading conditions under high, moist, and mid-range flows. Although mercury loads appear to be attenuated downstream in EFPC the same cannot be concluded of BC as it exhibits no significance difference in mercury loading upstream and downstream. Furthermore, results also show that the majority of the mercury in the creek is in the adsorbed form; accentuating the importance of suspended particles and its direct connection to the total mercury concentration in the creek. Even though mercury concentrations during high flood events decrease due to dilution; post hydrological events, the mercury concentration levels are restored. Standard mercury loads probabilities of exceedance were developed based on established limits for the site and a 90.24% reduction in loading appears to be required at Station 17.

The model is intended to serve as a useful remediation tool since the site was characterized using relevant historical records for precipitation, groundwater levels, and river discharges obtained from OREIS and ORNL databases, which were incorporated into the model in the form of boundary or calibration conditions. The incorporation of the ECO Lab module should better characterize the mercury processes in the EFPC environment since mercury species are known to diffuse from contaminated sediment pore water to creek water in the form of diffusive transport.

The ECO Lab water quality model was used to add the exchange of mercury between sediments and stream flow to the existing flow and transport model built in MIKE SHE/MIKE11 software, for the Upper East Fork Poplar Creek Watershed, located in Oak Ridge, Tennessee. The contribution of small mercury contaminated particles settling down into the riverbed and being resuspended by changes in hydrodynamic conditions in the creek is fundamental to the accurate simulation of mercury concentrations in streams. The higher surface area characteristic of clay and silt particles increases their capacity to adsorb higher concentrations of mercury when

compared with coarser particles, explaining the importance of studying the interaction between suspended sediments and the contaminant.

The transport processes in the ECO Lab module are defined by the constant interaction among four river sub-domains: dissolved mercury in the water, adsorbed mercury in the suspended solids in the water, dissolved mercury in the sediment pore water, and adsorbed mercury in the sediment. Adsorption/desorption of the metal occurs to and from particulate and dissolved phases in the water column and in the sediment bed. Diffusive transfer of dissolved metal occurs between the water column and the sediment pore water.

Results from the sensitivity analysis show that among all the parameters in the ECO Lab module, suspended solids have the highest sensitivity to critical current velocity; the resuspension rate is the most influential parameter for the simulation of TSS peaks while particle production rate and settling velocity have more influence for lower loads. In general, the TSS load increases when the resuspension rate and/or particle production rate increases, and when the settling velocity and/or the critical velocity decreases.

Among the ECO Lab variables controlling mercury concentration in the sediments, and water column, the organic carbon partition coefficient ($k_{oc)}$ has the largest effect on the dissolved mercury in the sediment. In general, as k_{oc} decreases, the dissolved mercury in the sediment increases, as it represents an increasing affinity of the contaminant for the liquid phase. The desorption rate of mercury in water (k_w) is the variable controlling the dissolved and adsorbed mercury in the water column; increase in this rate results in higher dissolved mercury and lower particulate mercury. The concentration of suspended solids in the water is also a major parameter in the simulation of adsorbed mercury in the water column.

Total mercury concentrations in the water column are strongly influenced by the hydrodynamics of the water body. The numerical model results show a high correlation between water flow, suspended solids load, and mercury concentration in the water, highlighting the importance of the exchange of small particles with the bed, which serves as a continuous source of mercury to the surface water. After considering the mass of mercury contributed by the outfalls it was

concluded that, in 2005, 32% of the mercury measured at Station 17 originated from non-point sources, most likely the exchange of sediments with the bed.

Mercury in water is found in both the dissolved and the particulate phase. In the dissolved phase, mercury binds to the dissolved organic carbon, and in the particulate phase it binds to suspended solids. According to the simulation results, approximately 73% of the total mercury in the water column is particulate bound. This behavior can be attributed to the high affinity of mercury to the organic matter content of the sediments; consequently, the higher the fraction of organic carbon, the higher the affinity of the metal for the particulate phase.

Improvements can be made to the study in several aspects. For instance, since the study is performed at a watershed scale it might be beneficial to consider the development and implementation of site-specific modeling applications to smaller areas at contaminated buildings and pipes. A more thorough understanding and modeling of the connections between concentrations of inorganic mercury precursors and methylmercury concentration is also needed to better predict future trends of mercury transport at the site. In the thesis research related to this task, the EPA water quality limits previously mentioned and based on water usage classification were used to establish a comparison between simulated and recorded mercury loading. An additional recommendation to improve the understanding of the EFPC system is to more specifically apply the model to understand the bioavailability and bioaccumulation in fish in order to establish a more direct connection between water quality and the DOE ROD set fish tissue concentration value of 0.3 milligrams methylmercury per kilogram of wet-weight fish tissue for the site.

This task is using the surface flow model for the East Fork Poplar Creek (EFPC) to determine the discharges from the stormwater drainage system (based on measured data of flow and concentration) and for each of the outfalls along the Upper East Fork Poplar Creek and to provide simulations of TMDL and NPDS discharges from the watershed. A new set of subsurface groundwater table boundary conditions were developed. Additionally, the boundary conditions which include rainfall, evapotranspiration, timeseries of outfalls, rivers and canals were updated.

The target for the total maximum daily load (TMDL) analyses is the numeric water quality criterion for mercury for the specified EFPC waterbody. The target concentration was selected based on the detailed description of water uses and regulations established by EPA, DOE, and TDEC. These numeric water quality targets were translated into TMDLs through the loading capacity or as defined by EPA as "the greatest amount of loading received without violating water quality standards".

Several target load-duration curves were developed for EFPC by applying the mercury target concentration of 51, 200, and 770 ppt to each ranked flow used to generate the flow duration curve. The mercury target maximum load corresponding to each ranked daily mean flow was computed by multiplying the recreation use water quality criterion (51 ppt) by the flow and by the appropriate unit conversion factor. The same calculation was performed for the Record of Decision (ROD) designated target concentration of 200 ppt and water quality criterion of 770 ppt established to sustain fish and aquatic life.

Target load reduction criteria were developed using percent reduction which was calculated as the difference between the mean and the water quality criteria, considering a confidence interval, and divided by the mean with the incorporated confidence interval. Figure 46 shows the standard water quality criteria compared to the simulated mercury loading for which the required percent reduction was applied. Figure 46 3-4 shows that the percent reduction places the simulated loading within the range of the 51 ppt water quality criteria and below the 200 ppt standard mandated by the DOE record of decision.

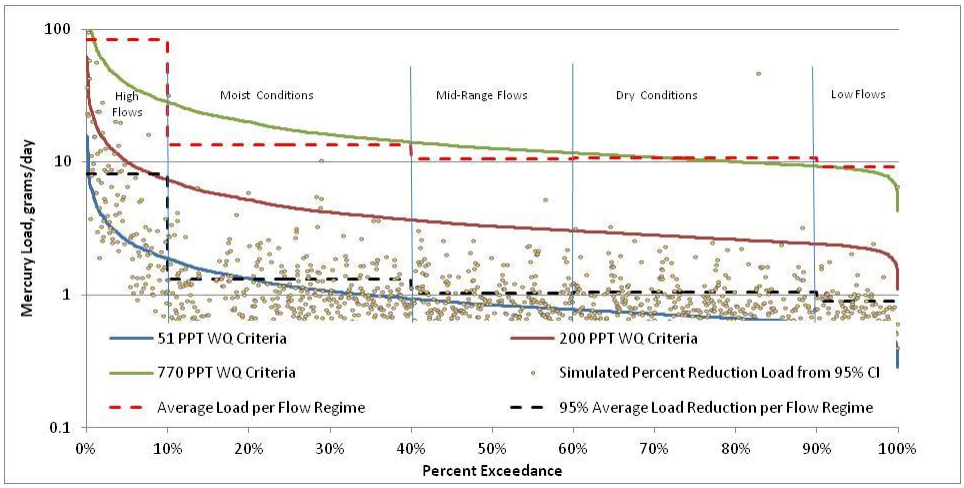

Figure 123. Comparison of simulated mercury loading with applied percent reduction and target TMDLs.

The model was used with the newly developed ECOLAB template which incorporates methylmercury into the set of kinetic and thermodynamic equations. A series of simulations were completed during this period to conduct calibration and validation.

The target for the total maximum daily load (TMDL) analyses is the numeric water quality criterion for mercury for the specified EFPC waterbody. The target concentration was selected based on the detailed description of water uses and regulations established by EPA, DOE, and TDEC. These numeric water quality targets were translated into TMDLs through the loading capacity or as defined by EPA as "the greatest amount of loading received without violating water quality standards".

The simulations were conducted using the MIKE SHE model with the newly developed ECOLAB template which incorporates methylmercury into the set of kinetic and thermodynamic equations. The task reviewed the requirements of TMDL studies as related to ORR, including:

- Impaired watershed characterization and status, which included: i) Impairment status – Understanding the basic physical, environmental, and human elements of the watershed. ii) Data gaps and monitoring report and the existing data to identify any additional data needs and monitoring recommendations. iii) Source assessment – Identification of

sources of pollutants, and magnitude of the sources. iv) Target identification – Establishment of water quality targets intended to restore or maintain beneficial uses. This step includes the calculation of the loading capacity using some analysis to link loading to water quality.

- Loading analysis: i) Linkage analyses – Select and apply approach to establish a link between pollutant loading and water quality. ii) Load calculations – Determination of natural pollutant load, and load from human activities (i.e. diffuse nonpoint sources and point discharges). ii) Loading capacity – Calculate allowable loading capacity.
- Loading allocation: i) Loading level – Select appropriate level (geographic, temporal and source) for allocations for successful implementation. ii) Allocation scenario – Evaluate allocation scenarios representing different combinations of load reductions (WLAs and LAs) and select the most appropriate and feasible allocation scenario.

The TMDL for EFPC was developed based on analysis of water quality data. Based on most recent data, (2000 to the present), the load reductions were estimated. The percent load reduction required to decrease the mercury concentration in water from the "mean + 95% confidence interval" to the desired target level was calculated at each sampling location. The percent load reductions ranged from 85.1% to 94.0%. The highest percent load reduction (at location OF125) was selected as the TMDL for the entire waterbody.

Table 55. Analysis of Mercury Concentration in Creek Water (2000 - Present)

	OF125 ppb	C11 ppb	92334 ppb	EFK 23.4 ppb	EFK 24.4 ppb	EFK 18.2 ppb	EFK 13.8 ppb	EFK 6.3 ppb
Number of samples	726	138	277	3673	25	14	11	11
Minimum	0.20		0.20	0.20	0.22	0.21	0.21	0.20
Mean	0.70	0.49	0.63	0.50	0.44	0.30	0.33	0.42
Standard Deviation	1.83	0.49	0.7453	0.6550	0.3270	0.0744	0.0959	0.3181
95% CI	0.13	0.082	0.0236	0.0212	0.1281	0.0390	0.0567	0.1190
Mean + 95% CI	0.84	0.57\	0.6546	0.5172	0.5721	0.3430	0.3857	0.5400
90% CI	0.11	0.0684	0.0198	0.0178	0.1075	0.0327	0.0476	0.0999
Mean + 90% CI	0.81	0.5584	0.6508	0.5138	0.5515	0.3367	0.3766	0.5209
Target	0.051	0.051	0.051	0.051	0.051	0.051	0.051	0.051
% Reduction from 90%	93.9%	91.0%	92.3%	90.3%	90.9%	85.1%	86.7%	90.4%
% Reduction from 95%	94.0%	91.3%	92.4%	90.3%	91.3%	85.4%	87.0%	90.7%

Note. The % Reduction from 95% is calculated as follows: % Reduction = [(Mean + 95% CI) - Target] *I* (Mean + 95% CI)

The % Reduction from 90% is calculated in a similar manner.

The objectives of the model were to determine the discharges from the stormwater drainage system and for each of the outfalls along EFPC. Subsequently the discharges were implemented in the surface and groundwater model which was developed for the entire EFPC. A series of simulations were conducted to provide analysis of contaminant flow and transport within the EFPC watershed and to determine the impact of model parameters on NPDES and TMDL regulations. Additionally, a series of simulations were executed to determine the significance of mercury reaction kinetic parameters on flow and transport within EFPC to provide analysis of the long term trends. Two periods were considered, prior to flow augmentation of Upper EFPC and after flow augmentation. The computed data provides additional insight of the effect for the entire range of hydrologic regimes (very wet to very dry conditions).

The PHREEQC model developed in this research, with a significantly enhanced Hg database, is capable of predicting the behavior of various Hg-species in a variety of processes. These include dissolution/precipitation, ion exchange, and surface complexation. In addition, the enhanced PHREEQC model, coupled with the transport model offers a computational tool to be used in site applications (specific site data input is required), to understand the fate and transport of Hg in the aquatic environments of interest.

The enhanced model was confirmed using documented experimental and field data. This strengthened the confidence in the model and its capability to simulate Hg processes and transport.

Using the experimental data documented in relevant literature, the enhanced model was tested to predict Hg species for a wide range of water pH conditions (2-10). Overall, the comparisons between the model results and those from literature were satisfactory.

The model was tested using SFWMD field data to study the capability to calculate major ions, which are typical constituents in all aqueous environments. The model prediction of major ions as function of salinity, were comparable with the observed data collected from over 30 monitoring wells in the SFWMD area. This indicates that: 1) the enhanced model is capable of simulating the geochemical processes for major ions, which are expected to interact with Hg in

aqueous environments; and 2) the enhanced model is capable of capturing the effect of salinity on chemical processes.

An Hg transport simulation was conducted using the enhanced PHREEQC model in order to study the solute transport in a groundwater setting at Oak Ridge, TN. The goal was to determine the effects of ion-exchange and surface complexation on Hg transport. The model results compared well with the empirical data and proved the capability of the PHREEQC coupled-transport model. The enhanced model is an effective tool and can be used to simulate the hydrogeochemical transport of Hg in a groundwater setting. There is a lot of potential for the enhanced PHREEQC model as a tool in the screening, selection and monitoring of remediation technologies, for Hg contaminated groundwater sites, such as EFPC.

The enhanced model showed that the Hg species concentrations were influenced by the pe and pH of water. Under oxidizing conditions, $HgCl_2$, HgClOH and $Hg(OH)_2$ were the dominant species. HgCl2 was dominant in the pH range of 2.0-7.0 and HgClOH in the range of 7.0 – 7.5. $Hg(OH)_2$ was the dominant species for pH > 7.5. Cinnabar was the dominant species under reducing water conditions for all pH.

The enhanced model showed that the exchangers affected the Hg concentration in the water through the ion exchange process in the order of Illite < Montmorillonite < Vermiculite. The effect of ion exchange increased with the CEC of the exchanger. This result was consistent with the previous studies. The model results, with the improved Hg surface complexation database for $Fe(OH)_3$, Gibbsite, and Kaolinite, showed that the surface complexation process affected the Hg concentration. These sorbents can complex strongly with Hg and hinder its transport. The effect of these minerals on Hg are in the order of Kaolinite < Gibbsite < $Fe(OH)_3$. The enhanced model also showed that $Hg(OH)_2$, $Hg(OH)^+$ and HgOHCl can complex with the minerals better than $HgCl_2$, $HgCl_3^-$ and $HgSO_4$ species for pH in the range 4.5-8.5.

The effect of ion exchange on Hg transport was observed to be low in the groundwater and surface water settings that were studied. This may be related to either the low exchange equilibrium constant or the low concentrations of exchangers that are both expected in typical ground and surface water settings.

The effect of surface complexation on Hg transport was also estimated in both typical groundwater and surface water settings for Gibbsite, Kaolinite and $Fe(OH)_3$. Kaolinite was observed to have no effect on Hg transport in the studied surface water setting. This may be attributed to its low equilibrium constant or low expected concentrations or both.

At the typical conditions of the water at East Fork Poplar Creek (EFPC) (water pH 7.0 - 9.2 and temperature of 25 °C), the most dominant species, as predicted by the model, were $Hg(OH)_2$ and HgClOH. The formation of $Hg(OH)_2$ increased with water pH and temperature. For water pH between 2.0-7.0, an increase in water pH and temperature favored the production of HgClOH.

Simulation results predicted the water to be supersaturated with Ferrihydrite, Goethite, Magnesioferrite, Hematite, FCO_3Aptite, Lepidocrocite, Hydroxylapatite, and Arogonite. The formation of these minerals increased with the water pH. In addition, an increase in water temperature favored the precipitation of Ferrihydrite, Goethite, Magnesioferrite, and Hematite. However, temperature did not favor the formation of FCO_3Aptite, Lepidocrocite, Hydroxylapatite, and Arogonite.

The Hg transport in ORR groundwater (Bear Creek Valley) was investigated using the enhanced model. The result showed that the Hg transport was influenced by ion-exchange and surface complexation with $Fe(OH)_3$ and Gibbsite. The water quality at GW-923 showed that water was supersaturated with cinnabar. Thus, it was hypothesized that, at the test well, the dissolution of cinnabar became a source of Hg. The dominant Hg species at GW-923 was $HgCl_2$. This indicated that, at this well location, the Cl-ligand promoted the mobilization of Hg. The presence of $Fe(OH)_3$ and Gibbsite at wells GW-363 and 369 reduced the Hg concentration in the solution and retarded the transport of Hg by surface complexation.

The enhanced model was employed to investigate the feasibility of using reduction in Hg loading as an Hg control strategy at EFPC. The model was used in the transport mode to assess the role of ion exchange and surface complexation in EFPC. Among other estimates, the application showed that the Hg concentration in EFPC can be reduced from 0.5 µg/L to about 0.08 µg/L within 60 years, if the Hg loading at the sources is reduced to 2.5 g/day. Furthermore, if the

loading is further reduced to 0.15 g/day, Hg concentrations in the creek will reach 0.05 µg/L within 45 years.

REFERENCES

1. Abbott, M. B., and J. C. Refsgaard. "Distributed Hydrological Modeling." Kluwer Academic: Dordrecht, 1996.
2. Allison, Jerry, and Terry Allison. "Partition Coefficients for Metals in Surface Water, Soil and Waste ." Office of Research and Development, US Environmental Protection Agency, Washington, DC, 2005.
3. Andrews, E.D. "Entrainment of gravel from naturally sorted riverbed material." Geological Society of America Bulletin 94 (October 1983): 1225-1231.
4. Ashwood, T.L., C.R. Olsen, I.L. Larsen, and P.D. Lowry. Sediment Contamination in Streams Surrounding the Oak Ridge Gaseous Diffusion Plant. Oak Ridge: Oak Ridge National Laboratory, 1986.
5. Bao, Yixing. "Predicting sediment and Cesium-137 transported to offsite during extreme floods." Oak Ridge National Laboratory. Environmental Science Division Publication 4853, 1999.
6. Bechtel Jacobs. "Determination of Site-Specific Aqueous Concentration Goals for Controlling Mercury Bioaccumulation in Fish in East Fork Poplar Creek: Result of Studies Undertaken by the Y-12 Biological Monitoring and Abatement Program (BMAP) at the Oak Ridge Y-12 Plant." Oak Ridge, TN, 1999.
7. Beheshti, A.A., and B. Ataie-Ashtiani. "Analysis of threshold and incipient conditions for sediment movement." Coastal Engineering, 2008: 423-430.
8. Brigham, Mark, Dennis Wentz, George Aiken, and David Krabbenhoft. "Mercury Cicling in Stream Ecosystems. 1. Water Column Chemistry and Transport." Environmental Science Technology 43 (2009): 2720-2725.
9. Brooks, S.C., and G.R. Southworth. "History of Mercury use and Environmental Contamination at the Oak Ridge Y-12 Plant." Environmental Pollution, 2011: 219-228.
10. Chapra, Steven. Surface Water-Quality Modeling . Long Grove, IL: Waveland Press, Inc, 1997.
11. Cheng, Nian-Sheng. "Simplified Settling Velocity Formula for Sediment Particle ." Journal of Hydraulic Engineering, 1997: 149-152.

12. Choi, Sung-Uk, and Seungjo Kwak. "Theoretical and Probabilistic Analysis of incipient motion of sediment particles." KSCE Journal of Civil Engineering 5, no. 1 (March 2001): 59-65.
13. DENR, NC. "North Carolina Department of Environment and Natural Resources. Total Maximum Daily Load for Mercury in the Cashie River, North Carolina. Public Review Draft 7/28/2004." NC DENR. 2004. North Carolina Department of Environment and Natural Resources. Total Maximum Daily Load for Mercury in the Cashie River, North Carolina. Public Review Draft 7/28/2004, North Carolina, 2004.
14. DHI. Heavy Metal Template ECO Lab Scientific Description. Hørsholm, Denmark: Danish Hydraulic Institute, 2009.
15. DHI. MIKE 11 A modelling system for rivers and channels, user guide. Hørsholm, Denmark: Danish Hydraulic Institute, 2009b.
16. DHI. MIKE 11 Short Descriptions . Hørsholm, Denmark: Danish Hydraulic Institute, 2008.
17. DOE. "East Fork Poplar Creek – Sewer Line Beltway Remedial Investigation Report, Volume I, Science applications International Corporation, 1994." 1994.
18. DOE. Instream Contaminant Study Task 5, Summary Report. Oak ridge, Tennessee: Office of Natural Resources and Economic Development Tennessee Valley of Authority, 1986b, 223, .
19. DOE. "Instream Contaminant Study Task 2, V2. Sediment Characterization." Office of Natural Resources and Economic Development Tennessee Valley of Authority, 1986.
20. DOE. "Proposed Plan for Interim Source Control Actions for Contaminated Soils, Sediments, and Groundwater (Outfall 51) which Contribute to Mercury and PCB Contamination to Surface Water in the Upper East Fork Poplar Creek Characterization Area." Oak Ridge, Tennessee: Department of Energy, 2001.
21. DOE. Recommendations to Address Technical Uncertainties in Mitigation and Remediation of Mercury at the Y-12 Plant, Oak Ridge. Office of Environmental Management, Department of Energy, Oak Ridge, Tennessee: Department of Energy, 2008.

22. DOE. Record of Decision for Phase II Interim Remedial Actions for Contaminated Soils and Scrapyard in Upper East Fork Poplar Creek. Oak Ridge, Tennessee: U.S. Department of Energy Office of Environmental Management, 2005.
23. DOE. Record of Decision for Soil, Buried Waste, and Subsurface Structure Actions in Zone 2, East Tennessee Technology Park. Oak Ridge, Tennessee: U.S. Department of Energy Office of Environmental Management, 2005b.
24. DOE. "Report on the Remedial Investigation of the Upper East Fork Poplar Creek Characterization Area at the Oak Ridge Y-12 Plant, Oak Ridge, Tennessee, Volume 1, DOE/OR/01-1641/V1&D2 ." 1998.
25. DOE. "Report on the Remedial Investigation of the Upper East Fork Poplar Creek Characterization Area at the Oak Ridge Y-12 Plant. Volume 1." Oak Ridge, Tennessee, 1998.
26. Ebinghaus, R., R.R. Turner, L.D. de Lacerda, O Vasiliev, and W Salomons. Mercury Contaminated Sites. New York: Springer, 1999.
27. Emmet et al., Owens. "Resuspension of Mercury-Contaminated Sediments from an In-Lake Industrial Waste Deposit." Journal of Environmental Engineering, July 2009: 526-534.
28. Gandhi et al., Nilima. "Development of a Mercury Speciation, Fate and Biotic Uptake (BIOTRANSPEC) Model; Application to Lahontan Reservoir (NEVADA, USA)." Environmental Toxicology and Chemistry 26, no. 11 (2007): 2260–2273.
29. Garde, R.J., and K.J. Tanga Raju. Mechanics of Sediment Transportation and Alluvial Stream Problems. Second Edition. John Wiley & Sons, 1985.
30. Gray, J. R., G.D Glysson, L.M Turcios, and G.E. Schwartz. Comparability of Suspended-Sediment Concentration and Total Suspended Solids Data, Water Resources Investigations Report 00-4191. Reston, Virginia.: U.S. Geological Survey, 2000.
31. Guo, Qizhong. "Correlation of Total Suspended Solids (TSS) and Suspended Sediment Concentration (SSC) Test Methods." Department of Civil and Environmental Engineering, The State University of New Jersey, Trenton, NJ, 2006.
32. Hallermeier, Robert. "Terminal Settling Velocity of Commonly Occurring Sand Grains." Sedimentology, 1981: 859-865.

33. Han, Fengxiang, et al. "extractability and Bioavailability of Mercury from a Mercury Sulfide Contaminated Soil in Oak Ridge. Tennessee, USA." Water Air Soil Pollution, 2008: 67-75.
34. Hill, Walter, Michael Ryon, John Smith, Marshall Adams, Harry Boston, and Arthur Stewart. "The Role of Periphyton in Mediating the Effects of Pollution in a Stream Ecosystem." Environmental Management, 2010: 563-576.
35. Honeyman, Bruce D, and H Peter Santschi. "Metals in Aquatic Systems." Environmental Science and Technology 22, no. 8 (1988): 862-871.
36. Kaleri, Cinthia. "Implementation Issues: Mercury Transport and Fate. combustion Risk Assessments in Region 6." EPA - Proceeding of the 12th International conference. Dallas - Texas, 2000.
37. Kuwabara, James, and others. Flux of Dissolved Forms of Mercury Across the Sediment-water Interface in Lahontan Reservoir, Nevada. U.S. Geological Survey, Nevada: U.S. Geological Survey, 2002.
38. LaGrega, Michael D, Philip L Buckingham, and Jeffrey C Evans. Hazardous Waste Management. Second. McGraw-Hill, 2001.
39. Levine, Daniel, William Hargrove, and Hoffman Forrest. "Characterization of Sediments in the Clinch River, Tennessee, Using Remote Sensing and Multidimensional GIS Techniques." Vancouver, British Columbia, 1995. 548-551.
40. Liao, Lixia, H.M. Selim, and R.D. DeLaune. "Mercury Adsorption-Desorption and Transport in Soils." Journal of Environmental Quality 38, no. July-August (2009): 1608-1616.
41. Lyon, B.F. "Calculation of Soil-Water and Benthic Partition Coefficients for Mercury." Chemosphere, 1997: 791-808.
42. Miller, Carrie L., George Southworth, Scott Brooks, and Baohua Gu. "Kinetic Controls in the Complexation between Mercury and Dissolved Organic Matter in a Contaminated Environment." Environmental Science Technology 43 (2009): 8548-8553.
43. Moran, Barry. "Modeling of the Hydrologic Transport of mercury in the Upper East Fork Poplar Creek." Knoxville (Tennessee), December 1996.

44. Morel, F. M., A.M. Kraepiel, and M Amyot. "The Chemical Cycle and Bioaccumulation of Mercury." Annual Review of Ecology and Systematics 29 (1998): 543-566.
45. Nriagu, Ed. The Biochemistry of Mercury in the Environment. Amsterdam, The Netherlands, North Holland: Biomedical Press, 1979.
46. Pant, P, and M Allen. "Interaction of Soil and Mercury as a Function of Soil Organic Carbon." Bull Environmental Contaminant Toxicology, 2007.
47. Parkpoin, Preeda, Waewtaa Thongra-ar, Ronald DeLaune, and Aroon Jugsujinda. "Adsorption and Desorption of Mercury by Bangpakong River Sediments as Influenced by Salinities." Journal of Environmental Science and Health, 2001: 623-640.
48. Pelcova, Pavlina, Jana Margetinova, Tomas Vaculovic, Josef Komarek, and Vlastimil Kuban. "Adsorption of Mercury Species on River Sediments - Effects of Selected Abiotic Parameters." Central European Journal of Chemistry, 2010: 116-125.
49. Reimers, Robert, and Peter Krenkel. "Kinetics of Mercury Adsorption and Desorption in Sediments." Water Pollution Control Federation 46, no. 2 (1974): 352-365.
50. Rothschild, E.R., et al. Investigation of Subsurface Mercury at the Oak Ridge Y-12 Plant, ORNL/TM-9092. Oak Ridge, TN: Oak Ridge National Laboratory, 1984.
51. Schnoor, Jerald L. Environmental Modeling. Fate and Transport of Pollutants in Water, Air, and Soil. New York: John Wiley & sons, Inc., 1996.
52. Southworth, G.R., et al. Controlling Mercury Release from Source Zones to Surface Water: Initial Results of Pilot Tests at the Y-12 National Security Complex. Oak Ridge, TN: ORNL, 2009.
53. Southworth, George, Max Greeley, Mark Peterson, Kenneth Lowe, and Richard Kettelle. Sources of Mercury to East Fork Poplar Creek Downstream from the Y-12 National Security Complex: Inventories and Export Rates. Oak Ridge: Oak Ridge National Laboratory, 2010.
54. TDEC, Tennessee Department of Environment and Conservation, Division of Water Pollution Control. "Proposed Total Maximum Daily Load (TMDL) for Mercury in East Fork Poplar Creek, Lower Clinch River Watershed, Preliminary Second Draft. Anderson and Roane Counties." Oak Ridge, TN, 2008.

55. Turner, R.R., and G.R. Southworth. “Mercury-Contaminated Industrial and Mining Sites in North America: an Overview with Selected Case Studies in Mercury Contaminated Sites,” R. Ebinghaus, R. R. Turner, L. D. de Lacerda, O. Vasiliev, and W. Salomons (Eds.). Berlin: Springer-Verlag, 1999.
56. USEPA. "Appendix A Chemical Specific Data Delisting Technical Support Document." October 2008. http://www.epa.gov/reg5rcra/wptdiv/hazardous/delisting/appda1.pdf (accessed September 08, 2010).
57. USEPA. Development of Duration-Curve Based Methods for Quantifying Variability and Change in Watershed Hydrology and Water Quality. Cincinnati, Ohio: United States Environmental Protection Agency, 2008.
58. USEPA. "Guidance on the Development, Evaluation, and Application of Environmental Models." Council for Regulatory Environmental Modeling, U.S. Environmental Protection Agency, Washington, DC, 2009.
59. USEPA. "Mercury Study Report to Congress. Volume III. Fate and Transport of Mercury in the Environment." 1997.
60. USEPA. "Standard Operating Procedure for the Analysis of Residue, non-filterable (Suspended Solids), Water, Method 160.2 NS (Gravimetric, 103-105oC)." Region 5 Central Regional Laboratory, 1999.
61. USGS. "Contaminant Sorption by Soil and Bed Sediment." 2000.
62. Van Rijn, L. "Sediment Transport, Part I, Bed Load Transport." Journal of Hydraulic Engineering, 1984: 1431-1456.
63. Van Rijn, Leo. "Sediment Transport, Part II: Suspended Load Transport." Journal of Hydraulic Engineering 110, no. 11 (November 1984b): 1613-1641.
64. Vermont Agency of Natural Resources. "Vermont Stream Geomorphic Assessment, Appendix O." 2009. http://bit.ly/gY33oq (accessed November 11, 2010).
65. Wehr, John, and Robert Sheath. Fresh water algae of North America, Ecology and classification. San Diego, CA: Academic Press, 2003.

66. Yin, Yujun, Herbert Allen, and C.P. Huang. "Kinetics of Mercury (II) Adsorption and Desorption in Soil." Environmental Science and Technology 31, no. 2 (1997): 496-502.(DHI), D. H. (2008). MIKE SHE Reference Manual.
67. (DHI), D. H. (2012). MIKE SHE User Manual.
68. (ORNL), O. R. (2011). *Conceptual Model of Primary Mercury Sources, Transport Pathways, and Flux at the Y-12 Complex and Upper East Fork Poplar Creek.* Oak Ridge, Tennessee.
69. Abbott, M. B., & Refsgaard, J. C. (1996). Distributed Hydrological Modeling. *Kluwer Academic: Dordrecht*.
70. Allison, J., & Allison, T. (2005). *Partition Coefficients for Metals in Surface Water, Soil and Waste* . US Environmental Protection Agency, Office of Research and Development, Washington, DC.
71. Andrews, E. (1983, October). Entrainment of gravel from naturally sorted riverbed material. *Geological Society of America Bulletin, 94*, 1225-1231.
72. Applied Research Initiative, R. o. (2013, February). Retrieved from Oak Ridge National Laboratory: http"//www.esd.oml.gov
73. Applied Research Initiative, R. o. (2013, February). Retrieved from Oak Ridge National Laboratory: http://www.esd.ornl.gov/romic_afrc/field_characterization.shtml
74. Ashwood, T., Olsen, C., Larsen, I., & Lowry, P. (1986). *Sediment Contamination in Streams Surrounding the Oak Ridge Gaseous Diffusion Plant.* Oak Ridge: Oak Ridge National Laboratory.
75. Bao, Y. (1999). Predicting sediment and Cesium-137 transported to offsite during extreme floods. *Oak Ridge National Laboratory. Environmental Science Division Publication 4853*.
76. Bechtel Jacobs. (1999). *Determination of Site-Specific Aqueous Concentration Goals for Controlling Mercury Bioaccumulation in Fish in East Fork Poplar Creek: Result of Studies Undertaken by the Y-12 Biological Monitoring and Abatement Program (BMAP) at the Oak Ridge Y-12 Plant.* Oak Ridge, TN.
77. Beheshti, A., & Ataie-Ashtiani, B. (2008). Analysis of threshold and incipient conditions for sediment movement. *Coastal Engineering*, 423-430.

78. Brigham, M., Wentz, D., Aiken, G., & Krabbenhoft, D. (2009). Mercury Cicling in Stream Ecosystems. 1. Water Column Chemistry and Transport. *Environmental Science Technology, 43*, 2720-2725.
79. Brigham, M., Wentz, D., Aiken, G., & Krabbenhoft, D. (2009). Mercury Cycling in Stream Ecosystems. 1. Water Column Chemistry and Transport. *Environmental Science Technology, 43*, 2720-2725.
80. Brooks, S., & Southworth, G. (2011). History of Mercury use and Environmental Contamination at the Oak Ridge Y-12 Plant. *Environmental Pollution*, 219-228.
81. Cabrejo, E. (2010). *Mercury Interaction with Suspended Solids at the Upper East Fork Poplar Creek, Oak Ridge, Tennessee.* Master Thesis, Florida International University, Environmental Engineering Department, Miami.
82. Cabrejo, E. (2011). *Mercury Interaction with Suspended Solids at the Upper East Fork Poplar Creek, Oak Ridge, Tennessee.* Master Thesis, Florida International University, Environmental Engineering Department, Miami.
83. Chapra, S. (1997). *Surface Water-Quality Modeling* . Long Grove, IL: Waveland Press, Inc.
84. Cheng, N.-S. (1997). Simplified Settling Velocity Formula for Sediment Particle . *Journal of Hydraulic Engineering*, 149-152.
85. Choi, S.-U., & Kwak, S. (2001, March). Theoretical and Probabilistic Analysis of incipient motion of sediment particles. *KSCE Journal of Civil Engineering, 5*(1), 59-65.
86. Danish Hydraulic Institute (DHI). (2008). MIKE 11 Short Descriptions.
87. Danish Hydraulic Institute (DHI). (2012). MIKE 11 Reference Manual.
88. Danish Hydraulic Institute. (2012, May). *Broward County, FL Employs MIKE SHE for Integrated Water Resources Master Plan.* Retrieved from MIKE by DHI: http://www.MIKEbydhi.com/~/media/Microsite_MIKEbyDHI/Publications/SuccessStories/MIKE%20by%20DHI%20Success%20Story-MSHE-BrowardCounty.ashx
89. DENR, N. (2004). *North Carolina Department of Environment and Natural Resources. Total Maximum Daily Load for Mercury in the Cashie River, North Carolina. Public Review Draft 7/28/2004.* NC DENR. 2004. North Carolina Department of Environment

and Natural Resources. Total Maximum Daily Load for Mercury in the Cashie River, North Carolina. Public Review Draft 7/28/2004, North Carolina.

90. DHI. (2008). *MIKE 11 Short Descriptions* . Hørsholm, Denmark: Danish Hydraulic Institute.
91. DHI. (2009). *Heavy Metal Template ECO Lab Scientific Description.* Hørsholm, Denmark: Danish Hydraulic Institute.
92. DHI. (2009b). *MIKE 11 A modelling system for rivers and channels, user guide.* Hørsholm, Denmark: Danish Hydraulic Institute.
93. DOE. (1986). *Instream Contaminant Study Task 2, V2. Sediment Characterization.* Office of Natural Resources and Economic Development Tennessee Valley of Authority.
94. DOE. (1986b). *Instream Contaminant Study Task 5, Summary Report.* Oak ridge, Tennessee: Office of Natural Resources and Economic Development Tennessee Valley of Authority.
95. DOE. (1994). *East Fork Poplar Creek – Sewer Line Beltway Remedial Investigation Report, Volume I, Science applications International Corporation, 1994.*
96. DOE. (1998). *Report on the Remedial Investigation of the Upper East Fork Poplar Creek Characterization Area at the Oak Ridge Y-12 Plant, Oak Ridge, Tennessee, Volume 1, DOE/OR/01-1641/V1&D2* .
97. DOE. (1998). *Report on the Remedial Investigation of the Upper East Fork Poplar Creek Characterization Area at the Oak Ridge Y-12 Plant. Volume 1.* Oak Ridge, Tennessee.
98. DOE. (1998). *Report on the Remedial Investigation of the Upper East Fork Poplar Creek Characterization Area at the Oak Ridge Y-12 Plant. Volume 1.* Oak Ridge, Tennessee.
99. DOE. (2001). Proposed Plan for Interim Source Control Actions for Contaminated Soils, Sediments, and Groundwater (Outfall 51) which Contribute to Mercury and PCB Contamination to Surface Water in the Upper East Fork Poplar Creek Characterization Area. Oak Ridge, Tennessee: Department of Energy.

100. DOE. (2005). *Record of Decision for Phase II Interim Remedial Actions for Contaminated Soils and Scrapyard in Upper East Fork Poplar Creek.* Oak Ridge, Tennessee: U.S. Department of Energy Office of Environmental Management.
101. DOE. (2005b). *Record of Decision for Soil, Buried Waste, and Subsurface Structure Actions in Zone 2, East Tennessee Technology Park.* Oak Ridge, Tennessee: U.S. Department of Energy Office of Environmental Management.
102. DOE. (2008). *Recommendations to Address Technical Uncertainties in Mitigation and Remediation of Mercury at the Y-12 Plant, Oak Ridge.* Department of Energy, Office of Environmental Management. Oak Ridge, Tennessee: Department of Energy.
103. DOE), U. D. (2006). *Record Decision for Phase II Interim Source Control Actions in Upper East Fork Poplar Creek Characterization Area, Oak Ridge, Tennessee.* U.S. Department of Energy, Office of Environmental Management, Oak Ridge, Tennessee.
104. DOE), U. D. (2009). *2009 Remediation Effectiveness Report for the U.S. Department of Energy Oak Ridge Reservation, Oak Ridge, Tennessee.* U.S. Department of Energy Office of Environmental Management, Oak ridge, Tennessee.
105. Ebinghaus, R., Turner, R., de Lacerda, L., Vasiliev, O., & Salomons, W. (1999). *Mercury Contaminated Sites.* New York: Springer.
106. Emmet et al., O. (2009, July). Resuspension of Mercury-Contaminated Sediments from an In-Lake Industrial Waste Deposit. *Journal of Environmental Engineering*, 526-534.
107. Gandhi et al., N. (2007). Development of a Mercury Speciation, Fate and Biotic Uptake (BIOTRANSPEC) Model; Application to Lahontan Reservoir (NEVADA, USA). *Environmental Toxicology and Chemistry, 26*(11), 2260–2273.
108. Gandhi, N., Bhavar, S. P., Diamond, M. L., Kuwabara, J. S., Marvin-DiPasquale, M., & Krabbenhoft, D. P. (2007). Development of mercury speciation, fate, and biotic uptake (BIOTRANSPEC). *Environmental Toxicology and Chemistry*, *26*, 2260-2273.
109. Garde, R., & Tanga Raju., K. (1985). *Mechanics of Sediment Transportation and Alluvial Stream Problems* (Second Edition ed.). John Wiley & Sons.
110. Gray, J. R., Glysson, G., Turcios, L., & Schwartz, G. (2000). *Comparability of Suspended-Sediment Concentration and Total Suspended Solids Data, Water Resources Investigations Report 00-4191*. Reston, Virginia.: U.S. Geological Survey.

111. Guo, Q. (2006). *Correlation of Total Suspended Solids (TSS) and Suspended Sediment Concentration (SSC) Test Methods.* The State University of New Jersey, Department of Civil and Environmental Engineering, Trenton, NJ.
112. Hallermeier, R. (1981). Terminal Settling Velocity of Commonly Occurring Sand Grains. *Sedimentology*, 859-865.
113. Han, F. X., Su, Y., Monts, D. L., Waggoner, C. A., & Plodinec, M. J. (2006, September). Binding, distribution, and plant uptake of mercury in a soil from Oak Ridge, Tennessee, USA. *Science of The Total Environment, 368*(2-3), 753-768.
114. Han, F., Shiyab, S., Chen, J., Su, Y., Monts, D., Waggoner, C., & Matta, F. (2008). extractability and Bioavailability of Mercury from a Mercury Sulfide Contaminated Soil in Oak Ridge. Tennessee, USA. *Water Air Soil Pollution*, 67-75.
115. Han, F., Shiyab, S., Chen, J., Su, Y., Monts, D., Waggoner, C., & Matta, F. (2008). Extractability and Bioavailability of Mercury from a Mercury Sulfide Contaminated Soil in Oak Ridge. Tennessee, USA. *Water Air Soil Pollution*, 67-75.
116. Hill, W., Ryon, M., Smith, J., Adams, M., Boston, H., & Stewart, A. (2010). The Role of Periphyton in Mediating the Effects of Pollution in a Stream Ecosystem. *Environmental Management*, 563-576.
117. Honeyman, B. D., & Santschi, H. P. (1988). Metals in Aquatic Systems. *Environmental Science and Technology, 22*(8), 862-871.
118. Institute, D. H. (2008). ECOLAB Reference Manual.
119. Institute, D. H. (2012). ECOLAB Short Scientific Description.
120. Kaleri, C. (2000). Implementation Issues: Mercury Transport and Fate. combustion Risk Assessments in Region 6. *EPA - Proceeding of the 12th International conference.* Dallas - Texas.
121. Kuwabara, J., & others. (2002). *Flux of Dissolved Forms of Mercury Across the Sediment-water Interface in Lahontan Reservoir, Nevada.* U.S. Geological Survey. Nevada: U.S. Geological Survey.
122. LaGrega, M. D., Buckingham, P. L., & Evans, J. C. (2001). *Hazardous Waste Management* (Second ed.). McGraw-Hill.

123. Levine, D., Hargrove, W., & Forrest, H. (1995). Characterization of Sediments in the Clinch River, Tennessee, Using Remote Sensing and Multidimensional GIS Techniques., (pp. 548-551). Vancouver, British Columbia.
124. Liao, L., Selim, H., & DeLaune, R. (2009). Mercury Adsorption-Desorption and Transport in Soils. *Journal of Environmental Quality*, *38*(July-August), 1608-1616.
125. Long, S. (2009). *An Integrated Flow and Transport Model to Study the Impact of Mercury Remediation Strategies for East Fork Poplar Creek Watershed, Oak Ridge, Tennessee.* Master Thesis, Florida International University, Environmental Engineering Department, Miami.
126. Lyon, B. (1997). Calculation of Soil-Water and Benthic Partition Coefficients for Mercury. *Chemosphere*, 791-808.
127. Malek-Mohammadi, S., Tachiev, G., Cabrejo, E., & Lawrence, A. (2012). Simulation of Flow and Mercury Transport in Upper East Fork Poplar Creek, Oak Ridge, Tennessee. *Remediation*, 119-131.
128. Miller, C. L., Southworth, G., Brooks, S., & Gu, B. (2009). Kinetic Controls in the Complexation between Mercury and Dissolved Organic Matter in a Contaminated Environment. *Environmental Science Technology*, *43*, 8548-8553.
129. Moran, B. (1996, December). Modeling of the Hydrologic Transport of mercury in the Upper East Fork Poplar Creek. Knoxville (Tennessee).
130. Morel, F. M., Kraepiel, A., & Amyot, M. (1998). The Chemical Cycle and Bioaccumulation of Mercury. *Annual Review of Ecology and Systematics, 29*, 543-566.
131. North Carolina Department of Environment and Natural Resources. (2004). *Total Maximum Daily Load for Mercury in the Cashie River, North Carolina, Public Review.* North Carolina Department of Environment and Natural Resources.
132. Nriagu, E. (1979). *The Biochemistry of Mercury in the Environment.* Amsterdam, The Netherlands, North Holland: Biomedical Press.
133. Pant, P., & Allen, M. (2007). Interaction of Soil and Mercury as a Function of Soil Organic Carbon. *Bull Environmental Contaminant Toxicology*.

134. Parkpoin, P., Thongra-ar, W., DeLaune, R., & Jugsujinda, A. (2001). Adsorption and Desorption of Mercury by Bangpakong River Sediments as Influenced by Salinities. *Journal of Environmental Science and Health*, 623-640.
135. Pelcova, P., Margetinova, J., Vaculovic, T., Komarek, J., & Kuban, V. (2010). Adsorption of Mercury Species on River Sediments - Effects of Selected Abiotic Parameters. *Central European Journal of Chemistry*, 116-125.
136. Reimers, R., & Krenkel, P. (1974). Kinetics of Mercury Adsorption and Desorption in Sediments. *Water Pollution Control Federation, 46*(2), 352-365.
137. Rothschild, E., Turner, R., Stow, S., Bogle, M., Hyder, L., Sealand, O., & Wyrick, H. (1984). *Investigation of Subsurface Mercury at the Oak Ridge Y-12 Plant, ORNL/TM-9092*. Oak Ridge, TN: Oak Ridge National Laboratory.
138. Schnoor, J. L. (1996). *Environmental Modeling. Fate and Transport of Pollutants in Water, Air, and Soil.* New York: John Wiley & sons, Inc.
139. Sorensen, H. R., Jacobsen, T. V., Kjelds, J. T., Yan, J., & Hopkins, E. (2012). *Application of MIKE SHE and MIKE 11 for Integrated Hydrological Modeling in South Florida.* South Florida Water Management District (SFWMD) & Danish Hydraulic Institute (DHI).
140. Southworth, G. R., Brooks, S., Peterson, M., Bogle, M. A., Miller, C., Elliot, M., & Liang, L. (2009). *Controlling Mercury Release from Source Zones to Surface Water: Initial Results of Pilot Tests at the Y-12 National Security Complex.*
141. Southworth, G. R., Greely, M., Peterson, M., Lowe, K., & Kettelle, R. (2010). *Sources of Mercury to East Fork Poplar Creek Downstream from the Y-12 National Security Complex: Inventories and Export Rates.* Oak Ridge National Laboratory, Oak Ridge.
142. Southworth, G., Brooks, S., Peterson, M., Bogle, M., Miller, C., Elliott, M., & Liang, L. (2009). *Controlling Mercury Release from Source Zones to Surface Water: Initial Results of Pilot Tests at the Y-12 National Security Complex.* Oak Ridge, TN: ORNL.
143. Southworth, G., Greeley, M., Peterson, M., Lowe, K., & Kettelle, R. (2010). *Sources of Mercury to East Fork Poplar Creek Downstream from the Y-12 National Security Complex: Inventories and Export Rates.* Oak Ridge: Oak Ridge National Laboratory.

144. TDEC, Tennessee Department of Environment and Conservation, Division of Water Pollution Control. (2008). *Proposed Total Maximum Daily Load (TMDL) for Mercury in East Fork Poplar Creek, Lower Clinch River Watershed, Preliminary Second Draft. Anderson and Roane Counties.* Oak Ridge, TN.
145. Tennessee Department of Environment and Conservation. (2008). *2008 303 (d) List.* Division of Water Pollution Control Planning and Standards Section.
146. Turner, R. R., Olsen, C. R., & Wilcox, W. J. (1985). Environmental Fate of Hg and 137 Cs Discharged from Oak Ridge Facilities. *CONF-8406143-2.*
147. Turner, R. R., & Southworth, G. R. (1999). Mercury contaminated industrial and mining sites in North America: an overview with selected case studies. *Springer-Verlag*, 89 -112.
148. Turner, R., & Southworth, G. (1999). *"Mercury-Contaminated Industrial and Mining Sites in North America: an Overview with Selected Case Studies in Mercury Contaminated Sites," R. Ebinghaus, R. R. Turner, L. D. de Lacerda, O. Vasiliev, and W. Salomons (Eds.).* Berlin: Springer-Verlag.
149. Turner, R.R., and Southworth, G.R. ((1999)). *Mercury-Contaminated Industrial and Mining Sites in North America: an Overview with Selected Case Studies in Mercury Contaminated Sites.* Berlin: Springer-Verlag.
150. U.S. Department of Energy (US DOE). (2002). *Record of Decision for Phase I Interim Source Control Actions in Upper East Fork Poplar Creek Characterization Area, Oak Ridge, Tennessee.* U.S. Department of Energy, Office of Environmental Management.
151. U.S. Department of Energy (US DOE). (2002). *Record of Decision for Phase I Interim Source Control Actions in Upper East Fork Poplar Creek Characterization Area, Oak Ridge, Tennessee.* U.S. Department of Energy, Office of Environmental Management.
152. U.S. Department of the Interior. U.S. geological Survey (USGS). (2000). Mercury in the Environment.
153. USEPA. (1997). *Mercury Study Report to Congress. Volume III. Fate and Transport of Mercury in the Environment.*

154. USEPA. (1999). *Standard Operating Procedure for the Analysis of Residue, non-filterable (Suspended Solids), Water, Method 160.2 NS (Gravimetric, 103-105oC).* Region 5 Central Regional Laboratory.
155. USEPA. (2008, October). *Appendix A Chemical Specific Data Delisting Technical Support Document.* Retrieved September 08, 2010, from http://www.epa.gov/reg5rcra/wptdiv/hazardous/delisting/appda1.pdf
156. USEPA. (2008b). *Development of Duration-Curve Based Methods for Quantifying Variability and Change in Watershed Hydrology and Water Quality.* Cincinnati, Ohio: United States Environmental Protection Agency.
157. USEPA. (2009). *Guidance on the Development, Evaluation, and Application of Environmental Models.* U.S. Environmental Protection Agency, Council for Regulatory Environmental Modeling, Washington, DC.
158. USGS. (2000). *Contaminant Sorption by Soil and Bed Sediment.*
159. Van Rijn, L. (1984). Sediment Transport, Part I, Bed Load Transport. *Journal of Hydraulic Engineering*, 1431-1456.
160. Van Rijn, L. (1984, November). Sediment Transport, Part II: Suspended Load Transport. *Journal of Hydraulic Engineering, 110*(11), 1613-1641.
161. Van Rijn, L. (1984b, November). Sediment Transport, Part II: Suspended Load Transport. *Journal of Hydraulic Engineering, 110*(11), 1613-1641.
162. Vermont Agency of Natural Resources. (2009). *Vermont Stream Geomorphic Assessment, Appendix O.* Retrieved November 11, 2010, from http://bit.ly/gY33oq
163. Wehr, J., & Sheath, R. (2003). *Fresh water algae of North America, Ecology and classification.* San Diego, CA: Academic Press.
164. Yin, Y., Allen, H., & Huang, C. (1997). Kinetics of Mercury (II) Adsorption and Desorption in Soil. *Environmental Science and Technology, 31*(2), 496-502.
165. Yin, Y., Allen, H., & Huang, C. (1997). Kinetics of Mercury (II) Adsorption and Desorption on soil. *Environmental Science and Technology*, 496-502.
166. (DHI), D. H. (2008). MIKE SHE Reference Manual.
167. (DHI), D. H. (2012). MIKE SHE User Manual.

168. (ORNL), O. R. (2011). *Conceptual Model of Primary Mercury Sources, Transport Pathways, and Flux at the Y-12 Complex and Upper East Fork Poplar Creek.* Oak Ridge, Tennessee.
169. Abbott, M. B., & Refsgaard, J. C. (1996). Distributed Hydrological Modeling. *Kluwer Academic: Dordrecht.*
170. Allison, J., & Allison, T. (2005). *Partition Coefficients for Metals in Surface Water, Soil and Waste* . US Environmental Protection Agency, Office of Research and Development, Washington, DC.
171. Andrews, E. (1983, October). Entrainment of gravel from naturally sorted riverbed material. *Geological Society of America Bulletin, 94*, 1225-1231.
172. Applied Research Initiative, R. o. (2013, February). Retrieved from Oak Ridge National Laboratory: http"//www.esd.oml.gov
173. Applied Research Initiative, R. o. (2013, February). Retrieved from Oak Ridge National Laboratory: http://www.esd.ornl.gov/romic_afrc/field_characterization.shtml
174. Ashwood, T., Olsen, C., Larsen, I., & Lowry, P. (1986). *Sediment Contamination in Streams Surrounding the Oak Ridge Gaseous Diffusion Plant.* Oak Ridge: Oak Ridge National Laboratory.
175. Bao, Y. (1999). Predicting sediment and Cesium-137 transported to offsite during extreme floods. *Oak Ridge National Laboratory. Environmental Science Division Publication 4853*.
176. Bechtel Jacobs. (1999). *Determination of Site-Specific Aqueous Concentration Goals for Controlling Mercury Bioaccumulation in Fish in East Fork Poplar Creek: Result of Studies Undertaken by the Y-12 Biological Monitoring and Abatement Program (BMAP) at the Oak Ridge Y-12 Plant.* Oak Ridge, TN.
177. Beheshti, A., & Ataie-Ashtiani, B. (2008). Analysis of threshold and incipient conditions for sediment movement. *Coastal Engineering*, 423-430.
178. Brigham, M., Wentz, D., Aiken, G., & Krabbenhoft, D. (2009). Mercury Cicling in Stream Ecosystems. 1. Water Column Chemistry and Transport. *Environmental Science Technology, 43*, 2720-2725.

179. Brigham, M., Wentz, D., Aiken, G., & Krabbenhoft, D. (2009). Mercury Cycling in Stream Ecosystems. 1. Water Column Chemistry and Transport. *Environmental Science Technology, 43*, 2720-2725.
180. Brooks, S., & Southworth, G. (2011). History of Mercury use and Environmental Contamination at the Oak Ridge Y-12 Plant. *Environmental Pollution*, 219-228.
181. Cabrejo, E. (2010). *Mercury Interaction with Suspended Solids at the Upper East Fork Poplar Creek, Oak Ridge, Tennessee.* Master Thesis, Florida International University, Environmental Engineering Department, Miami.
182. Cabrejo, E. (2011). *Mercury Interaction with Suspended Solids at the Upper East Fork Poplar Creek, Oak Ridge, Tennessee.* Master Thesis, Florida International University, Environmental Engineering Department, Miami.
183. Chapra, S. (1997). *Surface Water-Quality Modeling* . Long Grove, IL: Waveland Press, Inc.
184. Cheng, N.-S. (1997). Simplified Settling Velocity Formula for Sediment Particle . *Journal of Hydraulic Engineering*, 149-152.
185. Choi, S.-U., & Kwak, S. (2001, March). Theoretical and Probabilistic Analysis of incipient motion of sediment particles. *KSCE Journal of Civil Engineering, 5*(1), 59-65.
186. Danish Hydraulic Institute (DHI). (2008). MIKE 11 Short Descriptions.
187. Danish Hydraulic Institute (DHI). (2012). MIKE 11 Reference Manual.
188. Danish Hydraulic Institute. (2012, May). *Broward County, FL Employs MIKE SHE for Integrated Water Resources Master Plan.* Retrieved from MIKE by DHI: http://www.MIKEbydhi.com/~/media/Microsite_MIKEbyDHI/Publications/SuccessStories/MIKE%20by%20DHI%20Success%20Story-MSHE-BrowardCounty.ashx
189. DENR, N. (2004). *North Carolina Department of Environment and Natural Resources. Total Maximum Daily Load for Mercury in the Cashie River, North Carolina. Public Review Draft 7/28/2004.* NC DENR. 2004. North Carolina Department of Environment and Natural Resources. Total Maximum Daily Load for Mercury in the Cashie River, North Carolina. Public Review Draft 7/28/2004, North Carolina.
190. DHI. (2008). *MIKE 11 Short Descriptions* . Hørsholm, Denmark: Danish Hydraulic Institute.

191. DHI. (2009). *Heavy Metal Template ECO Lab Scientific Description.* Hørsholm, Denmark: Danish Hydraulic Institute.
192. DHI. (2009b). *MIKE 11 A modelling system for rivers and channels, user guide.* Hørsholm, Denmark: Danish Hydraulic Institute.
193. DOE. (1986). *Instream Contaminant Study Task 2, V2. Sediment Characterization.* Office of Natural Resources and Economic Development Tennessee Valley of Authority.
194. DOE. (1986b). *Instream Contaminant Study Task 5, Summary Report.* Oak ridge, Tennessee: Office of Natural Resources and Economic Development Tennessee Valley of Authority.
195. DOE. (1994). *East Fork Poplar Creek – Sewer Line Beltway Remedial Investigation Report, Volume I, Science applications International Corporation, 1994.*
196. DOE. (1998). *Report on the Remedial Investigation of the Upper East Fork Poplar Creek Characterization Area at the Oak Ridge Y-12 Plant, Oak Ridge, Tennessee, Volume 1, DOE/OR/01-1641/V1&D2* .
197. DOE. (1998). *Report on the Remedial Investigation of the Upper East Fork Poplar Creek Characterization Area at the Oak Ridge Y-12 Plant. Volume 1.* Oak Ridge, Tennessee.
198. DOE. (1998). *Report on the Remedial Investigation of the Upper East Fork Poplar Creek Characterization Area at the Oak Ridge Y-12 Plant. Volume 1.* Oak Ridge, Tennessee.
199. DOE. (2001). Proposed Plan for Interim Source Control Actions for Contaminated Soils, Sediments, and Groundwater (Outfall 51) which Contribute to Mercury and PCB Contamination to Surface Water in the Upper East Fork Poplar Creek Characterization Area. Oak Ridge, Tennessee: Department of Energy.
200. DOE. (2005). *Record of Decision for Phase II Interim Remedial Actions for Contaminated Soils and Scrapyard in Upper East Fork Poplar Creek.* Oak Ridge, Tennessee: U.S. Department of Energy Office of Environmental Management.

201. DOE. (2005b). *Record of Decision for Soil, Buried Waste, and Subsurface Structure Actions in Zone 2, East Tennessee Technology Park.* Oak Ridge, Tennessee: U.S. Department of Energy Office of Environmental Management.
202. DOE. (2008). *Recommendations to Address Technical Uncertainties in Mitigation and Remediation of Mercury at the Y-12 Plant, Oak Ridge.* Department of Energy, Office of Environmental Management. Oak Ridge, Tennessee: Department of Energy.
203. DOE), U. D. (2006). *Record Decision for Phase II Interim Source Control Actions in Upper East Fork Poplar Creek Characterization Area, Oak Ridge, Tennessee.* U.S. Department of Energy, Office of Environmental Management, Oak Ridge, Tennessee.
204. DOE), U. D. (2009). *2009 Remediation Effectiveness Report for the U.S. Department of Energy Oak Ridge Reservation, Oak Ridge, Tennessee.* U.S. Department of Energy Office of Environmental Management, Oak ridge, Tennessee.
205. Ebinghaus, R., Turner, R., de Lacerda, L., Vasiliev, O., & Salomons, W. (1999). *Mercury Contaminated Sites.* New York: Springer.
206. Emmet et al., O. (2009, July). Resuspension of Mercury-Contaminated Sediments from an In-Lake Industrial Waste Deposit. *Journal of Environmental Engineering*, 526-534.
207. Gandhi et al., N. (2007). Development of a Mercury Speciation, Fate and Biotic Uptake (BIOTRANSPEC) Model; Application to Lahontan Reservoir (NEVADA, USA). *Environmental Toxicology and Chemistry, 26*(11), 2260–2273.
208. Gandhi, N., Bhavar, S. P., Diamond, M. L., Kuwabara, J. S., Marvin-DiPasquale, M., & Krabbenhoft, D. P. (2007). Development of mercury speciation, fate, and biotic uptake (BIOTRANSPEC). *Environmental Toxicology and Chemistry*, *26*, 2260-2273.
209. Garde, R., & Tanga Raju., K. (1985). *Mechanics of Sediment Transportation and Alluvial Stream Problems* (Second Edition ed.). John Wiley & Sons.
210. Gray, J. R., Glysson, G., Turcios, L., & Schwartz, G. (2000). *Comparability of Suspended-Sediment Concentration and Total Suspended Solids Data, Water Resources Investigations Report 00-4191.* Reston, Virginia.: U.S. Geological Survey.
211. Guo, Q. (2006). *Correlation of Total Suspended Solids (TSS) and Suspended Sediment Concentration (SSC) Test Methods.* The State University of New Jersey, Department of Civil and Environmental Engineering, Trenton, NJ.

212. Hallermeier, R. (1981). Terminal Settling Velocity of Commonly Occurring Sand Grains. *Sedimentology*, 859-865.
213. Han, F. X., Su, Y., Monts, D. L., Waggoner, C. A., & Plodinec, M. J. (2006, September). Binding, distribution, and plant uptake of mercury in a soil from Oak Ridge, Tennessee, USA. *Science of The Total Environment, 368*(2-3), 753-768.
214. Han, F., Shiyab, S., Chen, J., Su, Y., Monts, D., Waggoner, C., & Matta, F. (2008). extractability and Bioavailability of Mercury from a Mercury Sulfide Contaminated Soil in Oak Ridge. Tennessee, USA. *Water Air Soil Pollution*, 67-75.
215. Han, F., Shiyab, S., Chen, J., Su, Y., Monts, D., Waggoner, C., & Matta, F. (2008). Extractability and Bioavailability of Mercury from a Mercury Sulfide Contaminated Soil in Oak Ridge. Tennessee, USA. *Water Air Soil Pollution*, 67-75.
216. Hill, W., Ryon, M., Smith, J., Adams, M., Boston, H., & Stewart, A. (2010). The Role of Periphyton in Mediating the Effects of Pollution in a Stream Ecosystem. *Environmental Management*, 563-576.
217. Honeyman, B. D., & Santschi, H. P. (1988). Metals in Aquatic Systems. *Environmental Science and Technology, 22*(8), 862-871.
218. Institute, D. H. (2008). ECOLAB Reference Manual.
219. Institute, D. H. (2012). ECOLAB Short Scientific Description.
220. Kaleri, C. (2000). Implementation Issues: Mercury Transport and Fate. combustion Risk Assessments in Region 6. *EPA - Proceeding of the 12th International conference.* Dallas - Texas.
221. Kuwabara, J., & others. (2002). *Flux of Dissolved Forms of Mercury Across the Sediment-water Interface in Lahontan Reservoir, Nevada.* U.S. Geological Survey. Nevada: U.S. Geological Survey.
222. LaGrega, M. D., Buckingham, P. L., & Evans, J. C. (2001). *Hazardous Waste Management* (Second ed.). McGraw-Hill.
223. Levine, D., Hargrove, W., & Forrest, H. (1995). Characterization of Sediments in the Clinch River, Tennessee, Using Remote Sensing and Multidimensional GIS Techniques., (pp. 548-551). Vancouver, British Columbia.

224. Liao, L., Selim, H., & DeLaune, R. (2009). Mercury Adsorption-Desorption and Transport in Soils. *Journal of Environmental Quality*, *38*(July-August), 1608-1616.
225. Long, S. (2009). *An Integrated Flow and Transport Model to Study the Impact of Mercury Remediation Strategies for East Fork Poplar Creek Watershed, Oak Ridge, Tennessee.* Master Thesis, Florida International University, Environmental Engineering Department, Miami.
226. Lyon, B. (1997). Calculation of Soil-Water and Benthic Partition Coefficients for Mercury. *Chemosphere*, 791-808.
227. Malek-Mohammadi, S., Tachiev, G., Cabrejo, E., & Lawrence, A. (2012). Simulation of Flow and Mercury Transport in Upper East Fork Poplar Creek, Oak Ridge, Tennessee. *Remediation*, 119-131.
228. Miller, C. L., Southworth, G., Brooks, S., & Gu, B. (2009). Kinetic Controls in the Complexation between Mercury and Dissolved Organic Matter in a Contaminated Environment. *Environmental Science Technology, 43*, 8548-8553.
229. Moran, B. (1996, December). Modeling of the Hydrologic Transport of mercury in the Upper East Fork Poplar Creek. Knoxville (Tennessee).
230. Morel, F. M., Kraepiel, A., & Amyot, M. (1998). The Chemical Cycle and Bioaccumulation of Mercury. *Annual Review of Ecology and Systematics, 29*, 543-566.
231. North Carolina Department of Environment and Natural Resources. (2004). *Total Maximum Daily Load for Mercury in the Cashie River, North Carolina, Public Review.* North Carolina Department of Environment and Natural Resources.
232. Nriagu, E. (1979). *The Biochemistry of Mercury in the Environment.* Amsterdam, The Netherlands, North Holland: Biomedical Press.
233. Pant, P., & Allen, M. (2007). Interaction of Soil and Mercury as a Function of Soil Organic Carbon. *Bull Environmental Contaminant Toxicology*.
234. Parkpoin, P., Thongra-ar, W., DeLaune, R., & Jugsujinda, A. (2001). Adsorption and Desorption of Mercury by Bangpakong River Sediments as Influenced by Salinities. *Journal of Environmental Science and Health*, 623-640.

235. Pelcova, P., Margetinova, J., Vaculovic, T., Komarek, J., & Kuban, V. (2010). Adsorption of Mercury Species on River Sediments - Effects of Selected Abiotic Parameters. *Central European Journal of Chemistry*, 116-125.
236. Reimers, R., & Krenkel, P. (1974). Kinetics of Mercury Adsorption and Desorption in Sediments. *Water Pollution Control Federation, 46*(2), 352-365.
237. Rothschild, E., Turner, R., Stow, S., Bogle, M., Hyder, L., Sealand, O., & Wyrick, H. (1984). *Investigation of Subsurface Mercury at the Oak Ridge Y-12 Plant, ORNL/TM-9092*. Oak Ridge, TN: Oak Ridge National Laboratory.
238. Schnoor, J. L. (1996). *Environmental Modeling. Fate and Transport of Pollutants in Water, Air, and Soil.* New York: John Wiley & sons, Inc.
239. Sorensen, H. R., Jacobsen, T. V., Kjelds, J. T., Yan, J., & Hopkins, E. (2012). *Application of MIKE SHE and MIKE 11 for Integrated Hydrological Modeling in South Florida.* South Florida Water Management District (SFWMD) & Danish Hydraulic Institute (DHI).
240. Southworth, G. R., Brooks, S., Peterson, M., Bogle, M. A., Miller, C., Elliot, M., & Liang, L. (2009). *Controlling Mercury Release from Source Zones to Surface Water: Initial Results of Pilot Tests at the Y-12 National Security Complex.*
241. Southworth, G. R., Greely, M., Peterson, M., Lowe, K., & Kettelle, R. (2010). *Sources of Mercury to East Fork Poplar Creek Downstream from the Y-12 National Security Complex: Inventories and Export Rates.* Oak Ridge National Laboratory, Oak Ridge.
242. Southworth, G., Brooks, S., Peterson, M., Bogle, M., Miller, C., Elliott, M., & Liang, L. (2009). *Controlling Mercury Release from Source Zones to Surface Water: Initial Results of Pilot Tests at the Y-12 National Security Complex.* Oak Ridge, TN: ORNL.
243. Southworth, G., Greeley, M., Peterson, M., Lowe, K., & Kettelle, R. (2010). *Sources of Mercury to East Fork Poplar Creek Downstream from the Y-12 National Security Complex: Inventories and Export Rates.* Oak Ridge: Oak Ridge National Laboratory.
244. TDEC, Tennessee Department of Environment and Conservation, Division of Water Pollution Control. (2008). *Proposed Total Maximum Daily Load (TMDL) for Mercury in East Fork Poplar Creek, Lower Clinch River Watershed, Preliminary Second Draft. Anderson and Roane Counties.* Oak Ridge, TN.

245. Tennessee Department of Environment and Conservation. (2008). *2008 303 (d) List.* Division of Water Pollution Control Planning and Standards Section.
246. Turner, R. R., Olsen, C. R., & Wilcox, W. J. (1985). Environmental Fate of Hg and 137 Cs Discharged from Oak Ridge Facilities. *CONF-8406143-2.*
247. Turner, R. R., & Southworth, G. R. (1999). Mercury contaminated industrial and mining sites in North America: an overview with selected case studies. *Springer-Verlag*, 89 -112.
248. Turner, R., & Southworth, G. (1999). *"Mercury-Contaminated Industrial and Mining Sites in North America: an Overview with Selected Case Studies in Mercury Contaminated Sites," R. Ebinghaus, R. R. Turner, L. D. de Lacerda, O. Vasiliev, and W. Salomons (Eds.).* Berlin: Springer-Verlag.
249. Turner, R.R., and Southworth, G.R. ((1999)). *Mercury-Contaminated Industrial and Mining Sites in North America: an Overview with Selected Case Studies in Mercury Contaminated Sites.* Berlin: Springer-Verlag.
250. U.S. Department of Energy (US DOE). (2002). *Record of Decision for Phase I Interim Source Control Actions in Upper East Fork Poplar Creek Characterization Area, Oak Ridge, Tennessee.* U.S. Department of Energy, Office of Environmental Management.
251. U.S. Department of Energy (US DOE). (2002). *Record of Decision for Phase I Interim Source Control Actions in Upper East Fork Poplar Creek Characterization Area, Oak Ridge, Tennessee.* U.S. Department of Energy, Office of Environmental Management.
252. U.S. Department of the Interior. U.S. geological Survey (USGS). (2000). Mercury in the Environment.
253. USEPA. (1997). *Mercury Study Report to Congress. Volume III. Fate and Transport of Mercury in the Environment.*
254. USEPA. (1999). *Standard Operating Procedure for the Analysis of Residue, non-filterable (Suspended Solids), Water, Method 160.2 NS (Gravimetric, 103-105oC).* Region 5 Central Regional Laboratory.
255. USEPA. (2008, October). *Appendix A Chemical Specific Data Delisting Technical Support Document.* Retrieved September 08, 2010, from http://www.epa.gov/reg5rcra/wptdiv/hazardous/delisting/appda1.pdf

256. USEPA. (2008b). *Development of Duration-Curve Based Methods for Quantifying Variability and Change in Watershed Hydrology and Water Quality.* Cincinnati, Ohio: United States Environmental Protection Agency.
257. USEPA. (2009). *Guidance on the Development, Evaluation, and Application of Environmental Models.* U.S. Environmental Protection Agency, Council for Regulatory Environmental Modeling, Washington, DC.
258. USGS. (2000). *Contaminant Sorption by Soil and Bed Sediment.*
259. Van Rijn, L. (1984). Sediment Transport, Part I, Bed Load Transport. *Journal of Hydraulic Engineering*, 1431-1456.
260. Van Rijn, L. (1984, November). Sediment Transport, Part II: Suspended Load Transport. *Journal of Hydraulic Engineering, 110*(11), 1613-1641.
261. Van Rijn, L. (1984b, November). Sediment Transport, Part II: Suspended Load Transport. *Journal of Hydraulic Engineering, 110*(11), 1613-1641.
262. Vermont Agency of Natural Resources. (2009). *Vermont Stream Geomorphic Assessment, Appendix O.* Retrieved November 11, 2010, from http://bit.ly/gY33oq
263. Wehr, J., & Sheath, R. (2003). *Fresh water algae of North America, Ecology and classification.* San Diego, CA: Academic Press.
264. Yin, Y., Allen, H., & Huang, C. (1997). Kinetics of Mercury (II) Adsorption and Desorption in Soil. *Environmental Science and Technology, 31*(2), 496-502.
265. Yin, Y., Allen, H., & Huang, C. (1997). Kinetics of Mercury (II) Adsorption and Desorption on soil. *Environmental Science and Technology*, 496-502.
266. (DHI), D. H. (2008). MIKE SHE Reference Manual.
267. (DHI), D. H. (2012). MIKE SHE User Manual.
268. (ORNL), O. R. (2011). *Conceptual Model of Primary Mercury Sources, Transport Pathways, and Flux at the Y-12 Complex and Upper East Fork Poplar Creek.* Oak Ridge, Tennessee.
269. Abbott, M. B., & Refsgaard, J. C. (1996). Distributed Hydrological Modeling. *Kluwer Academic: Dordrecht*.

270. Allison, J., & Allison, T. (2005). *Partition Coefficients for Metals in Surface Water, Soil and Waste* . US Environmental Protection Agency, Office of Research and Development, Washington, DC.

271. Andrews, E. (1983, October). Entrainment of gravel from naturally sorted riverbed material. *Geological Society of America Bulletin, 94*, 1225-1231.

272. Applied Research Initiative, R. o. (2013, February). Retrieved from Oak Ridge National Laboratory: http"//www.esd.oml.gov

273. Applied Research Initiative, R. o. (2013, February). Retrieved from Oak Ridge National Laboratory: http://www.esd.ornl.gov/romic_afrc/field_characterization.shtml

274. Ashwood, T., Olsen, C., Larsen, I., & Lowry, P. (1986). *Sediment Contamination in Streams Surrounding the Oak Ridge Gaseous Diffusion Plant.* Oak Ridge: Oak Ridge National Laboratory.

275. Bao, Y. (1999). Predicting sediment and Cesium-137 transported to offsite during extreme floods. *Oak Ridge National Laboratory. Environmental Science Division Publication 4853*.

276. Bechtel Jacobs. (1999). *Determination of Site-Specific Aqueous Concentration Goals for Controlling Mercury Bioaccumulation in Fish in East Fork Poplar Creek: Result of Studies Undertaken by the Y-12 Biological Monitoring and Abatement Program (BMAP) at the Oak Ridge Y-12 Plant.* Oak Ridge, TN.

277. Beheshti, A., & Ataie-Ashtiani, B. (2008). Analysis of threshold and incipient conditions for sediment movement. *Coastal Engineering*, 423-430.

278. Brigham, M., Wentz, D., Aiken, G., & Krabbenhoft, D. (2009). Mercury Cicling in Stream Ecosystems. 1. Water Column Chemistry and Transport. *Environmental Science Technology, 43*, 2720-2725.

279. Brigham, M., Wentz, D., Aiken, G., & Krabbenhoft, D. (2009). Mercury Cycling in Stream Ecosystems. 1. Water Column Chemistry and Transport. *Environmental Science Technology, 43*, 2720-2725.

280. Brooks, S., & Southworth, G. (2011). History of Mercury use and Environmental Contamination at the Oak Ridge Y-12 Plant. *Environmental Pollution*, 219-228.

281. Cabrejo, E. (2010). *Mercury Interaction with Suspended Solids at the Upper East Fork Poplar Creek, Oak Ridge, Tennessee.* Master Thesis, Florida International University, Environmental Engineering Department, Miami.

282. Cabrejo, E. (2011). *Mercury Interaction with Suspended Solids at the Upper East Fork Poplar Creek, Oak Ridge, Tennessee.* Master Thesis, Florida International University, Environmental Engineering Department, Miami.

283. Chapra, S. (1997). *Surface Water-Quality Modeling* . Long Grove, IL: Waveland Press, Inc.

284. Cheng, N.-S. (1997). Simplified Settling Velocity Formula for Sediment Particle . *Journal of Hydraulic Engineering*, 149-152.

285. Choi, S.-U., & Kwak, S. (2001, March). Theoretical and Probabilistic Analysis of incipient motion of sediment particles. *KSCE Journal of Civil Engineering, 5*(1), 59-65.

286. Danish Hydraulic Institute (DHI). (2008). MIKE 11 Short Descriptions.

287. Danish Hydraulic Institute (DHI). (2012). MIKE 11 Reference Manual.

288. Danish Hydraulic Institute. (2012, May). *Broward County, FL Employs MIKE SHE for Integrated Water Resources Master Plan.* Retrieved from MIKE by DHI: http://www.MIKEbydhi.com/~/media/Microsite_MIKEbyDHI/Publications/SuccessStories/MIKE%20by%20DHI%20Success%20Story-MSHE-BrowardCounty.ashx

289. DENR, N. (2004). *North Carolina Department of Environment and Natural Resources. Total Maximum Daily Load for Mercury in the Cashie River, North Carolina. Public Review Draft 7/28/2004.* NC DENR. 2004. North Carolina Department of Environment and Natural Resources. Total Maximum Daily Load for Mercury in the Cashie River, North Carolina. Public Review Draft 7/28/2004, North Carolina.

290. DHI. (2008). *MIKE 11 Short Descriptions* . Hørsholm, Denmark: Danish Hydraulic Institute.

291. DHI. (2009). *Heavy Metal Template ECO Lab Scientific Description.* Hørsholm, Denmark: Danish Hydraulic Institute.

292. DHI. (2009b). *MIKE 11 A modelling system for rivers and channels, user guide.* Hørsholm, Denmark: Danish Hydraulic Institute.

293. DOE. (1986). *Instream Contaminant Study Task 2, V2. Sediment Characterization.* Office of Natural Resources and Economic Development Tennessee Valley of Authority.

294. DOE. (1986b). *Instream Contaminant Study Task 5, Summary Report.* Oak ridge, Tennessee: Office of Natural Resources and Economic Development Tennessee Valley of Authority.

295. DOE. (1994). *East Fork Poplar Creek – Sewer Line Beltway Remedial Investigation Report, Volume I, Science applications International Corporation, 1994.*

296. DOE. (1998). *Report on the Remedial Investigation of the Upper East Fork Poplar Creek Characterization Area at the Oak Ridge Y-12 Plant, Oak Ridge, Tennessee, Volume 1, DOE/OR/01-1641/V1&D2* .

297. DOE. (1998). *Report on the Remedial Investigation of the Upper East Fork Poplar Creek Characterization Area at the Oak Ridge Y-12 Plant. Volume 1.* Oak Ridge, Tennessee.

298. DOE. (1998). *Report on the Remedial Investigation of the Upper East Fork Poplar Creek Characterization Area at the Oak Ridge Y-12 Plant. Volume 1.* Oak Ridge, Tennessee.

299. DOE. (2001). Proposed Plan for Interim Source Control Actions for Contaminated Soils, Sediments, and Groundwater (Outfall 51) which Contribute to Mercury and PCB Contamination to Surface Water in the Upper East Fork Poplar Creek Characterization Area. Oak Ridge, Tennessee: Department of Energy.

300. DOE. (2005). *Record of Decision for Phase II Interim Remedial Actions for Contaminated Soils and Scrapyard in Upper East Fork Poplar Creek.* Oak Ridge, Tennessee: U.S. Department of Energy Office of Environmental Management.

301. DOE. (2005b). *Record of Decision for Soil, Buried Waste, and Subsurface Structure Actions in Zone 2, East Tennessee Technology Park.* Oak Ridge, Tennessee: U.S. Department of Energy Office of Environmental Management.

302. DOE. (2008). *Recommendations to Address Technical Uncertainties in Mitigation and Remediation of Mercury at the Y-12 Plant, Oak Ridge.* Department of Energy, Office of Environmental Management. Oak Ridge, Tennessee: Department of Energy.

303. DOE), U. D. (2006). *Record Decision for Phase II Interim Source Control Actions in Upper East Fork Poplar Creek Characterization Area, Oak Ridge, Tennessee.* U.S. Department of Energy, Office of Environmental Management, Oak Ridge, Tennessee.

304. DOE), U. D. (2009). *2009 Remediation Effectiveness Report for the U.S. Department of Energy Oak Ridge Reservation, Oak Ridge, Tennessee.* U.S. Department of Energy Office of Environmental Management, Oak ridge, Tennessee.

305. Ebinghaus, R., Turner, R., de Lacerda, L., Vasiliev, O., & Salomons, W. (1999). *Mercury Contaminated Sites.* New York: Springer.

306. Emmet et al., O. (2009, July). Resuspension of Mercury-Contaminated Sediments from an In-Lake Industrial Waste Deposit. *Journal of Environmental Engineering*, 526-534.

307. Gandhi et al., N. (2007). Development of a Mercury Speciation, Fate and Biotic Uptake (BIOTRANSPEC) Model; Application to Lahontan Reservoir (NEVADA, USA). *Environmental Toxicology and Chemistry, 26*(11), 2260–2273.

308. Gandhi, N., Bhavar, S. P., Diamond, M. L., Kuwabara, J. S., Marvin-DiPasquale, M., & Krabbenhoft, D. P. (2007). Development of mercury speciation, fate, and biotic uptake (BIOTRANSPEC). *Environmental Toxicology and Chemistry, 26*, 2260-2273.

309. Garde, R., & Tanga Raju., K. (1985). *Mechanics of Sediment Transportation and Alluvial Stream Problems* (Second Edition ed.). John Wiley & Sons.

310. Gray, J. R., Glysson, G., Turcios, L., & Schwartz, G. (2000). *Comparability of Suspended-Sediment Concentration and Total Suspended Solids Data, Water Resources Investigations Report 00-4191.* Reston, Virginia.: U.S. Geological Survey.

311. Guo, Q. (2006). *Correlation of Total Suspended Solids (TSS) and Suspended Sediment Concentration (SSC) Test Methods.* The State University of New Jersey, Department of Civil and Environmental Engineering, Trenton, NJ.

312. Hallermeier, R. (1981). Terminal Settling Velocity of Commonly Occurring Sand Grains. *Sedimentology*, 859-865.

313. Han, F. X., Su, Y., Monts, D. L., Waggoner, C. A., & Plodinec, M. J. (2006, September). Binding, distribution, and plant uptake of mercury in a soil from Oak Ridge, Tennessee, USA. *Science of The Total Environment, 368*(2-3), 753-768.

314. Han, F., Shiyab, S., Chen, J., Su, Y., Monts, D., Waggoner, C., & Matta, F. (2008). extractability and Bioavailability of Mercury from a Mercury Sulfide Contaminated Soil in Oak Ridge. Tennessee, USA. *Water Air Soil Pollution*, 67-75.

315. Han, F., Shiyab, S., Chen, J., Su, Y., Monts, D., Waggoner, C., & Matta, F. (2008). Extractability and Bioavailability of Mercury from a Mercury Sulfide Contaminated Soil in Oak Ridge. Tennessee, USA. *Water Air Soil Pollution*, 67-75.

316. Hill, W., Ryon, M., Smith, J., Adams, M., Boston, H., & Stewart, A. (2010). The Role of Periphyton in Mediating the Effects of Pollution in a Stream Ecosystem. *Environmental Management*, 563-576.

317. Honeyman, B. D., & Santschi, H. P. (1988). Metals in Aquatic Systems. *Environmental Science and Technology, 22*(8), 862-871.

318. Institute, D. H. (2008). ECOLAB Reference Manual.

319. Institute, D. H. (2012). ECOLAB Short Scientific Description.

320. Kaleri, C. (2000). Implementation Issues: Mercury Transport and Fate. combustion Risk Assessments in Region 6. *EPA - Proceeding of the 12th International conference.* Dallas - Texas.

321. Kuwabara, J., & others. (2002). *Flux of Dissolved Forms of Mercury Across the Sediment-water Interface in Lahontan Reservoir, Nevada.* U.S. Geological Survey. Nevada: U.S. Geological Survey.

322. LaGrega, M. D., Buckingham, P. L., & Evans, J. C. (2001). *Hazardous Waste Management* (Second ed.). McGraw-Hill.

323. Levine, D., Hargrove, W., & Forrest, H. (1995). Characterization of Sediments in the Clinch River, Tennessee, Using Remote Sensing and Multidimensional GIS Techniques., (pp. 548-551). Vancouver, British Columbia.

324. Liao, L., Selim, H., & DeLaune, R. (2009). Mercury Adsorption-Desorption and Transport in Soils. *Journal of Environmental Quality, 38*(July-August), 1608-1616.

325. Long, S. (2009). *An Integrated Flow and Transport Model to Study the Impact of Mercury Remediation Strategies for East Fork Poplar Creek Watershed, Oak Ridge, Tennessee.* Master Thesis, Florida International University, Environmental Engineering Department, Miami.

326. Lyon, B. (1997). Calculation of Soil-Water and Benthic Partition Coefficients for Mercury. *Chemosphere*, 791-808.

327. Malek-Mohammadi, S., Tachiev, G., Cabrejo, E., & Lawrence, A. (2012). Simulation of Flow and Mercury Transport in Upper East Fork Poplar Creek, Oak Ridge, Tennessee. *Remediation*, 119-131.

328. Miller, C. L., Southworth, G., Brooks, S., & Gu, B. (2009). Kinetic Controls in the Complexation between Mercury and Dissolved Organic Matter in a Contaminated Environment. *Environmental Science Technology, 43*, 8548-8553.

329. Moran, B. (1996, December). Modeling of the Hydrologic Transport of mercury in the Upper East Fork Poplar Creek. Knoxville (Tennessee).

330. Morel, F. M., Kraepiel, A., & Amyot, M. (1998). The Chemical Cycle and Bioaccumulation of Mercury. *Annual Review of Ecology and Systematics, 29*, 543-566.

331. North Carolina Department of Environment and Natural Resources. (2004). *Total Maximum Daily Load for Mercury in the Cashie River, North Carolina, Public Review.* North Carolina Department of Environment and Natural Resources.

332. Nriagu, E. (1979). *The Biochemistry of Mercury in the Environment.* Amsterdam, The Netherlands, North Holland: Biomedical Press.

333. Pant, P., & Allen, M. (2007). Interaction of Soil and Mercury as a Function of Soil Organic Carbon. *Bull Environmental Contaminant Toxicology*.

334. Parkpoin, P., Thongra-ar, W., DeLaune, R., & Jugsujinda, A. (2001). Adsorption and Desorption of Mercury by Bangpakong River Sediments as Influenced by Salinities. *Journal of Environmental Science and Health*, 623-640.

335. Pelcova, P., Margetinova, J., Vaculovic, T., Komarek, J., & Kuban, V. (2010). Adsorption of Mercury Species on River Sediments - Effects of Selected Abiotic Parameters. *Central European Journal of Chemistry*, 116-125.

336. Reimers, R., & Krenkel, P. (1974). Kinetics of Mercury Adsorption and Desorption in Sediments. *Water Pollution Control Federation, 46*(2), 352-365.

337. Rothschild, E., Turner, R., Stow, S., Bogle, M., Hyder, L., Sealand, O., & Wyrick, H. (1984). *Investigation of Subsurface Mercury at the Oak Ridge Y-12 Plant, ORNL/TM-9092*. Oak Ridge, TN: Oak Ridge National Laboratory.

338. Schnoor, J. L. (1996). *Environmental Modeling. Fate and Transport of Pollutants in Water, Air, and Soil.* New York: John Wiley & sons, Inc.

339. Sorensen, H. R., Jacobsen, T. V., Kjelds, J. T., Yan, J., & Hopkins, E. (2012). *Application of MIKE SHE and MIKE 11 for Integrated Hydrological Modeling in South Florida.* South Florida Water Management District (SFWMD) & Danish Hydraulic Institute (DHI).

340. Southworth, G. R., Brooks, S., Peterson, M., Bogle, M. A., Miller, C., Elliot, M., & Liang, L. (2009). *Controlling Mercury Release from Source Zones to Surface Water: Initial Results of Pilot Tests at the Y-12 National Security Complex.*

341. Southworth, G. R., Greely, M., Peterson, M., Lowe, K., & Kettelle, R. (2010). *Sources of Mercury to East Fork Poplar Creek Downstream from the Y-12 National Security Complex: Inventories and Export Rates.* Oak Ridge National Laboratory, Oak Ridge.

342. Southworth, G., Brooks, S., Peterson, M., Bogle, M., Miller, C., Elliott, M., & Liang, L. (2009). *Controlling Mercury Release from Source Zones to Surface Water: Initial Results of Pilot Tests at the Y-12 National Security Complex.* Oak Ridge, TN: ORNL.

343. Southworth, G., Greeley, M., Peterson, M., Lowe, K., & Kettelle, R. (2010). *Sources of Mercury to East Fork Poplar Creek Downstream from the Y-12 National Security Complex: Inventories and Export Rates.* Oak Ridge: Oak Ridge National Laboratory.

344. TDEC, Tennessee Department of Environment and Conservation, Division of Water Pollution Control. (2008). *Proposed Total Maximum Daily Load (TMDL) for Mercury in East Fork Poplar Creek, Lower Clinch River Watershed, Preliminary Second Draft. Anderson and Roane Counties.* Oak Ridge, TN.

345. Tennessee Department of Environment and Conservation. (2008). *2008 303 (d) List.* Division of Water Pollution Control Planning and Standards Section.

346. Turner, R. R., Olsen, C. R., & Wilcox, W. J. (1985). Environmental Fate of Hg and 137 Cs Discharged from Oak Ridge Facilities. *CONF-8406143-2.*

347. Turner, R. R., & Southworth, G. R. (1999). Mercury contaminated industrial and mining sites in North America: an overview with selected case studies. *Springer-Verlag*, 89 - 112.

348. Turner, R., & Southworth, G. (1999). *"Mercury-Contaminated Industrial and Mining Sites in North America: an Overview with Selected Case Studies in Mercury Contaminated Sites," R. Ebinghaus, R. R. Turner, L. D. de Lacerda, O. Vasiliev, and W. Salomons (Eds.).* Berlin: Springer-Verlag.

349. Turner, R.R., and Southworth, G.R. ((1999)). *Mercury-Contaminated Industrial and Mining Sites in North America: an Overview with Selected Case Studies in Mercury Contaminated Sites.* Berlin: Springer-Verlag.

350. U.S. Department of Energy (US DOE). (2002). *Record of Decision for Phase I Interim Source Control Actions in Upper East Fork Poplar Creek Characterization Area, Oak Ridge, Tennessee.* U.S. Department of Energy, Office of Environmental Management.

351. U.S. Department of Energy (US DOE). (2002). *Record of Decision for Phase I Interim Source Control Actions in Upper East Fork Poplar Creek Characterization Area, Oak Ridge, Tennessee.* U.S. Department of Energy, Office of Environmental Management.

352. U.S. Department of the Interior. U.S. geological Survey (USGS). (2000). Mercury in the Environment.

353. USEPA. (1997). *Mercury Study Report to Congress. Volume III. Fate and Transport of Mercury in the Environment.*

354. USEPA. (1999). *Standard Operating Procedure for the Analysis of Residue, non-filterable (Suspended Solids), Water, Method 160.2 NS (Gravimetric, 103-105oC).* Region 5 Central Regional Laboratory.

355. USEPA. (2008, October). *Appendix A Chemical Specific Data Delisting Technical Support Document.* Retrieved September 08, 2010, from http://www.epa.gov/reg5rcra/wptdiv/hazardous/delisting/appda1.pdf

356. USEPA. (2008b). *Development of Duration-Curve Based Methods for Quantifying Variability and Change in Watershed Hydrology and Water Quality.* Cincinnati, Ohio: United States Environmental Protection Agency.

357. USEPA. (2009). *Guidance on the Development, Evaluation, and Application of Environmental Models.* U.S. Environmental Protection Agency, Council for Regulatory Environmental Modeling, Washington, DC.

358. USGS. (2000). *Contaminant Sorption by Soil and Bed Sediment.*

359. Van Rijn, L. (1984). Sediment Transport, Part I, Bed Load Transport. *Journal of Hydraulic Engineering*, 1431-1456.

360. Van Rijn, L. (1984, November). Sediment Transport, Part II: Suspended Load Transport. *Journal of Hydraulic Engineering, 110*(11), 1613-1641.

361. Van Rijn, L. (1984b, November). Sediment Transport, Part II: Suspended Load Transport. *Journal of Hydraulic Engineering, 110*(11), 1613-1641.

362. Vermont Agency of Natural Resources. (2009). *Vermont Stream Geomorphic Assessment, Appendix O.* Retrieved November 11, 2010, from http://bit.ly/gY33oq

363. Wehr, J., & Sheath, R. (2003). *Fresh water algae of North America, Ecology and classification.* San Diego, CA: Academic Press.

364. Yin, Y., Allen, H., & Huang, C. (1997). Kinetics of Mercury (II) Adsorption and Desorption in Soil. *Environmental Science and Technology, 31*(2), 496-502.

365. Yin, Y., Allen, H., & Huang, C. (1997). Kinetics of Mercury (II) Adsorption and Desorption on soil. *Environmental Science and Technology*, 496-502.

366. Adams, D.H., and Onorato G.V. (2005). "Mercury concentrations in red drum, Sciaenops ocellatus, from estuarine and offshore waters of Florida." Marine Pollution Bulletin. 50 (3): 291-300.

367. Ahlberg, I. (1962). "Studies on the hydrolysis of metal ions." Acta Chemica 16 (2): 887-902.

368. AJA TECHNICAL SERVICES, INC. (1998). "Groundwater protection program calendar year 1998 evaluation of groundwater quality data for the chestnut ridge hydrogeologic regime at the U.S. Department of Energy y-12 Plant, Oak Ridge, Tennessee." Under Subcontract No. 70Y-MVM64, Report No. Y/SUW/99-MVM64V/3.

369. Amirbahman, A., Reid, A.L., Haines, T.A., Kahl, J.S., and Arnold, C. (2002). "Association of methylmercury with dissolved humic acids." Environmental Science &Technology. 36 (4): 690-695.

370. Appelo, C.A.J., and Postma, D. (2005). "Geochemistry, Groundwater and Pollution." CRC Press Taylor & Francis Group, Boca Raton, Florida.

371. Atre, S.R., and Carpenter, P.J. (2010). "Identification of cross-valley faults in the naynardville limestone Oak Ridge Reservation, Tennessee, suing seismic refraction tomography." Environmental Earth Science, 60: 1245-1256.
372. Arias, M., Barral, M.T., Da Silva-Carvalhal, J., Mejuto J.C., and Rubinos, D. (2004). "Interaction of Hg(II) with kaolin-humic acid complexes." Clay Minerals. 39 (1): 35-45.
373. Axelrad, D.M., Lange, T., Gabriel, M., Atkeson, T.D., Pollman, C.D., Orem, W.H., Scheidt, D.J., Kalla, P.I., Frederick, P.C., and Gilmour, C.C. (2008) "South Florida Environmental Report." South Florida Water Management District.
374. Banks, D., Younger, P.L., and Dumpleton, S. (1996). "The historical use of mine drainage and pyrite-oxidation waters in the central and eastern England, United Kingdom." Hydrogeology Journal. 4 (4): 55–68.
375. Barlow, P.M., and Reichard, E.G. (2010). "Saltwater intrusion in coastal regions of North America." Hydrogeology Journal. 18 (1): 247-260.
376. Bates, A.L., Orem, W.H., Harvey, J.W., and Spike, E.C. (2002) "Tracing sources of sulfur in the Florida Everglades." Journal of Environmental Quality. 31 (1): 287-299.
377. Bengtsson, G., and Picado, F. (2008). "Mercury sorption to sediments: Dependence on grain size, dissolved organic carbon, and suspended bacteria." Chemosphere. 73 (4): 526-531.
378. Benoit, J.M., Gilmour, C.C., Marson, R.P. Heyes, R., (1999). "Sulfide controls on mercury speciation and bioavailability of mercury." Applied and Environmental Microbiology." Environmental Science &Technology. 33: 951-957.
379. Benoit, J.M., Mason, R.P., Gilmour, C.C., and Aiken, G.R. (2001). "Constants for mercury binding by dissolved organic matter isolates from the Florida Everglades." Geochimica et Cosmochimica Acta. 65 (24): 4445-4451.
380. Bergaya, F., and Vayer, M. (1997). "CEC of clays: measurement by adsorption of a copper ethylenediamine complex." Applied Clay Science. 12 (3): 275-280.
381. Black, F.J., Bruland, K.W., and Flegal, A.R. (2007). "Competing ligand exchange-solid phase extraction method for the determination of the complexation of dissolved inorganic mercury(II) in natural waters." Analytica Chemica Acta. 598 (2): 318-333.

382. Blanco, R.I., Naja, G.M., Rivero, R.G., Price, R.M. (2013). "Spatial and temporal changes in groundwater salinity in South Florida." Applied Geochemistry. 38: 48-58.
383. Bloom, N.S., and Crecelius, E.A. (1983). "Determination of mercury in seawater at sub-nanogram per liter levels." Marine Chemistry. 14 (1): 49-59.
384. Brooks, S.C., and Southworth, G.R. (2011). "History of mercury use and environmental contamination at the Oak Ridge Y-12 plant." Environmental Pollution. 159 (1): 219-228.
385. Bruggenwert, M.G.M., and Kamphorst, A. (1979). "Survey of experimental information on cation exchange in soil systems. Developments in Soil Science. 5: 141-204.
386. Cai, Y., Jaffe, R., and Jones, R.D. (1999). "Interactions between dissolved organic carbon and mercury species in surface waters of the Florida everglades." Applied Geochemistry. 14 (3): 395-407.
387. Campbell, K., Capece, J.C., and Tremwel, T.K. (1995) "Surface/subsurface hydrology and phosphorus transport in the Kissimmee river basin, Florida." Ecological Engineering, 5: 301-330.
388. Chattopadhyay, S., and Ickes, J. (2001). "Report on characterization and Eh/pH-based leaching tests of mercury-containing mining wastes from the sulfur bank mercury mine, Lake County, California." United States Environmental Protection Agency. EPA/600/R-02/032.
389. Choi, J., Harvey, J.W. (2000). "Quantifying time-varying groundwater discharge and recharge in wetlands: a comparison of methods in the Florida Everglades" Wetlands. 20 (3): 500–511.
390. Conaway, C.H., Squire, S., Mason, P.R., and Flegal A.R. (2003). "Mercury speciation in the San Francisco Bay estuary." Marine Chemistry. 80 (2-3): 199-225.
391. Cox, C.D., Shoesmith, M.A., and Ghosh, M.M. (1996). "Electrokinetic remediation of mercury-contaminated soils using Iodine/Iodide lixiviant." Environmental Science and Technology. 30: 1933-1938.

392. Cruz-Guzman, M., Celis, R., Hermosin, M.C., Leone, P., Negre, M., and Cornejo, J. (2003). "Sorption-desorption of lead (II) and mercury (II) by model associations of soil colloids." Soil Science Society of America Journal. 67 (5): 1378-1387.
393. Davis, A., Bloom, N.S., and Que-Hee, S.S. (1997). "The environmental geochemistry and bioaccessibility of mercury in soils and sediments: a review." Risk Analysis. 17 (5): 557-569.
394. DBHYDRO (Environmental Data), South Florida Water Management District http://www.sfwmd.gov/portal/page/portal/xwebenvironmentalmonitoring/dbhydro application. Accessed on 09/26/2011.
395. Depledge, M.H. (1999). "Recovery of ecosystems and their components following exposure to pollution." Journal of Aquatic Ecosystem Stress and Recovery. 6: 199–206.
396. Dong, W., Liang, L., Brooks, S., Southworth, G., and Gu, B. (2010). "Roles of dissolved organic matter in the speciation of mercury and methylmercury in a contaminated ecosystem in Oak Ridge, Tennessee." Environmental Chemistry. 7 (1): 94-102.
397. Dreier, R.B., Early, T.O., and King, H.L., (1993). "Results and interpretation of groundwater data obtained from multiport-instrumented boreholes (GW-131 through GW-135)." Fiscal years 1990 and 1991, Environmental Management Department, Oak Ridge, Tennessee.
398. Drexel, R.T., Haitzer, M.H., Ryan, J.N., Aiken, G.R., and Nagy, K.L. (2002). " Mercury(II) sorption to two Florida Everglades peats: evidence for strong and weak binding and competition by dissolved organic matter released from the peat." Environmental Science Technology. 36 (19): 4058-4064.
399. Driese, S.G., McKay, L.D., and Penfield, C.P. (2001) "Lithologic and pedogenic influences on porosity distribution and groundwater flow in fractured sedimentary saprolite: A new application of environmental sedimentology." Journal of Sedimentary Research, 71(5); 843-857.
400. Duvall, S.E., and Barron, M.G. (2000). "A Screening level probabilistic risk assessment of mercury in Florida Everglades food webs." Ecotoxicology and Environmental Safety, 47 (3): 298-305.

401. Dyrssen, D., Tyrell, V. (1961). “A miniature solubility column and its application to a study of the solubility of red mercury (II) oxide in acid 3M NaClO solutions.” Acta Chemica Scandinavica. 15 (1): 1622.
402. Dzombak, D.A., Morel, F.M.M. (1990). “Surface complexation modeling: Hydrous ferric oxide.” John Wiley & Sons, New York.
403. Elliott, H.A., and Huang, C.P. (1981). “The Adsorption of Cu(II) Complexes onto Aluminosilicates.” Water Research. 15(7): 849-855.
404. Elvado Environmental LLC. (2009) “Calendar year 2009 groundwater monitoring report” U.S. Department of Energy Y-12 National Security Complex, Oak Ridge, TN. Y/SUB/10-073231/1.
405. Elvado Environment LLC. (2011) “Calendar year 2011 groundwater monitoring report” U.S. Department of Energy Y-12 National Security Complex, Oak Ridge, TN. Y/SUB/12-073231/1.
406. Evans, D.W., and Engel, D.W. (1994). “Mercury bioaccumulation in finfish and shellfish from Lavaca Bay, Texas: descriptive models and annotated bibliography.” NOAA Technical Memoris NMFSSEFSC-348: 1-89.
407. Evans, C.D., Monteith, D.T., and Cooper, D.M. (2005). “Long-term increases in surface water dissolved organic carbon: Observations, possible causes and environmental impacts.” Environmental Pollution. 137: 55-71.
408. Facemire, C., Augspurger, T., Bateman, D., Brim, M., Conzelmann, P., Delchamps, S., Douglas, E., Inmon, L., Looney, K., Lopez, F., Masson, G., Morrison, D., Morse, N., and Robison, A. (1995). “Impacts of mercury contamination in the southeastern United States.” Water, Air, and Soil Pollution. 80 (1-4): 923-926.
409. Farley, K.J., Dzombak, D.A., and Morel, F.M.M. (1984). “A surface precipitation model for the sorption of cations on metal oxides.” Journal of Colloid and Interface Science. 106 (1): 226-242.
410. Feng, X., Jiang, H., Qiu, G., Yan, H., Li, G., and Li, Z. (2009). “Geochemical processes of mercury in Wujianddu and Dongfeng reservoirs, Guizhou, China.” Environmental Pollution. 157(11): 2970-2984.

411. Florida coastal everglades long term ecological research website. "www. Fcelter.fiu.edu" Accessed on 01/10/2011.
412. Gårdfeldt, K., Munthe, J., StrÖmberget, D., and Lindqvist, O. (2003). "A kinetic study on the abiotic methylation of divalent mercury in the aqueous phase." The Science of the Total Environment. 304 (1-3): 127–136.
413. Gårdfeldt, K., Sommar, J., StrÖmberg, D., and Feng, X. (2001) "Oxidation of atomic mercury by hydroxyl radicals and photoinduced decomposition of methylmercury in the aqueous phase." Atmosphere Environment. 35(17): 3039-3047.
414. Garett, A., and Hirschler, A. (1938). "The solubilities of red and yellow mercuric oxides in water, in alkali, and in alkaline salt solutions. The acid and basic dissociation constants of mercuric hydroxide." Journal of American Chemical Society. 60 (2): 299-306.
415. GEMS, GEM-Selektor Geochemical Software http://gems.web.psi.ch/overview.html. Accessed on 11/02/2011
416. Grassi, S., and Netti, R. (2002). "Sea water intrusion and mercury pollution of some coastal aquifers in the province of Grosseto (Southern Tuscany-Italy)." Journal of Hydrology. 237 (3-4): 198-211.
417. Guentzel, J.L., Landing, W.M., Gill, G.A., and Pollman, C.D. (2001). "Processes influencing rainfall deposition of mercury in Florida." Environmental Sciences & Technology, 35 (5): 863-873.
418. Haitzer, M., Aiken, G.R., and Ryan, J.N. (2002). "Binding of mercury (II) to dissolved organic matter: the role of the mercury-to-DOM concentration ratio." Environmental Sciences & Technology. 36 (16): 3564-3570.
419. Haitzer, M., Aiken, G.R., and Ryan, J.N. (2003). "Binding of mercury(II) to aquatic humic substances: influence of pH and source of humic substances." Environmental Sciences & Technology. 37 (11): 2436-2441.
420. Halim, C.E., Stephen, S.E., Scott, J.A., Amal, R., and Low, G. (2005). "Modelling the leaching of Pb, Cd, As, and Cr from cementitious waste using PHREEQC." Journal of Hazardous Materials. 125 (1-3): 45-61.

421. Han, F.X., Su, Y., Shi, Z., Xia, Y., Tian, W., Philips, V., Monts, D.L., Gu, M., and Liang, Y. (2012) "Mercury distribution and speciation in floodplain soils and uptake into native earthworms." Geogerma. 170: 261-268.
422. Han, S.H., and Gill, G.A. (2005). "Determination of mercury complexation in coastal and estuarine waters using competitive ligand exchange method." Environmental Sciences & Technology. 39 (17): 6607-6615.
423. Harmon, S.M., King, J.K., Gladden, J.B., Chandler, G.T., and Newman, L.A. (2004). "Methylmercury Formation in a wetland mesocosm amended with sulfate." Environmental Sciences & Technology. 38 (2): 650-656.
424. Harris, W. (2011). Mineral distribution and weathering in the greater everglades: implications for restoration." Environmental Sciences & Technology. 41 (2): 4-27.
425. Harris, W.G., Fisher, M.M., Cao, X., Osborne, T., and Ellis, L. (2007). "Magnesium-rich minerals in sediment and suspended particulates of south Florida water bodies: implications for turbidity." Journal of Environmental Quality. 36 (6): 1670-1677.
426. Harvey, J.W., Choi, J., and Mooney, R.H. (2000) "Hydrologic interactions between surface water and ground water in Taylor Slough, Everglades National Park," U.S. Geological Survey open-file report 00-449.
427. Harvey, J.W., Krupa, S.L., Gefvert, C., Mooney, R.H., Choi, J., King, S.A., and Giddings, J.B., (2002). "Interactions between surface water and ground water and effects on mercury transport in the north-central Everglades." U.S. Geological Survey Water-Resources Investigations Report, 02–4050:1- 82.
428. Harvey, J.W., Newlin, J.T., and Krupa, S.L. (2005). "Modeling decadal timescale interactions between surface water and ground water in the central Everglades, Florida, USA." Journal of Hydrology. 320 (2006): 400-420.
429. Hayes, K.F., and Leckie, J.O. (1986). "In geochemical processes at mineral surfaces." in: Davis, J.A., Hayes, K.F. (Eds.). American Chemical Society, Washington, DC. 323:115-141.
430. Hietanen, S., Hogfeldt, E. (1976). "On the hydrolysis of Hg(I) perchlorate in 3M(Na)ClO_4." Chemica Scripta 10 (2): 41-44.

431. Hill, W.R., Mulholland, P.J., and Marzolf, E.R. (2001). “Stream ecosystem responses to forest leaf emergence in spring.” Ecology. 82:2306–2319.
432. Hill, W.R., Ryon, M.G., Smith, J.G., Adams A.M., Boston, H.L., and Stewart, A.J. (2010). “The role of Periphyton in mediating the effect of pollution in a stream ecosystem.” Environmental Management. 45 (3): 563–576.
433. Hintelmann, H., Welbourn, P.M., and Evans R.D. (1997). “Measurement of complexation of methylmercury compounds by freshwater humic substances using equilibrium dialysis.” Environmental Sciences & Technology. 31 (2): 489-495.
434. Hurley, J.P., Kranbbenhoft, D.P., Babiarz, C.L., Andren, A.W. (1994). “Cycling of mercury across sediment-water interface in seepage lake. In: Baker, L.A. (Ed.), Environmental chemistry of lakes and reservoirs.” American Chemical Society, Washington, DC. 425-449.
435. Hurley, J.P., Kranbbenhoft, D.P., Cleckner, L.B., Olson, M.L. Aiken, G.R., Rawlik Jr., P.S. (1998). “System controls on the aqueous distribution of mercury in the northern Florida Everglades.” Biogeochemistry. 40 (2-3): 293-311.
436. Jago, W.K., Loffman, R.S., Motley, C.A. (1995). “Chapter 7: Groundwater.” Annual report, Oak Ridge National Laboratory, Oak Ridge, Tennessee.
437. Jay J.A., Morel F.M.M. and Hemond, H.F. (2000). “Mercury speciation in the presence of polysulfides.” Environmental Sciences & Technology. 34 (11): 2196–2200.
438. Jeremiason, J.D., Engstrom, D.R., Swain, E.B., Nater, E.A., Johnson, B.M., Almendinger, J.E., Monson, B.A., and Kolka, R.K. (2006). “Sulfate addition increases methylmercury production in an experimental wetland.” Environmental Sciences & Technology. 40 (12): 3800-3806.
439. Karlsson, T., and Skyllberg, U. (2003). “Bonding of ppb levels of methyl mercury to reduced sulfur groups in soil organic matter.” Environmental Sciences & Technology. 37 (21): 4912-4918.
440. KBN Engineering and Applied Sciences (KBN). (1992). “Mercury emissions to the atmosphere in Florida.” Prepared for the Florida Department of Environmental Regulation, Tallahassee.

441. Kelkar, S., Roback, R., Robinson, B., Srinivasan, G., Jones, C., Reimus, P. (2006). "Saturated Zone Plume in Volcanic Rock: Implications for Yucca Mountain." Technical Information Center Oak Ridge Tennessee, DE2006-893920.
442. Khan, A.A., and Alam, M.M. (2004). "New and novel organic-inorganic type crystalline 'polypyrrolel/polyantimonic acid' composite system: preparation, characterization and analytical applications as a cation-exchange material and Hg(II) ion-selective membrane electrode." Analytica Chemica Acta. 504 (2): 253-264.
443. Kim, C.S., Rytuba, J.J., Brown, G.E. (2004) "EXAFS study of mercury (II) sorption to Fe-Al-(hydro)oxides: II. Effects of chloride and sulfate." Journal of Colloid and Interface Science. 270(1): 9-20.
444. Krupa, S., Hill, S., and Bevier, C. (2001). "Miami-Dade County Northwest Wellfield Groundwater Velocity Investigation." Technical Publication WS-1, South Florida Water Management District.
445. Lamborg, C.H., Tseng, C.M., Fitzgerald, W.F., Balcom, P.H., and Hammerschmidt, C.R. (2003) "Determination of the mercury complexation characteristics of dissolved organic matter in natural water with reducible Hg titrations." Environmental Sciences & Technology. 37 (15): 3316-3322.
446. Leonard, L., Croft, A., Childers, D., Mitchell-Bruker, S., Solo-Gabriele, H., and Ross, M., (2006). "Characteristics of surface-water flows in the ridge and slough landscape of Everglades National Park: implications for particulate transport." Hydrobiologia. 569 (1): 5-22.
447. Li, Y., Mao, Y., Liu, G., Tachiev, G., Roelant, D., Feng, X., and Cai, Y. (2010). "Degradation of methylmercury and its effects on mercury distribution and cycling in the Florida everglades." Environmental Sciences & Technology. 44 (17): 6661-6666.
448. Liang, P., Li, Y., Zhang, C., Wu, S., Cui, H., Yu, S., and Wong, M.H. (2013). "Effects of salinity and humic acid on the sorption of Hg on Fe and Mn hydroxides." Journal of Hazardous Materials. 244-245: 322-328.
449. Libich, S., and Robenstein, D. (1973). "Nuclear magnetic resonance studies of the solution chemistry of metal complexes." Analytical Chemistry. 45 (1): 118-124.

450. Little, M.E. (2006). "Distribution of arsenic and mercury in terrestrial and marine environments impacted by gold mine tailings, Wine Harbour, Nova Scotia." Dalhousie University, Halifax, Nova Scotia. 161 pages.
451. Loar, J.M., Stewart, A.J., and Smith, J.G. (2011). "Twenty-five years of ecological recovery of East Fork Poplar Creek: Review of environmental problems and remedial actions." Environmental Management. 47 (6): 1010-1020.
452. Loren, G.H., and Olofsson, G. (1975). "Mercury: Thermodynamic Properties, chemical equilibria, and standard potentials." Chemical Reviews. 75 (5): 585-602.
453. Lui, G., Cai, Y., Philippi, T., Kalla, P., Scheidt, D., Richards, J., Scinto, L., and Appleby, C. (2008). "Distribution of total and methylmercury in different ecosystem compartments in the Everglades: Implications for mercury bioaccumulation." Environmental Pollution. 153 (2): 257-265.
454. Mackay, D., Wania, F., and Schroeder, W.H. (1995). "Prospects for modeling the behavior and fate of mercury, globally and in aquatic systems." Water, Air, and Soil Pollution. 80: 941-950.
455. Magos, L., and Clarkson, T.W. (2006). "Overview of the clinical toxicity of mercury." Annals of clinical biochemistry. 43 (4): 257-268.
456. Margaritz, M., Goldenberg, L., Kafri, U., and Arad, A. (1980). "Dolomite formation in the seawater–freshwater interface." Nature, 287 (1): 622–624.
457. Martell, A.E., and Smith R.M. (2001). "NIST critically selected stability constants of metal complexes, version 6 Gaithersburg." National Institute of Standards and Technology, Maryland.
458. Matsuyama, A., Eguchi, T., Sonoda, I., Tada, A., Yano, S., Tai, A., Marumoto, K., Tomiyasu, T., and Akagi, H. (2011). "Mercury speciation in the water of Minamata Bay, Japan." Water Air and Soil Pollution. 218: 399-412.
459. Meng, X.G., and Letterman, R.D. (1993). "Effect of component oxide interaction on the adsorption properties of mixed oxides." Environmental Science Technology. 27 (5); 970-975.
460. MINEQL+, Geochemical Software. www.mineql.com. Accessed on 11/02/2011.

461. MINTEQA2, Geochemical Software. http://www.epa.gov/ceampub/mmedia/minteq/. Accessed on 11/01/2011.
462. Miretzky, P., Bisinoti, M.C., and Jardim W.F. (2005). "Sorption of mercury (II) in Amazon soils from column studies." Chemosphere. 60 (11):1583-1589.
463. Morel, F.M.M., and Hering, J.G. (1993). "Principles and applications of aquatic chemistry." John Wiley & Sons, Inc.
464. Nativ, R., Halleran, A., and Hunley, A. (1997). "Evidence for ground-water circulation in the brine-filled aquitard, Oak Ridge, Tennessee." Ground Water. 35 (4): 647-656.
465. Oak Ridge National Laboratory Website: www.esd.ornl.gov. Access on 01/12/2012.
466. OREIS (Oak Ridge Environmental Information System) http://www-oreis.ettp.energy.gov.
467. Osborne, T.Z., Bruland, G.L., Newman, S., Reddy, K.R., and Grunwald, S. (2011). "Spatial distributions and eco-partitioning of soil biogeochemical properties in the Everglades National Park." Environmental Monitoring Assessment. 183 (1-4): 395-408.
468. Pacyna, E.G., and Pacyna, J.M. (2002). "Global emission of mercury from anthropogenic sources in 1995." Water, Air, and Soil Pollution. 137 (1-4): 149-165.
469. Parkhurst, D.L., (1995). "User's guide to PHREEQC a computer program for speciation, reaction path, advective transport, and inverse geochemical calculation." US Geological Survey Water Resource Investigations Report, 95-4227: 1-143.
470. Parkhurst, D.L., and Appelo, C.AJ. (1999) "User's guide to PHREEQC (version 2)-A computer program for speciation, batch-reaction, one-dimensional transport, and inverse geochemical calculations." U.S. Geological Survey water-resources investigations report: 1-312.
471. Parkhurst, D.L., Kipp, K.L., and Charlton, S.R. (2010). "PHAST version 2-a program for simulating groundwater flow, solute transport, and multicomponent geochemical reactions." U.S. Department if the Interior and U.S. Geological Survey, 1-235.
472. Pichler, T., Price, R., Lazareva, O., and Dippold, A. (2011) "Determination of arsenic concentration and distribution in the Floridan Aquifer System" Journal of Geochemical Exploration,111: 84-96.

473. Plummer, L.N., and Sprinkle, C.L. (2001) "Radiocarbon dating of dissolved inorganic carbon in groundwater confined parts of the Upper Floridan aquifer, Florida, USA." Hydrogeology Journal. 9 (2): 127-150.
474. Plummer, L.N., Busby, J.F., Lee, R.W., and Hanshaw, B.B. (1990) "Geochemical modeling of the Madison aquifer in parts of Montana, Wyoming and South Dakota." Water Resources Research. 26 (9): 1981–2014.
475. Powell K.J., Brown P.L., Byrne R.H., Gajda T., Hefter G., Sjoberg S., and Wanner H. (2005). "Chemical speciation of environmentally significant heavy metals with inorganic ligands. Part 1: The Hg^{2+} – Cl^-, OH^-, CO_3^{2-}, SO_4^{2-}, and PO_4^{2-} aqueous systems." Pure and Applied Chemistry. 77 (4): 739–800.
476. Price, R.M., Swart, P.K., and Fourqurean, J.W. (2006). "Coastal groundwater discharge an additional source of phosphorus for the oligotrophic wetlands of the Everglades." Hydrobiologia. 569 (1): 23-36.
477. Price, R.M., Top, Z., Happell, J.D., and Swart, P.K. (2003). "Use of tritium and helium to define groundwater flow conditions in Everglades National Park." Water Resources Research. 39 (9): 1267-1280.
478. Pulido-Leboeuf, P. (2004). "Seawater intrusion and associated process in small coastal complex aquifer (Castell de Ferro, Spain)." Applied Geochemistry. 19 (10): 1517-1527.
479. Qian, J., Skyllberg, U., Frech, W., Bleam, W.F., Bloom, P.R., and Petit, P.E. (2002). "Bonding of methyl mercury to reduced sulfur groups in soil and stream organic matter as determined by X-ray absorption spectroscopy and binding affinity studies." Geochimica et Cosmochimica Acta. 66 (22): 3873- 3885.
480. Quarfort-Dahlman, I. (1975). "On some phosphate equilibria." Chemica Scripta. 8 (2): 112-125.
481. Ravichandran, M. (2004). "Interactions between mercury and dissolved organic matter." Chemosphere. 55 (3): 319-331.
482. Reddy, M., and Aiken, G.R. (2001). "Fulvic acid-sulfide ion competition for mercury ion binding in the Florida Everglades." Water, Air, and Soil Pollution. 132 (1-2): 89-104.

483. Riese, A.C. (1982). "Adsorption of radium and thorium onto quartz and kaolinite, a comparison of solution surface equilibria models." Doctoral thesis, Colorado School of Mines, Golden, Colorado, 210 pp.
484. Samborska, K., and Halas, S. (2010). "34S and 18O in dissolved sulfate as tracers of hydrogeochemical evolution of the triassic carbonate aquifer exposed to intense groundwater exploitation (Olkusz–Zawiercie region, southern Poland)." Applied Geochemistry. 25 (9): 1397–1414.
485. Sarkar, D., Essington, M.E., and Misra, K.C. (1999). "Adsorption of mercury(II) by variable charge surfaces of quartz and gibbsite." Soil Science Society of America Journal. 63 (6); 1626-1636.
486. Sarkar, D., Essington, M.E., and Misra, K.C. (2000). "Adsorption of mercury(II) by kaolinite." Soil Science Society of America Journal. 64 (6): 1968-1975.
487. Schlüter, K. (1995). "Sorption of inorganic mercury and monomethyl mercury in an iron-humus podzol soil of southern Norway studied by batch experiments." Environmental Geology. 30 (3-4):266-279.
488. Schlüter, K., and Gäth, S. (1997). "Modelling leaching of inorganic Hg(II) in a Scandinavian iron-humus podzol-volidation and long-term leaching under various deposition rates." Water, Air, and Soil Pollution, 96 (1-4): 301-320.
489. Schulze-Makuch, D. (200. "Longitudinal dispersivity data and implications for scaling behavior.". Ground Water, 43(3):443-457.
490. Schwarzenbach, G., and Schellenberg, M. (1965). "The chemistry of methylmercury-complexes." Helvetica Chimica Acta. 48 (1): 28-46.
491. Shen, C., Niu, J., Anderson, E.J., and Phanikumar, M.S. (2010). "Estimating longitudinal dispersion in rivers using acoustic doppler current profilers." Advances in Water Resources, 33: 615-623.
492. Sigel, A., and Sigel, H. (1997). "Metal ions in biological systems: mercury and its effects on environment and biology." CRC press. 648 pages.
493. Singh, S.P.N., and Mattigod, S.V. (1992). "Modeling boron adsorption on kaolinite." Clays and Clay Minerals. 40 (2): 192-205.

494. Skyllberg, U., Bloom, P.R., Qian, J., Lin, C.M., Bleam, W.F. (2006). "Complexation of mercury(II) in soil organic matter: EXAFS evidence for linear two-coordination with reduced sulfur groups." Environmental Sciences Technology. 40 (13): 4174-4180.
495. Southworth, G.R., and Brooks, S.C. (2011). "History of mercury use and environmental contamination at the Oak Ridge Y-12 Plant." Environmental Pollution. 159 (1): 219-228.
496. Southworth, G.R., Turner, R.R., Peterson, M.J., and Bogle, M.A. (1995). "Form of mercury in steam fish exposed to high concentrations of dissolved inorganic mercury" Chemosphere. 30 (4): 779-787.
497. Southworth, G.R., Turner, R.R., Peterson, M.J., Bogle, M.A., and Ryon, M.G. (1999). "Response of mercury contamination in fish to decreased aqueous concentrations and loading of inorganic mercury in a small stream." Environmental Monitoring and Assessment. 63 (3): 481-494.
498. Stafford, P., Toran, L., McKay, L. (1998). "Influence of fracture truncation on dispersion: A dual permeability model." Journal of Contamination Hydrology. 30: 79-100.
499. Stewart, A.J., Haynes G.J., and Martinez, M.I. (2009). "Fate and biological effects of contaminated vegetation in Tennessee stream." Environmental Toxicology and Chemistry. 11 (5): 653-664.
500. Stewart, A.J., Smith, J.G., and Loar, J.M. (2011). "Long-term water-quality changes in East Fork Poplar Creek, Tennessee: Background, trends, and potential biological consequences." Environmental Management. 47: 1021-1032.
501. Stoessell, R.K., Ward, W.C., and Schuffert, J.D. (1989). "Water chemistry and CaCO3 dissolution in the saline part of an open-flow mixing zone coastal Yucatan Peninsula, Mexico." Geological Society of America Bulletin. 101 (1): 159-169.
502. Stumm, W., and Morgan, J. J. (1996). "Aquatic chemistry: Chemical equilibria and rates in natural waters." (3rd ed.), A Wiley-Interscience publication, New York.
503. Stumm, W., and Morgan, J.J. (1981). "Aquatic Chemistry. An introduction emphasizing chemical equilibria in natural water." (2nd ed.), Wiley, New York: 1-780.

504. Tibbals, C.H. (1990). "Hydrology of the Floridan aquifer system in east-central Florida." United States Geological Survey, Professional Paper; (USA), 1403E.
505. Tiruta-Barna, L. (2008). "Using PHREEQC for modelling and simulation of dynamic leaching tests and scenarios." Journal of Hazardous Materials. 157 (2-3): 525-533.
506. Toran, L.E., and Saunders, J.A. (1999). "Modeling alternative paths of chemical evolution of Na-HCO3 – type groundwater near Oak Ridge, Tennessee, USA." Hydrogeology. 7 (4): 355-364.
507. Tsuda, T., Yorifuji, T., Takao, S., Miyai, M., and Babazono, A. (2009). "Minamata disease: Catastrophic poisoning due to a failed public health response." Journal of Public Health Policy. 30 (1): 54-67.
508. U.S. Geology Survey, PHREEQC Software version 2 http://wwwbrr.cr.usgs.gov/projects/GWC_coupled/phreeqc/index.html Accessed on 02/10/2011.
509. Vasquez, J. (2008). "Chemical reduction/volatilization to remove mercury from East Fork Poplar Creek (EFPC)." Student Summer Internship Technical Report for U.S. Department of Energy, Office of Environmental Management under Contract No. DE-FG01-05EW07033.
510. Vertacnik, A., Prohic, E., Juracic, M.,Barisic, D., and Lulic, S. (1997). "Selected element concentrations in alluvial sediments under garbage disposal site (Zagreb, Croatia)." Water Resources. 31 (6): 1421-1429.
511. Visual MINTEQ, Geochemical Software www2.lwr.kth.se/English/OurSoftware/vminteq/. Accessed on 11/01/2011.
512. Walton Jr, T.L. (2007). "Projected sea level rise in Florida." Ocean Engineering. 34: 1832-1840.
513. Wang, H., Waldon, M.G., Meselhe, E.A., Arceneaux, J.C., Chen, C., and Harwell, M.C. (2009). "Surface water sulfate dynamics in the northern Florida Everglades." Journal of Environmental Quality. 38 (2): 734-741.
514. Wang, J.S., Huang, P.M., Liaw, W.K., and Hammer, U.T. (1991). "Kinetics of the desorption of mercury form selected freshwater sediments as influenced by chloride." Water, Air, and Soil Pollution. 56 (1): 533-542.

515. Wang, Q., Kim, D., Dionysiou, D.D., Sorial, G.A., and Timberlake, D. (2004). "Sources and remediation for mercury contamination in aquatic systems - a literature review." Environmental pollution. 131 (2): 323-336.
516. Watanabe, A., Moroi, K., Sato, H., Tsutsuki, K., Maie, N., Melling, L., and Jaffé, R. (2012). "Contributions of humic substances to the dissolved organic carbon pool in wetlands from different climates." Chemosphere. 88: 1265-1268.
517. Weaver, K., Payne, G., and Xue, S. K. (2008). "Chapter 3A: Status of water quality in the Everglades protection area, 2008 South Florida environmental report." South Florida Water Manage District, West Palm, FL.
518. Weerasooriya, R., Tobschall, H.J., Seneviratne, W., and Bandara, A. (2007). "Transition state kinetics of Hg(II) adsorption at gibbsite-water interface." Journal of Hazardous Materials. 147(3): 971-978.
519. Wnalin, L., Kim, E., and Mason, R. (2007). "Factor influencing the oxidation, reduction, methylation and demethylation of mercury species in coastal waters." Marine Chemistry. 107 (3): 278-294.
520. Xia, K., Skyllberg, U.L., Bleam, W.F., Bloom, P.R., Nater, E.A., and Helmke, P.A. (1999). "X-ray absorption spectroscopic evidence for the complexation of Hg(II) by reduced sulfur in soil organic matter." Environmental Science & Technology. 33 (2): 257–261.
521. Yasunaga, T., and Ikeda, T. (1986). "In geochemical processes at mineral surfaces." in: Davis, J.A., Hayes, K.F. (Eds.). American Chemical Society, Washington, DC. 323: 231-253.
522. Yin, Y., Allen, H.E., and Huang, C.P. (1997). "Kinetics of mercury(II) adsorption and desorption on soil." Environmental Sciences Technology. 31 (2): 496-503.
523. Zachara, J.M., Cowan, C.E., Schmidt, R.L., and Ainsworth, C.C. (1988). "Chromate adsorption by kaolinite." Clays and Clay Minerals. 36 (4): 317-326.
524. Zahir, F., Rizwi S.J., Haq, S.K., and Khanb, R.H. (2005). "Low dose mercury toxicity and human health." Environmental Toxicology and Pharmacology. 20: 351-360.

525. Zhong, H., and Wang, W. (2009). "Inorganic mercury binding with different sulfur species in anoxic sediments and their gut juice extractions." Environmental Toxicology and Chemistry. 28 (9): 1851–1857.
526. Zhu, C. (2002). "Estimation of surface precipitation constants for sorption of divalent metals onto hydrous ferric oxide and calcite." Chemical Geology. 188 (1-2): 23-32.
527. Zhu, Y., Ma, L.Q., Gao, B., Bonzongo, J.C., Harris, W., and Gu, B. (2012). Transport and interactions of kaolinite and mercury in saturated sand media." Journal of Hazardous Materials. 213-214: 93-99.

APPENDICES

APPENDIX A

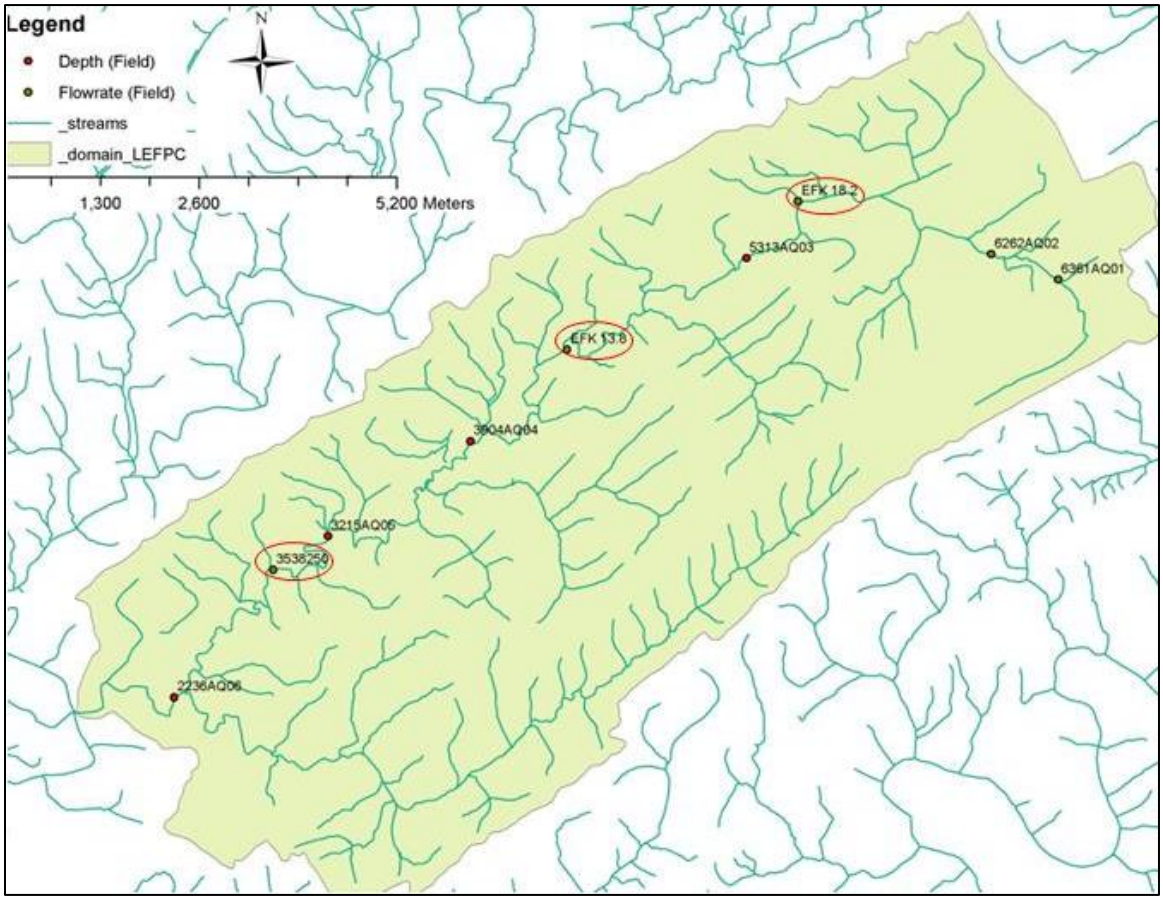

Figure 124. Highlighted stations represent flow data observation points added to the model as time-series.

Table 56. EFPC Model Network Branches

Name	Downstream Chainage	Downstream Connection Name	Downstream Connection Chainage
BC-A-N01	2627.00852	Bear Creek	9274.97319
BC-A-S01	1731.03357	Bear Creek	8228.22922
Bear Creek	12393.1962	EFPC	23342.328
Branch100	570.515326	Bear Creek	1708.63916
Branch101	645.54787	Bear Creek	1238.53279
Branch102	371.057499	Bear Creek	1994.64616
Branch103	367.130677	Bear Creek	2873.2586
Branch104	676.627975	Bear Creek	502.095608
Branch105	738.47401	Bear Creek	855.648999
Branch106	320.135532	EFPC	17698.0082
Branch107	494.19464	EFPC	20073.4189
Branch108	337.941501	EFPC	20996.8015
Branch109	272.418154	BC-A-N01	1027.66123
Branch110	928.093627	Bear Creek	7040.48431
Branch111	512.962161	Branch110	505.555117
Branch112	407.512497	Branch110	505.555117
Branch113	915.067283	EFPC	9091.23597
Branch18	623.430043	EFPC	3679.62887
Branch19	767.032449	EFPC	4382.24429
Branch20	1562.3612	EFPC	5085.13617
Branch21	747.976283	EFPC-A-S04	1394.2137
Branch22	479.446328	EFPC-A-N04	2412.89544
Branch23	733.906826	EFPC-A-N04	1365.18116
Branch24	1062.82743	EFPC-A-N04-N01	1475.16897
Branch25	574.90101	EFPC-A-N04-N01	755.286944
Branch26	1349.79425	EFPC	7282.7484
Branch27	305.550978	Branch26	645.560017
Branch28	1385.65267	EFPC	7647.66632
Branch29	411.312158	EFPC-A-S04	1078.92038
Branch30	1220.46903	EFPC	8026.57498
Branch31	1100.44229	EFPC-A-S04	1625.79832
Branch32	1119.24833	Milton Branch	2212.74766
Branch33	640.394531	Milton Branch	2215.26565
Branch34	394.470438	Milton Branch	1906.67759
Branch35	1094.31462	Milton Branch	1906.67759
Branch36	555.989773	Branch37	1241.65263
Branch37	1389.40442	Milton Branch	1417.23759
Branch38	258.90626	Milton Branch	299.935879
Branch39	763.967426	Branch37	998.198308
Branch40	349.971877	Branch37	863.709821

Continuation of Table 56

Name	Downstream Chainage	Downstream Connection Name	Downstream Connection Chainage
Branch41	306.896242	Branch39	600.112762
Branch42	648.620057	Milton Branch	893.27888
Branch43	410.206634	EFPC	13730.9602
Branch44	341.965487	EFPC	11930.5444
Branch45	345.398656	EFPC	11105.8086
Branch46	1343.24789	EFPC	10541.2185
Branch47	491.932802	Branch46	635.497021
Branch48	1123.56862	EFPC	12342.9044
Branch49	613.000721	EFPC-A-N03	672.619034
Branch50	1074.72944	EFPC-A-N03	1426.07585
Branch51	1674.47658	EFPC	14936.3057
Branch53	1168.69096	Branch51	1362.24078
Branch54	614.27993	Branch51	1308.53024
Branch55	420.959085	EFPC-A-N02	689.961838
Branch56	1506.09017	EFPC	18288.5517
Branch57	349.039006	Branch56	1036.12
Branch58	367.643714	Branch56	376.299345
Branch59	1362.67434	EFPC	18651.3516
Branch60	785.591557	EFPC	18651.3516
Branch61	455.319439	EFPC-A-N01	509.372774
Branch62	1090.51342	EFPC	20466.32
Branch63	1095.59976	EFPC-A-N01	1615.37626
Branch64	1783.7922	EFPC	24812.5811
Branch65	365.341176	Pinhook Branch	877.595397
Branch66	406.584377	Pinhook Branch	1141.96693
Branch67	565.599776	Pinhook Branch	1141.96693
Branch68	625.023043	Pinhook Branch	467.553892
Branch69	710.859381	Gum Hollow Branch	2607.62585
Branch70	604.115881	GHB-A-S05	875.782043
Branch71	646.687734	GHB-A-S05	1162.66811
Branch72	466.240066	GHB-A-S05	1629.21892
Branch73	1553.5932	Gum Hollow Branch	1495.13032
Branch74	957.998954	Branch73	1304.78772
Branch75	565.605786	Branch73	611.384598
Branch76	386.093979	Gum Hollow Branch	3961.40439
Branch77	757.166531	EFPC-A-S01	1940.3623
Branch78	1180.43707	Bear Creek	10308.0545
Branch79	747.814346	Bear Creek	10203.6514
Branch80	656.335209	Bear Creek	8506.0781
Branch81	1061.41327	Bear Creek	8506.0781

Continuation of Table 56

Name	Downstream Chainage	Downstream Connection Name	Downstream Connection Chainage
Branch82	455.792787	BC-A-S01	813.365846
Branch83	459.796837	Branch82	426.125736
Branch84	1335.56282	Bear Creek	8161.14718
Branch85	287.505808	Branch84	703.608893
Branch86	1598.99258	Bear Creek	8951.6694
Branch87	1219.09375	Bear Creek	7238.97864
Branch88	1504.98443	Bear Creek	6349.44565
Branch89	602.005039	Bear Creek	5917.48305
Branch90	776.620137	Bear Creek	5988.19373
Branch91	508.739969	Bear Creek	5288.30912
Branch92	619.209188	Bear Creek	4969.5992
Branch93	696.968113	Bear Creek	4839.21515
Branch94	628.918276	Bear Creek	4133.97608
Branch95	643.724335	Bear Creek	3766.44731
Branch96	574.72635	Bear Creek	3372.95977
Branch97	643.289247	Bear Creek	2873.2586
Branch98	608.276871	Bear Creek	2496.828
Branch99	568.290615	Bear Creek	2105.09977
EFPC	25485.1953		
EFPC-A-N01	1820.50769	EFPC	21183.8791
EFPC-A-N02	1546.16389	EFPC	14936.3057
EFPC-A-N03	1616.78645	EFPC	12948.7807
EFPC-A-N04	2934.28761	EFPC	6498.75737
EFPC-A-N04-N01	1611.75264	EFPC-A-N04	2100.35832
EFPC-A-S01	2243.13258	EFPC	22905.6146
EFPC-A-S02	1435.42326	EFPC	19750.8333
EFPC-A-S03	1671.92188	EFPC	13831.4589
EFPC-A-S04	2306.03929	EFPC	5746.31448
GHB-A-S05	1829.8496	Gum Hollow Branch	2253.28604
Gum Hollow Branch	4259.9214	EFPC	16319.3026
Milton Branch	3414.31997	EFPC	10778.9293
Pinhook Branch	2016.48484	EFPC	16958.969

Table 57. EFPC Model, network point for branch BC-A-N01 and BC-A-S01

X Coordinate	Y Coordinate	Branch	Chainage Type	Chainage
750360	181500	BC-A-N01	System Defined	0
750190	181600	BC-A-N01	System Defined	197.23083
750060	181510	BC-A-N01	System Defined	355.34471
749940	181500	BC-A-N01	System Defined	475.76066
749930	181420	BC-A-N01	System Defined	556.38324
749710	181260	BC-A-N01	System Defined	828.41265
749520	181200	BC-A-N01	System Defined	1027.6612
749420	181100	BC-A-N01	System Defined	1169.0826
749270	181060	BC-A-N01	System Defined	1324.3243
749210	180930	BC-A-N01	System Defined	1467.5025
749120	180790	BC-A-N01	System Defined	1633.9357
749120	180680	BC-A-N01	System Defined	1743.9357
749100	180430	BC-A-N01	System Defined	1994.7344
749180	180140	BC-A-N01	System Defined	2295.5666
748960	180030	BC-A-N01	System Defined	2541.5341
748940	179980	BC-A-N01	System Defined	2595.3857
748950	179950	BC-A-N01	System Defined	2627.0085
748370	178730	BC-A-S01	System Defined	0
748704.07	178836.58	BC-A-S01	System Defined	350.65372
748941.5	178880.67	BC-A-S01	System Defined	592.14686
749120	178750	BC-A-S01	System Defined	813.36585
749230	178740	BC-A-S01	System Defined	923.81946
749390	178820	BC-A-S01	System Defined	1102.7049
749390	178920	BC-A-S01	System Defined	1202.7049
749450	179000	BC-A-S01	System Defined	1302.7049
749520	179290	BC-A-S01	System Defined	1601.0336
749640	179340	BC-A-S01	System Defined	1731.0336

Table 58. EFPC Model boundary conditions per branch

Boundary Description	Boundary Type	Branch Name	Chainage	Boundary ID
Open	Inflow	Bear Creek	0	N/A
Open	Inflow	Branch100	0	N/A
Open	Inflow	Branch101	0	N/A
Open	Inflow	Branch102	0	N/A
Open	Inflow	Branch103	0	N/A
Open	Inflow	Branch104	0	N/A
Open	Inflow	Branch105	0	N/A
Open	Inflow	Branch106	0	N/A
Open	Inflow	Branch107	0	N/A
Open	Inflow	Branch108	0	N/A
Open	Inflow	Branch109	0	N/A
Open	Inflow	Branch110	0	N/A
Open	Inflow	Branch111	0	N/A
Open	Inflow	Branch112	0	N/A
Open	Inflow	Branch113	0	N/A
Open	Inflow	Branch18	0	N/A
Open	Inflow	Branch19	0	N/A
Open	Inflow	Branch20	0	N/A
Open	Inflow	Branch21	0	N/A
Open	Inflow	Branch22	0	N/A
Open	Inflow	Branch23	0	N/A
Open	Inflow	Branch24	0	N/A
Open	Inflow	Branch25	0	N/A
Open	Inflow	Branch26	0	N/A
Open	Inflow	Branch27	0	N/A
Open	Inflow	Branch28	0	N/A
Open	Inflow	Branch29	0	N/A
Open	Inflow	Branch30	0	N/A
Open	Inflow	Branch31	0	N/A
Open	Inflow	Branch32	0	N/A
Open	Inflow	Branch33	0	N/A
Open	Inflow	Branch34	0	N/A
Open	Inflow	Branch35	0	N/A
Open	Inflow	Branch36	0	N/A
Open	Inflow	Branch37	0	N/A
Open	Inflow	Branch38	0	N/A

Continuation of Table 58

Boundary Description	Boundary Type	Branch Name	Chainage	Boundary ID
Open	Inflow	Branch39	0	N/A
Open	Inflow	Branch40	0	N/A
Open	Inflow	Branch41	0	N/A
Open	Inflow	Branch42	0	N/A
Open	Inflow	Branch43	0	N/A
Open	Inflow	Branch44	0	N/A
Open	Inflow	Branch45	0	N/A
Open	Inflow	Branch46	0	N/A
Open	Inflow	Branch47	0	N/A
Open	Inflow	Branch48	0	N/A
Open	Inflow	Branch49	0	N/A
Open	Inflow	Branch50	0	N/A
Open	Inflow	Branch51	0	N/A
Open	Inflow	Branch53	0	N/A
Open	Inflow	Branch54	0	N/A
Open	Inflow	Branch55	0	N/A
Open	Inflow	Branch56	0	N/A
Open	Inflow	Branch57	0	N/A
Open	Inflow	Branch58	0	N/A
Open	Inflow	Branch59	0	N/A
Open	Inflow	Branch60	0	N/A
Open	Inflow	Branch61	0	N/A
Open	Inflow	Branch62	0	N/A
Open	Inflow	Branch63	0	N/A
Open	Inflow	Branch64	0	N/A
Open	Inflow	Branch65	0	N/A
Open	Inflow	Branch66	0	N/A
Open	Inflow	Branch67	0	N/A
Open	Inflow	Branch68	0	N/A
Open	Inflow	Branch69	0	N/A
Open	Inflow	Branch70	0	N/A
Open	Inflow	Branch71	0	N/A
Open	Inflow	Branch72	0	N/A
Open	Inflow	Branch73	0	N/A
Open	Inflow	Branch74	0	N/A
Open	Inflow	Branch75	0	N/A
Open	Inflow	Branch76	0	N/A
Open	Inflow	Branch77	0	N/A
Open	Inflow	Branch78	0	N/A

Continuation of Table 58

Boundary Description	Boundary Type	Branch Name	Chainage	Boundary ID
Open	Inflow	Branch79	0	N/A
Open	Inflow	Branch80	0	N/A
Open	Inflow	Branch81	0	N/A
Open	Inflow	Branch82	0	N/A
Open	Inflow	Branch83	0	N/A
Open	Inflow	Branch84	0	N/A
Open	Inflow	Branch85	0	N/A
Open	Inflow	Branch86	0	N/A
Open	Inflow	Branch87	0	N/A
Open	Inflow	Branch88	0	N/A
Open	Inflow	Branch89	0	N/A
Open	Inflow	Branch90	0	N/A
Open	Inflow	Branch91	0	N/A
Open	Inflow	Branch92	0	N/A
Open	Inflow	Branch93	0	N/A
Open	Inflow	Branch94	0	N/A
Open	Inflow	Branch95	0	N/A
Open	Inflow	Branch96	0	N/A
Open	Inflow	Branch97	0	N/A
Open	Inflow	Branch98	0	N/A
Open	Inflow	Branch99	0	N/A
Open	Inflow	EFPC	0	N/A
Point Source	Inflow	EFPC	0	N/A
Point Source	Inflow	EFPC	7.69702308	200
Point Source	Inflow	EFPC	15.1815578	135
Point Source	Inflow	EFPC	28.5337035	134
Point Source	Inflow	EFPC	93.2045032	126
Point Source	Inflow	EFPC	99.9074534	125
Point Source	Inflow	EFPC	144.267419	114
Point Source	Inflow	EFPC	253.302757	113
Point Source	Inflow	EFPC	318.675028	110
Point Source	Inflow	EFPC	364.903089	109
Point Source	Inflow	EFPC	370.037803	102
Point Source	Inflow	EFPC	390.364968	99
Point Source	Inflow	EFPC	459.803948	87
Point Source	Inflow	EFPC	459.803948	88
Point Source	Inflow	EFPC	484.094043	86

Continuation of Table 58

Boundary Description	Boundary Type	Branch Name	Chainage	Boundary ID
Point Source	Inflow	EFPC	487.198636	83
Point Source	Inflow	EFPC	551.868787	71
Point Source	Inflow	EFPC	582.150378	67
Point Source	Inflow	EFPC	622.587496	62
Point Source	Inflow	EFPC	628.418544	64
Point Source	Inflow	EFPC	632.571374	63
Point Source	Inflow	EFPC	697.070226	58
Point Source	Inflow	EFPC	701.909704	57
Point Source	Inflow	EFPC	716.780429	55
Point Source	Inflow	EFPC	741.47639	51
Point Source	Inflow	EFPC	764.022982	54
Point Source	Inflow	EFPC	785.40445	48
Point Source	Inflow	EFPC	787.82346	47
Point Source	Inflow	EFPC	804.502318	46
Point Source	Inflow	EFPC	820.952263	44
Point Source	Inflow	EFPC	845.446533	42
Point Source	Inflow	EFPC	883.151953	41
Point Source	Inflow	EFPC	933.004587	34
Point Source	Inflow	EFPC	943.002728	33
Point Source	Inflow	EFPC	1020.78772	21
Point Source	Inflow	EFPC	1059.24245	20
Point Source	Inflow	EFPC	1177.78284	19
Point Source	Inflow	EFPC	1347.73701	16
Point Source	Inflow	EFPC	1399.69678	14
Point Source	Inflow	EFPC	1946.26967	6
Point Source	Inflow	EFPC	2050.32925	7
Point Source	Inflow	EFPC	2398.76723	3
Point Source	Inflow	EFPC	2456.77397	2
Open	Q-h	EFPC	25485.2	N/A
Open	Inflow	EFPC-A-N01	0	N/A
Open	Inflow	EFPC-A-N02	0	N/A
Open	Inflow	EFPC-A-N03	0	N/A
Open	Inflow	EFPC-A-N04	0	N/A
Open	Inflow	EFPC-A-N04-N01	0	N/A
Open	Inflow	EFPC-A-S01	0	N/A
Open	Inflow	EFPC-A-S02	0	N/A
Open	Inflow	EFPC-A-S03	0	N/A
Open	Inflow	EFPC-A-S04	0	N/A
Open	Inflow	GHB-A-S05	0	N/A

Continuation of Table 58

Boundary Description	Boundary Type	Branch Name	Chainage	Boundary ID
Open	Inflow	GHB-A-S05	0	N/A
Open	Inflow	Gum Hollow Branch	0	N/A
Open	Inflow	Milton Branch	0	N/A
Open	Inflow	Pinhook Branch	0	N/A
Closed		BC-A-S01	0	N/A
Closed		BC-A-N01	0	N/A

Table 59. Wentworth grade scale for particle size to standardize sieve diameters [29]

Range in mm (Sieve diameter)	Class Name
>256	Boulders
256-128	Large Cobbles
128-64	Small Cobbles
64-32	Very Coarse Gravel
32-16	Coarse Gravel
16-8	Medium Gravel
8-4	Fine Gravel
4-2	Very Fine Gravel
2-1	Very Coarse Sand
1-1.5	Coarse Sand
0.5-0.25	Medium Sand
0.25-0.125	Fine Sand
0.125-0.062	Very Fine Sand
0.062-0.031	Coarse Silt
0.031-0.016	Medium Silt
0.016-0.008	Fine Silt

Range in mm (Sieve diameter)	Class Name
0.008-0.004	Very Fine Silt
0.004-0.002	Coarse Clay
0.002-0.001	Medium Clay
0.0010-0.0005	Fine Clay
0.0005-0.00024	Very Fine Clay

Table 60. Suspended sediments characterization [19]

Km from downstream	Sieve % <0.0005 mm	Sieve % <0.002 mm	Sieve % <0.008 mm	Sieve % <0.016 mm	Sieve % <0.062 mm	Sieve % <0.125 mm	Sieve % <0.500 mm	Sieve % < 2.0 mm
2	7.7	26.7	41.9	49.3	64.0			
4	7.0	14.5	24.2	29.9	44.0			
4	8.3	17.0	28.7	35.5	48.6			
4					29.2	35.5	71.3	98.9
6	9.9	19.8	33.2	39.1	56.6	33.0	59.5	97.7
6					26.6			
7	13.9	27.0	44.2	51.6	81.9			
9	11.6	21.3	36.8	48.4	64.6			
9					31.1	40.2	63.4	90.3
11	1.7	16.4	23.2	24.0	26.1	53.0	90.4	98.2
11					44.2			
13	10.7	17.2	26.2	32.4	41.0			
13					18.1		45.2	87.3
13					31.9		40.9	84.4
13					33.7		75.6	87.9
15	8.9	16.1	26.0	30.6	40.3			
16	9.3	16.9	27.6	33.1	42.2			
18	9.1	15.8	25.3	28.8	41.5			
20	13.2	22.3	32.3	42.1	53.0			
21	5.1	11.2	18.0	21.7	31.9			
22	4.8	7.5	12.2	14.9	24.1	36.6	60.3	86.4

Km from downstream	Sieve % <0.0005 mm	Sieve % <0.002 mm	Sieve % <0.008 mm	Sieve % <0.016 mm	Sieve % <0.062 mm	Sieve % <0.125 mm	Sieve % <0.500 mm	Sieve % < 2.0 mm
22	6.1	9.2	12.9	16.0	23.5	36.4	66.2	93.8
22	3.6	8.6	15.5	18.6	35.7			
22	4.6	11.7	19.4	23.9	28.5	47.9	69.2	94.7
23	2.8	8.1	20.2	32.5	47.5	59.3	85.2	97.4
23	10.0	16.2	24.6	29.7	44.4	55.0	83.8	96.3

Table 61. Data Collected for the bed sediment characterization [43]

Station	Grain size, mm	% Passing	Station	Grain size, mm	% Passing
64	38.1	100	48	38.1	97.533
64	25.4	94.5323	48	25.4	89.602
64	19.1	86.144	48	19.1	81.428
64	12.7	69.115	48	12.7	68.416
64	9.5	58.787	48	9.5	58.617
64	4.76	41.061	48	4.76	39.748
64	2	21.816	48	2	23.329
64	1	11.584	48	1	11.707
64	0.5	5.758	48	0.5	4.384
64	0.243	3.558	48	0.243	3.091
64	0.118	2.956	48	0.118	2.468
64	0.063	2.488	48	0.063	2.034
64	0.035	2.104	48	0.035	1.8
64	0.02	1.658	48	0.02	1.496
64	0.005	0.639	48	0.005	0.913
64	0.00043	0	48	0.00043	0
56	38.1	100	40	38.1	96.058
56	25.4	97.537	40	25.4	94.594
56	19.1	89.634	40	19.1	88.16
56	12.7	74.622	40	12.7	73.882
56	9.5	61.911	40	9.5	62.434
56	4.76	40.393	40	4.76	43.326
56	2	24.015	40	2	28.355
56	1	13.354	40	1	16.03
56	0.5	6.681	40	0.5	6.294
56	0.243	5.608	40	0.243	3.116

Station	Grain size, mm	% Passing	Station	Grain size, mm	% Passing
56	0.118	4.944	40	0.118	2.412
56	0.063	4.308	40	0.063	1.953
56	0.035	3.994	40	0.035	1.63
56	0.02	3.548	40	0.02	1.3
56	0.005	2.25	40	0.005	0.585
56	0.00043	0	40	0.00043	0.011
32	38.1	96.058	6	38.1	100
32	25.4	94.594	6	25.4	100
32	19.1	88.16	6	19.1	92.575
32	12.7	73.882	6	12.7	79.817
32	9.5	62.434	6	9.5	71.089
32	4.76	43.326	6	4.76	53.623
32	2	28.355	6	2	33.278
32	1	16.03	6	1	19.813
32	0.5	6.294	6	0.5	9.244
32	0.243	3.116	6	0.243	3.297
32	0.118	2.412	6	0.118	2.258
32	0.063	1.953	6	0.063	1.613
32	0.035	1.63	6	0.035	1.317
32	0.02	1.3	6	0.02	1.08
32	0.005	0.585	6	0.005	0.002
32	0.00043	0.011	6	0.00043	0
24	38.1	97.499	2	38.1	100
24	25.4	90.22	2	25.4	100
24	19.1	79.006	2	19.1	100
24	12.7	67.361	2	12.7	90.088
24	9.5	58.232	2	9.5	81.112
24	4.76	41.957	2	4.76	58.447

Station	Grain size, mm	% Passing	Station	Grain size, mm	% Passing
24	2	27.399	2	2	30.214
24	1	15.314	2	1	16.724
24	0.5	6.803	2	0.5	5.419
24	0.243	2.96	2	0.243	2.185
24	0.118	2.158	2	0.118	1.529
24	0.063	1.758	2	0.063	1.189
24	0.035	1.473	2	0.035	0.76
24	0.02	1.166	2	0.02	0.643
24	0.005	0.528	2	0.005	0
24	0.00043	0	2	0.00043	0
Lake reality	38.1	100	USGS Station 17	38.1	100
Lake reality	25.4	98.08	USGS Station 17	25.4	95.329
Lake reality	19.1	97.813	USGS Station 17	19.1	86.842
Lake reality	12.7	95.256	USGS Station 17	12.7	73.016
Lake reality	9.5	92.613	USGS Station 17	9.5	60.515
Lake reality	4.76	82.299	USGS Station 17	4.76	39.703
Lake reality	2	68.108	USGS Station 17	2	23.446
Lake reality	1	52.978	USGS Station 17	1	13.696
Lake reality	0.5	39.235	USGS Station 17	0.5	6.895
Lake reality	0.243	28.447	USGS Station 17	0.243	4.55
Lake reality	0.118	14.921	USGS Station 17	0.118	3.484
Lake reality	0.063	9.139	USGS Station 17	0.063	2.83
Lake reality	0.035	6.778	USGS Station 17	0.035	2.459
Lake reality	0.02	5.752	USGS Station 17	0.02	2.055
Lake reality	0.005	3.677	USGS Station 17	0.005	1.195
Lake reality	0.00043	0	USGS Station 17	0.00043	0

Table 62. Boundary conditions for East Fork Poplar Creek

Boundary Description	Boundary Type	Chainage
Open	Q-h	2663.78
Open	Inflow	0.00
Point Source (outfalls)	Inflow	7.70
Point Source (outfalls)	Inflow	15.18
Point Source (outfalls)	Inflow	28.53
Point Source (outfalls)	Inflow	93.20
Point Source (outfalls)	Inflow	99.91
Point Source (outfalls)	Inflow	144.27
Point Source (outfalls)	Inflow	253.30
Point Source (outfalls)	Inflow	318.68
Point Source (outfalls)	Inflow	364.90
Point Source (outfalls)	Inflow	370.04
Point Source (outfalls)	Inflow	390.36
Point Source (outfalls)	Inflow	459.80
Point Source (outfalls)	Inflow	459.80
Point Source (outfalls)	Inflow	484.09
Point Source (outfalls)	Inflow	487.20
Point Source (outfalls)	Inflow	551.87
Point Source (outfalls)	Inflow	582.15
Point Source (outfalls)	Inflow	622.59
Point Source (outfalls)	Inflow	628.42
Point Source (outfalls)	Inflow	632.57
Point Source (outfalls)	Inflow	697.07
Point Source (outfalls)	Inflow	701.91
Point Source (outfalls)	Inflow	716.78
Point Source (outfalls)	Inflow	741.48
Point Source (outfalls)	Inflow	764.02

Boundary Description	Boundary Type	Chainage
Point Source (outfalls)	Inflow	785.40
Point Source (outfalls)	Inflow	787.82
Point Source (outfalls)	Inflow	804.50
Point Source (outfalls)	Inflow	820.95
Point Source (outfalls)	Inflow	845.45
Point Source (outfalls)	Inflow	883.15
Point Source (outfalls)	Inflow	933.00
Point Source (outfalls)	Inflow	943.00
Point Source (outfalls)	Inflow	1020.79
Point Source (outfalls)	Inflow	1059.24
Point Source (outfalls)	Inflow	1177.78
Point Source (outfalls)	Inflow	1347.74
Point Source (outfalls)	Inflow	1399.70
Point Source (outfalls)	Inflow	1946.27
Point Source (outfalls)	Inflow	2050.33
Point Source (outfalls)	Inflow	2398.77
Point Source (outfalls)	Inflow	2456.77
Open	Q-h	2663.78
Closed		0.00

Table 63. UEFPC cross-sections description for chainages 0m and 2663m

Chainage	Level	Cross sec.	Hydraulic	Width	Resist.
(m)	(m)	area (m2)	radius m)	(m)	factor
0	281.575	0	0	0	30
	281.775	0.648	0.161	4.645	30
	281.976	1.677	0.333	5.573	30
	282.176	2.862	0.507	6.24	30
	282.377	4.176	0.679	6.863	30
	282.578	5.615	0.847	7.497	30
	282.778	7.19	1.01	8.208	30
	282.979	8.906	1.168	8.882	30
	283.179	10.746	1.326	9.444	30
	283.38	12.67	1.487	9.74	30
	283.58	14.653	1.654	10.037	30
	283.781	16.696	1.822	10.334	30
	283.981	18.793	1.991	10.562	30
	284.182	20.932	2.163	10.766	30
	284.383	23.112	2.336	10.971	30
	284.583	25.332	2.509	11.175	30
	284.784	27.594	2.683	11.38	30
	284.984	29.897	2.857	11.584	30
	285.185	32.24	3.03	11.757	30
	285.385	34.608	3.205	11.864	30
2663.775	266.37	0	0	0	1
	266.706	1.31	0.327	4.164	1
	267.042	2.798	0.638	4.69	1
	267.378	4.462	0.937	5.217	1
	267.714	6.303	1.226	5.744	1
	268.05	8.322	1.506	6.27	1

Chainage	Level	Cross sec.	Hydraulic	Width	Resist.
	268.386	10.516	1.779	6.784	1
	268.722	12.879	2.048	7.279	1
	269.058	15.408	2.313	7.764	1
	269.394	18.086	2.577	8.175	1
	269.73	20.902	2.841	8.586	1
	270.066	23.856	3.104	8.997	1
	270.402	26.948	3.365	9.401	1
	270.738	30.146	3.63	9.631	1
	271.074	33.42	3.9	9.86	1
	271.41	36.772	4.174	10.089	1
	271.746	40.2	4.45	10.318	1
	272.082	43.706	4.726	10.547	1
	272.418	47.288	5.002	10.828	1
	272.754	51.346	5.214	13.071	1

Table 64. Dissolved and particulate mercury in the water column, observed data from UEFPC-Station 17 [6]

Date	TSS mg/L	Diss. Hg ug/L	Part. Hg ug/L	Total Hg ug/L	Part.Hg %	Diss. Hg%
02/19/97	2.20	0.114	0.506	0.620	82%	18%
06/20/97	2.90	0.089	0.409	0.498	82%	18%
11/20/97	2.79	0.075	0.441	0.516	85%	15%
08/11/98	11.07	0.070	0.922	0.992	93%	7%
12/17/98	7.01	0.100	0.426	0.526	81%	19%
Average	5.19	0.090	0.541	0.630	85%	15%

Table 65. Observed dissolved mercury in pore water, UEFPC (Source: OREIS database)

Station	Date	Concentration mg/L
UEFPC-3	12/11/1996	4.00E-08
UEFPC-2	12/11/1996	4.00E-08
UEFPC-1	12/11/1996	4.00E-08
UEFPC-4	12/12/1996	1.20E-07
UEFPC-1	12/11/1996	1.70E-07
UEFPC-5	12/12/1996	6.90E-07
UEFPC-1	12/11/1996	7.29E-06
UEFPC-1	12/11/1996	7.29E-06
UEFPC-3	12/11/1996	2.33E-05
UEFPC-4	12/12/1996	3.67E-05
UEFPC-5	12/12/1996	5.00E-05
UEFPC-2	12/11/1996	7.63E-05
UEFPC-5	12/12/1996	2.00E-03
UEFPC-4	12/12/1996	2.00E-03
UEFPC-3	12/11/1996	2.00E-03
UEFPC-2	12/11/1996	2.00E-03
UEFPC-1	12/11/1996	2.00E-03
UEFPC-1	12/11/1996	2.00E-03
Average		6.78E-04
St. Dev.		9.62E-04

Table 66. Observed adsorbed mercury in sediment, UEFPC (OREIS database)

Station	Date	Concentration mg/kg
UEFPC-2	12/11/1996	5.26
UEFPC-1	12/11/1996	5.95
UEFPC-1	12/11/1996	6.37
UEFPC-1	12/11/1996	7.22
UEFPC-1	12/11/1996	7.48
UEFPC-1	12/11/1996	12.70
UEFPC-1	12/11/1996	14.08
UEFPC-5	12/12/1996	26.60
UEFPC-5	12/12/1996	28.53
UEFPC-4	12/12/1996	29.73
UEFPC-3	12/11/1996	30.08
UEFPC-4	12/12/1996	35.40
UEFPC-3	12/11/1996	38.65
UEFPC-5	12/12/1996	38.68
UEFPC-3	12/11/1996	46.60
UEFPC-4	12/12/1996	50.99
UEFPC-2	12/11/1996	100.50
UEFPC-2	12/11/1996	125.31
Average		33.90
St. Dev.		32.56

APPENDIX B1 - PHREEQC Capabilities and Limitations

[Quoted from Parkhurst, D. L. and C. A. J. Appelo, User's Guide to PHREEQC (Version 2), U.S. Geological Survey, U.S. DOI, Denver, CO (1999)]

PHREEQC version 2 is a computer program for simulating chemical reactions and transport processes in natural or polluted waters. The program is based on equilibrium chemistry of aqueous solutions interacting with minerals, gases, solid solutions, exchangers, and sorption surfaces, but also includes the capability to model kinetic reactions with rate equations that are completely user-specified in the form of basic statements. Kinetic and equilibrium reactants can be interconnected, for example by linking the number of surface sites to the amount of a kinetic reactant that is consumed (or produced) during the course of a model period. A 1D transport algorithm comprises dispersion, diffusion, and various options for dual porosity media. A powerful inverse modeling capability allows identification of reactions that account for observed water compositions along a flowline or in the time course of an experiment. A chemical data base allows application of the reaction, transport, and inverse-modeling capabilities to chemical reactions that are recognized as influencing rain, soil, ground and surface water quality.

PHREEQC is based on the FORTRAN program PHREEQE (Parkhurst and others, 1980). PHREEQE was capable of simulating a variety of geochemical reactions for a system including mixing of waters, addition of net irreversible reactions to solution, dissolving and precipitating phases to achieve equilibrium with the aqueous phase, and effects of changing temperature.

PHREEQE calculated concentrations of elements, molalities and activities of aqueous species, pH, pe, saturation indices, and mole transfers of phases to achieve equilibrium as a function of specified reversible and irreversible geochemical reactions. PHREEQC version 1 (Parkhurst, 1995) was a completely new program written in the C programming language that implemented all of the capabilities of PHREEQE and added many capabilities that were not available in PHREEQE, including ion-exchange equilibria, surface-complexation equilibria, fixed-pressure gas-phase equilibria, and advective transport. Other improvements relative to PHREEQE included complete accounting for elements in solids and the aqueous and gas phase, mole

balance on hydrogen and oxygen to account for the mass of water in the aqueous phase, identification of the stable phase assemblage from a list of candidate phases, use of redox couples for definition of redox state in speciation calculations, and a more robust non-linear equation solver.

PHREEQC version 2 is a modification of PHREEQC version 1. All of the capabilities and most of the code for version 1 are retained in version 2 and several new capabilities have been added, including kinetically controlled reactions, solid-solution equilibria, fixed-volume gas-phase equilibria, variation of the number of exchange or surface sites in proportion to a mineral or kinetic reactant, diffusion or dispersion in 1D transport, 1D transport coupled with diffusion into stagnant zones, and isotope mole balance in inverse modeling. The numerical method has been modified to use several sets of convergence parameters in an attempt to avoid convergence problems. User-defined quantities can be written to the primary output file and (or) to a file suitable for importation into a spreadsheet, and solution compositions can be defined in a format that is more compatible with spreadsheet programs.

Beyond PHREEQC capabilities, it must be acknowledged that the model also has limitations that define the extent of its application and result in uncertainties. Limitations include for example the expressions used to account for non-ideality of aqueous solutions, consistency of databases, models defining ion exchange, surface complexation, solid solution activities, numerical dispersion, and convergence in transport modeling, among others.

APPENDIX B2 - PHAST Capabilities and Limitation

[Quoted from Parkhurst, D.L., Kipp, K.L., and Charlton, S.R., 2010, PHAST Version 2—A program for simulating groundwater flow, solute transport, and multicomponent geochemical reactions: U.S. Geological Survey Techniques and Methods 6–A35, 235 p.]

The computer program PHAST (PHREEQC And HST3D) simulates multicomponent, reactive solute transport in three-dimensional saturated groundwater flow systems. PHAST is a versatile groundwater flow and solute-transport simulator with capabilities to model a wide range of equilibrium and kinetic geochemical reactions. The flow and transport calculations are based on a modified version of HST3D that is restricted to constant fluid density and constant temperature. The geochemical reactions are simulated with the geochemical model PHREEQC, which is embedded in PHAST. Major enhancements in PHAST Version 2 allow spatial data to be defined in a combination of map and grid coordinate systems, independent of a specific model grid (without node-by-node input). At run time, aquifer properties are interpolated from the spatial data to the model grid; regridding requires only redefinition of the grid without modification of the spatial data. PHAST is applicable to the study of natural and contaminated groundwater systems at a variety of scales ranging from laboratory experiments to local and regional field scales. PHAST can be used in studies of migration of nutrients, inorganic and organic contaminants, and radionuclides; in projects such as aquifer storage and recovery or engineered remediation; and in investigations of the natural rock/water interactions in aquifers. PHAST is not appropriate for unsaturated-zone flow, multiphase flow, or density-dependent flow. A variety of boundary conditions are available in PHAST to simulate flow and transport, including specified-head, flux (specified-flux), and leaky (head-dependent) conditions, as well as the special cases of rivers, drains, and wells. Chemical reactions in PHAST include (1) homogeneous equilibria using an ion-association or Pitzer specific interaction thermodynamic model; (2) heterogeneous equilibria between the aqueous solution and minerals, ion exchange sites, surface complexation sites, solid solutions, and gases; and (3) kinetic reactions with rates that are a function of solution composition. The aqueous model (elements, chemical reactions, and equilibrium constants), minerals, exchangers, surfaces, gases, kinetic reactants, and rate expressions may be defined or modified by the modeler. The PHAST simulator may require

large amounts of memory and long Central Processing Unit (CPU) times. To reduce the long CPU times, a parallel version of PHAST has been developed that runs on a multiprocessor computer or on a collection of computers that are networked. The parallel version requires Message Passing Interface, which is freely available. The parallel version is effective in reducing simulation times. PHAST requires three input files. Only the flow and transport file is described in detail in this report. The other two files, the chemistry data file and the database file, are identical to PHREEQC files, and a detailed description of these files is in the PHREEQC documentation. PHAST Version 2 has a number of enhancements to allow simpler definition of spatial information and to avoid grid-dependent (node-by-node) input definitions. Formerly, all spatial data were defined with rectangular zones. Now wedge-shaped and irregularly shaped volumes may be used to specify the hydrologic and chemical properties of regions within the model domain. Spatial data can be imported from ArcInfo shape and ASCII raster files and from a simple X, Y, Z file format. To accommodate a grid that is not aligned with the coordinate system of the imported files, it is possible to define features in map and grid coordinate systems within the same input file.

New capabilities have been added to interpolate spatial data to the two- or three-dimensional locations of cells and elements. Two-dimensional interpolation is used to define surfaces for the tops and bottoms of three-dimensional regions within the model domain. Surfaces are created by two-dimensional interpolation of scattered X, Y points with associated elevation data. Within the bounds of the scattered points (the convex hull), natural neighbor interpolation is implemented, which uses an area weighting scheme to assign an elevation to a target point based on elevations at the nearest of the scattered points; outside the convex hull, the elevation of the closest point is assigned to a target point. A new capability has been added to aggregate flows of water and solute into an arbitrarily shaped region and through the boundary-condition cells included in the region. Any number of flow aggregation regions may be defined. These regions need not be mutually exclusive, and regions can be combined to define larger, possibly noncontiguous regions. A facility exists to save heads as a function of time and space for these regions, which then can be used to specify boundary-condition heads in a subsequent run.

APPENDIX C

Hg-speciation thermodynamic data for PHREEQC model database is shown in Tables C 1, C 2 and C 3. The exchange coefficients related to Hg(II) and the sorption coefficient of Hg on the surface of minerals are shown in Table C 4 and C 5 respectively.

Table C 1. Hg species thermodynamic reaction constant added to PHREEQC model

Hg species	Reactions	Log K	Ref.
$HgHPO_4$	$Hg(OH)_2 + HPO_4^{2-} + 2H^+ = HgHPO_4 + 2H_2O$	14.99	Powell et al. (2005)
$HgPO_4^-$	$Hg(OH)_2 + HPO_4^{2-} + H^+ = HgPO_4^- + 2H_2O$	9.44	Powell et al. (2005)
$HgCO_3$	$Hg(OH)_2 + CO_3^{2-} + 2H^+ = HgCO_3 + 2H_2O$	17.70	Powell et al. (2005)
$Hg(OH)CO_3^-$	$Hg(OH)_2 + OH- + CO_3^{2-} + 2H^+ = Hg(OH)CO^-_3 + 2H_2O$	25.53	Powell et al. (2005)
$HgHCO_3^+$	$Hg(OH)_2 + 3H^+ + CO_3^{2-} = HgHCO^+_3 + 2H_2O$	22.03	Powell et al. (2005)
HgS_2H^-	$Hg(OH)_2 + 2HS^- + OH^- + 2H^+ = HgS_2H^- + 3H_2O$	54.79	Hurley et al. (1994) and Benoit et al. (1999)
$[Hg(CH_3COO)]^+$	$Hg(OH)_2 + CH_3COO^- + 2H^+ = [Hg(CH_3COO)]^+ + 2H_2O$	10.49	Gårdfeldt et al. (2003)
$Hg(CH_3COO)_2$	$Hg(OH)_2 + 2CH_3COO^- + 2H^+ = Hg(CH_3COO)_2 + 2H_2O$	13.19	Gårdfeldt et al. (2003)
$[Hg(CH_3COO)_3]^-$	$Hg(OH)_2 + 3CH_3COO^- + 2H^+ = [Hg(CH_3COO)_3]^- + 2H_2O$	19.49	Gårdfeldt et al. (2003)

Hg species	Reactions	Log K	Ref.
$[Hg(CH_3COO)_3]^2$	$Hg(OH)_2 + 4CH_3COO^- + 2H^+ = [Hg(CH_3COO)_4]^{2-} + 2H_2O$	23.29	Gårdfeldt et al. (2003)
$HgRS^+$	$Hg(OH)_2 + RS^- + 2H^+ = HgRS^+ + 2H_2O$	34.69	Haitzer et al. (2002 and 2003)
$HgCl^+$	$Hg(OH)_2 + Cl^- + 2H^+ = HgCl^+ + 2H_2O$	12.85	Powell et al. (2005)
$HgCl_2$	$Hg(OH)_2 + 2Cl^- + 2H^+ = HgCl_2 + 2H_2O$	19.22	Powell et al. (2005)
$HgCl_3^-$	$Hg(OH)_2 + 3Cl^- + 2H^+ = HgCl_3^- + 2H_2O$	20.12	Powell et al. (2005)
$HgCl_4^{-2}$	$Hg(OH)_2 + 4Cl^- + 2H^+ = HgCl_4^{-2} + 2H_2O$	20.53	Powell et al. (2005)
HgClOH	$Hg(OH)_2 + Cl^- + H^+ = HgClOH + H_2O$	9.31	Powell et al. (2005)
HgF^+	$Hg(OH)_2 + F^- + 2H^+ = HgF^+ + 2H_2O$	8.08	Martell et al. (2001)
HgI^+	$Hg(OH)_2 + I^- + 2H^+ = HgI^+ + 2H_2O$	18.89	Martell et al. (2001)
HgI_2	$Hg(OH)_2 + 2I^- + 2H^+ = HgI_2 + 2H_2O$	30.10	Martell et al. (2001)
HgI_3^-	$Hg(OH)_2 + 3I^- + 2H^+ = HgI_3^- + 2H_2O$	33.79	Martell et al. (2001)
HgI_4^{-2}	$Hg(OH)_2 + 4I^- + 2H^+ = HgI_4^{-2} + 2H_2O$	35.78	Martell et al. (2001)
$HgOH^+$	$Hg(OH)_2 + H^+ = HgOH^+ + H_2O$	2.70	Hurley et al. (1994) and Benoit et al.

Hg species	Reactions	Log K	Ref.
			(1999)
$Hg(OH)_3^-$	$Hg(OH)_2 + H_2O = Hg(OH)_3^- + H^+$	15.00	Hurley et al. (1994) and Benoit et al. (1999)
HgS_2^{-2}	$Hg(OH)_2 + 2HS^- = HgS_2^{-2} + 2H_2O$	31.24	Hurley et al. (1994) and Benoit et al. (1999)
$Hg(HS)_2$	$Hg(OH)_2 + 2HS^- + 2H^+ = Hg(HS)_2 + 2H_2O$	43.82	Hurley et al. (1994) and Benoit et al. (1999)
$HgSO_4$	$Hg(OH)_2 + SO_4^{-2} + 2H^+ = HgSO_4 + 2H_2O$	7.49	Hurley et al. (1994)

Table C 2. Hg thermodynamic data at 25 °C; aq is aqueous, c is condensed, g is gas, liq is liquid, $\Delta H_f°$ is standard heat of formation, ΔG_f is standard gibbs free energy, S is entropy (Hepler and Olofsson 1974)

Substance	$\Delta H_f°$, kJ mol^{-1}	$\Delta G_f°$, kJ mol^{-1}	S°, J K^{-1} mol^{-1}
Hg (liq)	0	0	76.02
Hg(g)	61.317	31.853	174.85
Hg(aq)	13.93	37.2	-2.1
Hg^+(g)	1074.53		
Hg^{2+}(g)	2890.4		
Hg^{2+}(aq)	170.16	164.703	-36.23

Substance	$\Delta H_f°$, kJ mol^{-1}	$\Delta G_f°$, kJ mol^{-1}	S°, J K^{-1} mol^{-1}
Hg^{3+}(g)	6192		
Hg_2(g)	109	68.2	287.9
Hg_2^{2+}(aq)	166.82	153.607	65.77
HgO (c, red, orthorh)	-90.83	-58.555	70.29
HgO (c, yellow,	-90.83	-58.450	69.87
HgO (c, red, hexag)	-90.33	-58.325	71.25
HgO(g)			241.8
HgH(g)	238	213	219.7
$Hg(OH)^+$(aq)	-84.5	-52.01	69.0
$Hg(OH)_2$(aq)	-359.8	-274.5	126.4
$Hg(OH)_3^-$(aq)		-427.2	
$HHgO_2^-$(aq)		-190.0	
HgF(g)	2.9	-18.4	248.28
HgF^+(aq)	-159.0	-123.0	-8
Hg_2F_2(c)	-485	-431	167
HgCl(g)	83.7	62.8	259.9
$HgCl^+$(aq)	-19.7	-5.0	71
$HgCl_2$(c)	-225.9	-180.3	146.0
$HgCl_2$(g)	-143.1	-141.8	294.68
$HgCl_2$(aq)	-217.1	-172.8	151
$HgCl_3^-$(aq)	-389.5	-308.8	205
$HgCl_4^{2-}$(aq)	-554.8	-446.4	289
HgCl(OH) (aq)	-288.7	-222.2	134
Hg_2Cl_2 (c)	-265.579	-210.773	191.42
HgBr(g)	105	67	271.5
$HgBr^+$(aq)	5.4	9.2	75
$HgBr_2$(c)	-170.7	-153.1	172

Substance	$\Delta H_f°$, kJ mol^{-1}	$\Delta G_f°$, kJ mol^{-1}	S°, J K^{-1} mol^{-1}
$HgBr_2$(g)	-86.6	-113.8	320.12
$HgBr_2$(aq)	-161.5	-142.7	167
$HgBr_3^-$ (aq)	-294.1	-259.0	255
$HgBr_4^{2-}$ (aq)	-431.8	-370.7	305
HgBr(OH) (aq)		-207.9	
HgBrCl(g)			299.4
HgBrCl(aq)		-161.5	
Hg_2Br_2(c)	-206.94	-181.084	217.6
HgI(g)	132.2	91.6	281.42
HgI^+(aq)	42.3	40.2	75
HgI_2(c, red)	-105.4	-101.7	180
HgI_2(c, yellow)	-102.9		
HgI_2(g)	-17.2	-59.8	336.02
HgI_2(aq)	-80.3	-74.9	172
HgI_3-(aq)	-153.6	-148.1	297
HgI_4^{2-}(aq)	-236.0	-211.3	356
HgI(OH) (aq)		-173.2	
HgICl (aq)		-128.4	
HgIBr(g)			320.45
HgIBr(aq)		-111.3	
$HgIBr_3^{2-}$(aq)		-336.69	
$HgI2Br_2^{2-}$(aq)		-297.40	
$HgI2Br^{2-}$(aq)		-255.6	
Hg_2I_2(c)	-121.34	-111.002	233.5
HgS(c, red)	-54.0	-46.4	82.4
HgS(c, black)	-50.2	-44.4	88.7
$HgSO_4$(c)	-707.5	-594	142

Substance	**$\Delta H_f°$, kJ mol^{-1}**	**$\Delta G_f°$, kJ mol^{-1}**	**S°, J K^{-1} mol^{-1}**
Substance	$\Delta H_f°$, kJ mol^{-1}	$\Delta G_f°$, kJ mol^{-1}	S°, J K^{-1} mol^{-1}
Hg_2SeO_3(c)		-297.5	
HgTe(c)	-33.9	-28.0	106.7
$Hg(N_3)^+$(aq)		468.6	
$Hg(N_3)_2$(aq)		774.0	
$Hg(N_3)_2$(c)	592.0	746.4	208.8
$Hg(NO_3)^+$(aq)		51.5	
$Hg(NO_3)_2$(aq)		-50.2	
$Hg(NO_2)_4^{2-}$ (aq)		-46.9	
$Hg(NH_3)_2^+$(aq)		87.9	
$Hg(NH_3)_2^{2+}$(aq)	-94.6	11.7	172
$Hg(NH_3)_3^{2+}$(aq)	-188.3	-20.5	259
$Hg(NH_3)_4^{2+}$(aq)	-283.7	-51.5	335
$HgNH_2Br$ (c, orthorh)			133.18
$HgNH_2Br$ (c, cubic)			130.08
$Hg_2(P_2O_7)^{2-}$ (aq)		-1820	
$Hg_2(OH)(P_2O_7)^{3-}$ (aq)		-2012	
$Hg_2(P_2O_7)_2^{6-}$ (aq)		-3694	
$Hg_2(OH)_2(P_2O_7)^{4-}$ (aq)		-2197	
$Hg(C_2O_4)$ (c)	-678.2		
$Hg_2(CO_3)$ (c)	-553.5	-468.2	180
$Hg_2(C_2O_4)$ (c)		-593.3	
$Hg_2(C_2O_4)_2^{2-}$ (aq)		-1234.3	
$Hg_2(OH)(C_2O_4)^-$ (aq)		-752.3	

Table C 3. Hg-Organic thermodynamicdata; aq is aqueous, c is condensed, g is gas, liq is liquid, $\Delta H_f°$ is standard heat of formation, ΔG_f is standard gibbs free energy, S is entropy (Hepler and Olofsson 1974)

Substance	$\Delta H_f°$, kJ mol^{-1}	$\Delta G_f°$, kJ mol^{-1}	S°, J K^{-1} mol^{-1}
$Hg(CH_3)$ (g)	167		
$Hg(CH_3)_2$ (liq)	59.8	140.2	209
$Hg(CH_3)_2$ (g)	94.39	146.0	305
$Hg(CH_3)(C_2H_5)$ (liq)	46.4		
$Hg(C_2H_5)_2$ (liq)	30.1		
$Hg(C_2H_5)_2$ (g)	75.3		
Hg biphenyl (c)	282.8		
Hg_2Ac_2 (c) (Ac- =	-841	-640.11	310
$Hg(CH_3)Cl$ (c)	-116.3		
$Hg(CH_3)Cl$ (g)	-52.3		
$Hg(C_2H_5)Cl$ (c)	-139.3		
$Hg(C_2H_5)Cl$ (g)	-62.8		
$HgCl_2$ CH_3 OH (c)	-474.9	-347.7	243
$HgCl_2$ $2CH_3$ OH (c)	-720	-514.6	335
$Hg(CH_3)Br$ (c)	-85.8		
$Hg(CH_3)Br$ (g)	-18.4		
$Hg(C_2H_5)Br$ (c)	-106.7		
$Hg(C_2H_5)Br$ (g)	-30.1		
$Hg(CH_3)I$ (c)	-42.7		
$Hg(CH_3)I$ (g)	21.8		
$Hg(C_2H_5)I$ (c)	-65.7		
$Hg(CN)^+$(aq)	224.7	238.5	66.1
Hg(CN)Cl (aq)		67.4	

Substance	$\Delta H_f°$, kJ mol^{-1}	$\Delta G_f°$, kJ mol^{-1}	S°, J K^{-1} mol^{-1}
Hg(CN)Br(aq)		84.1	
Hg(CN)I(aq)		121.3	
$Hg(CN_2)$(c)	276		
$Hg(CN)_2$(c)	263.6		
$Hg(CN)_2$(g)	381		
$Hg(CN)_2$(aq)	277.4	312.5	161.1
$Hg(CN)_2Cl^-$ (aq)		182.8	
$Hg(CN)_3^-$ (aq)	396.2	463.6	219.7
$Hg(CN)_3Cl_2^-$ (aq)		335	
$Hg(CN)_3Br_2^-$ (aq)		356	
$Hg(CN)_2$(tu)(aq) (tu =	206.3		
$Hg(CN)_2(tu)_2$(aq)	105.0		
$Hg(ONC)_2$(c) (mercuric	268		
$Hg(SCN)^+$ (aq)		206.3	
Hg(SCN)Cl (aq)		35.6	
Hg(SCN)Br (aq)		51.5	
$Hg(SCN)_2$ (aq)	195.4		
$Hg(SCN)_3^-$ (aq)		329.7	
$Hg(SCN)_4^{2-}$ (aq)	325.5	411.7	452
Hg(OH)(SCN) (aq)		461.9	
$Hg(SCN)(CN)_3^{2-}$ (aq)		553.5	
$Hg_2(SCN)_2$(c)		226.4	
$Hg(ma)_2^+$(aq) (ma =		136.0	
$Hg(ma)_2^+$(aq)	-55.6	104.2	265.3
$HgCl(ma)_2^+$(aq)	-148.5	-34.7	168.6
$Hg(gl)^+$ (aq) (gl- =		-208.8	

Substance	$\Delta H_f°$, kJ mol^{-1}	$\Delta G_f°$, kJ mol^{-1}	S°, J K^{-1} mol^{-1}
$Hg(gl)_2$ (aq)	-860.2	-574.9	264
HgCl(gl) (aq)	-545.2	-376.1	192
$HgCl(en)^+$(aq)	-141.8		
Hg_2CrO_4(c)		-623.8	

Table C 4. Ion exchange coefficients for various ions related to Hg(II) (Khan and Alam, 2004)

Ions	Ion exchange coefficients $K_{Hg/M}$
Na^+	0.04
K^+	0.03
Mg^{2+}	0.02
Co^{2+}	0.04
Ni^{2+}	0.02
Cu^{2+}	0.03
Mn^{2+}	0.03
Zn^{2+}	0.02
Pb^{2+}	0.07
Al^{3+}	0.01
Fe^{3+}	0.05

Table C 5. The surface complexation and the intrinsic equilibrium constants (log Kint) of Hg(II) adsorption on ferrihydrite(≡Hfo), quartz (≡Sio), and gibbsite (≡Aloh) (Dzombak and Morel, 1990; Sarkar et al., 1999)

Sorption Reactions	Log K_{int}
$\equiv Hfo\_sOH + Hg(OH)_2 + H^+ = \equiv Hfo\_sOHg^+ + 2H_2O$	13.95
$\equiv Hfo\_wOH + Hg(OH)_2 + H^+ = \equiv Hfo\_wOHg^+ + 2H_2O$	12.64
$\equiv Sio\_OH + Na+ = \equiv Sio\_Na^+ + H^+$	-6.21
$\equiv Sio\_OH + Hg^{2+} + H_2O = \equiv Sio\_OHgOH + 2H^+$	-2.19
$\equiv Sio\_OH + Hg^{2+} + 2H_2O = \equiv Sio\_OHg(OH)_2^- + 3H+$	-7.75
$\equiv Sio\_OH + Hg^{2+} + Cl^- + H_2O = \equiv Sio\_OHgOHCl^- + 2H^+$	2.14
$\equiv Sio\_OH + Hg^{2+} + PO_4^{3-} + H_2O = \equiv Sio\_OPO_3Hg(OH)_2^{2-} + H^+$	11.61
$\equiv Aloh\_OH + H^+ = \equiv Aloh\_OH_2^+$	2.77
$\equiv Aloh\_OH = \equiv Aloh\_O^- + H^+$	-6.77
$\equiv Aloh\_OH + Na^+ = \equiv Aloh\_Na^+ + H^+$	-6.21
$\equiv Aloh\_OH + Hg^{2+} + H2O = \equiv Aloh\_OHgOH + 2H^+$	-2.19
$\equiv Aloh\_OH + Hg^{2+} + 2H_2O = \equiv Aloh\_OHg(OH)_2^- + 3H^+$	-7.75
$\equiv Aloh\_OH + Hg_{2+} + Cl^- + H_2O = \equiv Aloh\_OHgOHCl^- + 2H^+$	2.14
$\equiv Aloh\_OH + Hg^{2+} + PO_4^{3-} + H_2O = \equiv Aloh\_OPO_3Hg(OH)_2^{2-} + H^+$	11.61

APPENDIX D

EFPC Soil Physical and Chemical Characteristics

The Oak Ridge Reservation (ORR) (Figure E 1) was built as a part of Manhattan Project to develop the nuclear weapons during World War II in Tennessee, USA, in 1942. There were four plants constructed in ORR: K-25, S-50, Y-12 and X-10. X-10 plant is now known as Oak Ridge National Laboratory (ORNL). During 1940s-1950s, the Lithium isotope separation was performed at Y-12 plant. The separation using lithium amalgam which Li dissolved in Hg. As a result 11 million kg of Hg were used and more than 200,000 kg of Hg were accidentally released to the environment.

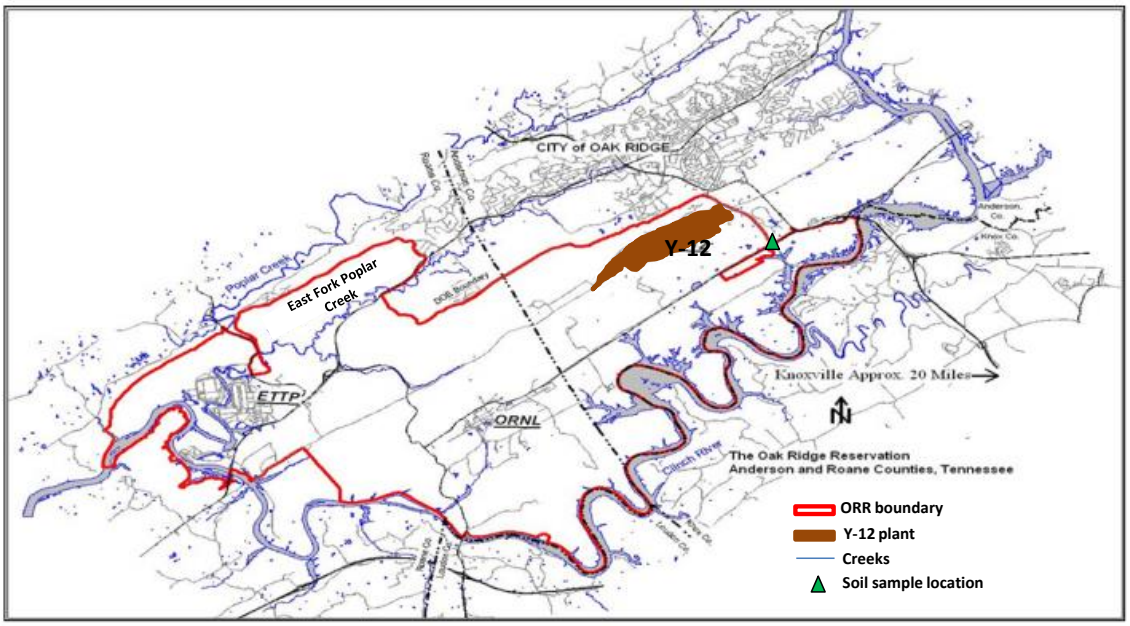

Figure E 1. Map of ORR and soil sample location (modified after www.esd.ornl.gov).

The released Hg was found accumulated in soil, sediment, bedrock which are continued sources for East Fork Poplar Creek (EFPC) that locates downstream of the Y-12 plant. The high concentration of Hg in EFPC raised the public concern on wild life and human health on contacting the contaminated water. Many attempts and remediation plans are made to remove and reduce the Hg concentration in the creek. To best understand the fate and transport of Hg in

the creek, the EFPC soil physical and chemical property data which play important role to Hg fate and transport were collected and described in this section.

The ORR soils are found consisted of properties sandstone, siltstone, and limestone. In this section the soil properties collected from Driese et al., 2001 are categorized by the type of soil described in Table D 1 – D 4 for top soil, sandstone, siltstone, and limestone respectively

Table D 1.Top soil property (Driese et al., 2001)

Parameter	Soil Property
Geologic/Pedologic Material	Soil Zone (A and Bw horizons); thin (20–60 cm), loamy-skeletal, mixed, thermic, Typic Dystrochrept (Soil Survey Staff 1990)
Detrital Mineralogy	40–60% monocrystalline quartz; 2% glauconite; 2–5% K-feldspar; ,1–2% plagioclase; ,2% muscovite 1 biotite; ,1% carbonate allochems; ,2% heavy minerals
Pedogenic Features	25–40% lithorelicts (saprolite clasts); 2–6% Fe/Mn-oxide/oxyhydroxide glaebules; 1–20% very coarse to fine roots; ,1% pedogenic clay

Matrix Porosity	Very high (40–50%), mostly intergranular and in root charnels; decreases progressively downward to contact with saprolite
Fracture Porosity	None; no soil fractures are apparent in field or in thin section

Table D 2. Sandstone soil property (Driese et al., 2001)

Parameter	Soil Property
Geologic/Pedologic Material	Sandstone saprolite derived from weathering of fractured, very fine-grained, parallel- to ripple cross-laminated, glauconitic, peloidal, feldspathic quartz arenite; estimated 20% of saprolite section
Detrital Mineralogy	55–65% monocrystalline quartz; 5–8% glauconite; 5–10% K-feldspar; ,5% plagioclase; 2–5% muscovite 1 biotite;

	,2% carbonate allochems; ,2% heavy minerals
Pedogenic Features	vadose pedogenic clay cements at detrital grain contacts (meniscus) and on undersides of grains (pendant); pedogenic clay infillings of fractures; Fe/ Mn oxide and oxyhydroxide coatings on grain surfaces and in fractures; ,1% roots
Matrix Porosity	High (20–30%), mostly in intergranular pores and to a lesser degree in dissolution intragranular (grain moldic) pores; matrix pore apertures range from 1–100 mm, with modal size in the 20–50 mm size range
Fracture Porosity	Few fracture pores (,5%) unfilled with pedogenic clays, with average spacing of 0.5–5 cm; fracture apertures

	(pre-clay infill) range from 5.0 mm to 0.5 mm, but open fractures range from 1–10 mm

Table D 3. Siltstone soil property (Driese et al., 2001)

Parameter	Soil Property
Geologic/Pedologic Material	Siltstone/shale saprolite derived from weathering of fractured, laminated to weakly bioturbated, illitic to chloritic clayey siltstone to silty shale; estimated 50% of saprolite section
Detrital Mineralogy	matrix consists of 50–80% illite, with subordinate chlorite; 10–30% monocrystalline quartz; 5–10% detrital biotite and muscovite; ,1% glauconite; ,1% heavy minerals

Pedogenic Features	abundant pedogenic clay random (disordered) smectite/chlorite or smectite/ vermiculite; pedogenic clay and Fe/Mn oxide and oxyhydroxide porefillings and coatings of fractures; 2–5% roots
Matrix Porosity	Probably high (30–50%), but cannot be resolved with petrographic microscope; matrix pore apertures probably ,1 mm
Fracture Porosity	Common fracture pores (10–20%), with average spacing of 0.5–3 cm; fracture apertures (pre-clay infill) range from 5.0 mm to 1.5 mm, with modal size of 10–20 mm for open fracture pores

Table D 4. Limestone soil property (Driese et al., 2001)

Parameter	Soil Property
Geologic/Pedologic Material	Limestone saprolite derived from weathering of fractured, intraclastic rudstone to floatstone that consists of 0.5–10 cm diameter, discoidal intraclasts comprised of sandy, peloidal and skeletal lime grainstone to packstone; estimated 30% of saprolite section
Detrital Mineralogy	matrix consists of mixture of 80–90% illite and random (disordered) smectite/ chlorite; 10–40% monocrystalline quartz; 2–5% detrital biotite and muscovite; 95% glauconite; ,1% heavy minerals
Pedogenic Features	abundant pedogenic clay random (disordered) smectite/chlorite or smectite/

	vermiculite; pedogenic clay and Fe/Mn oxide and oxyhydroxide porefillings and coatings of fractures; 2–5% roots
Matrix Porosity	High (30–50%), includes large root pores (up to 5 mm) in matrix, but many other matrix pores cannot be resolved with petrographic microscope; most matrix pore apertures probably ,5 mm
Fracture Porosity	Few fracture pores (,5%) unfilled with pedogenic clays, with average spacing of 0.5–5.0 cm; fracture apertures (pre-clay infill) range from 5.0 mm to 2 mm

The EFPC soil properties were obtained from Han et al. (2012). The soil samples included EFPC floodplain surface soil (n = 23), EFPC bank soil (n = 3), sediment and sediment soil profile (n = 10). Han et al. (2012) reported that the soil samples were analyzed for their mineral compositions: Fe_2O_3, Mn, and Carbon and the cation exchange capacity (CEC) (Table D 5). The soil Hg concentrations as cinnabar-Hg, non-cinnabar-Hg, and total-Hg were also analyzed (Table D 6).

Table D 5. EFPC Soil composition (Han et al., 2012)

Soil type	Depth	Fe_2O_3	Mn	CEC	Carbon	pH
Surface soil	0-20	2.45	0.11	18.50	4.44	7.04-7.46
Sediment	-	2.5	0.14	7.30	2.78	7.52
Bank soil	0.10	1.99	0.09	13.31	2.09	7.32-7.46
	50-60	2.91	0.08	6.96	1.29	7.40-7.84
Sediment soil profile	0-10	2.85	0.11	12.33	3.10	7.38-7.51
	50-60	2.15	0.08	11.33	1.34	7.37-7.99
	100-110	2.79	0.08	10.20	2.48	7.47-7.64

Table D 6. Concentrations of cinnabar mercury, non-cinnabar mercury and total mercury in bank soils and sediment of Lower East Fork Poplar Creek, Oak Ridge, TN obtained from Han et al. (2012)

Soil Type	Depth cm		Noncinnabar -Hg mg/kg	Cinnabar -Hg mg/kg	Total Hg mg/kg	Noncinnabar -Hg %	Cinnabar -Hg %
Bank soil	0-10	Average	51.4	1.0	52.3	98.2	1.8
		Standard deviation	4.7	0.7	5.3	1.1	1.1
		Maximum	56.3	1.7	58.1	98.9	3.0
		Minimum	47.0	0.5	47.5	97.0	1.1
	50-60	Average	23.2	17.9	41.1	63.0	37.0
		Standard deviation	26.9	28.5	20.0	53.9	53.9
		Maximum	52.9	50.8	53.9	98.2	99.0
		Minimum	0.5	1.0	18.1	1.0	1.8
Sediment	-		72.5	1.7	74.2	97.7	2.3

It can be seen in Table D 5 that the EFPC soils evidentially consists of minerals which are potentially absorb the Hg. Fe_2O_3 content in the bank soil increased with depth while there is no trend for sediment profile soil. Mn mineral concentrations show the decrease trend with depth for both bank and sediment profile soils.

Table D 6 shows the Hg concentrations in the EFPC soil, the data indicated that, for the bank soil, the noncinnabar-Hg decreases with depth while the cinnabar-Hg increases with depth. For the sediment soil, the Hg content is as high as 97.7 mg/kg-soil and 97% Hg content is noncinnabar-Hg.